

Multiscale Modelling of Plant Hormone
Signalling: Auxin Regulated Lateral Root
Emergence

Nathan Mellor

February 2013

Abstract

The formation of lateral roots is an important post-embryonic developmental process that allows plants to adapt to their environment via exploitation of soil mineral resources. New lateral roots initiate as lateral root primordia (LRP) in the pericycle cell layer adjacent to the central vascular tissue in the primary root, and must pass through the outer cell layers of endodermis, cortex and epidermis to emerge as mature roots. A key regulator of emergence is the plant hormone auxin and it has been shown previously that in *Arabidopsis* the auxin induced expression of the auxin influx carrier LAX3 in specific cortical cells over LRP is required for emergence to occur, as this leads to the expression of cell wall remodelling enzymes such as polygalacturonase (PG). By developing mathematical models of auxin transport and LAX3 expression the work in the thesis aims to test the existing conceptual models for lateral root emergence, and provide testable hypotheses for the existence of additional gene regulatory components. An initial single cell model demonstrates that hysteresis and bistability may explain the experimentally observed ‘all-or-nothing’ LAX3 spatial expression pattern in cortical cells containing a gradient of auxin concentrations. By fitting model parameters against experimental data, the model is then used to show that some auxin homeostasis mechanism is present, with both endogenous and exogenous sources of homeostasis investigated. The single cell model also investigates the validity of several alternative gene regulatory networks for LAX3, and its apparent repression by a key mediator of the auxin response, ARF19. Finally, the model is extended to a multicellular context, in which the auxin distribution from a simulated LRP source cell is used as a basis for the expression of LAX3, leading to the expression of PG in specific cells between which the LRP must pass.

Acknowledgments

The work was funded by the University of Nottingham as part of the IDTC program at the Multidisciplinary Centre for Integrative Biology (MyCIB). Thanks to my Supervisors John King, Malcolm Bennett, Matt Loose and Charlie Hodgman, and all at the Centre for Plant Integrative Biology (CPIB). In particular, thanks must go to Alistair Middleton for help and discussions, and to my experimental collaborators at Nottingham, Antoine Larrieu, Benjamin Péret and Silvana Porco, and at Umeå University, Ilkka Sairinen and Karin Ljung, for providing me with data throughout the project. Finally, thanks to Chris for all her support, and giving me the self-belief that i could actually do this!

Contents

1	Introduction	6
1.1	Biological Background	6
1.1.1	Motivation and objectives	6
1.1.2	Plant root architecture and cellular structure	8
1.1.3	Auxin and plant development	11
1.1.4	Auxin biosynthesis, metabolism and transport	14
1.1.5	Auxin signalling and gene activation	17
1.1.6	Lateral root development in <i>Arabidopsis</i>	20
1.2	Modelling of Plant Hormone Signalling	28
1.2.1	Auxin transport models	28
1.2.2	Auxin signalling and gene regulation models	29
1.2.3	Frameworks for model implementation	31
1.3	Thesis Summary	31
2	Gene Regulatory Network Model: One Auxin Response Factor (ARF7)	35
2.1	Initial LAX3 Gene Network Model	35
2.1.1	The LAX3 gene regulatory network	35
2.1.2	Model Formulation and Initial Parameter Estimates	36
2.1.3	Steady State Analysis	42
2.1.4	Time Course Simulations	48
2.2	Parameter Fitting and Predictions From Initial LAX3 Models	51
2.2.1	Fitting Algorithm	51
2.2.2	Parameter Fitting using Full Model	53
2.2.3	Model Simplifications	55
2.2.4	Parameter Fitting Using Reduced Model	61
2.3	Short and long term behaviour of Aux/IAA (DII-VENUS model)	64
2.3.1	Model formulation	65
2.3.2	Parameter Fitting	66
2.4	Model Predictions	69
2.4.1	IAA14 mRNA	70
2.4.2	LAX3 mRNA	71
2.5	Discussion and Conclusions	75
3	Auxin Inducible Auxin Conjugation	79
3.1	Introduction and Model Formulation	79
3.1.1	Model formulation	79

3.2	Parameter Fitting Using Conjugation Model	83
3.3	Time Course and Parameter Sensitivity	85
3.4	Steady State Analysis	87
3.4.1	Pulses In LAX3 expression	93
3.5	Discussion and Conclusions	93
4	Gene Regulatory Network Model: Two Auxin Response Factors (ARF7 and ARF19)	99
4.1	Biological Background	99
4.2	Simple ARF7 and ARF19 model	101
4.2.1	Model Formulation	101
4.2.2	ARF7 and ARF19 share parameter values	107
4.2.3	The ARF7 model can approximate the ARF7 and ARF19 model	111
4.2.4	ARF19 can act as a transcriptional repressor	111
4.3	Models with ARF19 activated repressors	114
4.3.1	ARF19 activates a single repressor	114
4.3.2	Two Repressor Pathway Model	120
4.4	ARF7-ARF19-LAX3 model with auxin homeostasis	124
4.4.1	Expression of LAX3 mRNA : <i>arf19</i> mutant	125
4.4.2	ARF19 Regulation Models	126
4.4.3	Regulation of LAX3 by ARF19	129
4.5	Discussion and Conclusions	134
5	Tissue Scale Models of Lateral Root Emergence	145
5.1	Introduction	145
5.1.1	Introduction and Biological Background	145
5.1.2	Model Formulation	147
5.1.3	Implementation	151
5.2	Auxin distribution: diffusion only	152
5.2.1	Simulation of auxin treatment	152
5.2.2	Apoplastic diffusion and Casparian strip	154
5.2.3	Simulation of primordium auxin source	158
5.3	Modelling of influx and efflux carriers	166
5.3.1	Fixed distribution of influx and efflux carriers	166
5.3.2	Threshold model for expression of LAX3	170
5.4	Discussion and conclusions	174
6	Multi-scale Models of Lateral Root Emergence	177
6.1	Initial conditions for auxin transport simulations	177
6.1.1	Exogenous auxin treatment	177
6.1.2	Simulation of LRP auxin source	179
6.2	Multiscale model of the DII-VENUS auxin sensor	181
6.3	Primary auxin response: expression of Aux/IAA	182
6.4	Secondary auxin response: expression of LAX3	186
6.5	Tertiary auxin response: expression of PG	190
6.6	Discussion	195

7	Concluding Remarks	200
7.1	Bistability in LAX3 mRNA expression	200
7.2	Sources of auxin homeostasis	201
7.3	The role of ARF19 in LAX3 expression	202
7.4	Multiscale Model and Ongoing Challenges	203

Chapter 1

Introduction

1.1 Biological Background

1.1.1 Motivation and objectives

Food security is defined by the World Health Organisation as ‘when all people, at all times, have access to sufficient, safe and nutritious food for a healthy life’ (World Health Organisation 2012a). They cite four basic components to achieving this goal: availability, access, utilisation, and stability (World Health Organisation 2012b). Availability refers to the overall quantity and consistency of food production, access refers to the presence of adequate financial or practical means to acquire food, utilisation refers to the proper use of food according to basic standards of nutrition and sanitation, and stability refers to the volatility of the food supply to temporal changes in conditions, such as sudden crises or seasonal shortages.

There are currently many major challenges to global food security, including increasing demand due to population growth, the impact of climate change, high or volatile food prices, and growing competition with biofuel production for land use. The current predictions are for these challenges to become more and more critical throughout the 21st century, with demand for food projected to increase by 50% by 2030, and double by 2050 (BBSRC 2012). While many of the problems with food security may be political or sociological in nature, the changes to water availability, temperature extremes, and pest and disease distribution, brought about by climate change may be addressed by science, with one of the stated aims of the BBSRC being ‘to use the same amount of land to grow more food of greater nutritional value, using less energy, water and pesticides whilst producing less waste’ (BBSRC 2012). Cereal crops, whether for use as feed for animals eaten as meat, or used directly for consumption by humans, play a critical role in global food production, with over 2000 million tonnes estimated to have been produced worldwide in 2011/2012 (Food and Agriculture Organization of the United Nations 2012). A key factor in crop yields is clearly the efficient utilisation by crop plants of soil nutrient, water and mineral resources, and central to this is an efficient root network (Lynch 1995; Smith and De Smet 2012).

Root systems perform several essential functions in the success of all crop plants, including uptake of water and minerals, the provision of anchorage

within the soil, and the establishment of biotic interactions in the rhizosphere (Lopez-Bucio et al. 2003). Maximising a plant's potential for growth in a heterogenous environment therefore requires an extensive, but efficient, exploration of the surrounding soil. Increasing the total root surface area may be achieved by growth of the primary root via cell division near the tip of the primary root, by the formation of root-hairs on the outer epidermal cells, or by the creation of lateral roots (Lopez-Bucio et al. 2003). The first lateral roots branch from the primary root but, as those lateral roots mature, laterals of laterals may be formed, and so on, creating a vast array of potential root architectures (Lynch 1995). The better adapted a crop's root architecture is to a particular environment, the greater the potential yield from that crop.

A plant's root architecture is not entirely pre-defined by its genotype, rather it is highly plastic and able to adapt to a range of environmental cues. These include the content and distribution of minerals within the soil, such as nitrogen, phosphorus, iron and sulphur, all of which have been shown to alter root architecture, either by affecting primary root growth, the growth of root hairs, or the formation of lateral roots (Lopez-Bucio et al. 2003; Smith and De Smet 2012). In particular, low levels of phosphate are known to increase the density of lateral root formation, while nitrogen is seen to have an effect on lateral root elongation rather than the formation of new laterals (Zhang and Forde 1998; Linkohr et al. 2002). Additional factors affecting root architecture include the heterogeneity or 'patchiness' of the soil matrix (Hinsinger et al. 2005; Hodge 2006), and biotic interactions, such as those with either pathogens or mycorrhizae (Osmont et al. 2007).

There is a broad and on-going body of research into the effect of environmental cues on plant root systems, and how this affects agricultural yields. The focus of this thesis however, is on a particular aspect of one of the fundamental developmental processes that defines a plant's root architecture, that of the emergence of new lateral roots. Like much of plant development, the growth of a new lateral root occurs post-embryonically and is an example of organogenesis. While this organogenesis can occur in response to exogenous cues from the environment, many of the endogenous mechanisms by which it takes place remain unknown. As will be discussed in more detail in Section 1.1.6, lateral roots are initiated in an inner cell layer adjacent to the central vascular tissue of the primary root, and develop via a series of cell divisions, which will ultimately form the new lateral root with a new meristem at its tip (Peret et al. 2009a). Before the lateral root can be fully formed, however, it must emerge through the outer cell layers of the root, without damaging the primary root, or exposing the plant to pathogens from the soil (Peret et al. 2009b). The number of cell layers through which the lateral root must emerge varies with different species, with three outer cell layers in the model plant species *Arabidopsis thaliana* (*Arabidopsis*), and as many as 15 to 20 cell layers in cereal crops such as rice and maize (Hochholdinger and Zimmermann 2008).

A better understanding of lateral root emergence will require an understanding of several inter-connected developmental processes. These include the intracellular signalling and gene regulatory events that lead up to the

expression of genes controlling emergence of new laterals, and how these signalling events are arranged spatially by cell position within the root. In particular, the plant hormone auxin is central to the current understanding and conceptual models of how emergence is regulated, as described in detail in Sections 1.1.3-1.1.6. In Swarup et al. (2008) it was proposed that the focusing of auxin into particular cells near to the developing lateral root leads to the expression of cell wall remodelling enzymes (CWREs) in these cells, allowing for cell separation, and facilitating emergence between them without further damage to root tissues. Mathematical modelling provides a means by which this conceptual model may be investigated further, and extended and refined in order to generate new hypotheses for testing. Since much of the existing literature and data on emergence relate to *Arabidopsis*, this species is chosen as a basis for the models developed. However, as discussed above, due to the importance of lateral root emergence on cereal crops, it is desirable for the framework for the models to be easily transferable to species with different cellular structures of their primary roots. The initial objectives for the work described in the thesis are therefore as follows:

1. Develop a gene network scale model of the key genes and auxin signalling events involved in lateral root emergence in *Arabidopsis*.
2. Develop a tissue scale model of the spatial distribution of auxin leading up to the expression of cell wall remodelling enzymes.
3. Combine the gene network and tissue scale models into a multi-scale model, which may be transferable to the different spatial cellular structures found in cereal roots.

1.1.2 Plant root architecture and cellular structure

Before looking in more detail at the role of auxin in plant development (Section 1.1.3), in particular its role in lateral root initiation, development and emergence (Section 1.1.6), we first describe some basic aspects of plant physiology important to the discussion, and compare the overall root architecture, morphology and cellular structure of *Arabidopsis* with cereals such as rice and maize.

One of the important differences between plants and animal species is the presence in plants of a cell wall made of cellulose, outside of the cell membrane, between every cell. This provides a rigid cellular structure, support and protection, and also a fixed matrix known as the apoplast, within which water and other small molecules such as plant hormones may travel. For a lateral root to emerge without damaging the primary root, specific cell walls must be softened and separated, but this process must be tightly controlled to maintain the integrity of the root.

In vascular plants there may be a secondary thickening of cell walls with lignin, providing even more rigidity, and a means to transport water, sugars, hormones and minerals over large distances. This vascular tissue consists of xylem, which conducts water and other solutes from the root

to the shoot and leaves, and phloem vessels, which conduct the products of photosynthesis from the leaves to the tissues of the shoot and the root. The plant embryo is part of the seed of a vascular plant and contains the precursor to the shoot, known as the hypocotyl, the precursor to the primary root, known as the radicle, and one or more cotyledons. Cotyledons form the first leaves of the plant post-germination. If a plant has one cotyledon, such as cereals or grasses, it is known as a monocot, if it has two cotyledons, as does *Arabidopsis*, it is a dicot.

Following germination, growth occurs at meristems, which are the small regions of the plant containing undifferentiated stem cells which are able to divide. The meristem near the tip of the shoot is known as the shoot apical meristem (SAM), while that near the tip of the primary root is the root apical meristem (RAM). Growth of the primary root is determined by cell division at the RAM. During the process of forming a lateral root, a new meristem must be formed near the tip of the emerging root.

Lynch (1995) defines root morphology as the surface appearance of a root system, including epidermal features such as root hairs, and also the pattern of appearance of daughter roots from the main axis of the plant. In general, cereals such as rice (*Oryza sativa*) and maize (*Zea mays*) have a relatively complex root morphology, with several different types of root present in addition to the primary root established during embryogenesis (Hochholdinger et al. 2004; Hochholdinger and Zimmermann 2008). Both maize and rice form shoot-borne roots, with those initiating below ground known as crown roots and those initiating above ground known as brace roots. In addition, maize has another type of root, known as seminal roots, which originate from the scutellar node, between the primary root and the mesocotyl, which is the section of the seedling between the primary root and the developing shoot (Hochholdinger et al. 2004).

In comparison to cereals, and many other plant species, *Arabidopsis* has a very simple root morphology, with the root system limited to the embryonic primary root, and laterals originating from the primary root. It is this simplicity which makes *Arabidopsis* suitable for use as a model plant organism for detailed study. Many genetic mutants affecting different aspects of root morphology have been identified, in both cereals and *Arabidopsis*. In cereals these mutants can affect the formation of either shoot-borne or lateral roots, primary root length, or formation of root hairs (for reviews, see Hochholdinger et al. (2004), Hochholdinger and Zimmermann (2008), Smith and De Smet (2012)). Mutants affecting lateral root formation in *Arabidopsis* are discussed further in Section 1.1.6.

Though cereal roots are generally much larger in diameter than *Arabidopsis* roots, the basic radial cellular structure of the primary root is similar in both, with a central group of cells forming vascular tissue known as the stele, surrounded by concentric rings of cell types, divided into four layers, known as the pericycle, endodermis, cortex and epidermis (Figure 1.1, Peret et al. (2009b)). In both cases, the pericycle is a single layer of cells surrounding the stele, the endodermis a single layer of cells surrounding the pericycle, and the epidermis is the outer cell layer where the root hairs are located on the outer surface of the root. The endodermis contains a band

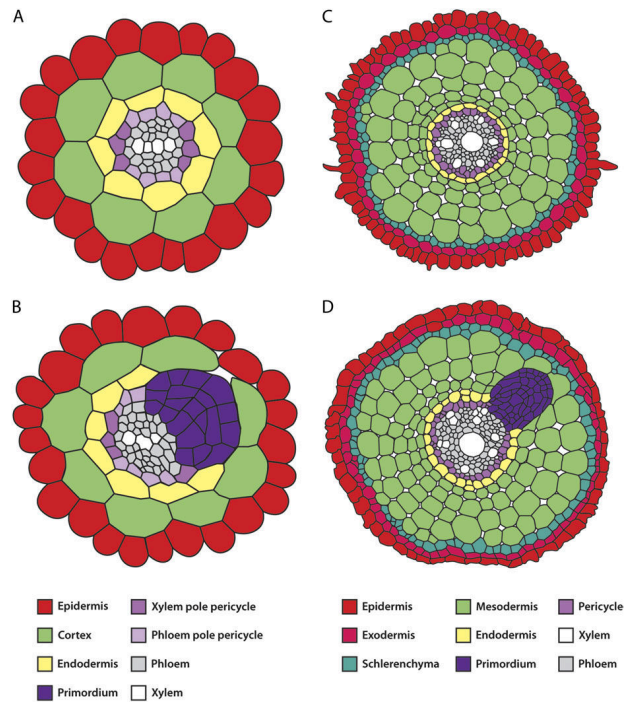


Figure 1.1: Cross section of *Arabidopsis* root without (A) and with (B) an emerging lateral root primordium. The root is arranged in well defined cell layers surrounding the central vascular tissue or stele. Lateral root primordia initiate and develop in the innermost layer, the pericycle, and to emerge as lateral roots must pass between cells in the outer layers, endodermis, cortex, and epidermis. The cell separation which allows for emergence is believed to be regulated by auxin induced expression of cell wall remodelling enzymes (CWREs) in specific cells in the outer cell layers. In cereals such as rice (*Oryza sativa*) there are many more cell layers comprising the outer cell layers, including the extra cell types exodermis and schlerenchyma (C), presenting a greater barrier to emergence of lateral root primordia (D) than in *Arabidopsis*. The *Arabidopsis* root diameter is $100\ \mu\text{m}$, that for rice is $300\ \mu\text{m}$. (Reproduced from Peret et al. (2009b).)

of differentiated cell wall known as the Casparian strip, a protective barrier which blocks passive flow of water and other solutes taken in by the root into the vascular tissue, and therefore the rest of the plant.

The main differences in primary root anatomy between *Arabidopsis* and cereals occur when comparing the composition and size of the stele, and also the number of cells comprising the cortex. In *Arabidopsis* the stele is generally much smaller than in cereals, with just two phloem poles and two xylem poles, while in cereals there may be as many as 10 xylem and 10 phloem poles in the stele (Smith and De Smet 2012). New lateral roots are initiated adjacent to alternating left-right xylem poles in *Arabidopsis*, but adjacent to phloem poles in cereals. In addition, in cereals the initial cells ultimately forming lateral roots may be in both the pericycle and the endodermis, while in *Arabidopsis* all lateral roots are initiated in the pericycle (Hochholdinger et al. 2004). In the context of lateral root emergence, perhaps the most important difference between *Arabidopsis* and cereals is the width of the cortex, which in cereals may consist of 10-15 cell layers, compared to just a single cell layer in *Arabidopsis* (Hochholdinger and Zimmermann 2008). The multiple cortical cell layers found in cereals mean that emergence of lateral roots through the outer tissues is likely to be a more complex process than in *Arabidopsis*, where just one cortical cell layer must be negotiated. Because of this, and the higher volume of data and literature available, we restrict the discussion from now on to root development in *Arabidopsis*, in particular in response to the plant hormone auxin.

Figure 1.2 (Peret et al. 2009a) shows a longitudinal section of the tip of an *Arabidopsis* root, showing the different cell types on the left, and the sites of auxin maxima on the right. The apical meristem region is the primary site of cell division and also contains the quiescent centre, which is a group of cells at the centre of the dividing undifferentiated cells of the meristem which themselves remain undivided. Above this is the basal meristem in which there is both division and elongation, and the elongation zone itself, which is the primary site of cell elongation and growth. Above the elongation zone, about 500 μm from the root tip, is the differentiation zone, in which the elongated cells differentiate into the mature root tissue as organised in Figure 1.1 (Dolan et al. 1993). As shown in Figure 1.2 the initialisation of lateral roots occurs very early on following the initial divisions in the apical meristem in response to maxima of the plant hormone auxin in the basal meristem region. This phytohormone is central to many plant developmental processes, in particular in relation to lateral root development, as discussed further in Sections 1.1.3-1.1.6

1.1.3 Auxin and plant development

Plant hormones

The development and growth of plants is regulated by a range of hormones, small molecules synthesised within plant cells, acting as signals for developmental changes to cells either local to the site of synthesis, or in cells at a distance from the hormone source. There are several main classes of plant hormones including auxin, cytokinin, brassinosteroids (BR), gibberellins or

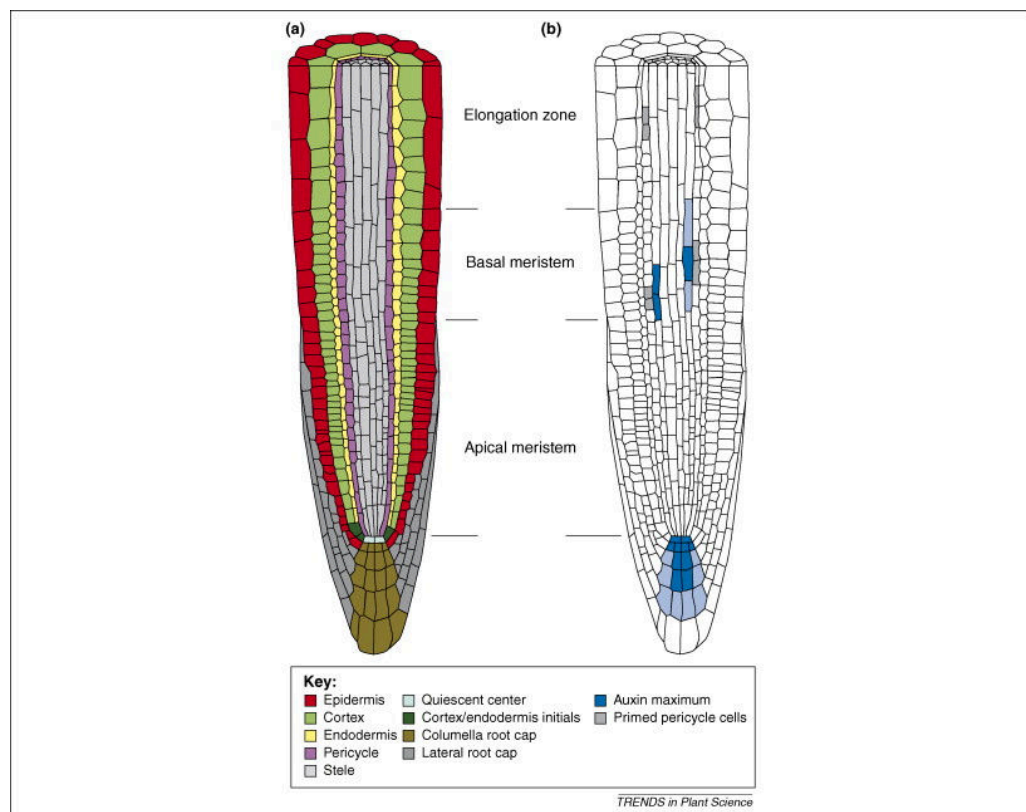


Figure 1.2: (a.) Schematic overview of the different cell types and developmental zones near the tip of the *Arabidopsis* root tip. (b.) Sites of auxin response maxima as detected by the DR5::GUS marker line. (Reproduced from Peret et al. (2009a).)

gibberellic acid (GA), abscisic acid (ABA), jasmonates or jasmonic acid (JA) and strigolactones. These hormones may act alone, or in combination with others to regulate a vast array of developmental processes (Depuydt and Hardtke 2011; Durbak et al. 2012), with the means of signal perception within the cell varying for different types of hormone (Santner and Estelle 2009; Shan et al. 2012). For example, brassinosteroids, ABA, and cytokinins are perceived by receptors at the cell membrane, resulting in a signalling cascade and transcription of target genes in the nucleus, while auxin, GA and JA are shown to accelerate the degradation of a repressor of target genes.

The hormones auxin, cytokinin, ethylene, ABA, BR, and GA have all been shown to affect root growth in different and interacting ways (Benkova and Hejtko 2009). Brassinosteroids are known mainly as promoters of organ growth via cell division and expansion (Gudesblat and Russinova 2011), with application of exogenous BR shown to increase the length of the primary root (Mussig et al. 2003). GA also regulates root growth by stimulating cell expansion in the endodermis, and this expansion limits the overall growth of the primary root (Ubeda-Tomas et al. 2008). Cytokinins are known to have a negative effect on root growth (Benkova and Hejtko 2009), and the interaction between cytokinin and auxin regulates the size of the root apical meristem (Nordstrom et al. 2004; Muraro et al. 2011).

Auxin

Of all the plant hormones, perhaps the best known and most studied is auxin, and it is involved in almost every aspect of plant development (Woodward and Bartel 2005; Teale et al. 2006; Benjamins and Scheres 2008). Perhaps the earliest recorded observation of an effect of auxin is given in Darwin and Darwin (1880), where the bending of grass coleoptiles towards the light, or phototropism, was observed. This was later found to be due to the accumulation of auxin on the side of the shoot furthest from the light source, promoting an increased growth rate on that side (Cholodny 1926; Went 1926). This effect of auxin in promoting growth in the shoot is reversed in the root, where it is shown to inhibit growth. This inhibitory effect on root growth is seen during gravitropism, the bending of roots toward a gravistimulus, where auxin accumulates on the lower side of the root, inhibiting growth on that side and bending the root downwards (Bennett et al. 1996).

In addition to tropisms, auxin is a key regulator in many important developmental processes, including embryo patterning (Friml et al. 2003; Jenik et al. 2007), leaf vein formation (Sieburth 1999; Rolland-Lagan and Prusinkiewicz 2005), and phyllotaxis (Bohn-Courseau 2010), the ordered formation of new leaves at the shoot apical meristem. In the root, in addition to its role in gravitropism (Bennett et al. 1996) and in controlling the size of the RAM (Sabatini et al. 1999), auxin is involved in root hair formation (Jones et al. 2009), and in every aspect of lateral root initiation, development and emergence (Section 1.1.6). Before discussing the role of auxin in lateral root development in detail, however, it is helpful to outline the existing knowledge on the mechanisms by which auxin is transported within the plant (Section 1.1.4), and how it is perceived by the cell, lead-

ing to the expression of genes which result in the numerous developmental changes described above (Section 1.1.5).

1.1.4 Auxin biosynthesis, metabolism and transport

The most common endogenous form of auxin is indole-3-acetic acid (IAA), of a similar structure to the amino acid tryptophan (Ljung et al. 2002), though other endogenous auxins including indole-3-butyric acid (IBA), 4-chloroindole-3-acetic acid (4-Cl-IAA) and phenylacetic acid (PAA) are present in the plant, and synthetic auxins such as 2,4-dichlorophenoxy acetic acid (2,4-D) and naphthalene-1-acetic acid (NAA) may also be used experimentally (Simon and Petresek 2011). The primary site of auxin synthesis is in the leaves, though all tissues within seedlings may synthesise some auxin (Ljung et al. 2001).

In general, the developmental changes brought about by auxin occur due to the establishment of concentration gradients within tissues, with morphological changes usually occurring at the site of auxin maxima, but in some cases at auxin minima (Sorefan et al. 2009). Though the principal determinant of the location of these maxima and minima is transport of auxin from source to site of action, they may also be controlled in part by local auxin biosynthesis and metabolism (Normanly 2010). Both tryptophan-dependent and tryptophan-independent auxin biosynthesis pathways have been characterised (Ljung et al. 2002; Normanly 2010), with many of the genes found to regulate these pathways, in *Arabidopsis* as well as other species, reviewed in Mano and Nemoto (2012). Ljung et al. (2002) describes several metabolic pathways by which the biologically active pool of auxin may be decreased, including oxidisation and conjugation of auxin to amino acids, peptides or sugars. In particular, a set of auxin responsive genes known as the GH3 family has been shown to conjugate auxin to amino acids (Staswick et al. 2005), which may provide an auto-regulatory or homeostatic mechanism by which cells can buffer high auxin concentrations.

The best described mechanism by which plants establish and maintain auxin gradients within organs and tissues, is by moving auxin from the source of biosynthesis to the site of activity. This is achieved by the organised polar localisation of auxin transporters on plant cell membranes, resulting in the directional flow of auxin within and between organs (Petresek and Friml 2009; Zazimalova et al. 2010). As a weak acid, auxin is present in both anionic and protonated forms, the proportions of which are determined by the local pH. The apoplast is relatively acidic ($\text{pH} \approx 5.5$) and so there is a significant proportion of auxin in the protonated form, while in the cytoplasm, with neutral pH, most auxin is present in the anionic form. This is important since auxin can only diffuse freely across the cell membrane in its protonated form, and in the anionic form active carriers for auxin are needed for it to cross the cell membrane, meaning that auxin is able to diffuse freely from the apoplast into the cytoplasm, but active efflux is required to move auxin from cytoplasm to apoplast (Kramer and Bennett 2006). This acid trapping in conjunction with polar or directional localisation of transporters allows the plant to move auxin over long dis-

tances within its tissues, and establish gradients within organs triggering developmental changes.

Auxin transporters are either efflux (from cell to apoplast) or influx (from apoplast to cell) carriers, with the main class of efflux carriers being the PIN gene family (Paponov et al. 2005), and the main class of influx carriers being the AUX/LAX gene family (Peret et al. 2012). An additional class of efflux carriers, the ABCB transporters, have also been shown to have a role in plant development (Petresek and Friml 2009). There are eight members of the PIN family in *Arabidopsis*, PIN1-8, which have been shown to have different and overlapping expression patterns and functions in development. Perhaps the most important of these is PIN1, which is the primary PIN facilitating polar auxin transport from shoot to root (Glweiler et al. 1998), as well as having a role in phyllotaxis at the shoot apical meristem (SAM) (Reinhardt et al. 2003; Benkova et al. 2003), the establishment of apical-basal cell polarity in developing embryos (Weijers et al. 2005), leaf vascular patterning (Scarpella et al. 2006), and in the development of lateral roots, along with PIN2 and PIN3 (Benkova et al. 2003). PIN2 (Muller et al. 1998), PIN3 (Friml et al. 2002b), along with PIN7 (Blilou et al. 2005), also have a role in root gravitropism, while PIN4 is involved in patterning at the root apical meristem (Friml et al. 2002a). Rather than localisation at the cell membrane causing auxin efflux out of the cell, PIN5 (Mravec et al. 2009) and PIN8 (Ding et al. 2012) are localised at the ER (endoplasmic reticulum) so that auxin may be compartmentalised within the cell, suggesting a role for PIN expression in intracellular auxin homeostasis.

The best known auxin influx carrier is AUX1, shown to have a role in gravitropism (Bennett et al. 1996), phyllotactic patterning (Bainbridge et al. 2008), and root hair growth (Jones et al. 2009). In contrast to PINs which are usually localised to a particular face, or faces of a cell, giving directionality to the flow of auxin, influx carriers such as AUX1 are generally localised to all faces of a cell, restricting the spread of auxin within the domain of expression. In addition to AUX1, there are three other members of the AUX/LAX family of influx carriers, LAX1, LAX2 and LAX3. LAX1-3 are shown to act redundantly with AUX1 to maintain regular phyllotactic patterning (Bainbridge et al. 2008), while LAX2 is shown to regulate vascular patterning in cotyledons (Peret et al. 2012). Of particular interest to the study of lateral roots, however, is the role of LAX3 in facilitating emergence (Swarup et al. 2008), discussed in detail in Section 1.1.6.

As with the AUX/LAX influx carriers, and in contrast to the PIN efflux carriers, the ABCB efflux carriers are generally localised to all cell membranes. Since they are efflux carriers, they are likely to prevent auxin accumulating in the cells where they are expressed. In particular ABCB19 and ABCB4 are expressed in the stele and the epidermis above the RAM, and ABCB1 and ABCB19 are expressed below the SAM (Petresek and Friml 2009). In addition, both ABCB1 and ABCB19 are shown to be involved in the initiation of lateral roots (Mravec et al. 2008).

Figure 1.3 summarises the location of the different carriers within root tissues. In the primary root this forms the basis of the auxin reflux/ re-

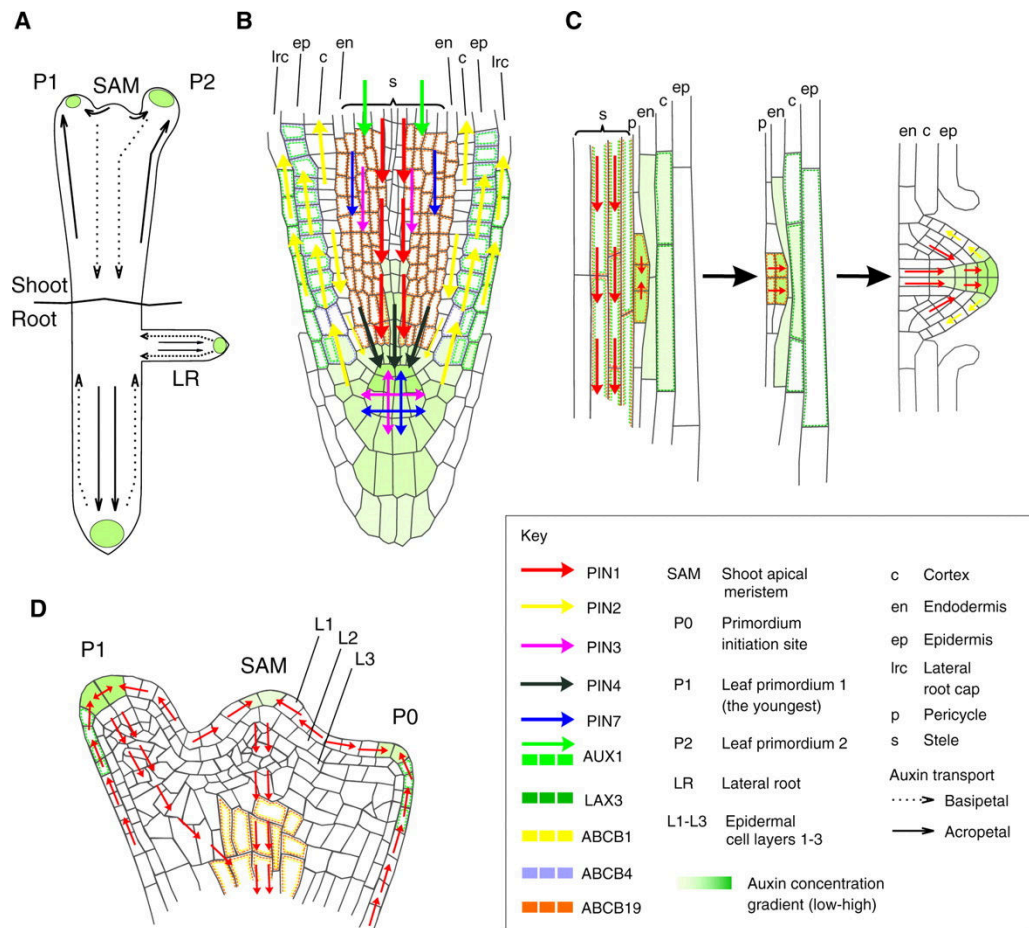


Figure 1.3: (A) Schematic overview of the direction of flow of auxin in the root and shoot of *Arabidopsis*. Location of auxin transporters in the root tip (B), developing lateral roots (C), and at the shoot apical meristem (D). Arrows indicate auxin flow due to a particular transporter, while the dotted lines represent the presence of transporters with no apparent polarity. (Reproduced from Petresek and Friml (2009))

verse fountain model (Petresek and Friml 2009; Peer et al. 2011), in which polar auxin transport mediated by PIN1 transports auxin through the vascular tissue towards the root tip, PINs 3,4 and 7 combine to move auxin through the columella and laterally into the root cap, and PIN2 and AUX1 in the cortex and epidermis transport auxin back towards the shoot. This reverse fountain model is partially mimicked during the development of a new lateral root, with PIN1 directing auxin towards the new root tip, and PIN2 directing auxin laterally and away from the root tip. Before looking in more detail at how auxin and auxin transport regulate the development and emergence of lateral roots in Section 1.1.6, the mechanisms by which auxin signals are detected and acted upon by plant cells are described in Section 1.1.5.

1.1.5 Auxin signalling and gene activation

The most established conceptual model for auxin signalling involves the interaction of two gene families, the ARFs and the Aux/IAAs (Overvoorde et al. 2005; Okushima et al. 2005; Teale et al. 2006). The ARFs may be either transcriptional activators or repressors and, in the absence of auxin, the Aux/IAAs are able to dimerise with the activating ARFs and repress transcription. In the presence of an auxin signal, however, the degradation of the Aux/IAAs is accelerated and the ARFs are free to activate a set of context-dependent response genes, leading to a range of developmental changes (Figure 1.4). Auxin is perceived in the cell via binding with a receptor complex, SCF^{TIR1} (TIR1). The Aux/IAAs then bind with the TIR1-auxin complex, and are targeted for degradation. Though an additional possible auxin receptor has been identified, ABP1, which may provide a mechanism for a more rapid auxin response than the SCF^{TIR1} receptor (Sauer and Kleine-Vehn 2011), it remains relatively poorly understood. Because of this, the attention of this thesis is restricted to the transcriptional changes brought about by auxin signalling via the SCF^{TIR1} pathway.

The SCF^{TIR1} complex is an ubiquitin (Ub) protein ligase, meaning that it catalyses the conjugation of a chain of polymerised Ub to its binding substrate, in this case the Aux/IAAs. Once ubiquitinated in this way, the proteins are then targeted for degradation by the 26s proteasome (Mockaitis and Estelle 2008). This interaction between TIR1 and Aux/IAA is shown to be dependent on auxin (Gray et al. 2001; Dharmasiri et al. 2003), and this occurs due to the direct binding of auxin to the TIR1 receptor (Dharmasiri et al. 2005; Kepinski and Leyser 2005). Furthermore, it is shown that the binding of auxin to TIR1 facilitates the binding of Aux/IAAs to the TIR1 receptors, thus forming a TIR1-auxin-Aux/IAA complex (Tan et al. 2007). Though TIR1 was the first such receptor to be found, there is a family of genes in *Arabidopsis* with high sequence similarity, named AFB1-AFB5 (Mockaitis and Estelle 2008). AFB1-AFB3 were shown to largely share expression domains with TIR1, and function redundantly in mediating the auxin response.

The Aux/IAA are a family of short-lived nuclear proteins, of which there are 29 identified in *Arabidopsis*, named IAA1-IAA20 and IAA26-IAA34,

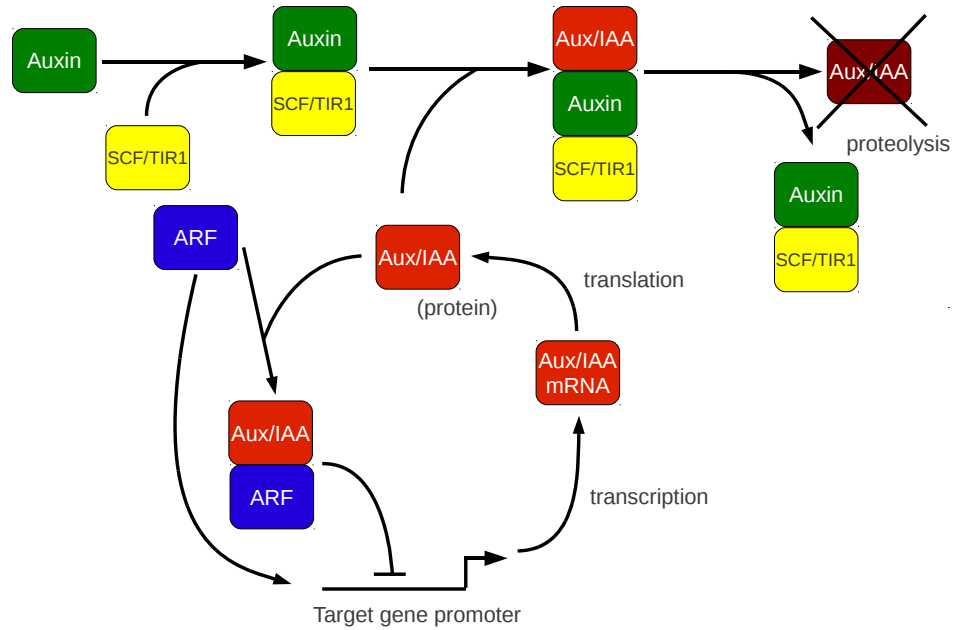


Figure 1.4: Auxin binds with the *SCF^{TIR1}* complex, which is then able to bind Aux/IAA. The Aux/IAAs are then be ubiquitinated and targeted for degradation by the 26S proteasome. The ARFs, free from dimerisation with Aux/IAAs, are then able to activate auxin responsive genes. When Aux/IAA is bound to on the target gene promoter ARF transcription is repressed. Unless stated the arrows represent binding of the different biomolecular complexes. (Figure adapted from Middleton et al. (2010))

which have a mostly conserved modular structure consisting of four domains (I-IV), in addition to a nuclear localisation sequence (Abel et al. 1994; Reed 2001; Overvoorde et al. 2005). Domain I gives the Aux/IAAs their ability to repress transcription (Tiwari et al. 2004), and in IAA12 this domain was shown to interact with the co-repressor TOPLESS (TPL), TPL being required to repress auxin responsive genes (Szemenyei et al. 2008). Domain II is required for interaction with the auxin receptor TIR1, and so it is this domain which causes the degradation of Aux/IAAs in the presence of auxin (Worley et al. 2000; Gray et al. 2001; Ouellet et al. 2001). In Brunoud et al. (2012), domain II of IAA28 was fused to the fast maturing fluorescent protein VENUS, to create a rapidly responding sensor for auxin with cellular resolution. Two of the Aux/IAAs, IAA20 and IAA30, lack a functional domain II and so are not responsive to auxin, though the physiological role for this is unclear (Sato and Yamamoto 2008). The final two domains, III and IV, are required for dimerisation with other Aux/IAAs (Kim et al. 1997) and with ARFs (Ulmasov et al. 1997a). The binding with ARFs is central to the conceptual model of auxin-mediated de-repression of ARFs by degradation of the Aux/IAAs.

The ARFs are a large gene family of transcription factors with 23 members, named ARF1-ARF23 and, as with the Aux/IAAs, they have a highly

conserved four domain structure (Okushima et al. 2005). Domains III and IV are similar to those found in the Aux/IAAs, and allow for dimerisation with both other ARFs and with Aux/IAAs (Ulmasov et al. 1997a, 1999a). Domain I is a DNA binding domain, allowing for the binding by ARFs to the DNA sequence TGTCTC on gene promoters, known as auxin response elements (AuxREs) (Ulmasov et al. 1997a). The gene sequence of domain II is thought to determine whether the ARF acts as a transcriptional activator or repressor (Ulmasov et al. 1999b; Tiwari et al. 2003). Those ARFs with a domain II rich in glutamine, serine and leucine residues (ARF5-ARF8 and ARF19) are thought to act as transcriptional activators, while the remaining ARFs are thought to act as repressors, with the exception of ARF23 which lacks a domain II altogether (Guilfoyle and Hagen 2007). ARF3, ARF13 and ARF17 have a repressing domain II but lack domains III and IV so cannot interact with Aux/IAAs and other ARFs in the usual way.

Among the first downstream targets of the activating or positive ARFs are the Aux/IAAs (Abel et al. 1994, 1995; Abel and Theologis 1996), meaning that there is a negative feedback on the auxin response. This is due to the increased Aux/IAA expression leading to increased Aux/IAA protein dimerisation and subsequent repression of ARF target genes. Other classes of genes known to respond rapidly to auxin are the GH3s and the SAURs (Abel and Theologis 1996). The GH3s have been shown to conjugate amino acids to auxin and other plant hormones such as jasmonic or salicylic acid, and so may play a role in auxin homeostasis and other signalling pathways (Staswick et al. 2005). The role of the SAURs, however, remains unknown (Okushima et al. 2005).

The size of the Aux/IAA and ARF gene families (29 and 23 members respectively) means that there are a large number of possible interactions between the key players in the auxin response. If different combinations of transcriptional activators and repressors are present in different tissues in the plant, this may account for the diverse range of developmental responses regulated by auxin (Lokerse and Weijers 2009). In particular, the specificity of different ARFs for different gene promoters, and the spatial and transcriptional regulation of different ARFs is likely to account for much of the variation in auxin response. A spatial expression map of the ARFs in the *Arabidopsis* root tip and developing embryo is given in Rademacher et al. (2011). Despite the potential number and complexity of interactions between the Aux/IAAs and ARFs, a study of all the possible connections using a yeast two-hybrid assay, as performed by Vernoux et al. (2011), reveals that certain modes of interactivity between the different classes of proteins occur, rather than full connectivity between every protein. Dividing the ARFs into positive or activating (ARF^+) and negative or repressing (ARF^-) ARFs, it is observed that by far the most common interactions are between the Aux/IAAs and the ARF^+ , and between pairs of Aux/IAAs. The ARF^- did not show high connectivity with each other, or with either the Aux/IAA or the ARF^+ . Because of this, it is hypothesised that the ARF^- act independently of the Aux/IAA ARF^+ auxin signalling system described above.

Via the study of mutant plant phenotypes, many Aux/IAAs and ARFs

have been identified as having important roles in the auxin response during a variety of developmental processes. For the Aux/IAAs, the mutants showing greatest developmental defects are gain of function mutants, which have mutations in domain II, meaning they are no longer degraded in response to auxin, and so repression of the downstream targets remains with or without an auxin signal. Examples of gain of function Aux/IAA mutants include *shy2/iaa3*, which affects lateral root formation, gravitopic response, hypocotyl length, and root curvature (Tian and Reed 1999), *bdl/iaa12* in which the root meristem fails to form during embryogenesis (Hamann et al. 2002), and *slr/iaa14* or *solitary root*, in which lateral root formation is blocked entirely (Fukaki et al. 2002). In general, loss of function or knockout mutants in Aux/IAAs do not show obvious phenotypic differences to wild type, most likely due to redundancy between the Aux/IAAs (Okushima et al. 2005). Loss of function mutants in the ARFs include *arf3/ett*, which affects gynoecium (the seed bearing organ in flowers) patterning (Nemhauser et al. 2000), *arf5/mp*, which has defects in the embryo and vascular patterning (Hardtke and Berleth 1998), and *arf7/nph4/msg1/tir5*, which shows a range of developmental defects (Okushima et al. 2005). ARF7 is also shown to affect lateral root formation in conjunction with ARF19 (Okushima et al. 2007), as will be discussed further in Section 1.1.6.

1.1.6 Lateral root development in *Arabidopsis*

In *Arabidopsis*, lateral roots originate from cells within the pericycle cell layer, which undergo a series of ordered cell divisions and develop into lateral root primordia (LRP) (Peret et al. 2009a). As the LRP grow they must pass between cells in the outer cell layers in order to emerge and develop into a mature lateral root (Peret et al. 2009b). Though the different processes in lateral root development are continuous and interlinked, it is helpful to divide them into three sections for study, namely priming, patterning and emergence, all of which are strongly regulated by auxin. Priming refers to the identification and marking of specific pericycle founder cells in the basal meristem to go on and develop into LRP, patterning refers to the initiation and regulation of divisions and growth of LRP, and emergence refers to the programming of the outer cell layers to allow for the passing of LRP between them as they grow.

Priming

As shown in Figure 1.1, lateral roots originate in the pericycle cell layer, the cell layer surrounding the stele. However, in addition to this, the pericycle can be divided into two distinct cell types with diarch symmetry (i.e. there are two right-angled intersecting planes of symmetry), with those cells adjacent to the xylem referred to as the xylem pole pericycle (XPP), and those adjacent to the phloem referred to as phloem pole pericycle (PPP), and it is only the XPP that have the potential to divide and from which lateral roots develop (Parizot et al. 2008). De Smet et al. (2007) showed

that in general, there is an alternate left-right pattern to lateral root initiation sites correlating to bends formed by lateral waving of the root as it grows. This left-right lateral root pattern was found to be dependent on the auxin influx carrier AUX1, which is also required for gravitropism, suggesting the priming of lateral roots is regulated by auxin. Furthermore, regular oscillations in auxin response with a period of 15 hours were detected in the basal meristem using the auxin reporter gene DR5 (Ulmasov et al. 1997b), correlating with the frequency of future lateral root production. These oscillatory auxin maxima were later shown by De Rybel et al. (2010) to correlate with the expression of the transcription factor GATA23, which in turn was shown to be dependent on auxin signalling mediated by the degradation of IAA28 and activation by one or all of ARF5, 6, 7, 8 and 19. It is also possible for the priming of lateral root founder cells to occur outside of the basal meristem, following experimentally induced local auxin production, showing that auxin alone is sufficient to prime cells to form new lateral roots (Dubrovsky et al. 2008).

Patterning

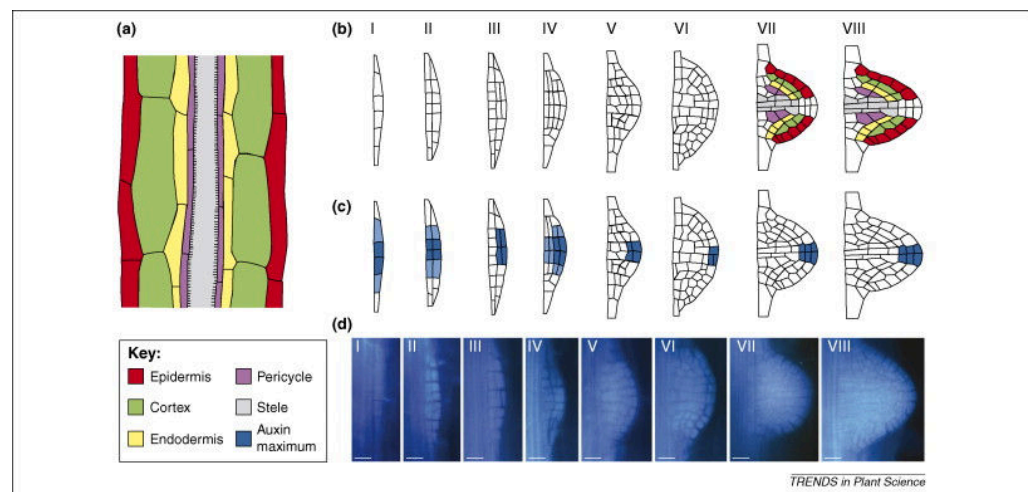


Figure 1.5: (a) Lateral roots originate in the pericycle cell layer adjacent to the central stele in *Arabidopsis*. (b) Cartoon of the eight stages of LRP development as defined by Malamy and Benfey (1997). (c) Cartoon of the auxin response maxima as detected by Benkova et al. (2003) using the DR5:GUS reporter gene. (d) Aniline-blue stained roots showing the cellular structure at each developmental stage. (Reproduced from Peret et al. (2009a).)

LRP are initiated by the migration of the nuclei of two primed cells in the same longitudinal file of XPP cells to their shared cell wall (De Smet et al. 2007). Following this there is a series of anticlinal (perpendicular to the primary root axis) cell divisions, creating what is referred to as a stage I primordium, of up to ten cells (Malamy and Benfey 1997), as shown in Figure 1.5. The next set of divisions are periclinal (parallel to the primary root axis), creating a stage II primordium with two layers. A sequential series of periclinal and anticlinal divisions during stages III-

VII, as defined by Malamy and Benfey (1997) and shown in Figure 1.5, result in the gradual formation of a dome structure, until the primordium emerges through the outer tissue layers at stage VIII. Though the priming of lateral roots occurs in the basal meristem less than 1mm from the root tip, the initial stage I divisions occur several millimetres from the RAM, and the first fully emerged lateral roots appear around 20mm from the root apex (Casimiro et al. 2001). Throughout all stages of development an auxin maximum is maintained at the tip of developing LRP (Benkova et al. 2003).

As with the priming of lateral roots, auxin is shown to have an important role in regulating the initiation and patterning of the developing LRP (Peret et al. 2009a). The gain of function IAA14 mutant *slr-1*, with a stabilised IAA14 insensitive to degradation by auxin is shown to fail to initiate lateral roots (Fukaki et al. 2002), and have impaired expression of cell-cycle genes (Vanneste et al. 2005). A similar phenotype is observed in the *arf7 arf19* double knock out mutant (Okushima et al. 2005; Wilmoth et al. 2005), and the interaction between IAA14 and both ARF7 and ARF19 is observed in a yeast two-hybrid assay (Fukaki et al. 2005), suggesting that an auxin signalling module involving ARF7, ARF19 and IAA14 is important for lateral root patterning. Overexpression of the transcription factors LDB16 and LDB29 was shown to rescue the mutant phenotypes of *slr-1* and *arf7 arf19* and, since the promoters of both LDB16 and LDB29 have ARF binding sites, it is likely that these transcription factors are direct targets of an ARF7 ARF19 auxin signalling module regulating lateral root patterning and development (Okushima et al. 2007). Another component in the development of lateral root primordia is the hormone cytokinin, elevated levels of which appear to disrupt normal cell division and patterning in the primordia by perturbing the expression of PIN efflux carriers, so preventing the formation of auxin gradients (Laplaze et al. 2007). Finally, the expression of a receptor-like kinase ACR4 is shown to be needed to restrict divisions in the cells flanking the primordia, and to prevent development of ectopic lateral roots (De Smet et al. 2008).

Emergence

In order for lateral roots to emerge from their site of initiation in the XPP, they must first pass through the outer cell layers of the endodermis, cortex and epidermis (Figure 1.1). In *Arabidopsis* these tissue types consist of one cell layer each, and the process of emergence presents a major disruption to the local structure of the primary root (Figure 1.6, Peret et al. (2009b)). For successful emergence, the LRP must be able to pass between cells in the outer layers without damaging the surrounding tissue. This requires the softening and separation of only the the specific cells between which the LRP must pass, and recent evidence shows that this cell separation process is highly regulated by auxin (Peret et al. 2009b). In cereals, the cortical tissue may consist of between 10 and 15 cell layers, presenting a even greater biomechanical challenge (Hochholdinger and Zimmermann 2008).

The link between auxin and cell separation was established by Boerjan et al. (1995), with the auxin over-producing mutant *superroot sur1* shown to have widespread separation of cells in the epidermal and cortical cell lay-

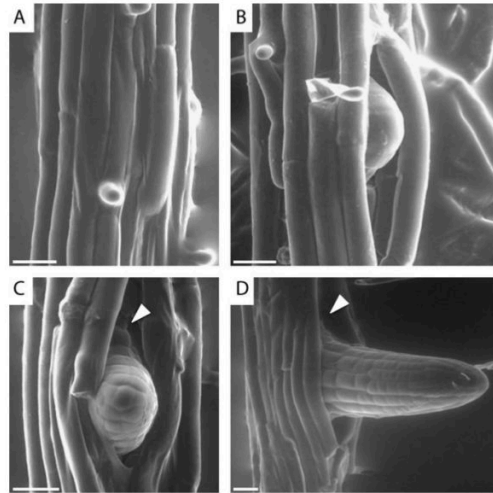


Figure 1.6: Environment scanning electron microscopy (ESEM) of 5 to 7 day old *Arabidopsis* seedlings; scale bars are 20 μm . Before emergence the epidermal cells are tightly attached (A), before detaching and separating during emergence (B),(C). Even after the lateral root is fully emerged, gaps, as shown by the small arrows, remain between the separated cells (D). (Reproduced from Peret et al. (2009b).)

ers in both the root and the hypocotyl, in addition to excessive numbers of lateral roots. In contrast to lateral root priming and initiation, the source of auxin required for emergence is demonstrated to be derived from the shoot, with plants with aerial tissue removed having fewer emerged LRP, while the number of LRP initiated remains unchanged (Bhalerao et al. 2002). The main mechanism by which auxin induces cell separation is proposed to be through the expression of a range of cell wall remodelling enzymes (CWREs), several of which, including pectate lyase, pectin methyl esterase, expansin and β -xylosidase, were shown to be induced following auxin treatment (Laskowski et al. 2006). More recently, several CWREs were found to be expressed locally to the specific cells in the outer tissues overlying LRP (Peret et al. 2009b). In particular, polygalacturonase (PG), a set of CWREs known to cleave pectin polymers in the cell wall (Kim et al. 2006), and have a role in cell separation in floral organs (Ogawa et al. 2009), is expressed in the outer cell layers in front of developing LRP (Gonzalez-Carranza et al. 2007; Swarup et al. 2008). Other CWREs with a similar expression pattern during emergence which may be involved in separation include xyloglucan endotransglucosylase/hydrolase (XTR6), pectate lyase (PLA2) and a subtilisin-like protease (AIR3) (Swarup et al. 2008).

LAX3 and emergence

As described above, the ARF7/ARF19 and IAA14 auxin signalling module is known to be an important regulator of LRP initiation and development (Fukaki et al. 2002; Okushima et al. 2005; Fukaki et al. 2005). However, due to the lack of developing primordia in the *slr-1* and *arf7arf19* mutants, its additional role in lateral root emergence was not noted until the publication by Swarup et al. (2008), in which the importance of the auxin influx carrier

LAX3 on emergence was described. LAX3 is a member of the same auxin influx carrier family as AUX1 and, while AUX1 is shown to promote LRP initiation (Marchant et al. 2002; De Smet et al. 2007), LAX3 is shown to promote emergence (Swarup et al. 2008). In *lax3* mutant plants, though there is an increased frequency of LRP compared to wild type, the ability of these LRP to emerge is significantly impaired. Genetic markers show that LAX3 expression in the root is limited to the stele and specific cortical and epidermal cells overlying developing LRP (Figure 1.7). Furthermore, this

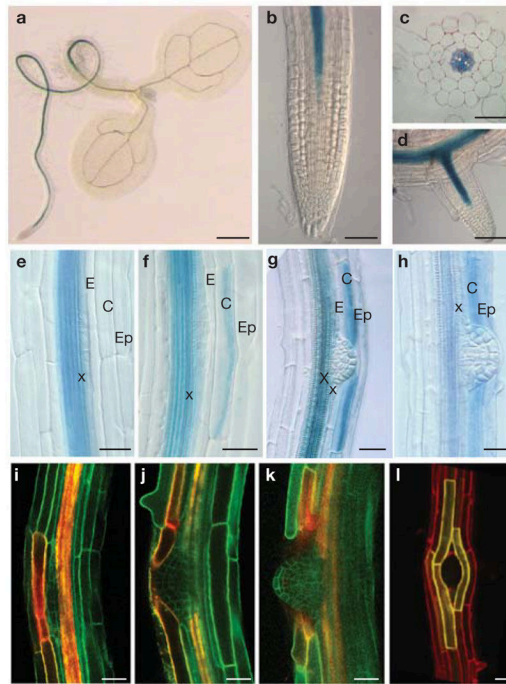


Figure 1.7: Spatial expression of LAX3, detected using the LAX3:GUS marker line in (a) seedling root stele, (b) extending root stele cells, (c) stele in radial cross section of root, (d) stele of root with emerged lateral root, (e) root section with stage I primordium, (f) stage II primordium (g) stage V primordium and (h) stage VII primordium. From stage II onwards LAX3:GUS is visible in the cortical cells over the developing LRP. LAX3pro:LAX3-YFP expression in cortical cells above (i) stage III, (j) stage V and (k) stage VII primordia. (l) LAX3pro:LAX3-YFP expression in epidermal cells separating to allow for emergence of LRP. (Reproduced from Swarup et al. (2008).)

restriction of LAX3 expression outside of the stele to cells directly in front of LRP matches that seen for the CWREs, PG, XTR6, PLA2 and AIR3, and expression of CWREs in these cells is reduced in the *lax3* mutant. A link between auxin and the expression of CWREs facilitating emergence is given by the inducibility of LAX3 throughout the cortex and epidermis following treatment with exogenous auxin ($1 \mu M$), and the dependence of PG expression and normal emergence on a supply of auxin from the shoot. This is corroborated by qRT-PCR data which shows elevated mRNA expression in LAX3, PG and other CWREs following auxin treatment, and reduced induction of the CWREs in the *lax3* mutant. Evidence that the

auxin maximum at the tip of the developing LRP is the source of the signal that programmes cells in the outer layers to express CWREs and facilitate emergence is given by the enhanced rate of emergence in the *pin2* mutant, which has greater accumulation of auxin at its tip. Finally, the role of the ARF7/ARF19 and IAA14 auxin signalling module is confirmed by the lack of induction of LAX3 in both the *slr-1* and *arf7arf19* mutants.

As well as the ARF7/ARF19 dependent expression of LAX3 and CWREs in the cortex and epidermis, the expression of IAA3 in the endodermis is also shown to regulate lateral root emergence (Swarup et al. 2008). In the loss of function IAA3 mutant allele *shy2-24* emergence is accelerated, while in *shy2*, a gain of function IAA3 mutant, emergence is delayed and induction of the CWREs GLH17 and PLA2 following auxin treatment is reduced. On the other hand, IAA14 does not appear to regulate the auxin response in the endodermis, with the expression of the auxin response reporter gene DR5 remaining unaffected in the stabilised IAA14 mutant *slr-1*. Because of this, the degradation of IAA3 in the endodermis leading to the expression of CWREs is hypothesised to facilitate emergence through the endodermis, though the ARF activator or activators paired with IAA3 in this context are undetermined.

The various lines of evidence given by Swarup et al. (2008) and described above lead to the proposal of the conceptual model shown in Figure 1.8. The auxin maximum at the centre of the LRP results in elevated auxin in the adjacent endodermal cell, degrading IAA3 and resulting in the activation of CWREs. Auxin is also elevated in the nearest cortical cell(s), but here IAA14 is degraded, inducing the expression of LAX3 via activation by ARF7/ARF19. Positive feedback on auxin in the cortical cell caused by influx from LAX3 activity elevates auxin concentration further, sufficient for the expression of CWREs. This expression of CWREs in the endodermis and cortex facilitates the emergence of the primordia through these cell layers, and moves the source of auxin closer to the epidermis. The process of IAA14 and ARF7/ARF19 dependent expression of LAX3, followed by increased auxin influx due to LAX3 and finally CWRE expression, is repeated in the epidermis, allowing for the full emergence of the LRP.

Further insight into the relationship between the known regulators of LAX3 expression, and their behaviour following auxin treatment, is given by the qRT-PCR data shown in Figure 1.9 (Benjamin Peret, Personal Communication). This shows 36 hour time course mRNA expression data for ARF7, ARF19, LAX3, IAA14 and PG, in wild type (Col-0), and *arf7*, *arf19*, and *lax3* mutant backgrounds, following treatment with 1 μ M exogenous auxin. The data show a clear distinction in the behaviour of ARF7 and ARF19 following auxin treatment. While ARF7 is unresponsive to auxin and present at similar level in all genotypes, ARF19 is induced by auxin, peaking in expression between 3 and 6 hours after treatment. The reduced induction of ARF19 in the *arf7* mutant suggests a partial role for ARF7 in ARF19 activation, while ARF19 expression is unaffected by the *lax3* mutation. IAA14 is induced by auxin, peaking in expression 12 to 18 hours post-treatment, and appears to be exclusively dependent on ARF7, and independent of ARF19. LAX3 is also induced by auxin, with a peak in

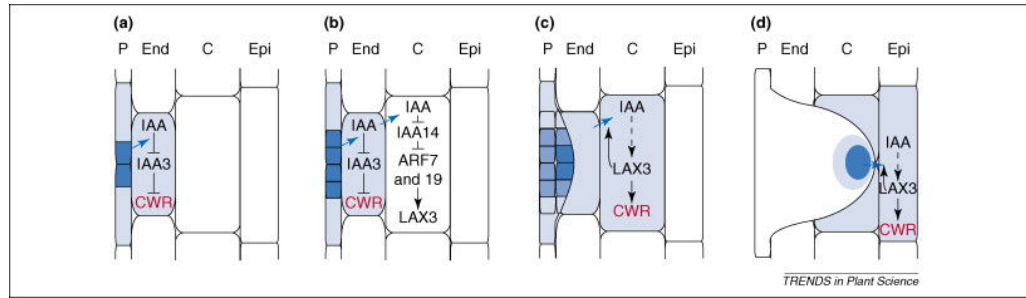


Figure 1.8: Conceptual model of LAX3 regulated lateral root emergence. (a) Auxin (IAA) diffuses from the LRP in the pericycle (P) into the endodermis (End) and degrades the Aux/IAA IAA3, leading to the expression of cell wall remodelling enzymes (CWR). (b) A lower level of auxin diffuses into the adjacent cortical cell (C), degrading IAA14 sufficiently to allow the ARF7/ARF19 mediated activation of LAX3. (c) The additional auxin influx provided by LAX3 positive feedback further elevates auxin in the cortical cell enough to activate CWR. (d) The expression of CWR in the endodermis and cortex facilitates the emergence of the growing LRP so that it is now below the epidermis (Epi), and as in the cortex, the increase of auxin, expression of LAX, and LAX3 positive feedback on auxin is enough to induce CWR. (Reproduced from Peret et al. (2009a).)

expression 12 hours post-treatment, and again is dependent on ARF7. The expression of LAX3 in the *arf19* mutant, however, is clearly increased, both at basal pre-treatment level, and at peak expression level, suggesting ARF19 may have a negative effect on LAX3 expression. Finally, the peak induction of PG following auxin treatment occurs at the time point following peak LAX3 expression, after 18 hours, and is reduced in the *lax3* mutant, and absent in the *arf7* mutant, demonstrating a link between the ARF7 dependent expression of LAX3 and the induction of CWREs.

The final key pieces of experimental evidence available suggest the existence of an additional, unidentified transcription factor (TF) downstream of ARF7, activating LAX3. Firstly, treatment with cycloheximide (CHX) in addition to auxin results in the decay of the LAX3 signal post-treatment, as shown in Figure 1.9 (Silvana Porco, personal communication). CHX is an inhibitor of protein translation and can be used experimentally to determine whether auxin responsive genes are direct targets of ARF activators, or an intermediate TF is required for induction. If a gene is activated directly by an ARF following the degradation of an Aux/IAA repressor, though the translation of the mRNA into protein will be blocked by CHX, the initial induction of the mRNA will be unaffected. If on the other hand the gene is a secondary response, i.e. it is itself a downstream target of a gene activated directly by auxin, although the mRNA of its activator will be up-regulated by auxin, the presence of CHX means that the mRNA is not translated to protein and so the target gene is not activated. Since the LAX3 mRNA signal decays post-auxin treatment in the presence of CHX, this suggests an additional TF needs to be expressed and translated in order for LAX3 up-regulation to occur. Nonetheless, the presence of a potential ARF binding

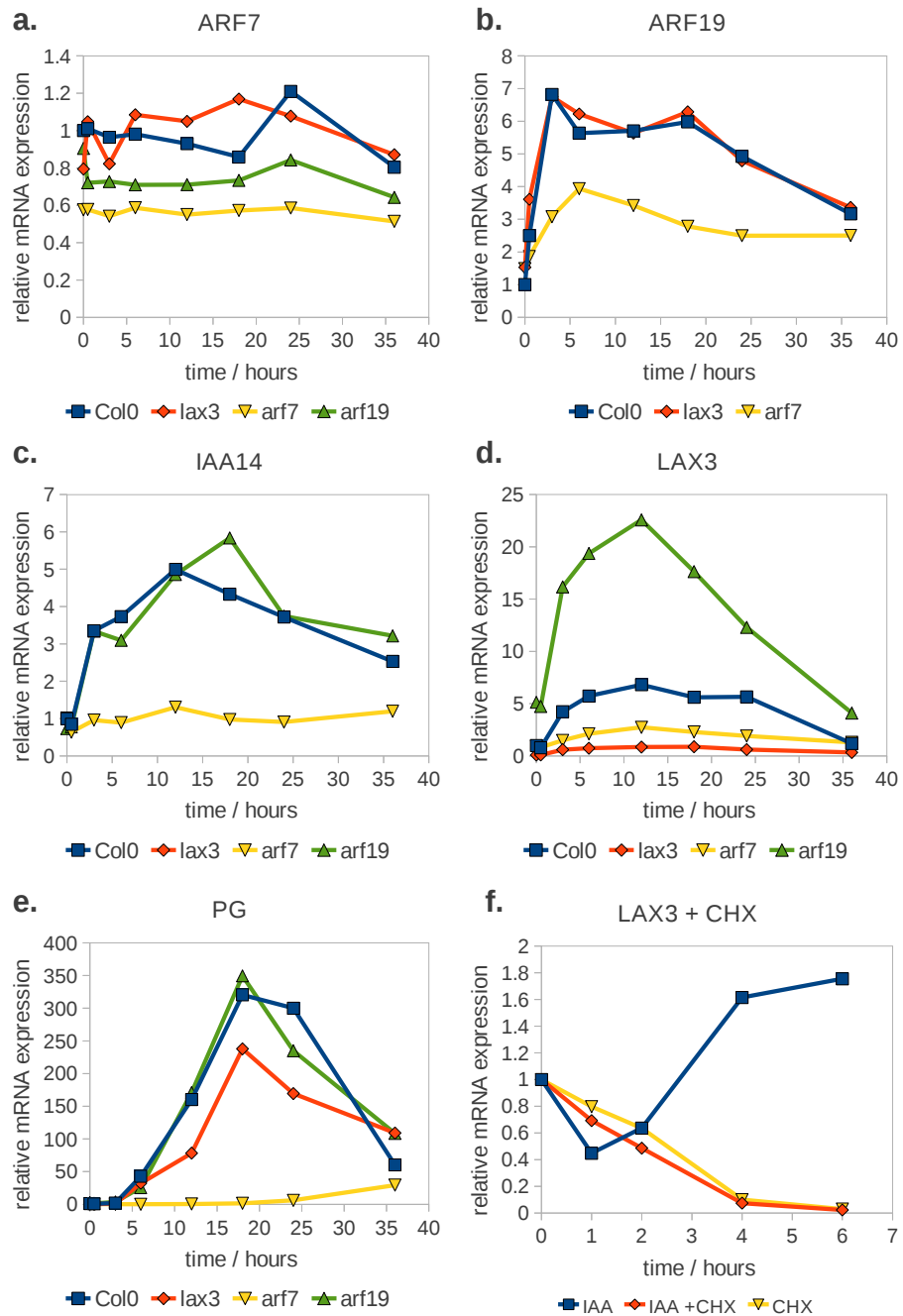


Figure 1.9: qRT-PCR time course data following $1 \mu\text{M}$ auxin treatment for (a) ARF7, (b) ARF19, (c) IAA14, (d) LAX3 and (e) PG mRNAs in wild type, *lax3*, *arf7*, and *arf19* mutant backgrounds (Benjamin Peret, personal communication). (f) Wild type LAX3 mRNA expression following treatment with $10 \mu\text{M}$ cyclohexamide (CHX), $1 \mu\text{M}$ auxin (IAA) and both CHX and IAA (Silvana Porco, personal communication).

site (AuxRE) on the LAX3 gene promoter may suggest that both the extra TF and an ARF are needed for LAX3 activation. However, mutation of this potential ARF binding site does not negatively affect the expression of LAX3 (Larrieu 2011), suggesting that LAX3 is activated exclusively by one or more indirect targets of ARF7. The simplest conceptual model for this is this addition of a TF, denoted tfX below, to the LAX3 regulatory module, directly activated by ARF7, and itself acting to activate LAX3 directly.

The currently available literature and experimental data point to the importance of the regulation of LAX3 by auxin to the process of lateral root emergence. A better understanding of how specific cells within the *Arabidopsis* root are reprogrammed by auxin to express LAX3, leading to the expression of CWREs, will be gained by the development of mathematical models of these processes. The first step in this is to create a single cell scale model of the LAX3 gene regulatory network, to be followed by a multiscale model in which the realistic spatial distribution of auxin and LAX3 expression between root cells is simulated. Existing modelling approaches to plant developmental processes, in particular relevant models of auxin signalling and transport, are reviewed briefly in Section 1.2.

1.2 Modelling of Plant Hormone Signalling

Computational modelling has been used to investigate many different aspects of plant growth and development, including the key processes relevant to lateral root emergence of hormone distribution and transport, genetic regulation, and growth and mechanics, as reviewed by Jonsson and Krupinski (2010). The growth and mechanical properties of root tissues are beyond the scope of this thesis and so we restrict attention here to models of hormone distribution and transport and of gene regulation, with particular attention on models involving auxin, the key hormone regulating lateral root emergence.

1.2.1 Auxin transport models

One of the most common topics for the application of computational modelling in plants is that of auxin transport, i.e. simulating the movement of auxin via either diffusion or carrier mediated active transport around plant tissues and organs. These models generally have some geometric framework throughout which auxin can move according to mathematically formulated rules based on biological rules and the hypothesis to be tested (Kramer 2008; Krupinski and Jonsson 2010). The frameworks often have the resolution of one compartment per cell, but may include sub-cellular compartments or alternatively, combine many cells together into larger compartments (Kramer 2008). Auxin transport models have been applied to several different morphological processes including development of vascular strands in leaves and stems (Smith and Bayer 2009), wood grain pattern formation (Kramer 2002), and phyllotaxis (Jonsson et al. 2006; de Reuille et al. 2006). The latter publications demonstrated that a pre-defined population of PIN auxin efflux carriers could produce local auxin maxima at the

shoot apical meristem (SAM) corresponding to the sites of new leaf primordia. Extending these models so that rather than the location of the PINs being pre-determined, the PINs are polarised to the cell membranes facing towards the cells with highest auxin, provides a pattern-forming mechanism by which the experimentally observed carrier distribution can be established (Jonsson et al. 2006; Smith et al. 2006).

In addition to the examples above, a number of auxin transport models based on processes within the root have also been published. Swarup et al. (2005) demonstrated the importance of auxin transport during gravitropism using a three-dimensional model of the outer cell layers in the root, where the asymmetry in auxin between the upper and lower surface of the root following a simulated gravitropic stimulus is maintained by the presence of the influx transporter AUX1 in the epidermis. A similar model framework was used by Jones et al. (2009) to describe the role of AUX1, which is expressed in cells without root hairs to maintain the level of auxin in adjacent files of cells which grow root hairs, but do not express AUX1. The reverse fountain model described in Section 1.1.4, in which the arrangement of efflux and influx carriers causes the polar flow of auxin through the stele towards an auxin maximum at the root tip, with some lateral and shootward reflux back toward the shoot in the outer tissue, was simulated by Grieneisen et al. (2007). In this model, a two-dimensional regular array of cells with a fixed distribution of carriers was able re-produce the experimentally observed maximum of auxin near the root tip. A similar model was used to show that a change of cellular geometry caused by root bending may produce auxin maxima corresponding to the site of lateral root initiation sites (Laskowski et al. 2008). Finally, in Band and King (2011) asymptotic methods were used to derive a continuum description of auxin transport in the root from a model with individual compartments for each cell and the apoplastic spaces between them. The cellular resolution model including the apoplast was first published by Perrine-Walker et al. (2010) and was selected as the basis for the auxin transport model used in Chapters 5 and 6 due to the presence of the apoplastic compartments in the model and the derivation of parameter estimates for the relative flux due to diffusion, influx and efflux, both in the direction of cytoplasm to apoplast and in the direction of apoplast to cytoplasm.

1.2.2 Auxin signalling and gene regulation models

Single cell scale gene regulatory models have been used on several occasions as a tool to investigate and simulate different gene regulatory and hormone signalling processes within plants. These include ordinary differential equation (ODE) models of the circadian clock (Locke et al. 2005) and gibberelin signalling (Middleton et al. 2012), and boolean and stochastic models of the regulation of floral genes (Espinosa-Soto et al. 2004; Alvarez-Buylla et al. 2008; Lenser et al. 2009). Jonsson et al. (2005) used an ODE model to put a gene regulatory network model of the regulation of the key regulatory genes in determining the size of the SAM, CLAVATA and WUSCHEL, into a tissue scale model with cellular resolution, in order to simulate the real-

istic spatial distribution of the key model components. This approach, of embedding a cellular scale ODE gene expression model into a tissue scale model with realistic cellular geometry through which key diffusive molecules can move is implemented in Chapter 6.

Compared to models of auxin transport and distribution on a tissue or organ scale, there are relatively few models published which simulate auxin activity on a biomolecular or gene network scale within a single cell. One such model is that published by Middleton et al. (2010) in which the transcription, translation and degradation of Aux/IAA proteins was modelled explicitly, via interactions with auxin, the auxin receptor TIR1 and the ARF transcription factors. When the ARFs are free of the repression by Aux/IAAs they are free to activate downstream targets, among which are the Aux/IAAs themselves, thus generating a negative feedback loop on Aux/IAA auxin activated expression. This model network was found to have parameter regimes in which the expression of Aux/IAA oscillates stably over time. These oscillations depend on the homodimerisation of the ARF activators occurring at a similar rate as the degradation of Aux/IAA mRNA and so if, as suggested by Vernoux et al. (2011), homodimerisation interactions between activating ARFs are uncommon, this reaction may not be present during auxin signalling in many cases. Nevertheless, the model equations in Middleton et al. (2010), with the omission of the ARF-ARF homodimerisation, provide the basis for the auxin signalling module used in the LAX3 expression model in Chapter 2. The auxin signalling network model published by Middleton et al. (2010) was also extended by Muraro et al. (2011), to include crosstalk from cytokinin signalling during the priming of new lateral root sites. Here, the antagonistic effect of cytokinin on the auxin response is shown to disrupt the stable oscillations in Aux/IAA expression seen in the previous model and decrease the level of auxin responsive expression of PIN carrier proteins.

In addition to the data on the full interactome of the 23 ARFs and 29 Aux/IAAs, Vernoux et al. (2011) also present a model for the auxin response at the SAM containing the two main motifs found in the ARF-Aux/IAA interactome, the first being the dimerisation of Aux/IAAs with positive or activating ARFs and homodimerisation with other Aux/IAAs, and the second being negative or repressing ARFs acting alone to compete for binding sites with the positive ARFs. The balance between the level of positive and negative ARFs was shown to affect the sensitivity of response genes to auxin, and the robustness of the level of expression to fluctuations in auxin input, with increased levels of the negative ARFs attenuating the fold-change response to an auxin signal. The impact of the ARF and Aux/IAA interactome on auxin signalling is investigated further by Bridge et al. (2012), in which model systems with two ARFs and Aux/IAAs are presented which may show bistability in dominant expression between two response genes depending on the strength of auxin signal. Though the model was formulated to investigate the mechanism for the initiation of root hairs, the number of possible interactions between the ARFs and the Aux/IAAs throughout the plant mean that the system could be applicable to a number of other developmental contexts.

1.2.3 Frameworks for model implementation

The single cell modelling in Chapters 2, 3, and 4 was implemented using the commercial software package MATLAB¹, with all the ODE solutions found using the ode15s solver. Also used were the parameter fitting algorithms *ga* and *fmincon* found in the MATLAB Optimization Toolbox package² in order to fit model parameter values to experimental data.

The bifurcation diagrams for model steady states in Chapters 2 and 3 were found using the open source software XPPAUT³ (Ermentrout 2002).

Finally, the multiscale model developed in Chapters 5 and 6 was implemented using the Python programming language, with the core topological structure of the model provided by packages from the open source software package Open Alea⁴, the ODEs solved by the python package SciPy⁵, and the graphical output produced by the python package Matplotlib⁶.

1.3 Thesis Summary

The plant hormone auxin is known to be central to virtually every aspect of plant root development, and in particular the formation of new lateral roots (Peret et al. 2009a,b). In *Arabidopsis*, lateral roots initiate as and develop from lateral root primordia (LRP) in the pericycle cell layer, adjacent to the central vascular tissue (stele) deep within the root, and in order to emerge as mature lateral roots the LRP must pass between cells in the outer cell layers without causing excessive tissue damage (Peret et al. 2009a,b). To facilitate emergence the cell walls in the outer layers over the LRP must first be softened via the expression of cell wall remodelling enzymes (CWREs), but only in the specific cells necessary for emergence. The auxin induced expression of the auxin influx transporter LAX3 in these cells was shown by Swarup et al. (2008) to be required for the expression of CWREs including polygalacturonase (PG), and for normal emergence. The main aim of the thesis is to use mathematical modelling to investigate whether the all or nothing spatial expression pattern of LAX3 and PG can be explained by the conceptual model shown in Figure 1.8. In doing so, the model will also be used to investigate in more detail the gene regulatory network leading to the expression of LAX3.

The modelling work presented in the thesis may be divided into two main sections. Firstly, in Chapters 2-4 the expression of the key gene required for emergence, LAX3, is modelled at a gene network scale, in order to address biological questions about how LAX3 may be regulated within a single cell. After this, in Chapter 5 the model is expanded to the multi-cellular scale by modelling auxin transport in a two-dimensional cross section of an *Arabidopsis* root, and in Chapter 6 this tissue scale model is combined with

¹<http://www.mathworks.co.uk/products/matlab/>

²<http://www.mathworks.co.uk/products/optimization/>

³<http://www.math.pitt.edu/~bard/xpp/xpp.html>

⁴<http://openalea.gforge.inria.fr>

⁵<http://www.scipy.org/>

⁶<http://matplotlib.sourceforge.net/>

the gene regulatory network model to create a multi-scale model of auxin transport and LAX3 expression.

Figure 1.10 shows an overview of the different gene network variants modelled in each thesis chapter. All of the models in some way include the core auxin signalling mechanism by which auxin binds with the TIR1 receptor, which can then bind the Aux/IAA IAA14, thus targeting it for degradation and freeing the repression of target genes caused by binding with the ARFs. In Chapter 2, a single cell model of the core LAX3 network is developed, with a single ARF, ARF7, activating the primary response genes IAA14 and the unknown transcription factor tfX, with tfX then activating LAX3 resulting in a positive feedback on auxin. With some parameter sets this model is shown to have a bistable switch between low and high LAX3 expression with increasing persistent auxin signal, providing a possible explanation for the experimentally observed all or nothing LAX3 spatial expression pattern. Parameter fitting is then used to fit the model with experimental data, with a key conclusion being that in order to match all the data some form of auxin homeostasis mechanism is needed in the model. Finally, the fitted model is used to make time course predictions for the model components for which no data is available, in particular the unidentified transcription factor tfX.

Chapter 3 presents a hypothetical auxin homeostasis mechanism, in which the auxin responsive expression of a member of the GH3 gene family increases the degradation rate of intracellular auxin by irreversibly conjugating it with amino acids (Figure 1.10). The parameter fitting shows that it is possible for this model to match the experimental data with long period damped oscillations of gene expression, the timing and magnitude of which are very sensitive to small changes in parameter values. Additionally, some parameter sets result in stable limit cycles in gene expression, meaning that the model provides an alternative mechanism to that given by Middleton et al. (2010) by which oscillations in the auxin response may be generated from a persistent auxin signal.

The effect of adding an additional ARF to the model is investigated in Chapter 4 by adding the auxin responsive ARF19. Of particular interest is the mechanism by which ARF19 appears to partially repress LAX3 expression (Figure 1.9). Several different mechanisms are investigated, with the model network producing the best fit with experimental data shown in Figure 1.10. Though the evidence for selecting this model above the others is inconclusive, it provides a conceptual basis for further experimental research.

In Chapter 5 the focus moves to a tissue scale model of auxin transport in a two-dimensional radial cross-section of an *Arabidopsis* root (Figure 1.11). The model is used to simulate the response of the tissue to both exogenous auxin treatment and the introduction of an auxin source in a single pericycle cell to represent a LRP. A key parameter in both simulations is the intracellular auxin turnover rate. In the primordium simulation it is shown that a high auxin turnover rate broadens the range of auxin concentrations between cortical cells which, in conjunction with a sharp switch in LAX3 expression with increasing auxin, may provide a basis for the spatial

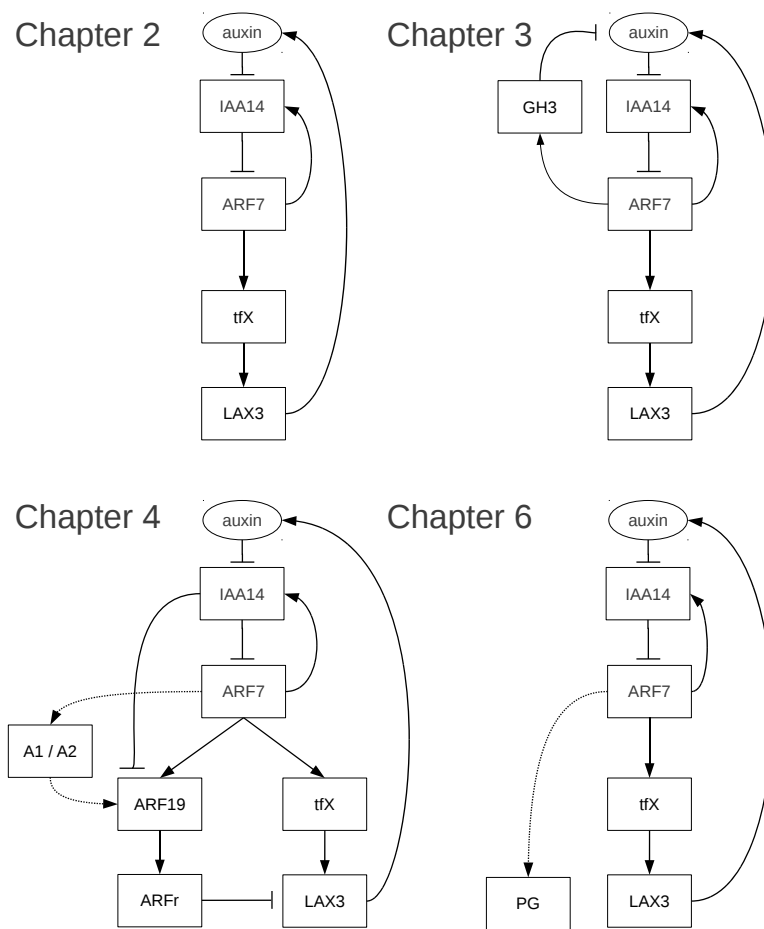


Figure 1.10: Overview of the gene network models described in Chapters 2, 3, 4 and 6. Each model has the core network in which the degradation of IAA14 is accelerated by auxin, freeing the repression of ARF7 activated IAA14 and tfX. IAA14 then feeds back negatively on the activation by ARF7, while tfX activates LAX3, which feeds back positively on the level of auxin. In Chapter 3 an auxin homeostasis mechanism is modelled by adding the auxin responsive gene GH3, which feeds back negatively on auxin by binding with it and conjugating it to amino acids, effectively removing it from the active pool of auxin. In Chapter 4 ARF19 is added and various model networks investigated. In the model shown here, in addition to being activated by ARF7, ARF19 is also activated by one or more other activators (A1, A2), and ARF19 itself activates a repressor of LAX3, ARFr. In Chapter 6 the core network is extended by the addition of the tertiary auxin response gene PG, and embedded in a multicellular context with the auxin transport model described in Chapter 5.

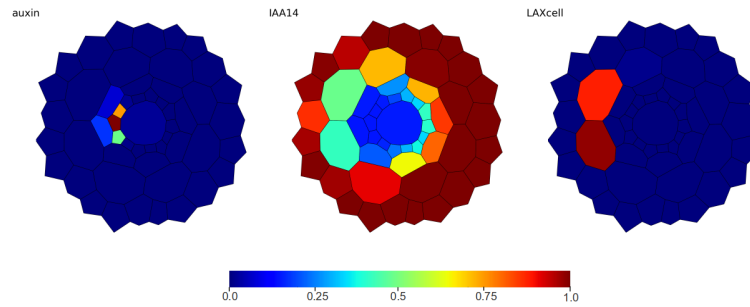


Figure 1.11: Example output from the multiscale model developed in Chapters 5 and 6. A strong auxin source in the pericycle representing a developing lateral root primordium results in degradation of Aux/IAA in adjacent and local cells. LAX3, which is restricted to expression in the cortex and epidermis, is strongly expressed only in the two cortical cells nearest the primordium auxin source.

LAX3 expression pattern. A high turnover rate is also shown to increase the power of LAX3 to amplify cellular auxin in a threshold based model for LAX3 expression.

The final chapter (Chapter 6) combines a gene regulatory network model of LAX3 and PG expression (Figure 1.10) with the tissue scale model from Chapter 5 to produce a multi-scale model for auxin transport and auxin responsive gene expression in an *Arabidopsis* root cross-section (Figure 1.11). The model is used to show that the spatial position of cortical cells relative to the primordium auxin source is sufficient to explain the experimentally observed LAX3 expression pattern, provided there is a reasonably sharp switch between low and high LAX3 expression with increasing auxin. Furthermore, this expression pattern can be consistently produced for a large range of primordium signal strengths. Finally, if PG has a similar switch like change in expression with increasing auxin, then provided the threshold for the switch from low to high expression is higher than that for LAX3, the model shows that the amplification on cellular auxin due to LAX3 expression is required for PG to be expressed. Removing LAX3 from the model to simulate the *lax3* mutant greatly reduces the expression of PG, meaning that the model can replicate the PG expression pattern in both wild type and the *lax3* mutant, demonstrating how the expression of LAX3 may be linked to the expression of cell wall remodelling enzymes and facilitate lateral root emergence.

Chapter 2

Gene Regulatory Network Model: One Auxin Response Factor (ARF7)

2.1 Initial LAX3 Gene Network Model

2.1.1 The LAX3 gene regulatory network

To investigate whether the conceptual model published by Swarup et al. (2008) can explain the observed expression pattern of LAX3 in specific cells overlying LRP, a mathematical model of auxin signalling and LAX3 expression in a single cortical cell was developed. This initial model was then used to find conditions under which the model can produce a bistable response, similar to the all or nothing response of LAX3 observed in Swarup et al. (2008), with a low level of expression at a low auxin signal, high expression at a high auxin signal, and the existence of both high and low steady states for some intermediate range of auxin concentrations.

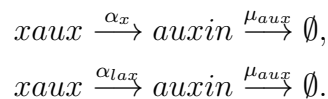
To refine the model further it was first compared qualitatively, and then fitted quantitatively, to qRT-PCR data for key model components. In doing so we found that several additional previously unidentified model components are needed to explain the experimental observations in full.

As discussed in section 1.1.6, the ARF7/ARF19 and IAA14 mediated induction of the auxin influx transporter LAX3 is shown to be required for normal emergence of lateral roots (Swarup et al. 2008). The qRT-PCR data shown in figure 1.9 gives further insight into the relationship between the key LAX3 regulators, IAA14, ARF7 and ARF19. The working hypothesis based on the experimental evidence is that both IAA14 and ARF19 are direct targets for activation by ARF7 following the release from repression by degradation of IAA14 with an auxin signal. While ARF7 has a positive effect on LAX3 expression, ARF19 has a negative effect. The evidence provided by mutation of the potential ARF binding site on the LAX3 promoter (Larrieu 2011), and the degradation of LAX3 mRNA seen following treatment with auxin and cyclohexamide (Larrieu 2011) indicates that at least one additional activatory step must be present between ARF7 and LAX3. This activation is proposed here to be due to an unidentified transcription

factor (tfX) directly activated by ARF7, itself binding directly with the LAX3 promoter to activate expression. A summary of the proposed wild type and mutant gene regulatory networks is given in figure 2.1. The mechanism by which ARF19 negatively regulates LAX3 is initially unclear and so, for simplicity, the model is first formulated with just ARF7 regulating LAX3 via tfX. A more complex model, including ARF19, is developed in chapter 4.

2.1.2 Model Formulation and Initial Parameter Estimates

In the absence of LAX3, auxin is assumed to enter the cell via diffusion only, at a low rate (α_x) proportional to extracellular concentration ($xaux$). We assume this transport occurs only from outside to inside the cell, not vice versa, due to the higher pH within the cell resulting in auxin dissociating into an anionic form, unable to diffuse freely back through the plasma membrane (Petresek and Friml 2009). Once in the cell, the pool of auxin available to other reactions ($auxin$) can then be depleted by several processes, including efflux via transporters such as PIN or PGP, conjugation with other molecules, and degradation. This depletion is initially approximated as linear in the auxin concentration with rate constant μ_{aux} . Assuming that the number of LAX3 transporters present at the plasma membrane at any time is proportional to the LAX3 concentration (LAX), and that extracellular auxin is not present in saturating quantities, the additional auxin influx due to transporter activity is proportional to the parameter α_{lax} :



To begin with, we assume the auxin maximum near the tip of the LRP and represented by $xaux$ is maintained throughout, regardless of the rate of diffusion and active transport into the cell. Both auxin diffusion and active transport happen at the plasma membrane, while the remainder of model reactions occur within the nucleus as we assume the Aux/IAs, ARFs and other transcription factors are localised to the nucleus. For this reason, another model simplification is that spatial effects of transport of auxin, LAX3, and other molecules within the cell are ignored.

Within the cell, auxin is able to bind reversibly with the SCF^{TIR1} complex (TIR), the resulting complex (TIR_a) itself being able to bind reversibly with Aux/IAA protein (IAA) to another complex (TIR_{ai}). Finally, Aux/IAA bound up in TIR_{ai} can be ubiquitinated (IAA^*), after which it is targeted for degradation (Dharmasiri et al. 2005; Kepinski and Leyser 2005). Since this step is assumed here to be irreversible, for the purposes of the model Aux/IAA is considered to be degraded following ubiquitination. The total concentration of SCF^{TIR1} complex in its various forms (tir_T) is assumed to be relatively stable, and is considered to be conserved:



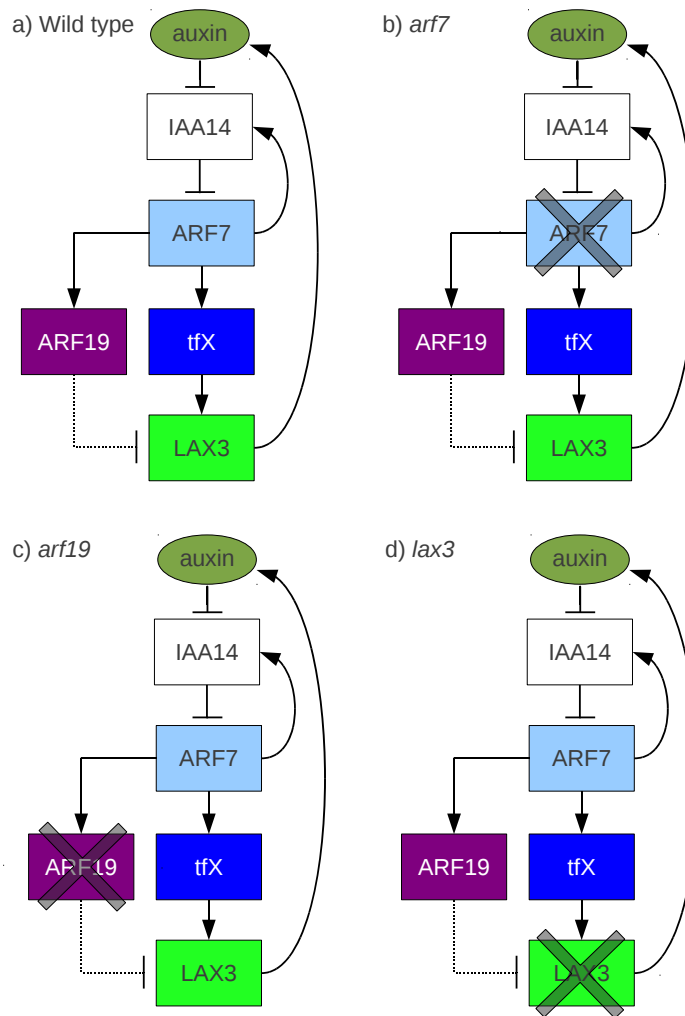
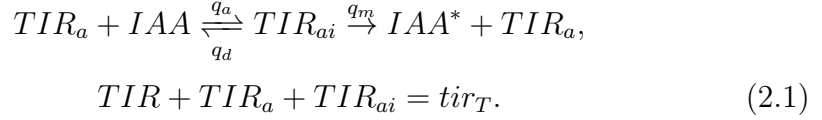


Figure 2.1: Hypothetical model network tested in Chapters 2 and 4 showing the site of simulated gene mutations. a) Wild type. Auxin enters the cell via diffusion and binds with the TIR1 complex. This complex can then bind Aux/IAA (IAA14) and target it for degradation. In the absence of auxin, Aux/IAA dimerises with ARF7, but once Aux/IAA is degraded ARF7 is free to activate auxin responsive genes. Among these genes is Aux/IAA itself, creating a negative feedback effect. Evidence suggests that while LAX3 is expressed in response to auxin, it is not itself a primary auxin gene; because of this an unknown transcription factor ‘tfX’ is included between ARF and LAX3. Once transcribed and translated, LAX3 acts as a positive feedback on auxin by actively transporting more into the cell. ARF19 production is activated by ARF7 and has a negative effect on LAX3 expression. b) *arf7*. Since ARF7 is required for activation of all genes in the model, in the *arf7* mutant no expression is possible. c) *arf19*. In the *arf19* mutant the negative effect of ARF19 on LAX3 is removed. d) *lax3*. In the *lax3* mutant the positive feedback on cellular auxin is removed.



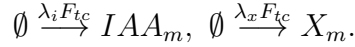
Auxin acts within the nucleus by accelerating the degradation of IAA by the pathway described above. When present (i.e. when there is no auxin signal so IAA is relatively stable) IAA can bind to ARF in a reversible reaction to form dimers (AI):



For the model, ARF transcription and degradation are assumed to be unaffected by auxin on the timescale of interest and so the total of bound and unbound ARF is conserved:



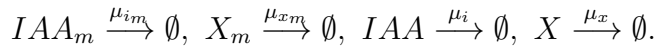
Following an auxin signal, Aux/IAA is degraded and the amount of free ARF protein increases, activating transcription of various mRNAs. These mRNAs include those of Aux/IAA itself, which acts as a negative feedback on the auxin response. Homodimerisation of ARF and Aux/IAA molecules is not considered. In the model, transcription of both IAA and the unknown transcription factor X mRNAs (IAA_m and X_m) are activated by ARF and repressed by AI :



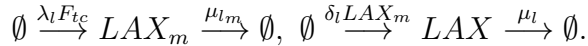
Translation of IAA_m and X_m into Aux/IAA and the unknown transcription factor X (X) occurs at different fixed rates, proportional to the current level of mRNA:



IAA and X mRNAs and proteins degrade at different linear rates:



Finally, $LAX3$ mRNA (LAX_m) is transcribed in response to X and degraded at a linear rate, and $LAX3$ protein (LAX) is translated at a rate proportional to LAX_m and degrades at a fixed linear rate:



In the notation the symbol used for each molecular species represents intracellular concentration and the symbol \emptyset refers to the pool of molecules from which mRNAs and proteins are transcribed and translated, and into which model species are degraded.

LAX3 model equations

With the reactions described above, the law of mass action gives an ODE model for $LAX3$ expression as stated in Equations 2.3a-2.4. The key differences from the model given by Middleton et al. (2010) are that for simplicity

ARF homodimers and ubiquitinated auxin are not included explicitly, the functions used for transcription are simplified, and the expression of LAX3 (via the intermediate transcription factor X) and its positive feedback effect on cellular auxin concentration are included; thus two ODEs from Middleton et al. (2010) are excluded and four extra ODEs for the variables X_m , X , LAX_m , and LAX are needed. Other than transcription, the reactions are assumed to take place according to the laws of mass action kinetics, giving the following dimensional model in twelve variables:

$$\begin{aligned} \frac{dauxin}{dt} &= xaux(\alpha_x + \alpha_{lax}LAX) - \mu_{aux}auxin \\ &\quad - p_a TIR auxin + p_d TIR_a, \end{aligned} \quad (2.3a)$$

$$\frac{dTIR}{dt} = -p_a TIR auxin + p_d TIR_a, \quad (2.3b)$$

$$\begin{aligned} \frac{dTIR_a}{dt} &= p_a TIR auxin - p_d TIR_a \\ &\quad + (q_d + q_m) TIR_{ai} - q_a TIR_a IAA, \end{aligned} \quad (2.3c)$$

$$\frac{dTIR_{ai}}{dt} = -(q_d + q_m) TIR_{ai} + q_a TIR_a IAA, \quad (2.3d)$$

$$\begin{aligned} \frac{dIAA}{dt} &= q_d TIR_{ai} - q_a TIR_a IAA - \mu_i IAA + \delta_i IAA_m \\ &\quad - k_a ARF IAA + k_d AI, \end{aligned} \quad (2.3e)$$

$$\frac{dARF}{dt} = -k_a ARF IAA + k_d AI, \quad (2.3f)$$

$$\frac{dAI}{dt} = k_a ARF IAA - k_d AI, \quad (2.3g)$$

$$\frac{dIAA_m}{dt} = \lambda_i F_{tc} \left(\frac{ARF}{\theta_{ia}}, \frac{AI}{\theta_{ir}}, n_i \right) - \mu_{im} IAA_m, \quad (2.3h)$$

$$\frac{dX_m}{dt} = \lambda_x F_{tc} \left(\frac{ARF}{\theta_{xa}}, \frac{AI}{\theta_{xr}}, n_x \right) - \mu_{xm} X_m, \quad (2.3i)$$

$$\frac{dX}{dt} = \delta_x X_m - \mu_x X, \quad (2.3j)$$

$$\frac{dLAX_m}{dt} = \lambda_l F_{tc} \left(\frac{X}{\theta_{la}}, 0, n_l \right) - \mu_{lm} LAX_m, \quad (2.3k)$$

$$\frac{dLAX}{dt} = \delta_l LAX_m - \mu_l LAX, \quad (2.3l)$$

where:

$$F_{tc}(ACT, REP, n) \equiv \frac{(ACT)^n}{1 + (ACT)^n + (REP)^n} \quad (2.4)$$

The functions for transcriptional activity are based on the models of Ackers et al. (1982) and Alon (2007) with the following assumptions. For the transcription of Aux/IAA and X, ARF monomers and ARF-Aux/IAA dimers compete for the same binding site(s). Aux/IAA monomers cannot bind to a promoter. If ARF is bound, transcription is activated, while if an ARF-Aux/IAA dimer is bound transcription is repressed. When X binds the LAX3 promoter, transcription is activated, otherwise LAX3 will not be expressed. Therefore there are three possible states for any binding

site, unbound, repressor bound and activator bound. The function (2.4) is based on the probability of the only situations in which transcription occurs, i.e. when it is bound by ARF, or by X in the case of LAX3. The co-operativity coefficient (n) allows for the possibility of more than one binding site. For $n = 1$ there is a single binding site, for $n > 1$ there is more than one binding site and the transcription function captures the probability of n sites being bound independently. Alternatively, the co-operativity could represent a number of copies of the same transcription factor binding together before binding to a single site, e.g. a co-operativity of two requires a homodimerisation before promoter binding.

Nondimensionalisation

In the following description the bar notation is used to represent the dimensional form of model quantities.

Given the total concentrations of ARF and TIR1 as arf_T and tir_T respectively, the respective conservation expressions (2.1) and (2.2) of TIR and ARF in various bound and unbound forms follows from the system of ODEs given by (2.3). A suitable scaling for the concentrations of bound and unbound ARF is then arf_T , so that $ARF = arf_T \overline{ARF}$ and $AI = arf_T \overline{AI}$. TIR in its various forms is similarly scaled with tir_T so that $TIR = tir_T \overline{TIR}$, $TIR_a = tir_T \overline{TIR}_a$, $TIR_{ai} = tir_T \overline{TIR}_{ai}$. The rate of Aux/IAA mRNA degradation should be a reasonable timescale over which auxin signalling evolves, and experimentally obtained values are available in the literature (Narsai et al. 2007), so we rescale time according to $t = \tau / \mu_{i_m}$. mRNA concentrations are scaled with the ratio of mRNA transcription and degradation so $IAA_m = \frac{\lambda_i}{\mu_{i_m}} \overline{IAA}_m$, $X_m = \frac{\lambda_x}{\mu_{x_m}} \overline{X}_m$, $LAX_m = \frac{\lambda_l}{\mu_{l_m}} \overline{LAX}_m$, and the corresponding protein concentrations are scaled with the product of the ratio between mRNA transcription and degradation and the ratio between protein translation and degradation, so that $LAX = \frac{\lambda_l \delta_l}{\mu_{l_m} \mu_l} \overline{LAX}$, $X = \frac{\lambda_x \delta_x}{\mu_{x_m} \mu_x} \overline{X}$; the exception is Aux/IAA protein which is scaled so that $IAA = \frac{\lambda_i \delta_i}{\mu_{i_m}^2} \overline{IAA}$, since we later assume that μ_i is negligible and omit the auxin independent degradation of Aux/IAA from the model. Finally, auxin is scaled relative to an arbitrary treatment concentration $xaux_T$ so that $auxin = xaux_T \overline{auxin}$. This means that when comparing the model response to experimental data, the cellular auxin concentration at any given time is expressed relative to a known treatment concentration.

Introducing the dimensionless parameters as shown in Table 2.1, and using t rather than τ for non-dimensional time, gives the dimensionless

model in twelve variables:

$$\begin{aligned} \frac{dauxin}{dt} &= xaux(\alpha_{aux} + \alpha_{lax}LAX) - \mu_{aux}auxin \\ &\quad + \eta_{tir}(-p_aTIR auxin + p_dTIR_a), \end{aligned} \quad (2.5a)$$

$$\frac{dTIR}{dt} = -p_aTIR auxin + p_dTIR_a, \quad (2.5b)$$

$$\begin{aligned} \frac{dTIR_a}{dt} &= p_aTIR auxin - p_dTIR_a + (q_d + q_m)TIR_{ai} \\ &\quad - q_aTIR_a IAA, \end{aligned} \quad (2.5c)$$

$$\frac{dTIR_{ai}}{dt} = -(q_d + q_m)TIR_{ai} + q_aTIR_a IAA, \quad (2.5d)$$

$$\begin{aligned} \frac{dIAA}{dt} &= \eta_{iaa}(q_dTIR_{ai} - q_aTIR_a IAA) + IAA_m \\ &\quad \eta_{arf}(-k_aARF IAA + k_dAI) - \mu_iIAA, \end{aligned} \quad (2.5e)$$

$$\frac{dARF}{dt} = -k_aARF IAA + k_dAI, \quad (2.5f)$$

$$\frac{dAI}{dt} = k_aARF IAA - k_dAI, \quad (2.5g)$$

$$\frac{dIAA_m}{dt} = F_{tc} \left(\frac{ARF}{\theta_{ia}}, \frac{AI}{\theta_{ir}}, n_i \right) - IAA_m, \quad (2.5h)$$

$$\frac{dX_m}{dt} = \mu_{x_m} \left(F_{tc} \left(\frac{ARF}{\theta_{xa}}, \frac{AI}{\theta_{xr}}, n_x \right) - X_m \right), \quad (2.5i)$$

$$\frac{dX}{dt} = \mu_x(X_m - X), \quad (2.5j)$$

$$\frac{dLAX_m}{dt} = \mu_{l_m} \left(F_{tc} \left(\frac{X}{\theta_{la}}, 0, n_l \right) - LAX_m \right), \quad (2.5k)$$

$$\frac{dLAX}{dt} = \mu_l(LAX_m - LAX), \quad (2.5l)$$

together with the conservation laws:

$$ARF + AI = 1, \quad (2.6a)$$

$$TIR + TIR_a + TIR_{ai} = 1 \quad (2.6b)$$

where, as before:

$$F_{tc}(ACT, REP, n) \equiv \frac{(ACT)^n}{1 + (ACT)^n + (REP)^n}. \quad (2.7)$$

Parameter Estimates

The initial default dimensionless parameter estimates are given in Table 2.1. A key assumption is that μ_i is negligible. This means that, even at very low auxin concentrations, the only way by which Aux/IAA is degraded is by the TIR1-auxin pathway. η_{tir} is the ratio of total receptor concentration to the $1\mu M$ treatment concentration and estimated to be very low, as are η_{arf} , and η_{iaa} which are respectively the ratios of total ARF and total receptor concentrations to the Aux/IAA rescaling. Since the model time is scaled using the rate of Aux/IAA mRNA decay (μ_{im}), the estimates for

μ_x , μ_{x_m} , μ_l , and μ_{l_m} are of $O(1)$. We set $\mu_x, \mu_{x_m} = 2$ to reflect the experimental observation that, while LAX3 is a secondary response gene, its peak in expression is relatively close to that of Aux/IAA, a primary response gene, suggesting that its activator, X, may peak sooner than Aux/IAA. The parameters relating to protein-protein and protein-auxin interaction are estimated to be much larger in size than those for mRNA/protein decay and so $p_a, p_d, k_a, k_d, q_a, q_d, q_m$ are all set ≥ 1000 . The auxin transport and decay parameters ($\alpha_x, \alpha_{lax}, \mu_{aux}$) are initially set in the range 1 to 10, but larger values can produce similar time-course expression profiles for model mRNA, provided all are increased by a similar order of magnitude. Swarup et al. (2005) estimate that active transport via AUX1, an influx transporter in the same family as LAX3, happens at a rate approximately 15 times that of auxin diffusion, and this ratio is used for α_{lax} and α_x . Basal cellular auxin concentration is estimated to be around 1nM and since we know the treatment concentration $x_{aux_T} = 1000nM$, we have the dimensionless parameter $x_{aux_0} = 0.001$. Following auxin treatment we set $x_{aux} = 1$. The binding thresholds for ARF binding sites are all set to 0.1 since non-dimensional ARF and ARF-Aux/IAA are limited to between 0 and 1, while the binding threshold for X on the LAX3 promoter is set to 1 to allow for sensitivity in the value of X, which varies between 0 and 1 depending on auxin concentration. The default values of the co-operativity coefficients n_i, n_x and n_l are initially set equal to one but the effect of increasing these values on steady state values is investigated further in section 2.1.3.

2.1.3 Steady State Analysis

To investigate the possibility that the model can explain the observed all-or-nothing expression pattern of LAX3 in cortical cells overlying LRP, we investigate its steady states as parameters are varied by plotting bifurcation diagrams using the computer software Xppaut (Ermentrout 2002). Xppaut has an interface with the programme AUTO, which can find the steady states of a system of ODEs as a parameter varies by continuation from an initial steady state, found using Xppaut. In particular, AUTO can identify any regions of parameter space where multistability occurs, and also give information on the stability of steady states and the location and type of any bifurcations present.

There are several examples of bistability due to interconnected positive and negative feedbacks producing all or nothing responses in biological systems, including in frogs during *Xenopus laevis* oocyte maturation (Ferrell and Xiong 2001), in bacteria during regulation of the lactose operon in *Escherichia coli* (Laurent and Kellershohn 1999), and in the yeast *Saccharomyces cerevisiae* (Becskei et al. 2001). Of particular interest then is whether or not, and if so under what conditions, bistability in LAX3 expression with increasing auxin signal can occur.

Increasing the co-operativity coefficient in the function for transcription for both X (n_x) and LAX3 (n_l) can introduce a bistable region of gene expression with increasing x_{aux} (figure 2.2). For the parameter set given in table 2.1, if either or both of n_x and n_l are greater than two, there is bista-

Table 2.1: Nondimensional parameters, with initial estimates and description.

Parameter	Estimate	Description
$\bar{\mu}_i = \frac{\mu_i}{\mu_{im}}$	0	Auxin independent Aux/IAA decay rate
$\bar{\eta}_{tir} = \frac{tir_T}{xau_{xT}}$	0.001	Total TIR relative to auxin treatment
$\bar{\eta}_{arf} = \frac{arf_T \mu_{im}^2}{\lambda_i \delta_i^2}$	0.001	Total ARF relative to IAA14 rescaling
$\bar{\eta}_{iaa} = \frac{tir_T \mu_{im}^2}{\lambda_i \delta_i}$	0.001	Total TIR relative to IAA14 rescaling
$\bar{\mu}_x = \frac{\mu_x}{\mu_{im}}$	2	X protein decay relative to IAA14 mRNA decay
$\bar{\mu}_{xm} = \frac{\mu_{xm}}{\mu_{im}}$	2	X mRNA decay relative to IAA14 mRNA decay
$\bar{\mu}_l = \frac{\mu_l}{\mu_{im}}$	1	LAX3 protein decay relative to IAA14 mRNA decay
$\bar{\mu}_{lm} = \frac{\mu_{lm}}{\mu_{im}}$	1	LAX3 mRNA decay relative to IAA14 mRNA decay
$\bar{p}_a = \frac{p_a xau_{xT}}{\mu_{im}}$	1000	Association of auxin with TIR1
$\bar{p}_d = \frac{p_d}{\mu_{im}}$	1000	Disassociation of auxin with TIR1
$\bar{q}_a = \frac{q_a \lambda_i \delta_i}{\mu_{im}^3}$	10000	Association of TIR1-auxin with Aux/IAA
$\bar{q}_d = \frac{q_d}{\mu_{im}}$	1000	Disassociation of TIR1-auxin with Aux/IAA
$\bar{q}_m = \frac{q_m}{\mu_{im}}$	100000	Ubiquitination of TIR1-auxin-Aux/IAA
$\bar{k}_a = \frac{k_a \lambda_i \delta_i}{\mu_{im}^3}$	1000	Association of ARF with Aux/IAA
$\bar{k}_d = \frac{k_d}{\mu_{im}}$	1000	Disassociation of ARF with Aux/IAA
$\bar{\alpha}_x = \frac{\alpha_x}{\mu_{im}}$	1	Rate of auxin diffusion into cell
$\bar{\alpha}_{lax} = \frac{\alpha_{lax} \lambda_l \delta_l}{\mu_{im} \mu_l \mu_{lm}}$	15	Rate of auxin transport by LAX3 into cell
$\bar{\mu}_{aux} = \frac{\mu_{aux}}{\mu_{im}}$	10	Rate of cellular auxin decay
$\bar{xau}_{x0} = \frac{xau_x}{xau_{xT}}$	0.001	Basal auxin concentration (relative to treatment of $1\mu\text{M}$)
$\bar{\theta}_{ia} = \frac{\theta_{ia}}{arf_T}$	0.1	Binding threshold on Aux/IAA promoter for free ARF relative to total ARF
$\bar{\theta}_{ir} = \frac{\theta_{ir}}{arf_T}$	0.1	Threshold on Aux/IAA promoter for ARF-Aux/IAA dimers relative to total ARF
$\bar{\theta}_{xa} = \frac{\theta_{xa}}{arf_T}$	0.1	Threshold on X promoter for free ARF relative to total ARF
$\bar{\theta}_{xr} = \frac{\theta_{xr}}{arf_T}$	0.1	Threshold on X promoter for ARF-Aux/IAA dimers relative to total ARF
$\bar{\theta}_{la} = \frac{\theta_{la} \mu_{xm} \mu_x}{\lambda_x \delta_x}$	1	Threshold on LAX3 promoter for X relative to its scaling factor
$\bar{n}_i = n_i$	1	Co-operativity coefficient of binding of transcription factors to the Aux/IAA promoter
$\bar{n}_x = n_x$	1	Co-operativity coefficient of binding of transcription factors to the tfX promoter
$\bar{n}_l = n_l$	1	Co-operativity coefficient of binding of transcription factors to the LAX3 promoter

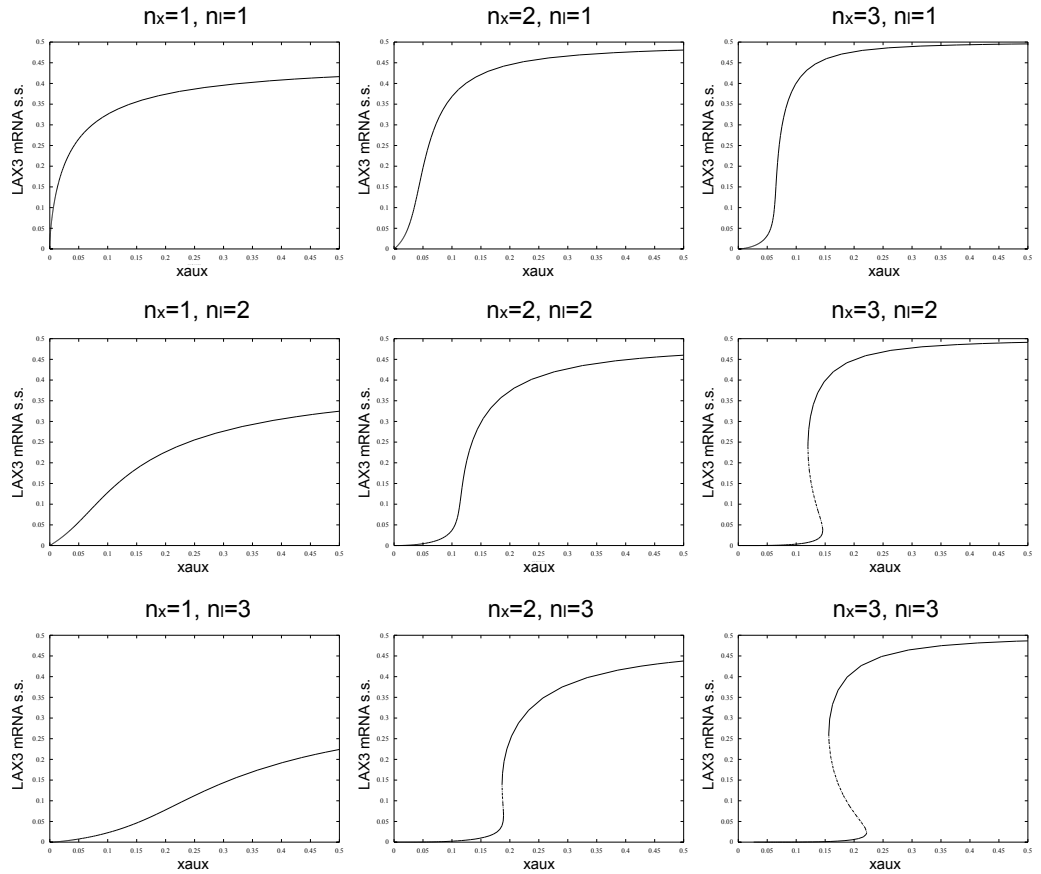


Figure 2.2: LAX3 steady state (s.s.) against x_{aux} (extracellular auxin concentration) for varying values for n_x (co-operativity in X promoter) and n_l (co-operativity on LAX3 promoter). Solid lines represent stable steady states, while thinner dotted lines represent unstable steady states.

bility. Increasing the co-operativity on the Aux/IAA promoter, n_i , above 1 always appears to reduce the width of the bistable region or remove bistability altogether (not shown). The bistable region means that for low and high $xaux$ there is a single stable steady state, but for a central range of values of $xaux$ there exist two stable steady states along with an intermediate unstable steady state (figure 2.2, middle right, bottom middle and bottom right). The result of this is that there is an intermediate steady state for LAX3 expression which is always unstable. In other words, depending on initial conditions, LAX3 can settle to either a high or a low range of expression. With the bistability present, if $xaux$ begins at a low level and is gradually increased, LAX3 expression will remain low until enough auxin accumulates to switch LAX3 expression to the higher steady state. Once this occurs, even if auxin levels drop slightly LAX3 expression will remain high; once the lower critical value is reached LAX3 expression will drop into the lower range once more. This hysteretic effect associated with bistability would have the effect that LAX3 expression could be buffered from small fluctuations in auxin concentration.

Without co-operativity ($n_x = 1, n_l = 1$) LAX3 expression increases approximately linearly from zero at low $xaux$, before saturating at higher $xaux$. In this case an all or nothing LAX3 expression pattern cannot be explained by the single cell model, unless there are extreme differences in auxin concentration between adjacent cells. For higher co-operativities that do not show bistability e.g. $n_x = 2, n_l = 2$, there is ultra-sensitivity. This means that for low and high ranges of $xaux$ there is little difference in expression for small perturbations in auxin, but for a specific central range of $xaux$ a small increase in $xaux$ will result in a large change in LAX3 expression. This could result in an all or nothing expression pattern even for small differences in auxin between adjacent cells. However, this expression pattern would be unstable due to the sensitivity of adjacent cells to small auxin fluctuations, which is biologically undesirable in comparison to the bistable case where the bistable region acts as a buffer between high and low expression.

For the parameter set used in figure 2.2, when $n_x = 2$ and $n_l = 2$ there is no bistability, only a sigmoidal or ultra-sensitive response of LAX3 expression to increasing auxin. However, it is possible to achieve bistability for these co-operativity values if the ratio α_{lax}/α_x , of auxin active transport to diffusion rate is increased. Figure 2.3 shows how the values of the upper and lower critical values for bistability in LAX3 expression of $xaux$ vary with increasing α_{lax} , for the case $n_x = 2$ and $n_l = 2$. For values of α_{lax} below about 20 there are no critical values, and hence no bistability, but above this there is bistability for an increasing large range of $xaux$ for increasing α_{lax} . For large α_{lax} (> 100) the bistability range appears to approach a limit. Figure 2.3 has μ_{aux} set to 100. Lowering it to 10 as in figure 2.2 produces a similar diagram, but with a greatly reduced range for $xaux$ critical values (around 0 to 0.1).

Auxin turnover rate (μ_{aux}) also affects the width of any bistable re-

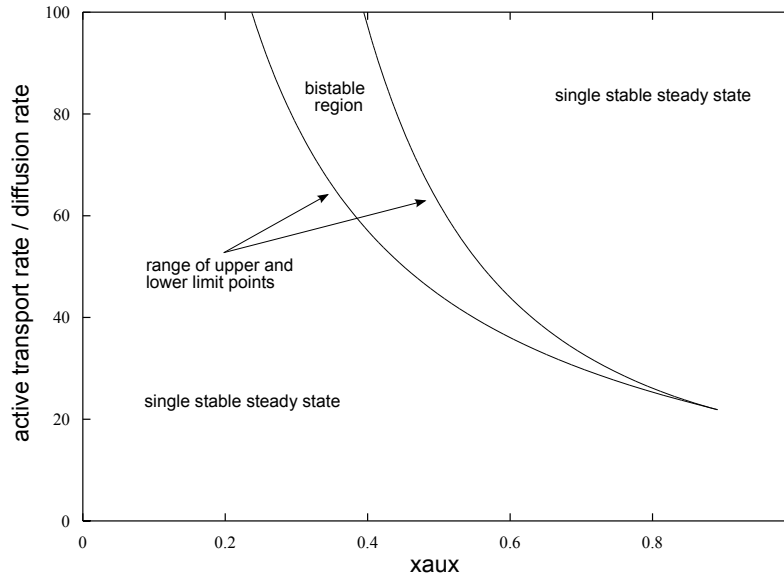


Figure 2.3: Upper and lower limit values of x_{aux} for the bistable region of steady state LAX3 expression with increasing α_{lax} with $\alpha_x = 1$. Parameter values are set as in table 2.1, except $\mu_{aux} = 100$, $n_x = 2$, and $n_l = 2$.

gion and the position of the upper and lower critical values (figure 2.4). Increasing μ_{aux} increases both the lower and upper critical values for the bistable region. The upper critical value increases at a higher rate than the lower, causing the width of the bistable region to increase with increasing μ_{aux} . A biological interpretation for this is that a higher basal turnover rate for cellular auxin results in increased robustness in LAX3 expression to small fluctuations in cellular auxin.

While bistability is possible in the model, it relies either on high co-operativity (figure 2.2) or on lower co-operativity in conjunction with a high value for active auxin transport relative to diffusion (figure 2.3). The estimate given in Swarup et al. (2005) is of around 15:1 transport to diffusion, which is not high enough to give bistability for the case $n_x = 2$ and $n_l = 2$ for the parameter set used here. This estimate was based though on a fixed concentration of AUX1 transporters on the cell membrane, while here we assume that the rate of transport is proportional to a variable amount of LAX3 present at any time, and it may be that when strongly expressed there are many more LAX3 transporters present than AUX1 for the previous estimate.

Co-operativity may result from multiple promoter binding sites and/or transcription factor dimerisation, but more experimental evidence would be needed to support whether or not this is the case for LAX3 expression. In particular, the auxin responsive transcription factor that is assumed to activate LAX3 is still unidentified, so its behaviour and possible binding

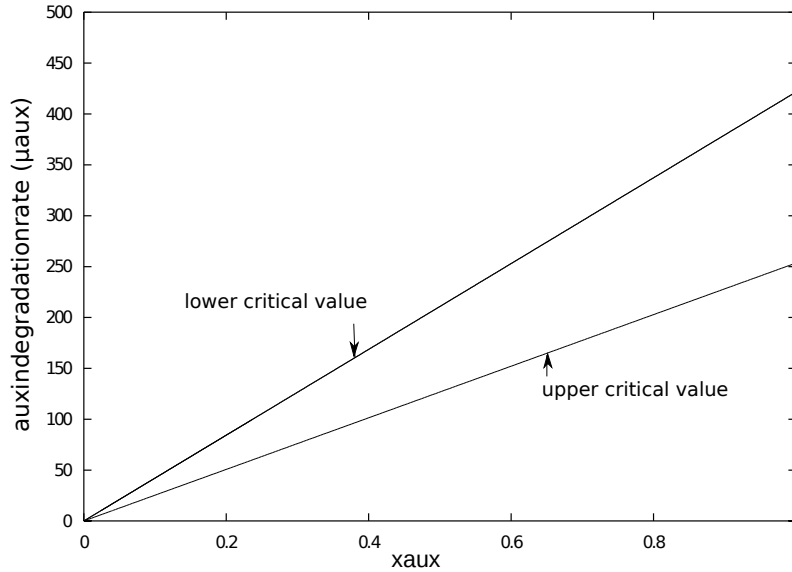


Figure 2.4: Upper and lower limit values of x_{aux} for the bistable region of steady state LAX3 expression with increasing auxin degradation or turnover rate μ_{aux} . Parameter values are set as in table 2.1, except $\alpha_{lax} = 100$, $n_x = 2$, and $n_l = 2$.

sites remain unknown. Nonetheless, Swarup et al. (2008) give evidence for a nonlinear relationship between increasing treatment concentrations of the synthetic auxin 2,4-D and *LAX3* mRNA expression. There appears to be a sharp step increase in expression between treatment at $0.1\mu M$ and $1\mu M$. These PCR results were taken from whole root data, but *LAX3* expression appears more or less uniform throughout the cortex at the $1\mu M$ treatment concentration, so we assume the PCR results are a reasonable approximation for what is happening in a single cortical cell. It seems likely that some co-operativity effect of auxin inducible transcription factors on the *LAX3* promoter is acting in conjunction with the positive feedback due to increased auxin influx via *LAX3* active transport to produce a switch in *LAX3* expression with increasing auxin signal. For treatment with exogenous auxin there will be a strong auxin signal throughout the length of the root and so expression is uniform. A weaker source of auxin from a specific cell or cells within the root could instead produce spatially restricted expression patterns of *LAX3*, due to the switch like response of *LAX3* to increasing auxin.

Bistability may be desirable in the expression of *LAX3* to ensure consistency in the spatial expression pattern. Assuming there are two cortical cells nearest the LRP that need to express *LAX3* and CWREs in order for the LRP to pass between them, then their two neighbouring cortical cells ought not to express *LAX3* in order to maintain the structural integrity of the root. Assuming all the cortical cells have low auxin concentration before the auxin signal from the LRP reaches them, all the cells begin on the

low expression branch of the bifurcation diagram. As the signal strength increases, the auxin in the two cortical cells nearest the LRP (central cells) ought to increase higher than that in the two neighbouring cells. With a high enough signal, and difference between the two pairs of cells, LAX3 expression will jump to the high expression branch of the bifurcation diagram in the two central cells while remaining on the low expression branch in the two neighbouring cells. Furthermore, the expression of LAX3 in the central cells will reduce auxin in the neighbouring cells due to increased auxin influx into the LAX3 expressing cells, ensuring expression in those cells remains on the low expression branch. The bistability ensures that even if the auxin signal from the LRP drops slightly, either temporarily or permanently, expression in the two central cortical cells remains on the higher branch of the bifurcation diagram, so that LAX3 expression is kept switched on, and the required spatial expression pattern is maintained.

2.1.4 Time Course Simulations

Simulation of Auxin Treatment

To simulate the addition of exogenous auxin to 7 day old seedlings as in the qRT-PCR data we first run the model to steady state using a value of $x_{aux} = 0.001$, then change to $x_{aux} = 1$ and run the model from the previous steady state. Initially we assume this increase in x_{aux} is constant throughout the time course. If the treatment concentration represented by $x_{aux} = 1$ is $1\mu M$ auxin, then the basal estimate for endogenous auxin of $x_{aux} = 0.001$ represents a concentration of $1nM$. All numerical solutions of the model presented here were found using the ode15s ODE solver within the MATLAB software package. The model time course response using the parameters in table 2.1 is given in figure 2.5. The model species concentrations are dimensionless, but time is shown in hours using a value for the scaling parameter $\mu_{im} = 0.4$, obtained from an average of values for Aux/IAA mRNA decay rates given in Narsai et al. (2007).

As expected, initially there is a rapid increase in auxin followed by a decrease to near zero of Aux/IAA within around 2 hours due to the perception of auxin by TIR1 accelerating its degradation. Levels of free ARF increase while ARF-Aux/IAA dimers decrease leading to expression of the primary response genes, Aux/IAA and X, then the secondary response gene LAX3. LAX3 then feeds back into the pool of intracellular auxin with an additional auxin increase after 5 hours. The main qualitative difference between this and the observed expression data is that the expression data peak after 12 hours before tailing off (figure 1.9), while the model mRNAs stay upregulated as long as the auxin signal persists.

Time Course with Bistability

Figure 2.6 shows model LAX3 mRNA against time using a parameter set identified to have bistability in section 2.1.3. The parameters are as given in table 2.1, but with the co-operativity coefficients for binding of ARF to the tFX promoter (n_x), and the binding of tFX to the LAX3 promoter (n_l) set

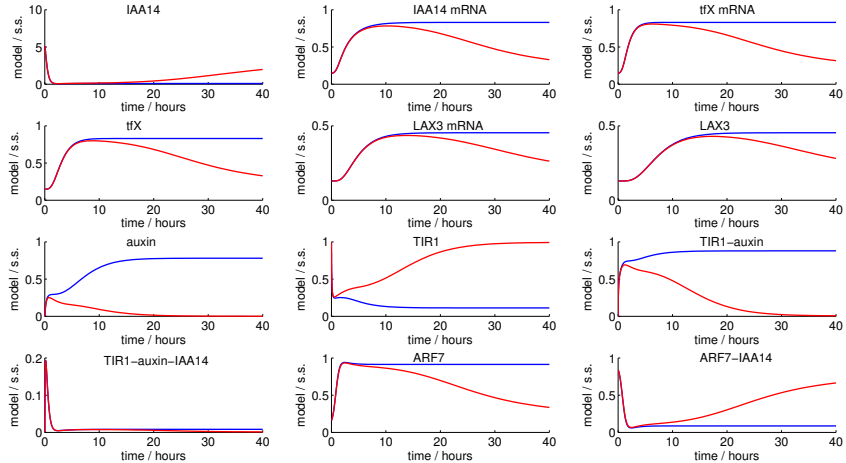


Figure 2.5: Model response (y-axis) against time (hours, x-axis) for each model species using the parameter estimates given in table 2.1, following an increase in signal at $t = 0$. Blue lines: persistent auxin signal, red lines: exponential decay of auxin signal ($\mu_{tr} = 0.5$). Nondimensional time is scaled into hours using a value for the rescaling parameter $\mu_{im} = 0.4$.

equal to 3. In each case the model is run from steady state, at either a basal auxin level of $x_{aux_0} = 0.01$, or $x_{aux_0} = 0.03$, following a change in x_{aux} to a range of treatment values between the upper and lower basal concentrations. For the lowest two treatment concentrations ($x_{aux} = 0.01, 0.015$) steady state LAX3 mRNA is very low regardless of the initial concentration, while for the higher treatments ($x_{aux} = 0.025, 0.03$) steady state LAX3 expression is relatively high regardless of the initial concentration. For $x_{aux} = 0.02$, however, LAX3 mRNA can have either a high steady state, if the initial level of auxin is high, or a low steady state if the initial auxin level is low.

The steady state analysis (section 2.1.3), and the time course described above, show that it is possible for the LAX3 model to have bistability, and that this may explain the all-or-nothing LAX3-YFP expression observed in cortical cells during lateral root emergence. This possibility will be investigated in the spatial context using tissue and multi-scale modelling in chapters 5 and 6. In particular, greater consideration will be given to the time-scales over which changes in auxin diffusion and transport are taking place. In figure 2.6, while the possibility of bistability is shown, when using the current parameter values for auxin turnover, transport and diffusion, the time-scales over which changes in LAX3 expression occur can be many hours. Further investigation is needed to establish whether or not these parameter values are biologically realistic. In the following sections, we compare the existing model with the qRT-PCR data following auxin treatment shown in figure 1.9.

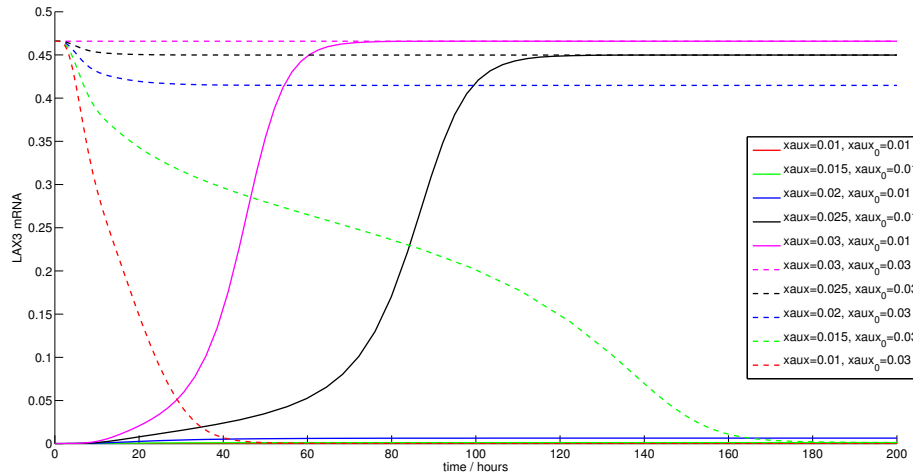


Figure 2.6: Model response (y-axis) against time (hours, x-axis) for LAX3 mRNA using the parameter estimates given in table 2.1, but with $n_x, n_l = 3$, following a change in auxin signal at $t = 0$ (see figure legend). Solid lines are the model response from steady state at $xaux_0 = 0.01$, dashed lines the response from $xaux_0 = 0.03$. For a change in signal to $xaux = 0.02$ (blue lines) there is a different steady state depending on initial conditions, demonstrating bistability. For all other values there is a single steady state regardless of initial conditions. Nondimensional time is scaled into hours using a value for the rescaling parameter $\mu_{im} = 0.4$.

Decay of auxin signal

With the initial parameter estimates, we see that in order for the model to match experimental data (figure 1.9), even qualitatively, an additional model component is needed which will result in downregulation of genes over the latter part of the time course simulation. The simplest mechanism by which this can occur is that following the initial treatment the exogenous auxin signal is degraded exponentially over time so that:

$$xaux(t) = xaux_0 + (xaux_{tr} - xaux_0)e^{-\mu_{tr}t}, \quad (2.8)$$

where $xaux_0$ represents the basal auxin concentration pre-treatment, $xaux_{tr}$ is the auxin treatment concentration, and μ_{tr} is the rate of exponential decay of the signal.

With an initial estimate of $\mu_{tr} = 0.5 \text{ hour}^{-1}$, the model gives a much improved qualitative comparison between model and experiment as shown in figure 2.5. After the initial rapid increase in cellular auxin following treatment, rather than continuing to increase with the expression of LAX3, auxin gradually returns toward its initial basal level. Though this would appear to negate the effect of LAX3 expression, it should be noted that the aim here initially is to simulate the genetic response of the plant to an excess ($1\mu M$ concentration) of exogenous auxin, rather than model the effect of LAX3 expression on cellular auxin during normal lateral root emergence. The effect of LAX3 on cellular accumulation of auxin and the spatial distribution of auxin within the root will be investigated in detail in chapters

5 and 6. As the auxin in the cell decreases, so this is perceived by the TIR1 receptors, causing a recovery of Aux/IAA protein, which results in the repression of free ARF, and ultimately a decrease in the rate of expression of the response mRNAs causes the levels of mRNAs and response proteins to drop back toward basal levels.

There are a number of mechanisms that may cause the decay in signal. There may be a degradation of auxin in the experimental medium due to high exposure to light (Dunlap and Robacker 1988). Alternatively there may be a mechanism endogenous to the plant such as increased auxin conjugation to amino acids, following which its signalling capability is removed (Ljung et al. 2002), reduced auxin biosynthesis, or compartmentalisation of auxin away from detection in the nucleus. Two of these mechanisms in particular, auxin inducible auxin conjugation and the decay in the experimental medium, are investigated further in sections 3.1 and 2.2.4 respectively.

2.2 Parameter Fitting and Predictions From Initial LAX3 Models

Previously, we saw that using the initial parameter estimates and adding an exponential decay to the initial auxin signal it is possible to match qualitatively the experimentally observed behaviour of model components. In this section we test the model further by optimising parameter values to fit the model response with quantitative experimental data.

After first describing the fitting algorithm used, we show the best fit of the model with LAX3 and IAA14 mRNA expression data, with unconstrained parameters, and no decay of the auxin signal. Next, by noting that there is likely to be a separation of timescales between protein-protein/auxin-receptor interactions and gene expression, we simplify the model and, using the parameter fitting algorithm again, establish that with this separation of timescales the decay in auxin signal is required. Finally, we show new data that supports the model predictions, while also suggesting that an additional auxin homeostasis mechanism is needed in the model to simulate the temporal response of LAX3 and IAA14 to auxin treatment.

2.2.1 Fitting Algorithm

The parameter fitting in this section and throughout was done using the optimization toolbox within MATLAB. A hybrid of two fitting algorithms was used. First an evolutionary or genetic algorithm (MATLAB function ‘ga’) was used to search the global parameter space. The genetic algorithm starts at the first iteration with a randomly generated population of parameter sets and for this and each further generation of iteration selects a subset of the the best fits of the model with the data according to a pre-defined objective or fitness function. For each further iteration the subset of best fits is added not only to a new set of randomly generated parameter sets, but also to a set of parameter sets of slightly altered or ‘mutated’ versions and recombined pairs or ‘offspring’ of the best fits from the previous itera-

tion. In this way, at each generation a better fit to the data is found, or the best fit from the previous iteration is retained, until a stopping criterion is reached. This may be a maximum number of iterations, or a threshold in the fitness function, or no change in the fitness function for a number of generations, any other user-definable criteria. Because the genetic algorithm is a stochastic process however, it may need to be run a number of times to improve the likelihood of finding a good fit to the data, or to help establish that no good agreement between model and data is possible. The parameter space searched was chosen to be logarithmic (base 10) so that e.g. a value of between 0.001 and 0.01 is as likely to be selected as a value between 100 and 1000. Initially, bounds were placed on parameter values of between 10^{-10} and 10^{10} , with the exception of co-operativity coefficients which are bounded between 1 and 4, and basal cellular auxin (x_{aux_0}) which is bounded between 10^{-4} and 1.

The best solution found with the genetic algorithm was then optimised further using the Matlab function 'fmincon'. Taking the result of the genetic algorithm as a starting point, at each iteration a small step is taken in n-dimensional space (where n is the number of parameters being fitted) along the line of steepest descent in the fitness function. This continues until a local minimum is found. Adding the local minimum search generally improves the result found by the genetic algorithm. For both algorithms the objective function to be minimised is the sum of squared differences between each data point and the model value at that time point relative to steady state at $t = 0$, relative to the squared sum of differences between the mean of the data and the data themselves (i.e. the variance of the data):

$$f = \frac{\sum_{i=1}^n \left(\frac{model_i}{model_{ss}} - data_i \right)^2}{\sum_{i=1}^n (\overline{data} - data_i)^2},$$

where n is the number of time points, $model_{ss}$ is model steady state at $t = 0$, $model_i$ and $data_i$ are the respective model and data values at the i^{th} time point, and \overline{data} is the mean of the data values.

Since all the quantitative data used for the parameter fitting represents relative values or fold-changes from time=0, all model values are scaled relative to their steady state values. Similarly, scaling the objective function with the variance of the data allows for similar weights to be given to multiple data series when optimising the model parameters against them all simultaneously. For example, in the following section the model is optimised against data series for both LAX3 and IAA14 mRNAs. The magnitude of auxin response of LAX3 and IAA14 may differ greatly, but evaluating the objective function for a given parameter set for each separately, scaling with the variance of the data, and then adding the values helps to give equal weighting to both data series. This can prevent the algorithm preferentially fitting the model to the data series with the greatest magnitude response.

Since time is scaled in the non-dimensional model so that $t = \tau/\mu_{i_m}$, where τ is non-dimensional time and t dimensional time, the time points in the data series are also scaled into non-dimensional time using a value

of $\mu_{i_m} = 0.4 \text{ hour}^{-1}$ before the parameter fitting algorithm is run. When using the fitted parameter values therefore, time must be rescaled back to dimensional time in order to compare with the data on the same axes. In general, most of the fitted parameters values given from now on will be non-dimensional, while the plots will be shown in dimensional time using $\mu_{i_m} = 0.4 \text{ hour}^{-1}$.

2.2.2 Parameter Fitting using Full Model

Though we estimate that protein-protein and auxin-receptor reaction rates are likely to be an order of magnitude greater than mRNA and protein turnover rates, we first attempt to fit the model with the qRT-PCR data shown in figure 1.9 for wild type LAX3 and IAA14 mRNA following treatment with $1\mu M$ auxin, using a persistent auxin signal, and with wide bounds (10^{-10} to 10^{10}) on the rate parameter values. With these criteria, it is possible to find parameter sets for which model and data show good agreement ($f = 0.0315$, figure 2.7, for parameter values see table 2.2). The parameter set presented here is one of several found using the fitting algorithm with similar values for f , and while individual parameter values differ between them, the overall behaviour is representative and conclusions made are similar for all parameter sets fitted in this way.

The model behaviour using the fitted parameter values can be explained as follows. For any fixed value of exogenous auxin, there will be a corresponding steady state value of Aux/IAA, the key regulator of auxin genes (with this parameter set there is no bistability, see figure 2.8(a)). If, as here, the rates of protein-protein interactions and ubiquitination are sufficiently slow so that it takes many hours for Aux/IAA to reach its steady state, shortly following the introduction of the auxin signal there is a temporary low level of Aux/IAA allowing response genes to be expressed, before there is a gradual accumulation of Aux/IAA later on in the time course, as the positive feedback on Aux/IAA due to increased expression takes time to be perceived. Though there is a temporary dip in Aux/IAA before recovery over longer timescales, as long as the auxin signal remains the steady state Aux/IAA will always remain lower than the basal level without the signal. In this case however, the steady state with the signal is relatively close to the basal level and so, in conjunction with relatively slow rate parameters this causes the large drop, followed by re-accumulation of Aux/IAA to the new steady state, as required to simulate the mRNA time course profiles (figure 2.7) .

If we compare the steady state Aux/IAA with increasing auxin signal using the fitted parameter set 2.2 and the estimated parameters given in table 2.1, we see that the steady state auxin using the fitted parameters is much less sensitive, even to very large changes in auxin, than with the parameter estimates (figure 2.8(a)). It is only via the adding of auxin to excess, as in the qRT-PCR experiment, that a transient low level of Aux/IAA occurs, allowing a temporary genetic response. During endogenous processes within the plant however, changes in cellular auxin are likely to be much less dramatic, and so with this range of steady states for Aux/IAA

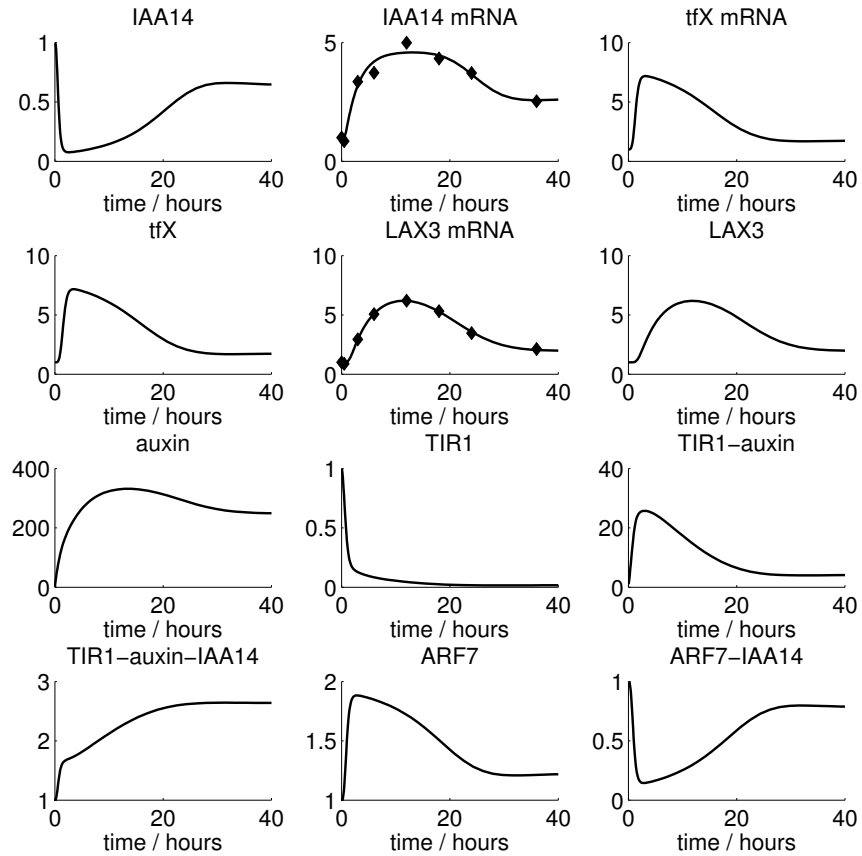


Figure 2.7: Response of model given by equations (2.5), relative to initial steady state, following simulated $1\mu M$ auxin treatment (y-axis) against time for each model species using the parameter estimates given in table 2.2 (solid lines). The initial conditions are the steady state values at the basal level of auxin, x_{aux_0} . Diamonds show experimental data points for LAX3 and IAA14 mRNAs. The model shows good agreement with the data, but this depends on relatively slow rates for protein-protein interactions and the rate of Aux/IAA ubiquitination.

Table 2.2: Fitted non-dimensional parameters used in figures 2.7 and 2.8. Other parameter sets were found, using the fitting algorithm, which produce similar results for all model species.

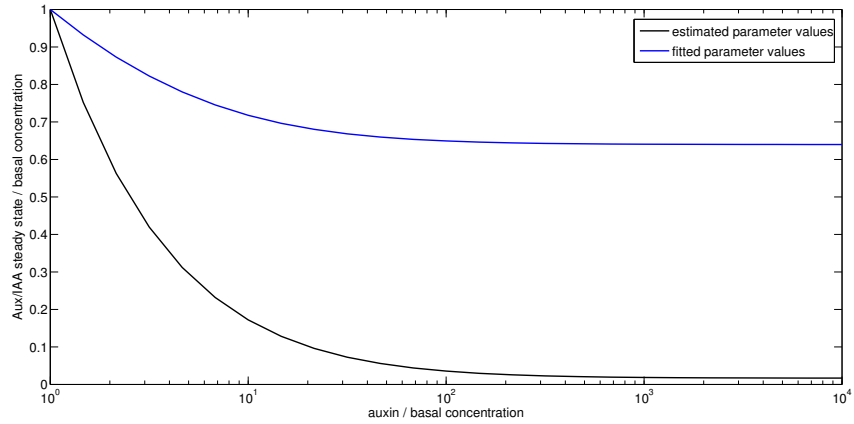
p_a	p_d	k_a	k_d	q_a	q_d	q_m
1.8080	2.6259	8.2037	12.3684	7.1601	0.3002	0.0746
η_{arf}	η_{iaa}	η_{tir}	$xaux_0$	α_x	α_{lax}	μ_{aux}
1.1473	8.0930	0.2375	0.0044	9.9254	11.9277	1.7213
n_i	θ_a	θ_r	μ_l	μ_{l_m}	n_l	ψ_x
3.5732	0.1566	0.1127	7.0816	0.6072	1.3975	0.5369
μ_x	μ_{x_m}	n_x	ϕ_a	ϕ_r		
11.4126	11.2955	1.5197	0.0417	0.0400		

the cells will be relatively unresponsive to auxin.

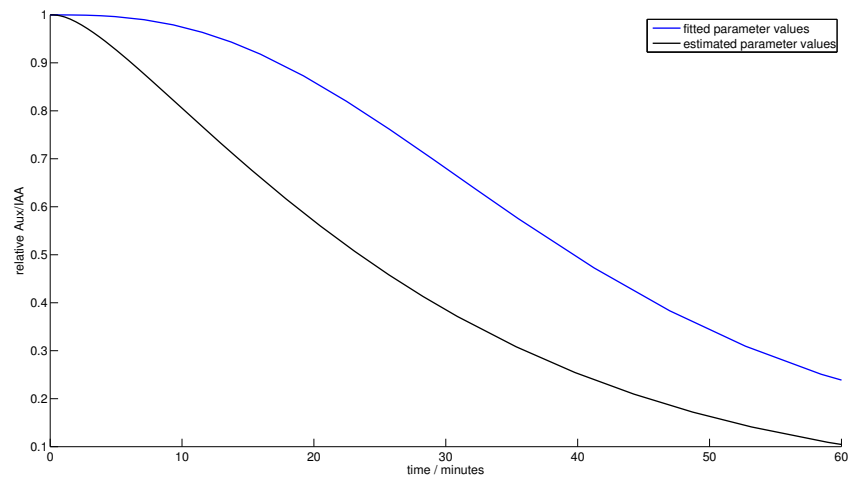
Another argument against the biological relevance of this fitted parameter set is given by looking at the very early response of Aux/IAA to the auxin treatment (figure 2.8(b)). Looking at the first hour there is a sigmoidal shape, with a delay of around 5 to 10 minutes before the Aux/IAA begins to be rapidly degraded. This is contrary to previous experimental observations in which there is more rapid reponse in the degradation of Aux/IAAs (2 minutes in PS-IAA4 and PS-IAA6 (Abel et al. 1994), 2 minutes for IAA1 (Zenser et al. 2001), 2.5 minutes for IAA17 (Dreher et al. 2006)). For this and the reasons above, while the model can show agreement with the mRNA data, the parameter set required is not biologically realistic, and the early response of model Aux/IAA is qualitatively different to that previously observed experimentally. In particular, data and modelling shown in the recent publication by Band et al. (2012) give evidence that auxin mediated degradation of Aux/IAA is at its maximum rate within 2 minutes following auxin treatment. The data published in that paper will be used to refine the model further in section 2.2.4.

2.2.3 Model Simplifications

The model given by equations (2.5a)-(2.5l), with a persistent auxin signal, is able to simulate mRNA data for LAX3 and IAA14 mRNAs, provided protein-protein, receptor-auxin, and ubiquitination reactions are permitted to occur on a similar or slower timescale than mRNA and protein turnover rates. However, for reasons discussed in section 2.2.2 this is unlikely to be biologically realistic. It would be possible to adjust the bounds on the parameter values in question during the parameter fitting to within a more biologically realistic range, however since we estimate some parameter values to be large in magnitude compared to the others this allows for one or more quasi-steady state approximations to be made, and so simplify the model, as described below.



(a) Steady state Aux/IAA protein with increasing exogenous auxin. Auxin is relative to the estimated or fitted basal concentration, while Aux/IAA is relative to the steady state at basal auxin.



(b) Aux/IAA protein against time for 60 minutes following simulated $1\mu M$ auxin treatment.

Figure 2.8: Comparison of steady state (figure 2.8(a)) and early time course (figure 2.8(b)) Aux/IAA for both the fitted parameters given in table 2.2 (blue line), and the estimated parameters given in table 2.1 (black line).

Protein-protein auxin-receptor and ubiquitination reactions

If we assume that the nondimensional parameter values k_a , k_d , p_a , p_d , q_a , q_d , and q_m are large in magnitude in comparison to the nondimensional timescale μ_{i_m} , we can neglect the derivatives in equations (2.5b)-(2.5d) and (2.5f)-(2.5g). Rearranging, we have the following quasi-steady state values for TIR , TIR_a , TIR_{ai} , ARF and AI (the * notation indicates quasi-steady state values):

$$TIR^* = \frac{QP}{QP + Qauxin + auxinIAA}, \quad (2.9)$$

$$TIR_a^* = \frac{Qauxin}{QP + Qauxin + auxinIAA}, \quad (2.10)$$

$$TIR_{ai}^* = \frac{auxinIAA}{QP + Qauxin + auxinIAA}, \quad (2.11)$$

$$ARF^* = \frac{K}{IAA + K}, \quad (2.12)$$

$$AI^* = \frac{IAA}{IAA + K}, \quad (2.13)$$

where we define $K \equiv \frac{k_d}{k_a}$, $P \equiv \frac{p_d}{p_a}$, $Q \equiv \frac{(q_d+q_m)}{q_a}$, and $\eta \equiv \eta_{iaa}q_m$. Substituting for TIR , TIR_a , TIR_{ai} , ARF and AI in the original model (2.5a)-(2.5l) we have the following nondimensional model in 7 variables:

$$\frac{d auxin}{dt} = x aux(t)(\alpha_{aux} + \alpha_{lax} LAX) - \mu_{aux} auxin, \quad (2.14a)$$

$$\frac{d IAA}{dt} = \frac{-\eta auxin IAA}{QP + Qauxin + auxin IAA} + IAA_m, \quad (2.14b)$$

$$\frac{d IAA_m}{dt} = F_{tc} \left(\frac{K}{\theta_{ia}(IAA + K)}, \frac{IAA}{\theta_{ir}(IAA + K)}, n_i \right) - IAA_m, \quad (2.14c)$$

$$\frac{d X_m}{dt} = \mu_{x_m} \left(F_{tc} \left(\frac{K}{\theta_{xa}(IAA + K)}, \frac{IAA}{\theta_{xr}(IAA + K)}, n_x \right) - X_m \right), \quad (2.14d)$$

$$\frac{d X}{dt} = \mu_x (X_m - X), \quad (2.14e)$$

$$\frac{d LAX_m}{dt} = \mu_{l_m} \left(F_{tc} \left(\frac{X}{\theta_{la}}, 0, n_l \right) - LAX_m \right), \quad (2.14f)$$

$$\frac{d LAX}{dt} = \mu_l (LAX_m - LAX), \quad (2.14g)$$

Of particular note are the quasi-steady state substitutions for ARF and AI given in equations (2.12) and (2.13), which depend only on the values of the constant K and the variable IAA at any given time. This is a consequence of the assumption that ARF remains constant, as seen in the ARF7 expression data, and means that the rate of expression of ARF7 responsive genes depends only on the level of Aux/IAA protein and the parameter value K , which may be thought of as the equilibrium coefficient in the binding and unbinding of ARF with Aux/IAA. In other words, for a fixed amount of total ARF, K is the value of Aux/IAA at which unbound

ARF activator is equal to bound ARF-Aux/IAA repressor dimers. This relationship is shown in figure 2.9.

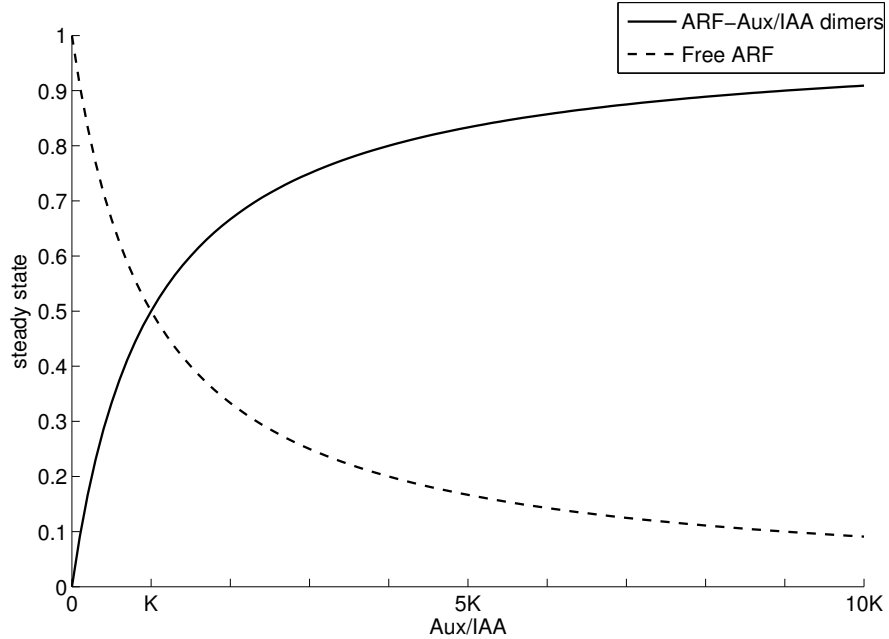


Figure 2.9: Quasi-steady state unbound ARF and ARF-Aux/IAA dimers for increasing fixed values of unbound Aux/IAA. Total bound and unbound ARF is always equal to one and, when Aux/IAA is equal to the parameter value K, the proportion of free ARF activators and ARF-Aux/IAA dimer repressors is equal.

Auxin diffusion, transport and turnover

The initial parameter estimates for auxin diffusion across the cell membrane (α_x), active transport (α_{lax}), and cellular turnover (μ_{aux}), are only around 10-fold greater than the turnover rates for the response mRNAs and proteins. However, the rapid response of plant tissues to auxin treatment suggests these estimates may be too small. If we assume then that α_x , α_{lax} , and μ_{aux} are all comparably large compared to the nondimensional timescale μ_{im} we can also neglect the derivative of *auxin* in (2.14a). Rearranging gives the following expression for quasi-steady state auxin (*auxin*^{*}):

$$auxin^* = xaux(t) \left(\frac{\alpha_x}{\mu_{aux}} \right) \left(1 + \frac{\alpha_{lax}}{\alpha_x} LAX \right) \quad (2.15)$$

Substituting this in (2.14b), rearranging, and setting $p \equiv P\mu_{lax}/\alpha_x$ and $\alpha \equiv \alpha_{lax}/\alpha_x$, we have the following nondimensional model in 6 variables:

$$\frac{dIAA}{dt} = \frac{-\eta xaux(t)(1 + \alpha LAX)IAA}{Qp + xaux(t)(1 + \alpha LAX)(Q + IAA)} + IAA_m, \quad (2.16a)$$

$$\frac{dIAA_m}{dt} = F_{tc} \left(\frac{K}{\theta_{ia}(IAA + K)}, \frac{IAA}{\theta_{ir}(IAA + K)}, n_i \right) - IAA_m, \quad (2.16b)$$

$$\frac{dX_m}{dt} = \mu_{x_m} \left(F_{tc} \left(\frac{K}{\theta_{xa}(IAA + K)}, \frac{IAA}{\theta_{xr}(IAA + K)}, n_x \right) - X_m \right), \quad (2.16c)$$

$$\frac{dX}{dt} = \mu_x(X_m - X), \quad (2.16d)$$

$$\frac{dLAX_m}{dt} = \mu_{l_m} \left(F_{tc} \left(\frac{X}{\theta_{la}}, 0, n_l \right) - LAX_m \right), \quad (2.16e)$$

$$\frac{dLAX}{dt} = \mu_l(LAX_m - LAX). \quad (2.16f)$$

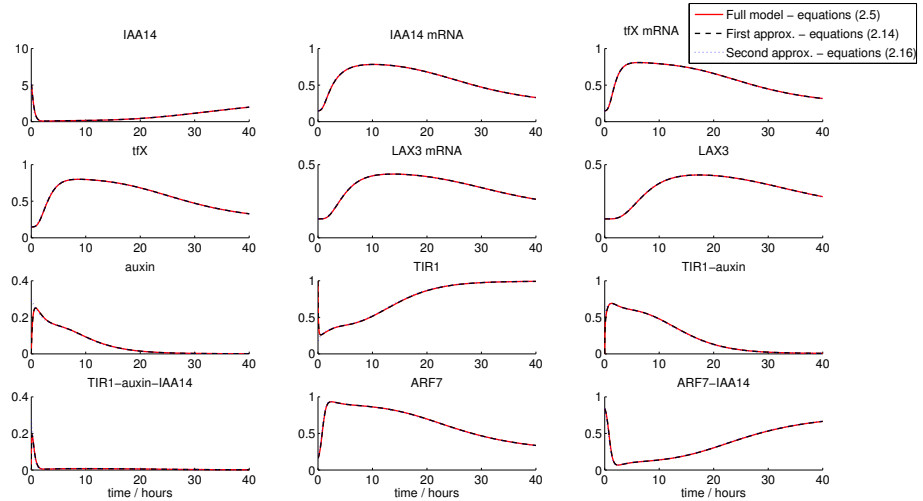
Comparison of model simplifications

We now have our original model and two successive simplifications: -

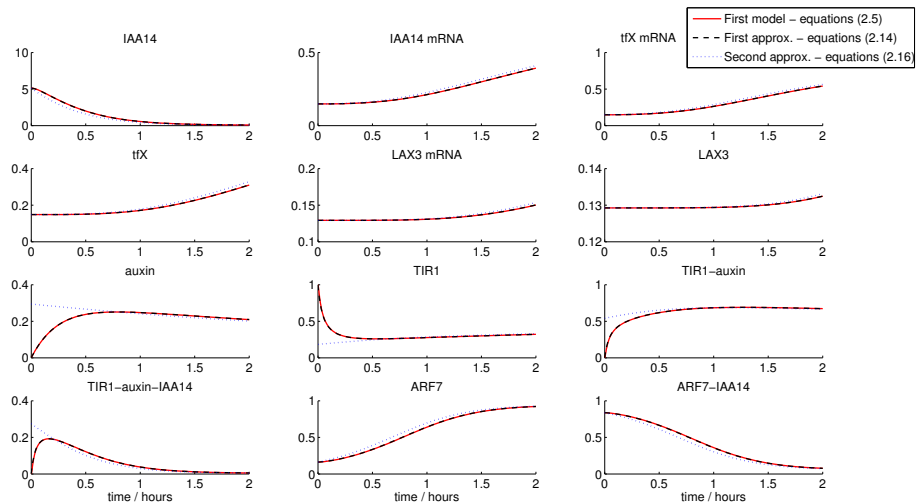
1. Original model in twelve variables - equations (2.5)
2. Assumption that auxin signalling via TIR1 and dimerisation of ARF and Aux/IAAs is rapid compared to nondimensional timescale - equations (2.14)
3. Assumption that auxin diffusion, transport and turnover is rapid compared to nondimensional timescale - equations (2.16)

Figure 2.10 shows a time course simulation using the default parameter set given in table 2.1 for each of the three models listed above. Over the longer 40-hour time scale shown in figure 2.10(a) all the models are clearly very similar for the given parameter regime. Even when looking closely over the first 2 hours as in figure 2.10(b), the original model is indistinguishable from the first approximation. There are however some differences between the second approximation and the other models. Firstly, the instantaneous change in auxin at $t = 0$ results in corresponding instantaneous changes in the balance between the concentrations of TIR1 in its different bound and unbound forms. In particular, TIR_{ai} is immediately many times greater than in the other models. The result of this is that IAA14 protein is degraded slightly more rapidly over the earliest part of the time course, though after two hours this difference is no longer apparent. The earlier degradation of Aux/IAA does, however, result in a slightly earlier increase in ARF and decrease in ARF-Aux/IAA dimers, and so the response mRNAs are initially up-regulated very slightly earlier. As we see in figure 2.10(a) though, there is little or no difference to the peak expression values attained.

While for the estimated parameters there does not appear to be much difference between the three models used over the longer time scale (tens of hours), the subtle differences in values for model species over the first two hours shown in the model with the second approximation compared



(a) Model response (y-axis) against time (hours, x-axis) for each model species using the parameter estimates given in table 2.1, for the original ‘full’ model and 2 approximations, following an increased auxin signal at $t = 0$, with a subsequent decay of that signal ($\mu_{tr} = 0.5$). Nondimensional time is scaled into hours using a value for the rescaling parameter $\mu_{i_m} = 0.4$.



(b) As 2.10(a) but only the first two hours of the time-course are shown.

Figure 2.10: Comparison of model response over time between original model, and two successive quasi-steady state simplifications.

to the other two models may be more significant when additional components are added to the model, and when, as in section 2.3 we attempt to fit model parameters relating to the early degradation of Aux/IAA. In addition, in section 3.1 we investigate possible auxin homeostasis mechanisms which may occur over longer time scales than diffusion and transport, meaning that the quasi-steady state approximation for auxin may no longer be valid. For these reasons, in the following sections we use the model given by equations (2.14) as a reasonable approximation for the full model given by equations (2.5), provided the assumption that protein-protein, auxin-receptor and ubiquitination reactions are relatively rapid holds. In Chapter 5 we investigate the processes and rate parameter values of auxin transport and turnover further, in the context of a multicellular model.

2.2.4 Parameter Fitting Using Reduced Model

Before testing the ability of the model to match the data with the addition of a decay in the auxin signal, we first run the parameter fitting algorithm using the reduced model with a persistent auxin signal. In addition to the constraints on parameter values described previously, we have the additional constraint that α_{lax} , the maximum rate of active transport, is between 1 and 100 times α_x , the rate of auxin diffusion. The fitting algorithm was run a total of five times for the model given by equations (2.14) and the best fit found had an f-value of 0.302. This is in comparison to the best f-value of 0.0315 found for the full model, as shown in figures 2.7 and 2.8. Figure 2.11 shows the best fit for simulated LAX3 and IAA14 mRNA in comparison with the PCR data, in addition to model IAA14 protein.

There is some down-regulation of the mRNAs following the initial induction, due to the positive feedback on IAA14 protein. However, the speed of key reactions means induction of the response mRNAs is arrested too quickly due to increased IAA14 protein, for the model to show good agreement with the data. The short and long term behaviour of Aux/IAA protein will be investigated further in section 2.3. For now however, if we keep the assumption of a separation of timescales between protein-protein interactions and mRNA and protein turnover, then we conclude the reduced model cannot show a good agreement with the data when simulating a persistent auxin signal.

Decay of Auxin Signal

As described in section 2.1.4, adding an exponential decay to the initial auxin signal (equation 2.8) will, in general, significantly improve the qualitative fit of the model with the mRNA data. Using the parameter fitting algorithm enables a quantitative fit with the data to be made, using the decay of exogenous auxin, as shown in figure 2.11. The best fit has an f-value of 0.0336, with the fitted parameter values given in Table 2.3.

In total the parameter fitting algorithm was run 5 times for the reduced models, with a threshold for a ‘good’ fit with the data of $f = 0.1$. For the best fit, the nondimensional signal decay rate $\mu_{tr} = 1.451$, which, with an estimate for $\mu_{im} = 0.4$, represents a dimensional decay rate of 0.58 hour^{-1} .

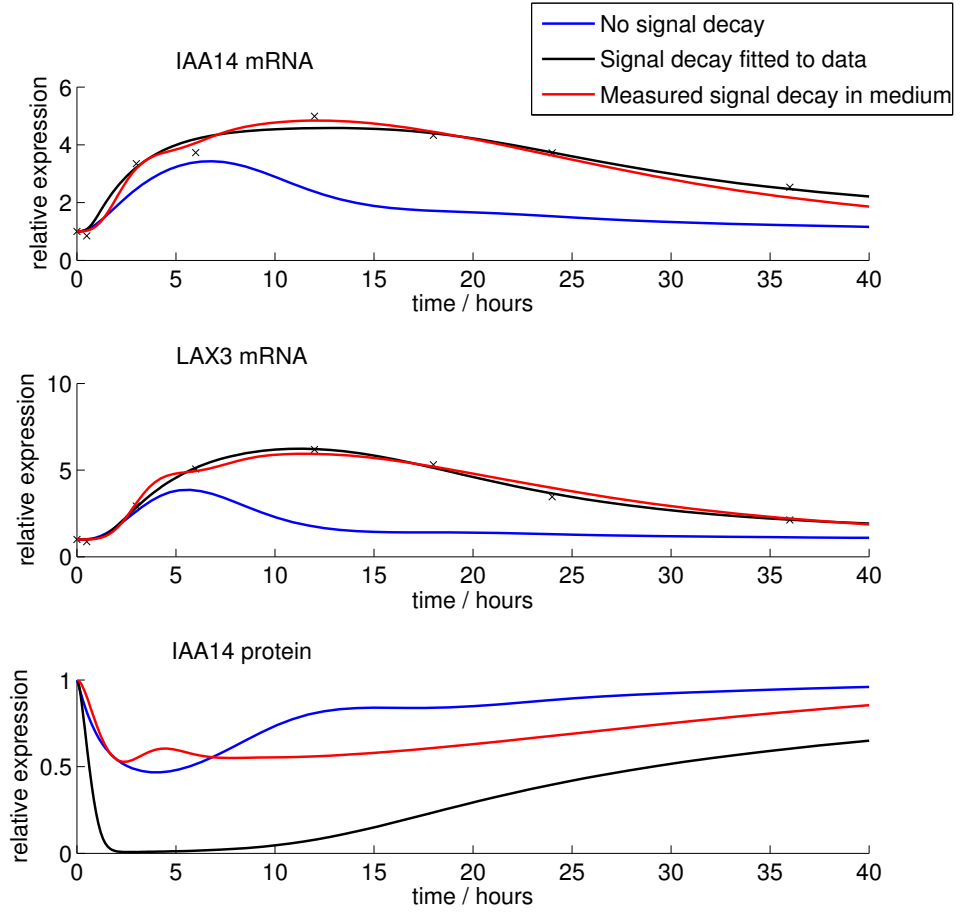


Figure 2.11: Best fits of the model IAA14 and LAX3 mRNAs with qRT-PCR data shown in figure 1.9 (Benjamin Peret, personal communication), following $1 \mu M$ simulated auxin treatment. Also shown is the model prediction for IAA14 protein. Blue lines have a persistent auxin signal, red lines have the measured decay of auxin on the experimental medium ($\mu_{tr} = 0.0729 \text{ hour}^{-1}$), while for the black lines the decay rate is fitted along with the other parameters ($\mu_{tr} = 0.58 \text{ hour}^{-1}$). The crosses represent the data points against which the parameters were fitted.

Table 2.3: Best fitted ($f = 0.0336$) non-dimensional parameters for the model given in equations (2.14a)-(2.14g) with decay of exogenous auxin signal (equation 2.8).

P	Q	K	η	x_{aux_0}	μ_{tr}	α_{lax}	α_x
4.0955	1.3724	2.1671	60.2363	0.0007	1.4514	53.6719	1.6135
μ_{aux}	n_i	θ_{ia}	θ_{ir}	μ_x	μ_{x_m}	n_x	θ_{xa}
1.4371	2.5026	0.0261	0.0660	241.1434	3.7905	1.1050	0.3830
θ_{xr}	μ_l	μ_{l_m}	n_l	θ_{la}	μ_{tr}		
0.9718	3.0628	0.6947	1.8588	0.9355	1.451		

In the following section, we investigate whether the degradation of auxin on the experimental medium is a plausible explanation for a decay rate of this magnitude.

Decay rate of auxin on experimental medium

A possible source of decay in the auxin signal is degradation in light of the auxin in the experimental medium itself. This decay was measured in the study by Dunlap and Robacker (1988), from which a half-life of approximately 2.4 days can be estimated, or a decay rate of 0.012 hour^{-1} . This decay rate was measured using a weaker light source than was used during the qRT-PCR experiment for which we have data, and so to establish the likely auxin decay rate for the data used to test the model a similar experiment was performed using the same light conditions (Ilkka Sairanen, personal communication). Both $1\mu M$ and $0.01\mu M$ auxin in liquid medium was exposed to light, and the auxin concentration was measured, relative to the initial value, after 2, 15, and 38 hours (figure 2.12).

For both auxin concentrations there was a clear decay over the time course, at a similar rate. This decay can be modelled using an exponential decay as in equation 2.8, but with x_{aux_0} , the basal auxin concentration, set to zero in the medium so that:

$$x_{aux}(t) = x_{aux_{tr}} e^{-\mu_{tr} t}, \quad (2.17)$$

with an optimal fitted decay rate (μ_{tr}) of 0.0729 hour^{-1} (figure 2.12). With an estimate of $\mu_{im} = 0.4$ for the timescale this gives a non-dimensional value of $\mu_{tr} = 0.182$.

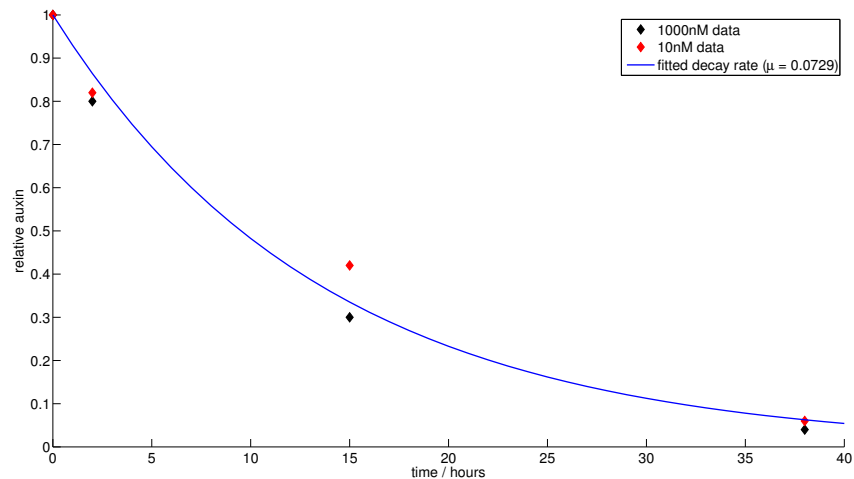


Figure 2.12: The degradation of auxin in light over time can be modelled with a exponential decay from the initial value, with decay rate 0.0729 hour^{-1} . $1\mu M$ and $0.01\mu M$ auxin in liquid medium was exposed to light, and the auxin concentration measured, relative to the initial value, after 2, 15, and 38 hours (Ilkka Sairanen, personal communication).

As would be expected when using a stronger light source than in the previous study, the auxin decay rate is higher. However, this value is less than one third of the value fitted to the mRNA data in the previous section. To test whether the measured value is still sufficient to account for the recovery of Aux/IAA needed to repress the auxin response genes following initial activation, the parameter fitting algorithm was again run a total of five times, but with a fixed value for $\mu_{tr} = 0.182$. Figure 2.11 shows the best fit of the model against the LAX3 and IAA14 mRNA data.

As shown in figure 2.11 it is possible for the model LAX3 and IAA14 mRNA to show good agreement with the data ($f = 0.0363$), using the experimentally determined rate for the decay of auxin on the medium. However, as in the case where there is no decay in the signal, this depends on a relatively small proportion of the total IAA14 to be degraded following the initial increase in auxin signal. In contrast to the zero decay case though, the recovery of Aux/IAA depends on a decrease of auxin in the cell, rather than the positive feedback of Aux/IAA expression but, in both cases, at the treatment concentration simulated, the degradation rate of Aux/IAA has not yet reached saturation, and so gene expression is more sensitive to smaller changes in Aux/IAA. For this case then, a relatively slow degradation rate of auxin is able to alter Aux/IAA sufficiently to reduce gene expression rates enough within the time frame in order to fit the data.

Close inspection of the data in figure 2.12 shows that after around 30 hours exposure to light, there is still around 10% of the initial value of auxin remaining. For $1\mu M$ treatment this represents $100nM$ remaining on the medium. As shown in Band et al. (2012) we would still expect to see strong degradation of Aux/IAA at this auxin concentration, and so even with degradation of auxin at the experimentally determined rate, there would be insufficient recovery of Aux/IAA within the timescale needed to down-regulate the response genes. In section 2.3 therefore, the parameterisation of the model will be improved further using the dose response data and modelling first published in Band et al. (2012), along with additional experimental results that give further evidence for a homeostatic response to auxin treatment on cellular auxin levels.

2.3 Short and long term behaviour of Aux/IAA (DII-VENUS model)

In section 2.2.4 it was shown that some form of decay of the auxin signal is required to fit the reduced model with the LAX3 and IAA14 qRT-PCR data shown in figure 1.9. However, to test whether the measured decay rate of auxin on the experimental medium is sufficiently fast to cause enough of a recovery in Aux/IAA within the time frame needed to down-regulate the response genes, closer attention must be paid to the short and long term behaviour of the Aux/IAA protein. In particular, the response of Aux/IAA to a range of auxin treatments must be considered.

In Band et al. (2012), the auxin sensor DII-VENUS, which is the Aux/IAA IAA28 domain II fused to the yellow fluorescent protein VENUS, was used

to quantify and model the response of roots to a range of auxin concentrations for two hours after treatment. A parameter fitting algorithm was used to obtain parameter estimates for the auxin influx rate for each treatment in the range, and estimates for the parameters relating to the degradation of DII-VENUS. In this section, an alternative version of the published DII-VENUS model is used to show that the dose response DII-VENUS data can still be modelled, even with the measured rate of auxin decay on the experimental medium. The prediction of the fitted model for DII-VENUS over a longer (30 hour) time scale is then compared with new DII-VENUS data over this longer time frame, and used to conclude that an additional auxin homeostasis mechanism is required to explain the apparent recovery of DII-VENUS levels over time.

2.3.1 Model formulation

Following Band et al. (2012), with the same notation as used here previously, we have the full dimensional model for DII-VENUS expression in five variables:

$$\frac{dTIR}{dt} = -p_a TIR \text{ auxin} + p_d TIR_a, \quad (2.18a)$$

$$\begin{aligned} \frac{dTIR_a}{dt} &= p_a TIR \text{ auxin} - p_d TIR_a \\ &\quad + (q_d + q_m) TIR_{av} - q_a TIR_a \text{ DII}^*, \end{aligned} \quad (2.18b)$$

$$\frac{dTIR_{av}}{dt} = -(q_d + q_m) TIR_{av} + q_a TIR_a \text{ DII}^*, \quad (2.18c)$$

$$\begin{aligned} \frac{dDII^*}{dt} &= q_d TIR_{av} - q_a TIR_a \text{ DII}^* - \lambda_v^* DII^* \\ &\quad + \delta_v DII_m^*, \end{aligned} \quad (2.18d)$$

$$\begin{aligned} \frac{dauxin^*}{dt} &= \alpha_0^* - \mu_{aux}^* auxin + \alpha_{tr}^* xaux(t) \\ &\quad - p_a TIR \text{ auxin} + p_d TIR_a, \end{aligned} \quad (2.18e)$$

$$TIR + TIR_a + TIR_{ai} = tir_T, \quad (2.18f)$$

where DII^* represents dimensional DII-VENUS, δ_v is the rate of translation of the constitutively expressed and constant quantity of DII mRNA, DII_m^* , and λ_v^* represents the rate of degradation of DII-VENUS due to photobleaching of the VENUS fluorescence during exposure under the confocal microscope. The key difference in the behaviour of DII-VENUS, compared to Aux/IAAs in general is that DII-VENUS mRNA is expressed constitutively, whereas Aux/IAA, in our case IAA14, is expressed in response to auxin. Replacing $xaux$, α_x , and α_{Iax} in the equation for $auxin$ there is a basal influx rate of auxin (α_0) plus an auxin treatment influx rate (α_{tr}^*) which is proportional to the time dependent exogenous auxin ($xaux(t)$).

To nondimensionalise, we use the same scaling for TIR , TIR_a , TIR_{ai} $auxin$ as in section 2.1.2, and also similarly to before we scale DII^* by the same factor as IAA so that:

$$DII = \frac{\lambda_i \delta_i}{\mu_{i_m}^2} DII^*.$$

If the auxin-receptor reactions are assumed to be rapid as before, we can make a similar quasi-steady state approximation as in section 2.2.3 and rearrange to give the reduced nondimensional model:

$$\frac{dDII}{dt} = \frac{-\eta auxin DII}{QP + Qauxin + auxin DII} - \lambda_v DII + \beta, \quad (2.19a)$$

$$\frac{d auxin}{dt} = \alpha_0 + \alpha_{tr} xaux(t) - \mu_{aux} auxin, \quad (2.19b)$$

where the nondimensional parameters Q , P , η and μ_{aux} are defined as before, and with $\alpha_{tr} = \frac{\alpha_{tr}^*}{xaux_T \mu_{im}}$, $\alpha_0 = \frac{\alpha_0^*}{xaux_T \mu_{im}}$, $\beta = \frac{\delta_v DII_m^* \mu_{im}}{\delta_i \lambda_i}$, and $\lambda_v = \frac{\lambda_v^*}{\mu_{im}}$. $xaux(t)$ remains a dimensional quantity, but when combined with α_{tr} becomes a dimensionless term in the model.

If we assume that DII-VENUS and IAA14 mRNA are translated at similar rates, and that the constitutive level of DII mRNA (DII_m^*) is a similar level as the maximum level of IAA14 mRNA ($\frac{\lambda_i}{\mu_{im}}$), then we can estimate $\beta = 1$. This value for β is used in the parameter fitting that follows, but the effect of using different values for β is investigated further in section 2.4.1.

The effect of the decay of auxin in the experimental medium is modelled as follows:

$$xaux(t) = (auxin_{tr} - auxin_0)e^{-\mu_{tr}t}, \quad (2.19c)$$

where $auxin_{tr}$ is the treatment concentration, $auxin_0 = \frac{\alpha_0^*}{\mu_{aux}}$ is the basal (no treatment) concentration of auxin, and μ_{tr} is the rate of degradation due to light exposure. Formulating $xaux$ in this way ensures that only when auxin on the medium is greater than the basal concentration in the root is there any flux from the medium to the root.

2.3.2 Parameter Fitting

Two hour dataset

Using the same parameter fitting algorithm as described in section 2.2 the model given by equations (2.19) was fitted with the data published in Band et al. (2012), using the experimentally measured rate of auxin decay on the experimental medium (0.0729 hour^{-1}). The dimensional units used for the auxin treatments are in nM , and the parameter values are bounded between 10^{-3} and 10^3 , with the exception of $auxin_0$ which is bound between 10^{-3} and 1, since as there is some reponse of DII to 1 nM auxin treatment we assume the basal auxin concentration is less than this value. Again the estimated value for the timescale is $\mu_{im} = 0.4$, and so we multiply the right hand side of both equations (2.19a)-(2.19b) by this when fitting with time dimensional data.

As shown in figure 2.13(a), even with a decay of auxin on the medium, the model is able to show good agreement with the data, with the minimum value for the objective function found of $f = 0.176$ (in this case the objective function used was just the sum of squared differences between model and data for each auxin treatment, rather than a scaled sum of squares as in section 2.2). The fitted parameter values are given in Table 2.4. To see

Table 2.4: Best fitted ($f = 0.176$) parameter values for the model given by equations 2.19a-2.19b, with the decay of exogenous auxin, $\mu_{tr} = 0.182$ (dimensional value 0.0729 hour^{-1} , with timescale $\mu_{i_m} = 0.4$).

P	Q	η	$auxin_0$	α_{tr}	μ_{aux}	λ_v	α_0
5.0006	0.6773	17.5942	0.2717	1.7252	8.2817	0.4229	2.250

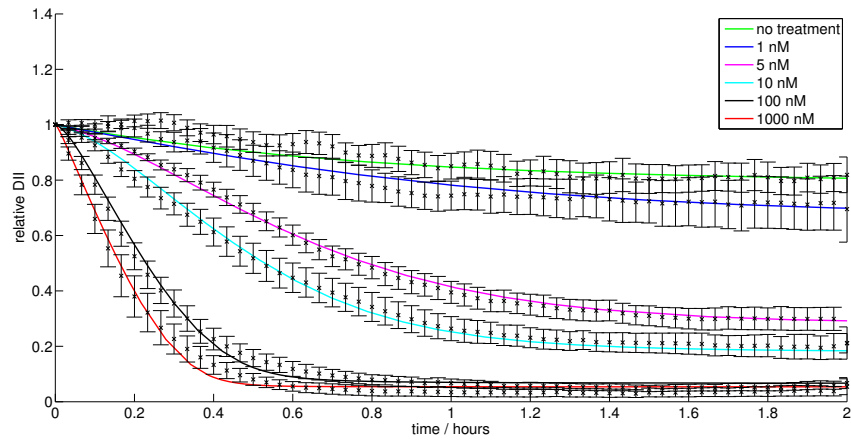
whether the measured auxin decay rate is sufficient to cause enough of a recovery in DII-VENUS, and by extension Aux/IAA, so explaining the down-regulation of IAA14 and LAX3 following auxin induction, we need to look at the longer term behaviour of DII-VENUS.

30 hour dataset

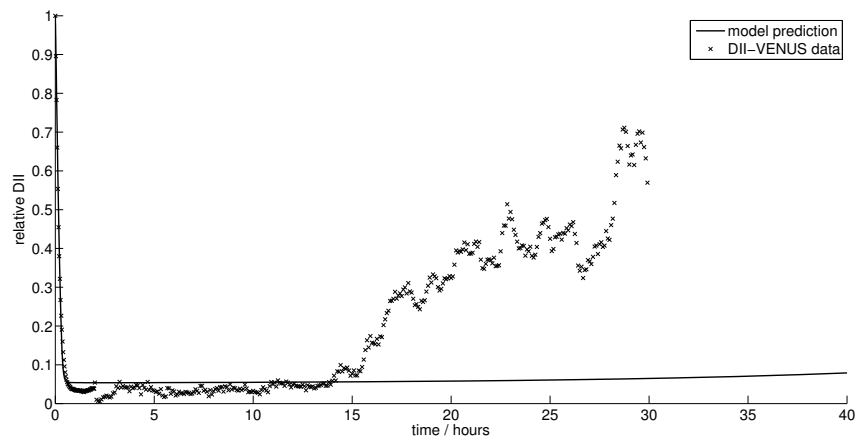
Figure 2.13(b) shows DII-VENUS quantification over a 30 hour timecourse following $1\mu M$ auxin treatment (Silvana Porco, personal communication), along with the simulated time course given by the model with the fitted parameters given in Table 2.4. We see that the measured rate of auxin decay on the medium is not fast enough to predict a significant recovery in DII-VENUS within the 36 hours of the qRT-PCR time course. This can also be inferred from the amount of DII-VENUS degradation seen following 100nM auxin treatment, which appears to be almost as great as for 1000nM treatment (figure 2.13(a)), and as we see in figure 2.12 even with the decay of auxin on the medium we would expect at least 10% of the initial auxin to remain for 30 hours post-treatment.

In figure 2.14, the parameter values given in table 2.4 were fixed, while instead of setting μ_{tr} to the experimentally determined value for degradation on the medium, μ_{tr} is fitted with the 30 hour DII-VENUS data. The fit between model and data is clearly imperfect, but the model appears to be able to match the overall trend of DII-VENUS recovery after about 10 hours post-auxin treatment, with a dimensional value for $\mu_{tr} = 0.264 \text{ hour}^{-1}$. The fitted value of μ_{tr} is 3.6 times greater in magnitude than the experimentally determined value for degradation on the medium. This difference between the estimate for the decay of exogenous auxin signal, and the apparent rate of recovery of DII-VENUS caused by removal of intracellular auxin suggests that an additional mechanism, endogenous to the plant root, is acting to maintain auxin homeostasis (chapter 3).

Using the fitted value for μ_{tr} does not seriously affect the behaviour of the model in comparison to data over the first two hours post-auxin. Using the parameter values given in table 2.4 with $\mu_{tr} = 0.264$ gives a value for the objective function $f = 0.184$ when fitted with the two hour dose response data, compared with $f = 0.176$ when $\mu_{tr} = 0.0729$. The goodness of fit is reduced, but the model prediction remains almost completely within the bounds of experimental error shown.



(a) DII-VENUS model (Equations 2.19) with decay of auxin on experimental medium set to the measured value of 0.0729 hour^{-1} fitted with data published in Band et al. (2012), following a range of auxin treatments. For parameter values see Table 2.4. The crosses represent the data with standard error bars shown, while the solid lines the model simulations at the range of auxin treatments(see key).



(b) Model with signal decay as in figure 2.13(a) ($\mu_{tr} = 0.0729 \text{ hour}^{-1}$) following simulated 1000 nM auxin treatment, over 40 hour time course (solid line), and DII-VENUS data (Silvana Porco, personal communication) following 1000nM auxin treatment for 30 hours post-treatment (crosses).

Figure 2.13: The DII-VENUS model with a decay in auxin signal is able to match the short term (2 hour) behaviour observed experimentally, but the measured rate of degradation of auxin on the medium is insufficient to account for the longer term (post 10 hours) recovery of DII-VENUS. Data in figure 2.13(a) published in Band et al. (2012), data in figure 2.13(b) courtesy of Silvana Porco, The University of Nottingham.

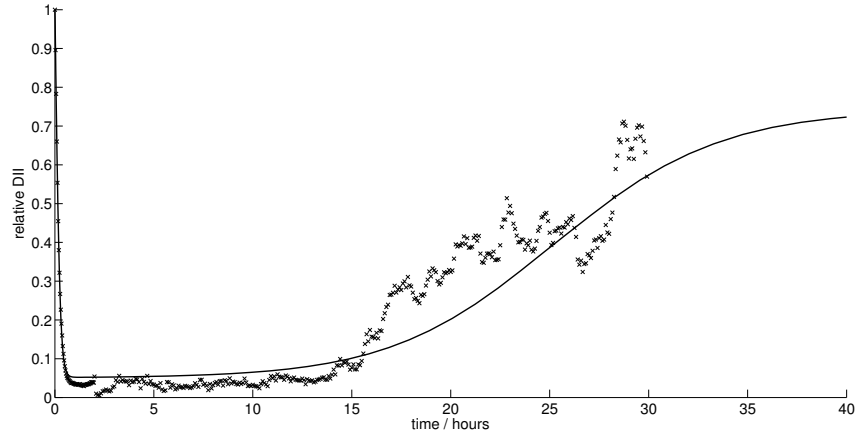


Figure 2.14: The model given by equations (2.19a)-(2.19c) with parameter values as given in table 2.4, and a faster rate of degradation of the auxin signal ($\mu_{tr} = 0.264 \text{ hour}^{-1}$), is able to match the observed recovery of DII-VENUS (Silvana Porco, personal communication) without significantly affecting the initial degradation.

2.4 Model Predictions

In section 2.3, it was shown that by adding an exponential decay of a sufficiently high rate to the initial auxin signal, the DII-VENUS model can show good agreement with the experimental data over both the 2 hour and 30 hour time-courses and, by assumption, approximate intracellular auxin over that time scale. In section 3.1 further consideration is given to the mechanism by which the apparent auxin homeostasis occurs, but in this section we assume that the decay in signal is a reasonable empirical model for the behaviour of intracellular auxin post-treatment.

The additional assumption when using this model for cellular auxin is that the positive feedback from LAX3 need not be included. Both the qRT-PCR and DII-VENUS data represent average values over a whole root and so while LAX3 auxin feedback is likely to affect auxin distribution and gene expression spatially within the root, the spatial variations ought to cancel each other out for whole root data. Even if LAX3 expression late on in the time course is affecting overall auxin concentration in the root it is taken into account when fitting μ_{tr} (the rate of auxin signal degradation). In short, any effect of LAX3 on auxin is already factored into the model by fitting the parameter values to match the DII-VENUS data.

With the assumption that LAX3 feedback is accounted for, and using the model and fitted parameter values for the DII-VENUS model (equations 2.19), we can then add back in the expression of IAA14, tfX, and LAX3 in a stepwise manner, and by fitting the known components to the mRNA expression data, make predictions for the unknown or unmeasured components in the model.

2.4.1 IAA14 mRNA

The first step is to add in the key regulator of LAX3, IAA14 (in conjunction with ARF7, which we assume is constitutively expressed). Though DII-VENUS contains domain II of IAA28 rather than that of IAA14, in the absence of further data we assume that IAA14 is degraded at a similar rate and dose response as DII-VENUS, and so can use the fitted parameter values for $Q, P, \eta, \alpha_0, \alpha_{tr}$ and μ_{aux} given in Table 2.4 in the following model of the evolution of IAA14 protein, IAA14 mRNA and auxin:

$$\frac{dIAA}{dt} = \beta IAA_m - \frac{\eta auxin IAA}{QP + Qauxin + auxin IAA}, \quad (2.20a)$$

$$\frac{dIAA_m}{dt} = \mu_{im}^* (F_{tc} \left(\frac{K}{\theta_{ia}(IAA + K)}, \frac{IAA}{\theta_{ir}(IAA + K)}, n_i \right) - IAA_m), \quad (2.20b)$$

$$\frac{dauxin}{dt} = \alpha_0 + \alpha_{tr} xaux(t) - \mu_{aux} auxin, \quad (2.20c)$$

where $xaux(t)$ is defined as in equation 2.19c.

The key difference in the equation for IAA14 protein compared to that for DII-VENUS (equation 2.19a) is the variable level of IAA_m , in contrast to the constitutive value for DII-VENUS mRNA. Since DII-VENUS was scaled so that the rate of translation was equal to 1, and the scaling of IAA_m used constrains it between 0 and 1, β then represents the maximum rate of translation of IAA14 relative to the constitutive rate of DII-VENUS translation. The equation for IAA14 mRNA expression is as (2.14c), with the additional parameter μ_{im}^* representing the true value of IAA14 mRNA turnover relative to the estimate used previously to scale time ($\mu_{im} = 0.4$). Adding this parameter allows a slower turnover rate for IAA14 mRNA than if it is fixed according to what may be an incorrect estimate, as was the case previously.

The three equations (2.20a)-(2.20c) then have 6 parameter values to be fitted to the IAA14 expression data ($K, \beta, \mu_{im}^*, \theta_{ai}, \theta_{ri}$ and n_i) using the parameter fitting algorithm described previously. Figure 2.15 shows the best fit for IAA14 mRNA, along with the resulting prediction for IAA14 protein, and by way of comparison, the DII-VENUS model fit, and both IAA14 mRNA and protein with no decay in auxin treatment signal ($\mu_{tr} = 0$). The fitted parameter values are given in Table 2.5. Using the fitted parameter values there is a reasonable agreement between model and experimental values for IAA14 mRNA. The resulting prediction for IAA14 protein is the expected rapid degradation within the first two hours, with Aux/IAA staying low for several hours after this. As the auxin signal is degraded, so the Aux/IAA level increases. However, in contrast to the DII-VENUS, there is positive feedback on Aux/IAA due to the induced expression of IAA14 mRNA, and so the result is a peak in Aux/IAA protein of around three times its initial value after about 30 hours. It is only the combination of low auxin and high mRNA that gives this peak in Aux/IAA as can be seen by comparing with the plot for $\mu_{tr} = 0$ in figure 2.15. Here auxin remains high and, while there is strong expression of mRNA, the degradation rate of the protein is also very high and so the protein cannot accumulate.

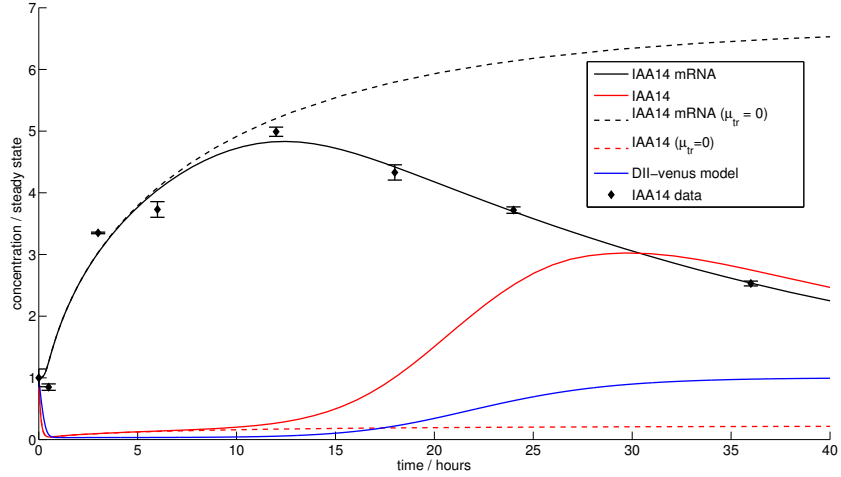


Figure 2.15: Model IAA14 mRNA fitted using a parameter fitting algorithm with qRT-PCR data, along with associated prediction for IAA14 protein. Also shown by way of comparison is the output of the same set of model parameters with the auxin signal decay set to zero, and the output of the DII-VENUS model. Only the combination of high mRNA and low auxin results in strong Aux/IAA protein levels.

Table 2.5: Best fitted ($f = 0.0282$) parameter values for IAA14 mRNA to the data in figure 1.9 using the model given by equations (2.21), plus the parameter values given in Table 2.4, and with $\mu_{tr} = 0.264 \text{ hour}^{-1}$.

K	μ_{i_m}	n_i	θ_{ai}	θ_{ri}
0.1011	0.0915	1.7432	0.1179	0.0021

The parameter fitting algorithm was repeated several times, and despite different sets of fitted parameter values, there was a high degree of consistency in the predictions for IAA14 protein (figure 2.16). In particular, there was large range of fitted values for the rate of mRNA translation ($\beta = 0.648$ to $\beta = 39.4$). Since this tightly coupled relationship between IAA14 protein and mRNA seems to be conserved, regardless of the value of β , we fix $\beta = 1$ and run the fitting algorithm once more, resulting in the set of parameters given in Table 2.5.

2.4.2 LAX3 mRNA

Using $\beta = 1$ in equation (2.20a), and equations (2.14d)-(2.14g) for tfX and LAX3 mRNA and protein gives the following model in seven variables for

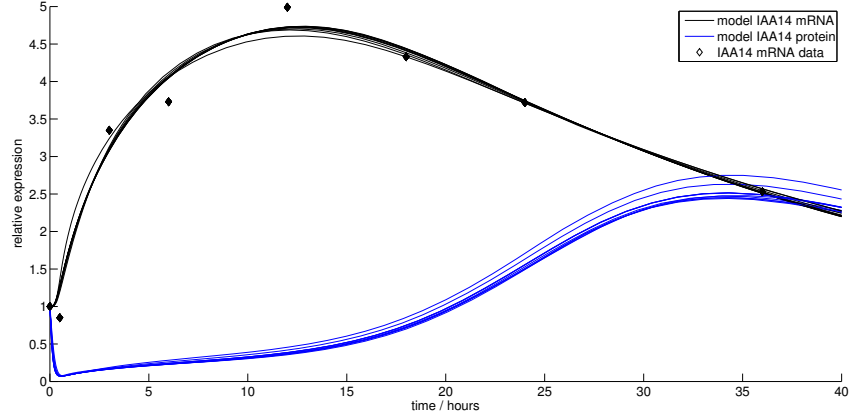


Figure 2.16: Multiple fits of the model in section 2.4.1 with the IAA14 mRNA data following auxin treatment, plus predictions for IAA14 protein. Each line of the same colour represents the result from a different parameter set (see figure legend). Despite differences in parameter values the predicted profile for both IAA14 mRNA and IAA14 protein remains the same.

LAX3 expression:

$$\frac{d\text{auxin}}{dt} = \alpha_0 + \alpha_{tr}x\text{aux}(t) - \mu_{\text{aux}}\text{auxin}, \quad (2.21a)$$

$$\frac{d\text{IAA}}{dt} = \frac{-\eta\text{auxinIAA}}{QP + Q\text{auxin} + \text{auxinIAA}} + \text{IAA}_m, \quad (2.21b)$$

$$\frac{d\text{IAA}_m}{dt} = \mu_{i_m} \left(F_{tc} \left(\frac{K}{\theta_{ia}(\text{IAA} + K)}, \frac{\text{IAA}}{\theta_{ir}(\text{IAA} + K)}, n_i \right) - \text{IAA}_m \right), \quad (2.21c)$$

$$\frac{dX_m}{dt} = \mu_{x_m} \left(F_{tc} \left(\frac{K}{\theta_{xa}(\text{IAA} + K)}, \frac{\text{IAA}}{\theta_{xr}(\text{IAA} + K)}, n_x \right) - X_m \right), \quad (2.21d)$$

$$\frac{dX}{dt} = \mu_x(X_m - X), \quad (2.21e)$$

$$\frac{d\text{LAX}_m}{dt} = \mu_{l_m} \left(F_{tc} \left(\frac{X}{\theta_{la}}, 0, n_l \right) - \text{LAX}_m \right), \quad (2.21f)$$

$$\frac{d\text{LAX}}{dt} = \mu_l(\text{LAX}_m - \text{LAX}), \quad (2.21g)$$

where as before $x\text{aux}(t)$ is defined as in equation (2.19c).

Using the parameter values in Tables 2.4 and 2.5, we can then fit the remaining parameters in the model (2.21) to the LAX3 mRNA data. Figure 2.17 shows the best five model fits to the data.

Though for each fit there is good agreement between model and data LAX3 mRNA ($0.0104 < f < 0.0107$), there is some variation in the predicted expression profile of tfX that, as the upstream activator of LAX3, will produce the required profile of LAX3. There are several reasons for this, each relating to parameters in the model. Firstly, there are obvious differences in the magnitude of the peak level of tfX expression. This will

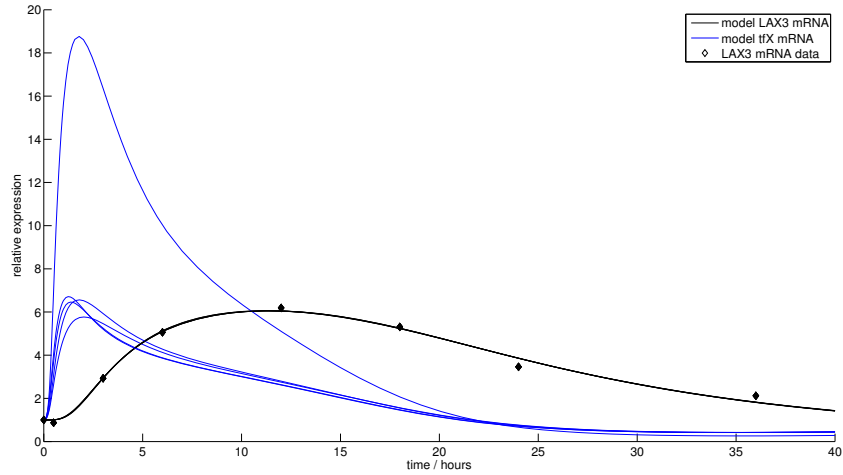


Figure 2.17: Best fits of the LAX3 mRNA in the model given by (2.21a)-(2.21g) (black lines) with the qRT-PCR data from figure 1.9 (black diamonds). Also shown are the predictions for tfX for each parameter set fitted. Five separate parameter sets are shown in total. While as may be expected there is consistency in the model prediction for LAX3, and good agreement with the data, there are variations in timing and magnitude of response for the predictions for tfX.

be due to differences in the parameter θ_{al} , which is the affinity of tfX to the LAX3 promoter. If this value is relatively high, more of the transcription factor is needed to cause the same level of expression of LAX3 as when the value is low, and more sensitive to tfX. In other words, changing this parameter means that different profiles of tfX can result in the similar expression profiles for LAX3.

There are also slight differences in the timing of peak tfX expression. This is due to the biological steps, represented in the model, between the expression of tfX mRNA and LAX3 mRNA. Firstly, there is a time delay due to the translation of tfX mRNA into protein. This is affected by the parameter μ_x , the turnover rate of tfX protein. A low value for this parameter results in longer delay between peak mRNA and peak protein, while a high value means that the peak protein occurs soon after the peak in mRNA expression. In a similar way, the turnover of tfX mRNA, μ_{x_m} , affects the timing of peak mRNA expression following the inductive auxin signal, with the speed of response increasing with increasing turnover rate. Because of this, variations in both μ_x and μ_{x_m} can result in different timings of expression profiles of tfX producing the same temporal profile of tfX protein, and since it is the tfX protein, rather than mRNA that affects LAX3 expression directly, it is this profile that is important in simulating the LAX3 expression data.

The second step between tfX and LAX3 mRNA expression is the transcription of LAX3 mRNA in response to the tfX protein. As with tfX, the turnover rate of LAX3 mRNA (μ_{l_m}) affects the speed of response following transcriptional activation. In this case, a high value for μ_{l_m} results in a close relationship in the timing of LAX3 mRNA and tfX protein, while

a low value results in a longer delay between the two. Again, this means different profiles for tfX protein can result in the same expression profile for LAX3 mRNA.

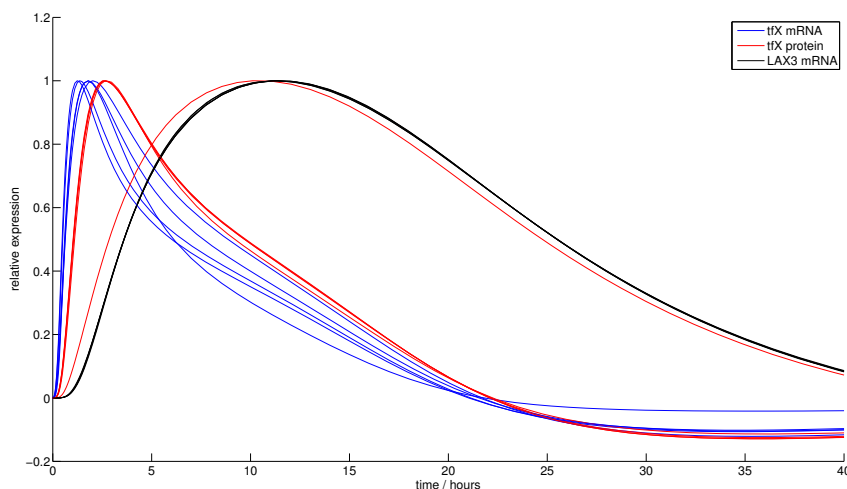


Figure 2.18: Comparison of model predictions for tfX mRNA, tfX protein, and LAX3 mRNA, for five different parameter sets fitted to the LAX3 mRNA data. Each profile was normalised by subtracting the basal level of each profile from every time-point, and then normalising with the peak value in each profile. Different profiles of tfX mRNA and protein can result in the same LAX3 mRNA profile.

Figure 2.18 demonstrates how different timings of both tfX mRNA and tfX protein can result in the same expression profile of LAX3 mRNA. The figure shows model predictions of tfX mRNA, tfX protein and LAX3 mRNA for the same five parameter sets as in Figure 2.17. In each case the model prediction has been normalised so that the magnitude of peak expression is the same. This was done by subtracting the basal level of each profile from every time-point, and then normalising with the peak value in each profile:

$$\bar{x} = \frac{\underline{x} - x_0}{\max(\underline{x} - x_0)},$$

where \bar{x} is the normalised value for each time point, x_0 is the steady state value at $t = 0$, and \underline{x} is the model value at each time point. By doing this each expression profile is restricted between zero and one (while expression remains above the basal level), and so comparisons in the relative timing can be made more directly.

For four out of the five parameter sets there is a high degree of consistency in the temporal profile of the tfX protein, with the peak level occurring between two and three hours post-treatment, while the fifth parameter set has a peak in tfX protein much later, occurring shortly before LAX3. Nevertheless, in each case the expression of LAX3 mRNA is nearly identical. As described above, this can be explained by the values of the parameter μ_{l_m} . For the four cases with a similar timing of peak tfX protein, the value of μ_{l_m} is also very similar ($0.179 < \mu_{l_m} < 0.180$), while the fifth parameter set where the protein peaks much later the value of μ_{l_m} is much higher

($\mu_{l_m} = 3.42$), which means that the level of LAX3 mRNA responds much more quickly to a change in the level of tfX. There is the most variety in the predictions for tfX mRNA, though the peak expression still occurs within a range of one or two hours. As discussed above, differences in the timing of the subsequent steps means that a range of expression profiles can result in the same expression profile for the downstream target.

2.5 Discussion and Conclusions

Steady State Analysis

By adding LAX3 expression and positive feedback via active auxin transport to an auxin signalling model it is shown that it is possible for the model to show bistability in steady state response to an increasing auxin signal. This bistability may represent a biological switch in gene expression, where at low auxin expression is very low, at high auxin there is strong gene expression, and in some intermediate region of auxin levels steady state expression may be either high or low depending on the previous state of the system. The observed all or nothing expression pattern of LAX3 (Swarup et al. 2008) may be explained by this bistable system, as in cells overlying the LRP we may expect auxin to be higher than in adjacent cells, meaning that in cells with sufficiently high auxin expression is switched on, while in cells with slightly less auxin LAX3 expression remains switched off.

The bistability in the model depends on two sets of key parameter values. Firstly, a relatively high value for the rate of active auxin transport relative to diffusion is needed. In particular, it should be noted that a higher value for this parameter is needed than that previously estimated in Swarup et al. (2005). However, this estimate was based on a fixed concentration of AUX1 transporters on the cell membrane, while here we assume that the rate of transport is proportional to a variable amount of LAX3 present at any time, and it may be that when strongly expressed there are many more LAX3 transporters present than there was AUX1 for the previous estimate.

The second set of key parameters affecting bistability are the co-operativity coefficients of binding of transcription factors to the tfX (the auxin responsive transcription factor that is assumed to activate LAX3), and LAX3 promoters. If either or both of these values are high enough there will be bistability, if both are low there will be a more linear response of LAX3 to increasing auxin, and for intermediate values there will be an ultrasensitive response where, though there is only one possible steady state, there is a range of auxin for which the response changes very rapidly. A high co-operativity value may represent a number of separate binding sites that must be occupied for transcription to occur, or a number of copies of a transcription factors binding with each other before binding the promoter. Since tfX remains unidentified, it is currently impossible to gather further evidence to support or weaken this hypothesis for the presence of co-operativity effects.

Parameter fitting - persistent auxin signal

The parameter fitting algorithm shows that it is possible for the full model with weakly constrained parameters to match the transient response of LAX3 and IAA14 mRNAs seen in the data (figure 1.9) with a persistent simulated auxin treatment. This is possible due to the negative feedback from increased Aux/IAA expression occurring relatively slowly, and being able to significantly change the level of ARF7-bound Aux/IAA. A key parameter value that allows this to happen is a slow rate of ubiquitination, which acts a rate limiting step in the degradation of Aux/IAA. In the case where there is a transient response of Aux/IAA, and so also the response mRNAs, the TIR1 receptors appear to be saturated with Aux/IAA due to the slow ubiquitination rate, and so when more Aux/IAA is translated in response to increased mRNA expression it has a greater relative effect on the current Aux/IAA protein level than when the Aux/IAA is degraded much more rapidly (figure 2.7). In general, this fit of the model with the data is only possible if the protein-protein, auxin-receptor, and protein-receptor reactions are allowed to occur at a similar or slower rate than transcription, translation, and protein and mRNA turnover, and this is unlikely to reflect the biological reality. Because of this the assumption was made that these reactions occur on a much faster time-scale, and so simplify the model.

Simplifying the model by assuming that the protein-protein and auxin-receptor interactions occur much more rapidly means that the model is no longer able to fit the data, in response to a persistent auxin signal. The mRNAs can still show a transient response, but the speed of the reactions means that the peak in mRNA occurs too soon to reflect the data. In addition, this depends on a relatively small proportion of Aux/IAA being degraded following the initial auxin signal, which is contrary to the response of Aux/IAA seen experimentally at the simulated $1 \mu M$ auxin treatment (Band et al. 2012).

Parameter fitting - decay in auxin signal

Though with some parameter sets the model is able to simulate, either qualitatively or quantitatively, the transient response of LAX3 and IAA14 mRNAs to auxin treatment, this results in a prediction for the early response of Aux/IAA contrary to that seen experimentally. If, instead of assuming the auxin treatment concentration remains constant, there is an exponential degradation of the auxin treatment concentration over time, it is straightforward to find parameter sets which qualitatively match experimental observation. for both LAX3 and IAA14 mRNA, and Aux/IAA protein (figure 2.5).

One possible source of decay in the auxin signal is decay in light of auxin in the experimental medium. Experimentally, measurements indicate a half-life of between 9 and 10 hours. The parameter fitting shows that this rate of decay is enough to simulate the mRNA data, but as before depends on a shallow initial response of Aux/IAA to the auxin signal. A faster exogenous auxin decay rate is however able to fit both the mRNA data and show a more realistic initial response by the Aux/IAA protein.

DII-VENUS model

To investigate the Aux/IAA response and exogenous auxin decay rate further, the modelling and data published in Band et al. (2012) was first tested with the experimentally determined decay rate of exogenous auxin. Though there will be differences in the actual fitted parameter values, including the degradation of auxin on the experimental medium (section 2.2.4) does not affect the ability of the model to match the DII-VENUS dose response time course data, for the first two hours post-auxin treatment (figure 2.13(a)). However, the experimentally determined rate of decay, $\mu_{tr} = 0.0729 \text{ hour}^{-1}$, is not sufficiently rapid to account for the observed recovery of DII-VENUS over the longer, 30 hour, time course (figure 2.13(b)). Using a faster rate of $\mu_{tr} = 0.264 \text{ hour}^{-1}$, the model is able to simulate the overall trend of recovery in DII-VENUS after around 10 hours following $1 \mu M$ auxin treatment (figure 2.14). Since we know that any degradation of the exogenous auxin signal is likely to be occurring at a lower rate than this, this suggests that there must be another mechanism, endogenous to the plant root, acting to maintain a homeostasis of intracellular auxin. One such mechanism, auxin inducible auxin conjugation by the auxin early response gene family GH3, is discussed and modelled in chapter 3.

Since even with the higher rate for μ_{tr} , so that the observed recovery of DII-VENUS occurs within the correct time frame, the early response of DII-VENUS is not greatly affected, then the exponential decay of the initial auxin signal at this rate would appear to be a reasonable empirical model for cellular auxin post-treatment. Because of this, the signal decay model was fitted to the available data, allowing predictions about the unknown or unmeasured model components to be made. In chapter 4 we also use this model as an approximation for intracellular auxin when simulating more complex regulatory networks for LAX3, under the influence of two auxin response factors (ARF7 and ARF19).

Predictions for mRNA expression

With the assumption that when modelling the whole root data the positive feedback on intracellular auxin from LAX3 can be omitted, it is straightforward to fit the model with first the IAA14 mRNA data, and then the LAX3 mRNA data. When fitting with the IAA14 mRNA data the model predicts that following the initial rapid degradation of the IAA14 protein, the combination of positive feedback on protein level, and the degradation of the exogenous auxin signal causing the Aux/IAA degradation rate to return to a lower rate results in a recovery in IAA14 protein after around 15-20 hours to a level higher than that seen pre-auxin treatment. As the rate of IAA14 mRNA expression returns to basal level, so does the level of the protein. It is only the combination of the auxin homeostasis and increased Aux/IAA mRNA expression that causes the high level of Aux/IAA, which will act to strongly repress auxin responsive genes. Without the auxin homeostasis, IAA14 mRNA expression remains high throughout the latter part of the time-course, but the high level of auxin remaining means that the translated protein is still rapidly degraded following binding with auxin bound

TIR1 , and so any recovery in Aux/IAA protein levels is limited.

Fitting the LAX3 mRNA expression data results in a number of parameter sets which all show good agreement with the data. These parameter sets produce a range of predictions for both tfX mRNA and tfX protein, which differ in magnitude of peak expression and in the timing of mRNA and protein, relative to LAX3 mRNA. The key parameters which allow for this variation in timing are the turnover rate of tfX protein, and the turnover rate of LAX3 mRNA. While the turnover rate of tfX is still unknown, measuring the rate for LAX3 mRNA would effectively fix a prediction for the tfX protein, from which a narrower range of predictions for the tfX mRNA could be inferred. Though Narsai et al. (2007) published a large dataset of mRNA degradation rates, LAX3 was not among them. However, the range of fitted values for LAX3 mRNA turnover is well within the measured physiological range, and can result in a prediction of the time of peak tfX protein level varying by several hours (figure 2.18). Nonetheless, there is some consistency in the prediction of the shape of the expression profile for tfX mRNA, which may be used to identify the best candidates for tfX from experimental data. In the above discussion we only consider the possibility that there is a single transcription factor activating LAX3. In general terms, adding more unknown components to the model will only add to the variety of expression profiles which an activator of LAX3 may take, and so any further conclusions are unlikely to be possible as long as any or all of the regulators remain unidentified.

Chapter 3

Auxin Inducible Auxin Conjugation

3.1 Introduction and Model Formulation

The initial LAX3 expression model relies on the decay over time of an initial exogenous auxin signal to model the experimentally observed behaviour of LAX3 mRNA following auxin treatment. However, as we saw in Section 2.2.4, the rate of decay of auxin on the experimental medium is insufficiently rapid to account fully for the down-regulation of mRNAs following the initial auxin response within the timescale observed experimentally. Because of this, it appears there may be at least one additional auxin homeostasis mechanism endogenous to the plant, which we seek to simulate within the single cell model. One such mechanism may be auxin conjugation, in which cellular auxin is conjugated to amino acids, removing its signalling capability (Ljung et al. 2002). A family of genes, the GH3s, have been shown to have some members which conjugate auxin via enzymatic activity (Staswick et al. 2005). In addition to this, GH3s are among the primary response genes identified to be upregulated in response to auxin (Abel and Theologis 1996).

In this section then, we add to the model the mechanism by which auxin conjugation removes auxin from the active pool depending on the level of the auxin conjugating GH3 genes present at any given time. These GH3 genes are themselves induced by an increase in cellular auxin. A simplified gene network diagram for the conjugation model showing the key model feedbacks is given in Figure 3.1. In Section 3.2 we fit this model to the qRT-PCR data, while in Sections 3.3 and 3.4 respectively we investigate the effect of different parameter values on model behaviour over time and at steady state. In particular, parameter sets for which sustained oscillations in gene expression occur are found, and key parameters affecting the agreement between model and data are identified.

3.1.1 Model formulation

GH3 mRNA (G_m) is expressed as a primary auxin response gene in a similar way as the other primary response genes. There is linear degradation pro-

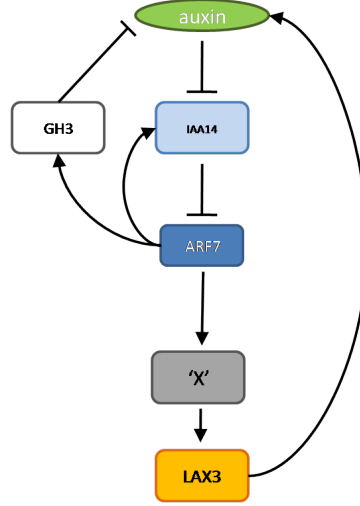
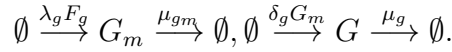
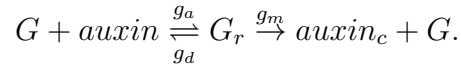


Figure 3.1: Model gene network with the inclusion of an auxin conjugating enzyme, which itself is induced by auxin (GH3). The conjugation of auxin has a negative effect on cellular auxin by removing it from the active signalling pool. As before there is a positive feedback on cellular auxin following expression of LAX3, and a negative feedback on activation by ARF7 following expression of IAA14.

portional to concentration of the mRNA and GH3 protein and the protein is itself translated at a fixed rate proportional to the mRNA concentration:



Additionally, GH3 can bind reversibly with auxin, and the complex of GH3 and auxin (G_r) can also disassociate to form conjugated auxin ($auxin_c$) and GH3:



This conjugating step is assumed to be irreversible, and once auxin is conjugated it is permanently removed from the pool of available signalling molecules (Figure 3.2).

These reactions are then governed by the following dimensional equations for the new model quantities:

$$\frac{dG}{dt} = \delta_g G_m - \mu_g G - g_a G auxin + (g_d + g_m) G_r, \quad (3.1a)$$

$$\frac{dG_m}{dt} = \lambda_g F_{tc} \left(\frac{ARF}{\theta_{ga}}, \frac{AI}{\theta_{gr}}, n_g \right) - \mu_{g_m} G_m, \quad (3.1b)$$

$$\frac{dG_r}{dt} = g_a G auxin - (g_d + g_m) G_r. \quad (3.1c)$$

In addition, the nondimensional equation for auxin previously given by (2.14a) is changed to:

$$\begin{aligned} \frac{d auxin}{dt} = & (x aux_0 + x aux(t))(\alpha_x + \alpha_{lax} LAX) - \mu_{aux} auxin \\ & - p_a TIR auxin + p_d TIR_a + g_d G_r - g_a G auxin. \end{aligned} \quad (3.1d)$$

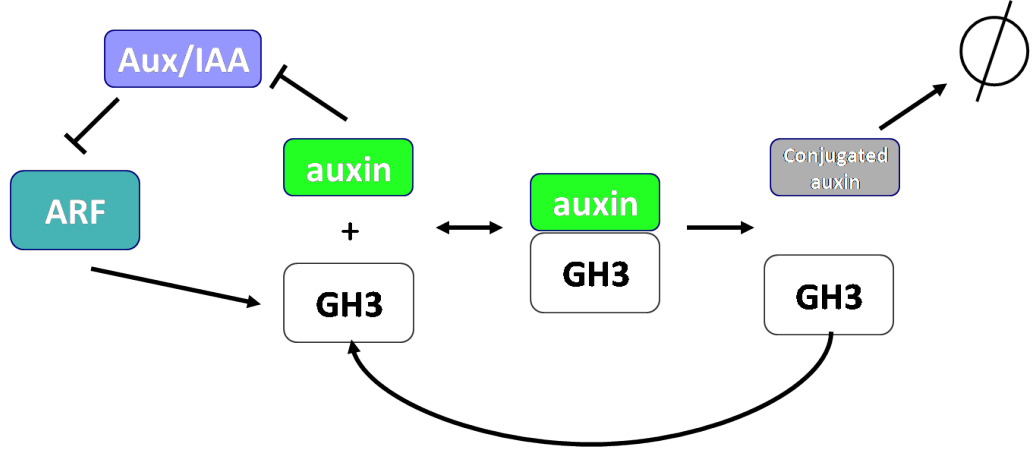


Figure 3.2: Additional interactions included in the auxin conjugation model. GH3 can bind reversibly with auxin, and GH3 bound auxin can be conjugated to amino acids leaving free GH3 once more. GH3 is itself activated by ARF which is repressed by IAA14, which is in turn degraded by unconjugated auxin.

Here, in addition to the extra reactions with GH3, we differentiate between the basal endogenous auxin concentration, x_{aux_0} , and any exogenous auxin treatment, $x_{aux}(t)$.

Before combining with the previous LAX3 expression model we first nondimensionalise where, as before, auxin is scaled with a nominal treatment concentration, and similar rescaling factors as for previous mRNAs and proteins are used, so that:

$$\overline{auxin} = \frac{\overline{auxin}}{x_{aux_T}}, \quad \overline{G} = \frac{\lambda_g \delta_g}{\mu_g \mu_{g_m}} \overline{G}, \quad \overline{G_r} = \frac{\lambda_g \delta_g}{\mu_g \mu_{g_m}} \overline{G_r}, \quad \overline{G_m} = \frac{\lambda_g}{\mu_{g_m}} \overline{G_m}$$

where the bars represent the nondimensional quantities. We also introduce the new non-dimensional parameters:

$$\overline{\eta_g} = \frac{\lambda_g \delta_g}{x_{aux_T} \mu_g \mu_{g_m}}, \quad \overline{g_a} = \frac{g_a x_{aux_T}}{\mu_{i_m}}, \quad \overline{g_d} = \frac{g_d}{\mu_{i_m}}, \quad \overline{g_m} = \frac{g_m}{\mu_{i_m}},$$

$$\overline{\mu_g} = \frac{\mu_g}{\mu_{i_m}}, \quad \overline{\mu_{g_m}} = \frac{\mu_{g_m}}{\mu_{i_m}}, \quad \overline{\alpha_0} = \frac{x_{aux_0} \alpha_x}{x_{aux_T} \mu_{i_m}}, \quad \overline{\alpha_{tr}} = \frac{\alpha_x}{x_{aux_T} \mu_{i_m}}, \quad \overline{\alpha_{lax}} = \frac{\alpha_{lax}}{\alpha_x}.$$

Dropping the bar notation and combining with the simplified model given by equations (2.14b)-(2.14g) then gives the non-dimensional model in ten

variables:

$$\begin{aligned} \frac{d\text{auxin}}{dt} &= (\alpha_0 + \alpha_{tr}x\text{aux}(t))(1 + \alpha_{lax}LAX) - \mu_{aux}\text{auxin} \\ &\quad + \eta_g(g_dG_r - g_aG \text{auxin}), \end{aligned} \quad (3.2a)$$

$$\frac{dIAA}{dt} = \frac{-\eta\text{auxin}IAA}{QP + Q\text{auxin} + \text{auxin}IAA} + IAA_m, \quad (3.2b)$$

$$\frac{dIAA_m}{dt} = F_{tc} \left(\frac{K}{\theta_{ia}(IAA + K)}, \frac{IAA}{\theta_{ir}(IAA + K)}, n_i \right) - IAA_m, \quad (3.2c)$$

$$\frac{dX_m}{dt} = \mu_{x_m} \left(F_{tc} \left(\frac{K}{\theta_{xa}(IAA + K)}, \frac{IAA}{\theta_{xr}(IAA + K)}, n_x \right) - X_m \right), \quad (3.2d)$$

$$\frac{dX}{dt} = \mu_x(X_m - X), \quad (3.2e)$$

$$\frac{dLAX_m}{dt} = \mu_{l_m} \left(F_{tc} \left(\frac{X}{\theta_{la}}, 0, n_l \right) - LAX_m \right), \quad (3.2f)$$

$$\frac{dLAX}{dt} = \mu_l(LAX_m - LAX), \quad (3.2g)$$

$$\frac{dG}{dt} = \mu_g(G_m - G) - g_aG \text{auxin} + (g_d + g_m)G_r, \quad (3.2h)$$

$$\frac{dG_m}{dt} = \mu_{g_m} \left(F_{tc} \left(\frac{K}{\theta_{ga}(IAA + K)}, \frac{IAA}{\theta_{gr}(IAA + K)}, n_g \right) - G_m \right), \quad (3.2i)$$

$$\frac{dG_r}{dt} = g_aG \text{auxin} - (g_d + g_m)G_r. \quad (3.2j)$$

Here we have the assumption that the binding of auxin and Aux/IAA with the TIR1 receptors, and the binding of Aux/IAA and ARF is rapid relative to the timescale of mRNA turnover and gene expression. Similarly, if binding, unbinding and conjugation of GH3 and auxin is also assumed to be rapid compared to mRNA decay, then a further approximation can be made by neglecting the derivative in equation (3.2j). Rearranging and substituting for G_r , equations (3.2a) and (3.2h) can then be replaced resulting

in the model in eight variables given by:

$$\frac{d\text{auxin}}{dt} = (\alpha_0 + \alpha_{tr}x\text{aux}(t))(1 + \alpha_{lax}LAX) - \mu_{aux}\text{auxin} - \gamma G \text{auxin}, \quad (3.3a)$$

$$\frac{dIAA}{dt} = \frac{-\eta\text{auxin}IAA}{QP + Q\text{auxin} + \text{auxin}IAA} + IAA_m, \quad (3.3b)$$

$$\frac{dIAA_m}{dt} = F_{tc} \left(\frac{K}{\theta_{ia}(IAA + K)}, \frac{IAA}{\theta_{ir}(IAA + K)}, n_i \right) - IAA_m, \quad (3.3c)$$

$$\frac{dX_m}{dt} = \mu_{x_m} \left(F_{tc} \left(\frac{K}{\theta_{xa}(IAA + K)}, \frac{IAA}{\theta_{xr}(IAA + K)}, n_x \right) - X_m \right), \quad (3.3d)$$

$$\frac{dX}{dt} = \mu_x(X_m - X), \quad (3.3e)$$

$$\frac{dLAX_m}{dt} = \mu_{l_m} \left(F_{tc} \left(\frac{X}{\theta_{la}}, 0, n_l \right) - LAX_m \right), \quad (3.3f)$$

$$\frac{dLAX}{dt} = \mu_l(LAX_m - LAX), \quad (3.3g)$$

$$\frac{dG_m}{dt} = \mu_{g_m} \left(F_{tc} \left(\frac{K}{\theta_{ga}(IAA + K)}, \frac{IAA}{\theta_{gr}(IAA + K)}, n_g \right) - G_m \right), \quad (3.3h)$$

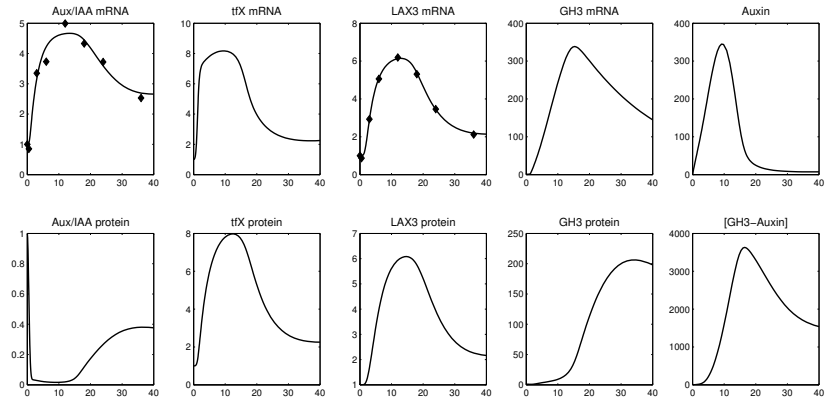
$$\frac{dG}{dt} = \mu_g(G_m - G), \quad (3.3i)$$

where $\gamma = \frac{\eta_g g_m g_a}{g_d + g_m}$.

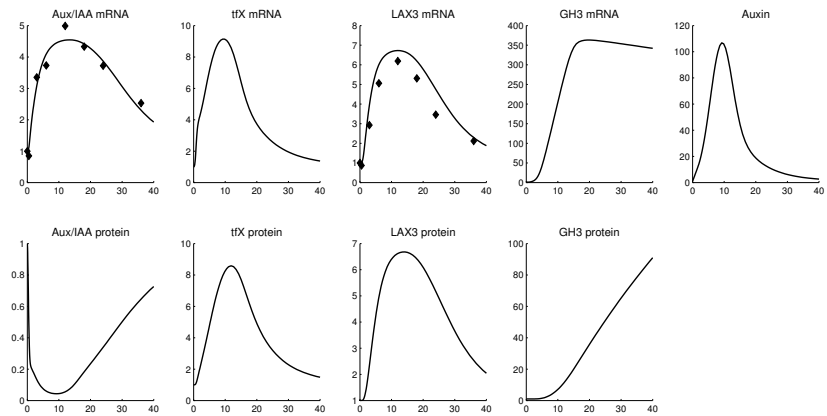
3.2 Parameter Fitting Using Conjugation Model

To test whether either or both conjugation models (3.2) and (3.3) are able to simulate the LAX3 and IAA14 data shown in Figure 1.9, the parameter fitting algorithm was run for each model with a fixed increase of $x\text{aux}$ from 0 to 1000 at $t = 0$. While the reduced model is able to show reasonable agreement with the data ($f = 0.095$), with the ‘full’ conjugation model a more precise fit is possible ($f = 0.032$). Plots of model time course and data for both parameter sets are shown in Figure 3.3, with the parameter values given in Table 3.1.

The fit for the reduced model is less precise than the initial conjugation model, so this suggests the fit of the model with the data relies in part on relatively slow binding of GH3 and auxin (g_a), and a relatively slow conjugation rate (g_m). In addition, it is notable that the fits optimise the rate of GH3-auxin disassociation (g_d) and conjugation independent auxin degradation (μ_{aux}) at or near zero. In other words once bound to GH3 auxin remains bound until it is conjugated, and that this is the only way that active auxin can be permanently removed from the cellular pool. If auxin remains bound to GH3 and the conjugation rate is low, a rapid increase in auxin will result in the available conjugating enzymes becoming rapidly saturated. This will leave a surplus of auxin and strong upregulation of the auxin responsive genes. Among these will be GH3 conjugating enzymes which will subsequently damp down the response.



(a) Best fit (solid lines) with LAX3 and IAA14 mRNA time course data (diamonds) using conjugation model given by equations (3.2). For parameter values see Table 3.1.



(b) Best fit (solid lines) with LAX3 and IAA14 mRNA time course data (diamonds) using reduced conjugation model given by equations (3.3). For parameter values see Table 3.1.

Figure 3.3: Both the full (Figure 3.3(a)) and reduced (Figure 3.3(b)) conjugation models are able to match the data shown in Figure 1.9 reasonably well. Closer agreement is possible with the full conjugation model. In both cases a relatively slow accumulation of GH3 protein allows for a transient peak of cellular auxin at around 10 hours post treatment, and results in the experimentally determined mRNA expression profiles.

Table 3.1: Best fitted non-dimensional parameters for the full conjugation model (A) ($f = 0.036$), and the reduced conjugation model (B) ($f = 0.095$).

	P	Q	K	η_{gh3}	η_{iaa}
(A)	4943	0.0125	0.0394	13739	10.7010
(B)	5677	4.6×10^{-5}	0.0058	N/A	20.9215
	g_a	g_d	g_m	γ	α_0
(A)	0.0102	0	0.6582	N/A	0.1172
(B)	N/A	N/A	N/A	1224	0.0015
	α_{tr}	α_{lax}	μ_{aux}	n_i	θ_a
(A)	0.1172	15.5017	0	1.7274	0.1245
(B)	0.00021	15.4344	0.00026	2.6061	0.1194
	θ_r	μ_l	μ_{l_m}	n_l	θ_{la}
(A)	4.4683	1.4427	4.7148	1.0006	2.1853
(B)	1.8447	1.5154	15.3352	1.9505	0.1736
	μ_x	μ_{x_m}	n_x	θ_{xa}	θ_{xr}
(A)	0.9768	6.5433	1.0000	0.1043	0.2237
(B)	0.9884	9.2310	1.0636	0.1494	0.1748
	μ_g	μ_{g_m}	n_g	θ_{ga}	θ_{gr}
(A)	0.1444	0.0962	2.0000	0.0303	0.0294
(B)	0.0239	0.0086	3.9811	0.0303	0.0294

For both models, the required mRNA expression profile occurs as a result of a transient peak of cellular auxin centred around ten hours. This is a result of increased auxin accumulation while LAX3 is expressed followed by expression of GH3 resulting in increased conjugation and a removal of auxin from the active pool. As we will see later on, this transient ‘pulse’ of expression is in fact a damped oscillation about a steady state, and with different parameter values sustained oscillations of cellular auxin and mRNAs is possible. The key point here is the relative timing in gene expression, with GH3 peaking after LAX3, i.e. the negative feedback occurs after the positive feedback. This will be discussed further in Section 3.3, where the fitted parameter set given in Table 3.1 for the full model (3.2) will be used as a basis for identifying key model parameters, and possible model behaviours over longer timescales will be identified.

3.3 Time Course and Parameter Sensitivity

The parameter set used as the basis for investigation by altering one or more parameters is given in Table 3.1, parameter set (A). Figure 3.4 shows model LAX3 expression when changing both μ_g and μ_{g_m} simultaneously. These are the degradation rates of GH3 enzyme and mRNA respectively (relative to IAA14 mRNA degradation rate), and increasing them has the effect of reducing the timescale over which the conjugating enzyme responds to a change in auxin concentration. In other words, GH3 will respond more

quickly to any change in transcription factor concentration, the larger μ_g and μ_{g_m} are. Changing these parameters should not, however, result in any change to the final steady state expression, as can be seen by setting the derivatives in (3.2h)-(3.2j) to zero. Instead, decreasing μ_g and μ_{g_m} results in damped oscillations of increasing magnitude and period about the steady state. In the case of the fit to the data, the match with the time points consists of one such damped oscillation, before settling on a steady state later on in time. Increasing μ_g and μ_{g_m} has the opposite effect and if sufficiently large will damp out oscillations altogether (Figure 3.4).

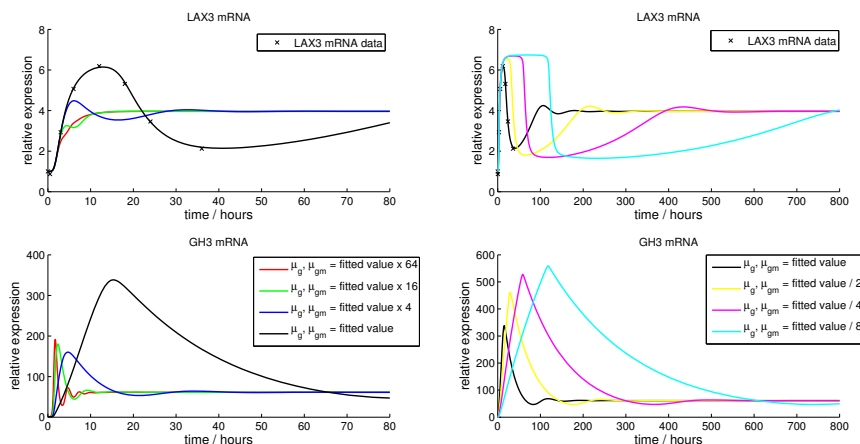


Figure 3.4: Model LAX3 and GH3 mRNA following a simulated auxin signal with successive increases in μ_g (GH3 protein turnover) and μ_{g_m} (GH3 mRNA turnover). See legend for numerical parameter values.

Oscillations, damped or otherwise, appear to depend on the relative timing of LAX3 and GH3 expression. Specifically, if LAX3 peaks before GH3, it appears that expression in both LAX3 and GH3 may oscillate with relatively long periods, while if GH3 peaks first, simulated here by increasing μ_g and μ_{g_m} , the system shows an increasingly smooth increase in LAX3 expression toward its higher steady state. Conversely, GH3 expression shows increasingly obvious damped oscillations, with shorter periods as μ_g and μ_{g_m} are increased. While changing the degradation rates of GH3 mRNA and protein can introduce or remove damped oscillations to LAX3 expression, increasing the rate of association between auxin and GH3 (g_a) appears to introduce a stable oscillatory steady state for the parameter set used (Figure 3.5). The existence of these stable limit cycles are confirmed and investigated further in Section 3.4. Though in a different context to that modelled here, relatively long period oscillations (around 15 hours) in the auxin response have been observed biologically by De Smet et al. (2007) in the basal meristem during the priming of lateral roots, so this model of competing positive and negative feedback loops may provide an alternative hypothesis to that presented by Middleton et al. (2010) as to how these oscillations may arise from a persistent auxin signal.

Other important parameters are μ_{aux} , g_d , and g_m . The effect of changing each over orders of magnitude is shown in Figure 3.6. Increasing either g_d and μ_{aux} from their fitted values of near zero damps out oscillations in LAX3

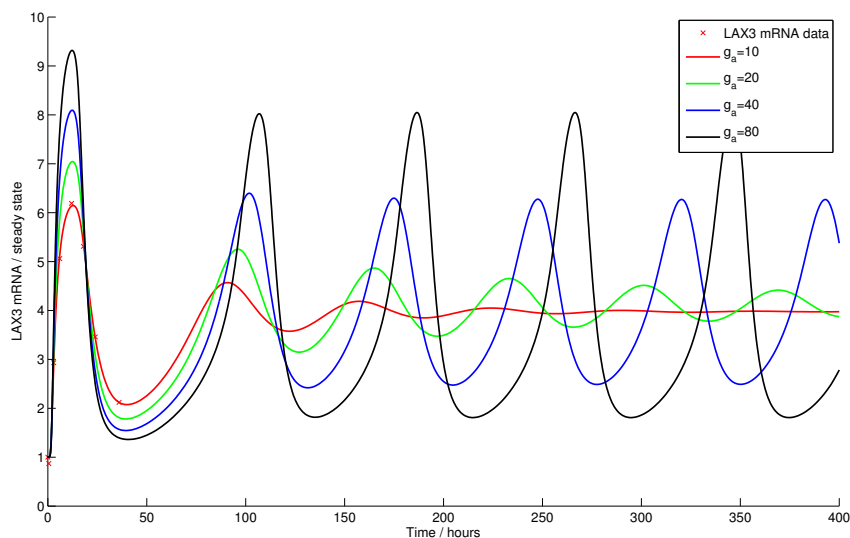


Figure 3.5: Model LAX3 following an initial auxin signal with successive increases in g_a (association rate of GH3 and auxin). See legend for numerical parameter values.

expression, while reducing g_m affects the period of oscillation. For the lowest values of g_m , expression appears to initially oscillate around a higher value for LAX3 expression than for higher values of g_m , before all return to similar steady states over longer time spans. The effect observed by increasing g_d and μ_{aux} may be expected as both decrease the effect of conjugation in different ways. g_d is the rate of disassociation of auxin and GH3, and so a high rate of disassociation results in less bound auxin available for conjugation. Increasing μ_{aux} has a similar effect but here this parameter affects the linear degradation rate of auxin itself and so auxin is degraded more quickly before binding with GH3 and conjugation. g_m is the rate of conjugation of bound auxin, and when both g_d and μ_{aux} are set to a low value so that the pool of GH3 for conjugation can be easily saturated, changing the rate of conjugation of bound auxin will affect the period of oscillations in the auxin available for signalling.

3.4 Steady State Analysis

To establish the existence of stable limit cycles for certain parameter sets used in the model given by equations (3.2a)-(3.2j) the bifurcation diagram of steady state LAX3 mRNA expression against g_a was plotted using Xppaut (Figure 3.7(a)). For the parameter set (A) in Table 3.1, with the auxin signal set to be $x_{aux} = 1000 \text{ nM}$, LAX3 steady state decreases with increasing g_a from zero until reaching a Hopf bifurcation at $g_a = 193.9$. Above this value there is an unstable steady state, and a stable limit cycle where LAX3 expression undergoes sustained oscillations. This critical point depends on x_{aux} , as shown in Figure 3.7(b). Here, g_a is set to the critical value for $x_{aux} = 1000$, and the steady states plotted for a range of values for x_{aux} .

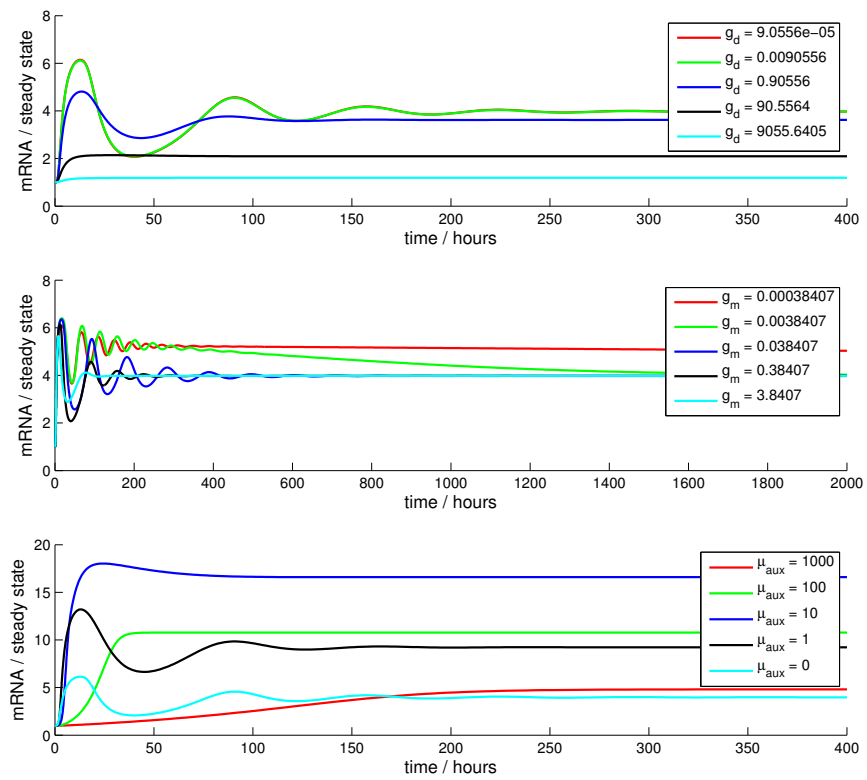
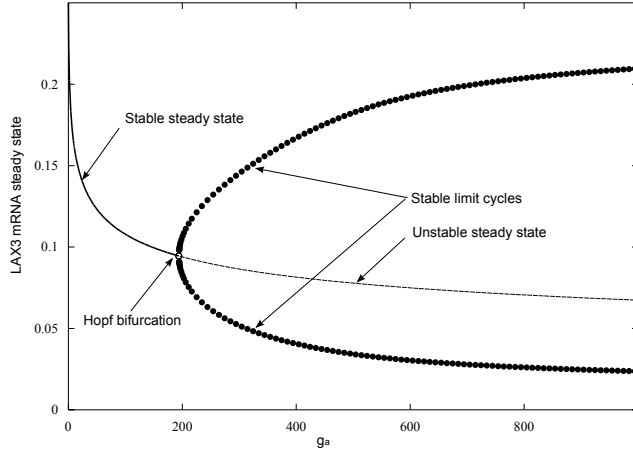
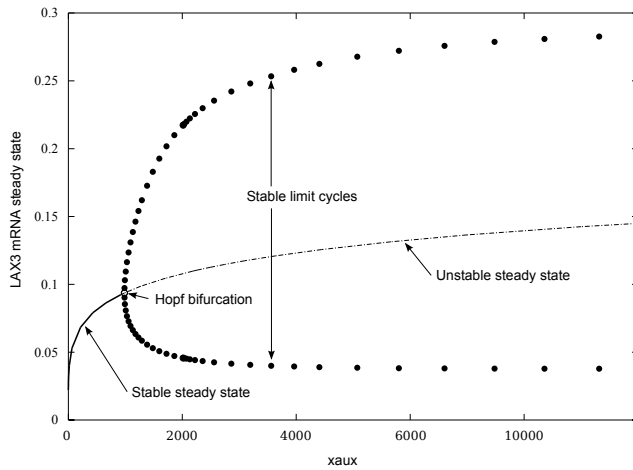


Figure 3.6: Model LAX3 mRNA expression for varying values of the parameters g_d (top), g_m (middle), and μ_{aux} (bottom) following an initial auxin signal. Increasing g_d and μ_{aux} from zero dampens oscillations in expression, while changing g_m affects the period of damped oscillations.



(a) Bifurcation diagram showing LAX3 steady states with increasing g_a . Thick line represents a single stable steady state, solid dots represent stable limit cycles, and the thinner line represents an unstable steady state. At a critical value of g_a there is a bifurcation, above which there exists a stable limit cycle and an unstable steady state, and below which there is a single steady state.



(b) Bifurcation diagram for LAX3 steady state with increasing x_{aux} (extracellular auxin concentration). g_a is set at the critical bifurcation value for $x_{aux} = 1000$. As with g_a there is a critical value for x_{aux} , above which there exists a stable limit cycle and an unstable steady state, and below which there is a single steady state.

Figure 3.7

Again, there is a Hopf bifurcation at the critical value ($xaux = 1000$), and prior to this LAX3 steady state increases with increasing $xaux$ (auxin signal) as expected. Above the critical value there are sustained oscillations in expression. The critical values of g_a and $xaux$ are interdependent, as shown in Figure 3.8(a) which shows the two distinct regions of parameter space. For high g_a and $xaux$ the model system has a stable limit cycle and an unstable steady state, while for low g_a and $xaux$ there is a single stable steady state. In general, if g_a is low $xaux$ needs to be very high before sustained oscillations will occur, and this critical value for $xaux$ decreases as the value of g_a decreases. In the region of parameter space where stable limit cycles cannot occur, there may still be oscillations but these will reduce in magnitude over time and eventually be damped to reach a single stable steady state.

The parameter set (A) in Table 3.1 used to produce the bifurcation diagrams in Figures 3.7(a), 3.7(b) and 3.8(a) has the co-operativity of ARF and ARF-Aux/IAA on the GH3 promoter $n_g = 2$. Figure 3.8(b) shows how the critical value for g_a changes as the co-operativity coefficient is reduced. For values less than around 1.7 no sustained oscillations will occur, even for high values of g_a . If the co-operativity represents the number of binding sites on the promoter, so that an integer value for co-operativity is generally used, then only more than one binding site will result in oscillations in the model.

The positive feedback due to active auxin transport by LAX3 is also essential to produce oscillations. Plotting the LAX3 steady state for increasing g_a with α_{lax} , the rate of LAX3 transport set to zero, shows that there is no Hopf bifurcation for $g_a < 1000$ (Figure 3.9(a)). In fact, testing for $g_a < 10^7$ shows there are no bifurcations within this range (not shown).

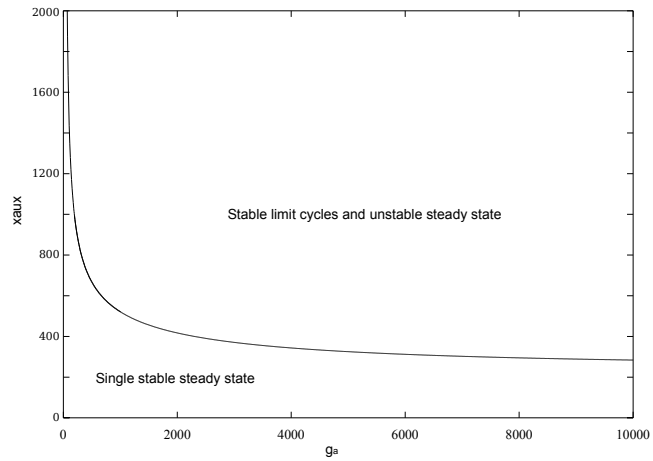
The same is not true for the negative feedback by IAA14. To remove the Aux/IAA negative feedback from the model is not as straightforward as removing the LAX3 feedback, since setting the rate of Aux/IAA expression to zero would result in all ARF activated genes being expressed at their maximum rate, regardless of the auxin concentration. However, if instead of being auxin responsive, IAA14 mRNA is expressed at some constant rate (β_i), then the negative feedback is effectively removed. The function for IAA14 transcription, as used in equation 2.14c then becomes:

$$F_{tc}(ARF, AI, n) = \beta_i \quad (3.4)$$

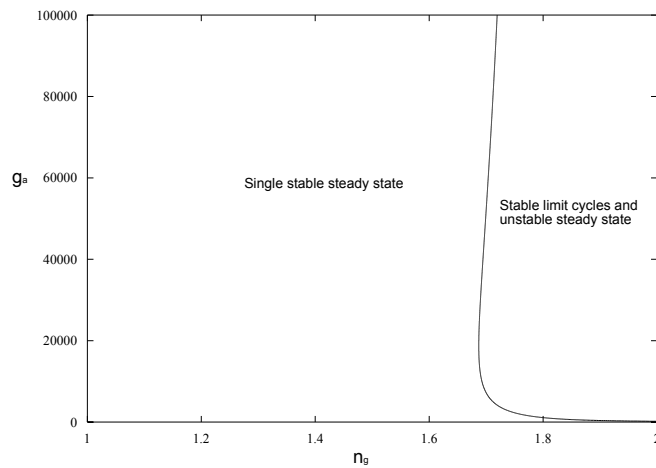
If the original model has a basal steady state expression of IAA14 mRNA, $IAA_m = IAA_m^*$ before auxin treatment, substituting (3.4) into (2.14c) and setting the derivative to zero at steady state gives:

$$\beta_i = IAA_m^* \quad (3.5)$$

Using this value for β_i will simulate removing the negative feedback loop since IAA14 expression will remain constant and equal to the initial expression in the Aux/IAA inducible model. Setting IAA14 expression to be constitutive and constant will still produce a Hopf bifurcation and stable limit cycles for sufficiently high g_a (Figure 3.9(b)).

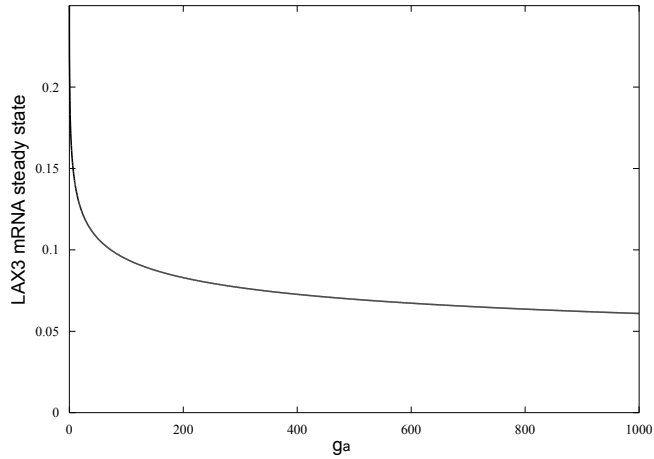


(a) Two-parameter continuation of locus of Hopf bifurcation for x_{aux} and g_a . For high x_{aux} and g_a there is a stable limit cycle and an unstable steady state, for low x_{aux} and g_a there is a single stable steady state.

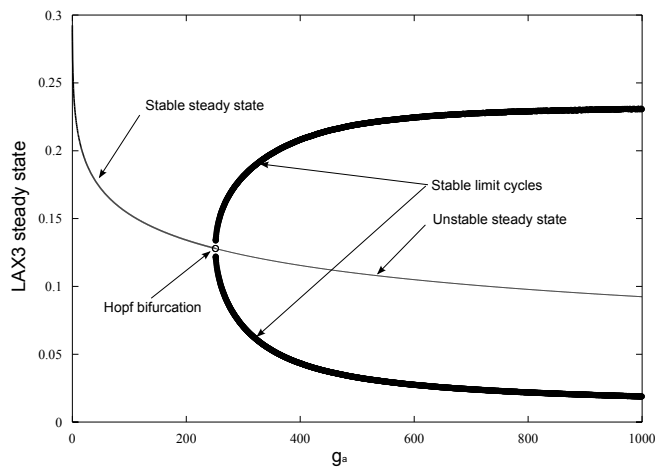


(b) Two-parameter continuation of locus of Hopf bifurcation for g_a and n_g (the co-operativity of the ARF binding site on the GH3 promoter). Even for high g_a an integer value less than 2 for n_g cannot result in stable oscillations.

Figure 3.8



(a) LAX3 mRNA steady state for increasing g_a with the removal of the LAX3 negative feedback by simulating zero active auxin transport. Even for very high values of g_a there is no Hopf bifurcation or stable limit cycles.



(b) LAX3 steady state for increasing g_a with the removal of the IAA14 negative feedback by simulating constant expression of IAA14. As before there is a value of g_a for which a Hopf bifurcation occurs, above which stable limit cycles exist along with an unstable steady state.

Figure 3.9

3.4.1 Pulses In LAX3 expression

Using the default parameter set (A) from Table 3.1, but increasing the rate of active transport a hundred-fold so that $\alpha_{lax} = 1550.17$ and the cooperativity in the transcription functions for X and LAX3 so that $n_x = 2$ and $n_l = 2$, so that the conditions for bistability in the initial model are met (Section 2.1.3), can result in a pulse or repeated pulses in LAX3 expression over time as the rate of g_a , the association of auxin and GH3, is increased (Figure 3.10(a)). For $g_a = 1$ (low binding of auxin and GH3) there is only a slight oscillation before LAX3 reaches a steady state of strong expression. For higher $g_a (= 2)$ the oscillations are damped more slowly, with at least one switch from high to low and back to high expression, before again settling on a steady state of high LAX3 expression. For $g_a = 10$ (close to our fitted value) there are repeated pulses of strong expression. Here, LAX3 oscillates between periods of strong expression and close to zero expression. Finally for the highest value of g_a shown ($= 1000$), there is a single pulse of strong LAX3 expression following the initial auxin signal, before expression is effectively turned off once more for the rest of the time course.

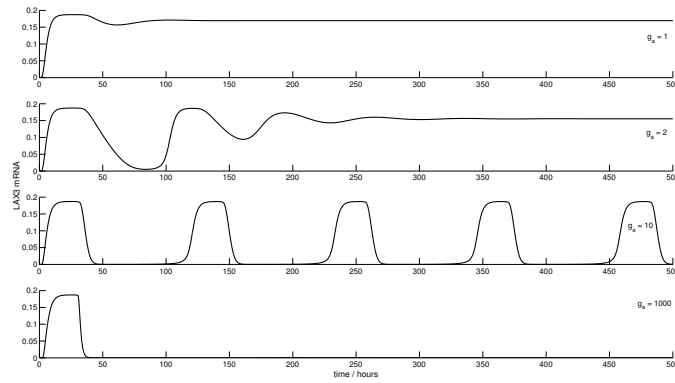
Fixing $g_a = 1$ and plotting the bifurcation diagram of steady state LAX3 mRNA shows that on increasing x_{aux} from zero there is initially a single steady state of low expression, followed by a region of stable limit cycles or oscillations in expression at intermediate values of x_{aux} before above a critical value there is once more a single steady state, at a relatively high level of expression (Figure 3.10(b)). Because of this neighbouring cells with marginally different auxin concentrations may show (temporarily at least) large differences in expression.

3.5 Discussion and Conclusions

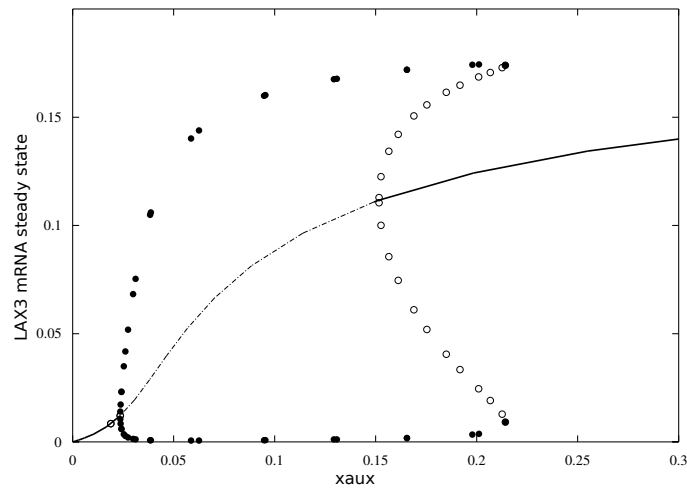
The modelling and data presented in Chapter 2 suggest that there is some endogenous mechanism in the plant root acting to provide auxin homeostasis following exogenous treatment. In this chapter, the hypothesis that one or more members of the auxin responsive GH3 gene family removes auxin from the active signalling pool by conjugating it with amino acids, was modelled and tested by comparison with the available data. It is possible for the conjugation model to simulate the transient transcriptional response seen in LAX3 and IAA14 over the 36 hours following treatment, and the fit with the data appears very sensitive to some particular parameter values, which lead to further biological questions.

Key Parameters

Firstly, in order to fit the experimental data, the GH3 independent auxin degradation needs to be at or near zero. In other words conjugation needs to be the primary pathway by which auxin is removed from the cell. If there is a basal level of expression of GH3, which increases with increasing auxin, this would ensure at least a basal rate of auxin turnover. However, setting the model up in this way does not take into account the possibility of other



(a) LAX3 expression against time following an initial increase in auxin signal from zero to $x_{aux} = 1000$ using the parameter set given in Table 3.1, with $\alpha_{I_{aux}} = 1550.17$, $n_x = 2$ and $n_l = 2$, for increasing values of the parameter g_a . For low g_a there is a high steady state expression, followed by damped oscillations as g_a is increased, then repeated oscillations between high and low expression as g_a is increased further, and finally a single pulse of high LAX3 expression before reaching a steady state of very low expression at the highest value for g_a .



(b) Simulated steady state LAX3 mRNA expression for increasing values of x_{aux} , the parameter corresponding to the concentration of extracellular auxin. Parameter values are as in Table 3.1 (A), but with $g_a = 1$, $\alpha_{I_{aux}} = 1550.17$, $n_x = 2$ and $n_l = 2$. For low x_{aux} there is a single steady state of low expression, for intermediate x_{aux} there are both stable limit cycles around an unstable steady state, and for high x_{aux} there is again a single steady state at relatively high LAX3 expression. There is also a range for x_{aux} (between approx. 0.15 and 0.22) where there are both stable and unstable limit cycles in addition to a stable steady state. Solid lines represent stable steady states, dotted lines unstable steady states, open circles unstable limit cycles, solid circles stable limit cycles.

Figure 3.10

catabolic pathways for auxin, and so needs further biological justification.

Also important is the slow accumulation over the time-course of the GH3 protein. While this appears to be in contradiction to the experimental data, which shows GH3s are early auxin response genes (Abel and Theologis 1996), it may be possible for a slow turnover rate of GH3 protein to result in a slow accumulation of the protein, in comparison to relatively rapid turnover of mRNA giving an early response to the auxin signal. Even if the timing of GH3 expression is not compatible with the model, there may be other auxin inducible genes further downstream from the primary response genes that affect homeostasis, such as genes involved in transport or catabolism. If so, these genes could provide a similar mechanism in the model as conjugation by GH3. In other words, the model as formulated can provide a mechanism to fit the LAX3 and IAA14 mRNA data, but the model may represent another mechanism in which auxin homeostasis is maintained by inducing a gene which accelerates removal of auxin from the cell. In a living cell, there may be several such mechanisms acting at different times during the auxin response, and a more complex model for homeostasis would need to take this into account.

The other key parameters appear to be the binding and unbinding rates of auxin and the GH3 enzyme. Setting the rate of unbinding of GH3 and auxin very low ensures the pathway by which auxin is conjugated is mostly one way, as unless conjugated and removed from the pool entirely, once bound to GH3 auxin remains bound. This means the GH3 enzymes may be periodically saturated by auxin, allowing for an oscillatory effect. It is these oscillations which allow for the fit between model and data. Increasing the rate of binding between auxin and GH3 may result in stable limit cycles in which gene expression oscillates indefinitely between states of high and low expression. By adding the conditions needed for bistability identified in Section 2.1.3, this can result in very sharp pulses of all or nothing expression (Figure 3.10(a)). However, with the parameters set as they are, the period of these oscillations are relatively long (days to weeks), and in the context of cortical cells over lateral root primordia, it is probably not relevant to consider gene expression much beyond the 36 hour dataset, since the auxin source at the tip of the primordia will usually be fully emerged by this time. However, oscillations over longer time-scales may be relevant to other tissues where auxin influx transporters (or another inducible positive auxin feedback) and auxin conjugating enzymes (or another inducible negative auxin feedback) are induced.

Model Predictions and Comparison with previous models

Figure 3.11 shows the conjugation model (3.2a)-(3.2j) predictions for Aux/IAA protein, tfX mRNA, tfX protein, and intracellular auxin, using the parameter values given in Table 3.1, with a simulated auxin treatment of 1000 nM at $t=0$. Also shown by way of comparison are the same model predictions using the fit using the full model described in Section 2.2.2 (persistent auxin model), and the fit using the reduced model with an exponential decay in the auxin signal described in Section 2.2.4 (signal decay model).

The most obvious qualitative differences between the models is seen in

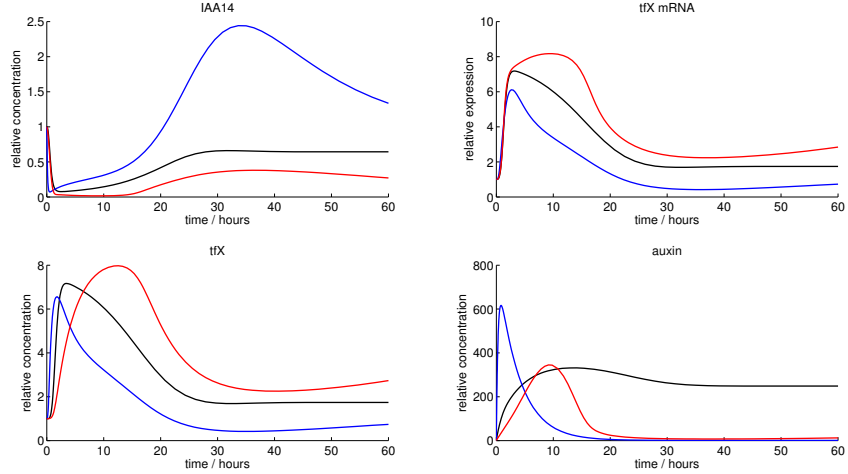


Figure 3.11: Comparison of model predictions for IAA14 protein, tfX mRNA and protein, and intracellular auxin, using the fitted parameter sets for three model variations. Black lines: full model with persistent auxin signal (Section 2.2.2). Blue lines: reduced model with decay in exogenous auxin signal (Section 2.4.2). Red lines: conjugation model (Section 3.1).

the level of intracellular auxin over time. The conjugation model has a relatively slow accumulation of intracellular auxin following the increase of exogenous auxin, with the peak auxin in the cell not occurring until around 10 hours post-treatment. This will be due in part to the increase of LAX3 over this time. After about 10 hours sufficient GH3 has accumulated to result in a net loss of auxin over the following 10 before settling at a relatively low level. Though not necessarily clear due to the scale of the figure, it should be noted that the final steady state of auxin is still several-fold higher than the basal level pre-treatment. In general this will always be the case, increasing the exogenous auxin signal will increase the steady state auxin level in the cell, even with increased conjugation. The conjugation effectively narrows the range of steady state auxin concentration, while the delay caused by the time taken for the GH3 protein to accumulate allows for a temporal increase in cellular auxin, possibly far outside the range of possible steady states. As we show above, it is even possible for oscillations to occur indefinitely, but these oscillations will always be about an unstable steady state auxin concentration higher than steady state before the increase in exogenous auxin.

In the full model with unconstrained parameters auxin peaks at around the same time as in the conjugation model, but remains relatively high throughout the time course (over 200-fold greater than the basal level). This is extremely unlikely based on the DII-VENUS data (Section 2.3), which shows a recovery of DII-VENUS after around 10 hours corresponding to a much lower level of intracellular auxin. In the model with an exponential exogenous auxin decay, peak auxin occurs much sooner, and since the model parameters were fitted to be consistent with the DII-VENUS, it is to be

assumed that this profile for cellular auxin over time is likely to be the most biologically realistic.

All three models show a recovery in IAA14 protein following the initial strong degradation. The biggest recovery is seen in the signal decay model, where the combination of high levels of transcript and low auxin results in a temporary abundance of protein over the second half of the time course. In the persistent signal model, auxin remains high and so the recovery of IAA14 protein is entirely due to an increase in transcript, rather than any significant reduction in degradation rate due to a reduction in auxin. The weakest recovery is seen in the conjugation model. Even though the levels of IAA14 mRNA transcript over the time course are very similar for all models (since they were all fitted to the same IAA14 mRNA data), and auxin is relatively much lower than in the persistent auxin model, the IAA14 protein does not recover above 50% of the basal level. This is because, for the parameter sets used, the range of dose response of the Aux/IAA protein degradation saturates at a much lower level of auxin in the conjugation model than in the persistent auxin signal model. Even a relatively low level of auxin compared to the simulated 1000 nM treatment will still cause rapid degradation of the Aux/IAA. Despite this, the dose response of the Aux/IAA protein predicted by the conjugation model (Figure 3.12) is still not as sensitive to lower levels of auxin as is DII-VENUS (Figure 2.13(a)). However, though we initially assume here that GH3 is regulated by IAA14, it could be any auxin responsive Aux/IAA, and DII-VENUS itself uses domain II of IAA28, and different Aux/IAs may have different dose-responsiveness and relative degradation rates.

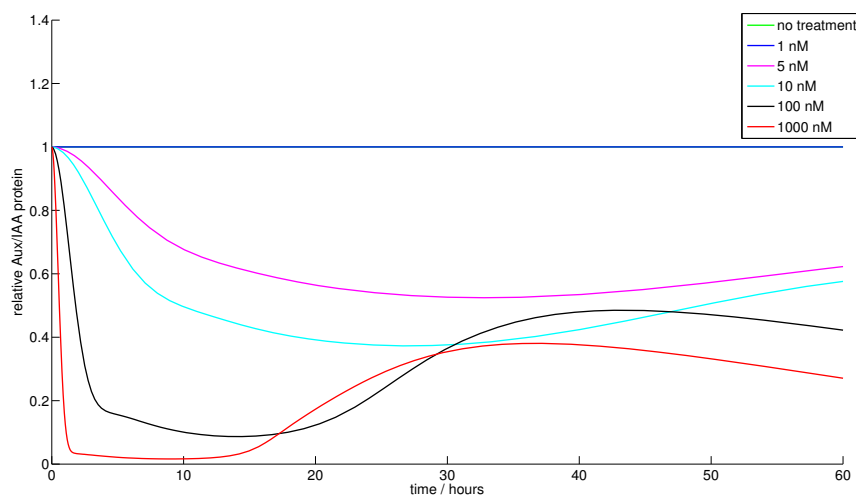


Figure 3.12: Response of Aux/IAA protein in the conjugation model using the fitted parameters in Table 3.1, to different simulated auxin treatments (see figure legend).

As discussed in Section 2.5 it is possible for a range of timings and magnitude of response for *tfX* mRNA and protein to result in the same expression profile for *LAX3* mRNA. Figure 3.11 shows that it is also possible for subtly

different shapes in expression profile to produce the same LAX3 expression, depending on the model for intracellular auxin used. All three models show a similar initial response of tfX mRNA to auxin, but each remains at peak expression for different time periods. The signal decay model is at peak expression for the shortest duration, followed by the persistent auxin model, and finally the conjugation model has high tfX mRNA expression for the longest time period.

Conclusions

The modelling shows that auxin inducible auxin conjugation is a possible mechanism for auxin homeostasis following exogenous treatment. However, when fitting with the LAX3 mRNA expression data, the predictions for intracellular auxin and Aux/IAA protein are not entirely consistent with the DII-VENUS data (Section 2.3). In addition, the qualitative behaviour of the model is sensitive to relatively small changes to some parameter values, meaning that the system may not be particularly robust to biological variation. For these reasons, in the discussion on more complex gene networks (Chapter 4), we use the signal decay model described in Section 2.2.4 as a simpler model for intracellular auxin following treatment. Despite this, the range of possible behaviours of the conjugation model means that there is scope for further study, particularly when more biological data relating to auxin conjugation or other homeostatic pathways become available.

Chapter 4

Gene Regulatory Network Model: Two Auxin Response Factors (ARF7 and ARF19)

4.1 Biological Background

In previous chapters, only the case where a single ARF (nominally ARF7), not transcriptionally responsive to increased auxin, activates a range of primary auxin response genes which feed back into the network model in various ways was considered. However, ARF7 is just one of a family of 23 genes which may affect the auxin response (Guilfoyle and Hagen 2007). Of these 23 ARFs, five gene products are believed to be transcriptional activators (ARFs 5,6,7,8, and 19), while the remainder are thought to be transcriptional repressors. Of particular importance to the lateral root emergence network and the induction of LAX3 are the activators ARF7 and ARF19 (Okushima et al. 2007; Swarup et al. 2008), both of which have been shown to interact with IAA14 (Fukaki et al. 2005). If, as the evidence suggests, both ARF7 and ARF19 are involved in the LAX3 expression network, further consideration is needed before we accept the assumption that the network can be modelled by a single ARF.

Firstly, comparing the qRT-PCR expression data following auxin treatment shown in Figure 4.1 for ARF7 and ARF19 suggests that they are differentially regulated. ARF7 remains at a relatively constant expression level following auxin treatment, while ARF19 is clearly upregulated by auxin. In the *arf7* mutant ARF19 expression is reduced, suggesting it is at least in part activated by ARF7. In the ARF19 mutant however, ARF7 is not affected, suggesting a stable pool of ARF7 independent of auxin treatment and ARF19. Secondly, ARF19 has previously been thought to be an activator similar to ARF7, so it may be expected that expression of ARF activated genes is lower in the ARF19 mutant, as less activator is present overall. However, IAA14 expression is similar, and LAX3 actually shows increased expression in the *arf19* mutant compared to wild type (Figure 4.1). Though ARF19 has previously been described as an activator similar to ARF7, in the regulation of LAX3 it appears to act as a repressor.

This chapter begins by formulating a simple model where ARF19 is

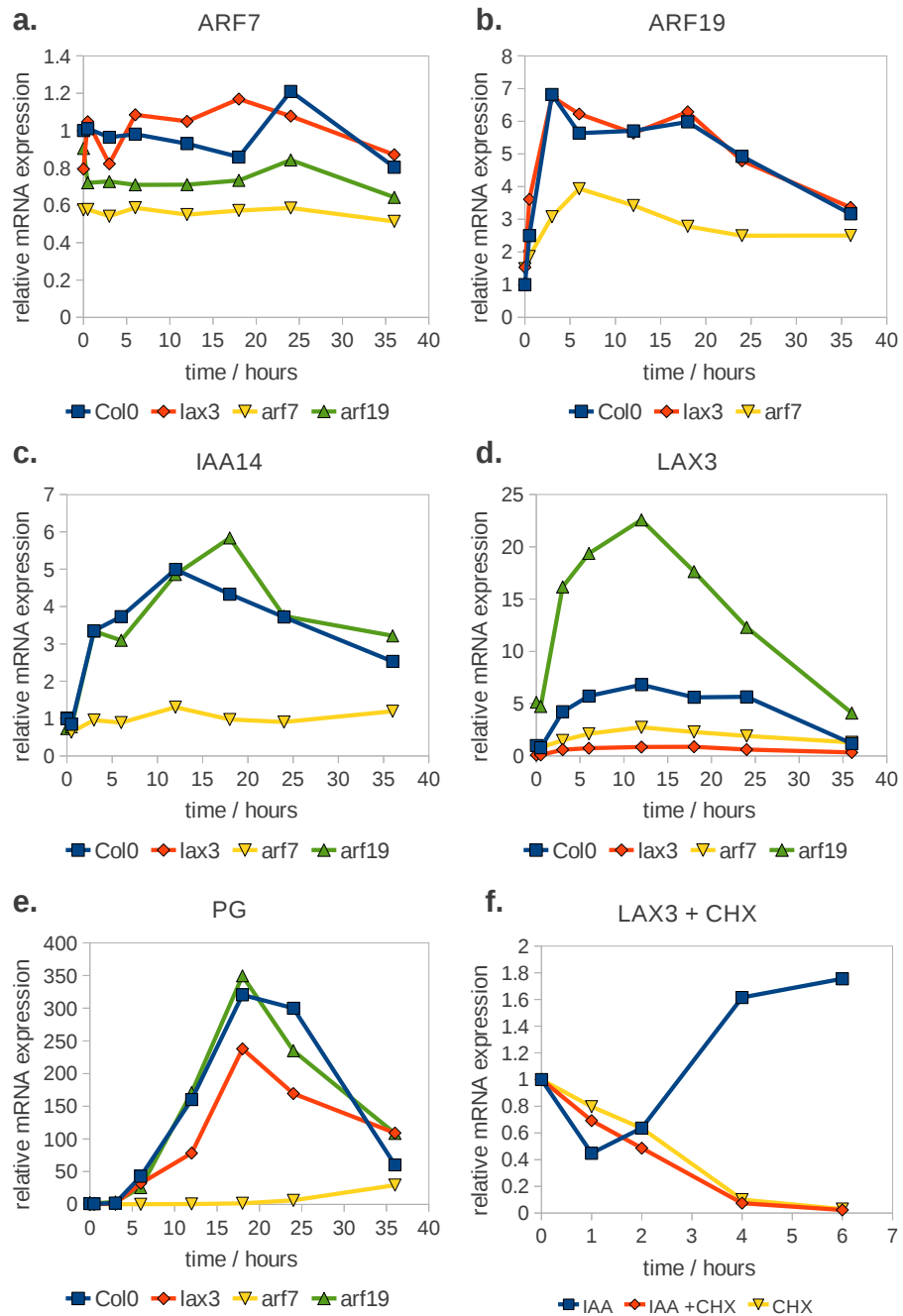


Figure 4.1: qRT-PCR time course data following $1 \mu\text{M}$ auxin treatment for (a) ARF7, (b) ARF19, (c) IAA14, (d) LAX3 and (e) PG mRNAs in wild type, *lax3*, *arf7*, and *arf19* mutant backgrounds (Benjamin Peret, personal communication). (f) Wild type LAX3 mRNA expression following treatment with $10 \mu\text{M}$ cyclohexamide (CHX), $1 \mu\text{M}$ auxin (IAA) and both CHX and IAA (Silvana Porco, personal communication).

activated by ARF7 (Section 4.2), and this is used to show that depending on parameter values ARF19 may either act as a transcriptional activator or effectively as a transcriptional repressor. In particular, the parameter values which allow ARF19 to act as a repressor are identified and linked with the biological mechanism they represent (Section 4.2.4). Also shown is a special case where the parameter values selected show that the model with both ARF7 and ARF19 can approximate the model with ARF7 only (Section 4.2.3).

Following this, we show that if ARF19 is an activator then an ARF19 inducible repressor can explain the temporal expression profile of LAX3, but that to fit both the wild-type and *arf19* mutant data, an additional ARF19 independent repressor may be required. In addition we also show that this model fails to account for the recovery in DII-VENUS observed experimentally (Section 2.3), and that some homeostatic mechanism for auxin is still needed.

Finally, by adding a decay in the exogenous signal to simulate the required auxin homeostasis, we investigate various models for both the transcriptional regulation of ARF19, and the regulation of LAX3 transcription by ARF19, and evaluate their ability to simulate the LAX3 expression data in the wild type, and the *arf19* mutant.

4.2 Simple ARF7 and ARF19 model

To begin comparing the models with and without the inclusion of ARF19 as an additional activator, we first consider a model network without the added complication of positive feedback via LAX3 expression, with just ARF19 and IAA14 expressed as primary auxin response genes (Figure 4.2).

We know from biological observation that IAA14 may bind with both ARF7 and ARF19 (Fukaki et al. 2005), and so the model must take into account both these interactions, and also the possibility that ARF19-IAA14 dimers may repress transcription as well as the ARF7-IAA14 dimers. We keep the assumption that free ARF7 bound to a responsive promoter will activate transcription, but in addition there is the possibility that free ARF19 bound to the promoter may act as an activator, making a total of four possible model species regulating transcription. It is conceivable that different targets may be regulated by different combinations of these four regulatory factors, but initially we consider the maximal model as shown in Figure 4.2.

4.2.1 Model Formulation

In this model both ARF7 and ARF19 are able to activate ARF19 and IAA14, unless they are dimerised with IAA14, which both ARFs are able to do reversibly. If either dimer is bound to a gene promoter transcription is repressed, while if ARF7 or ARF19 monomers bind, transcription is activated. ARF19 and IAA14 are induced by auxin, but ARF7 is not. All model species compete for the same binding site(s). Using similar notation and assumptions of mass action kinetics as for previous models, we have

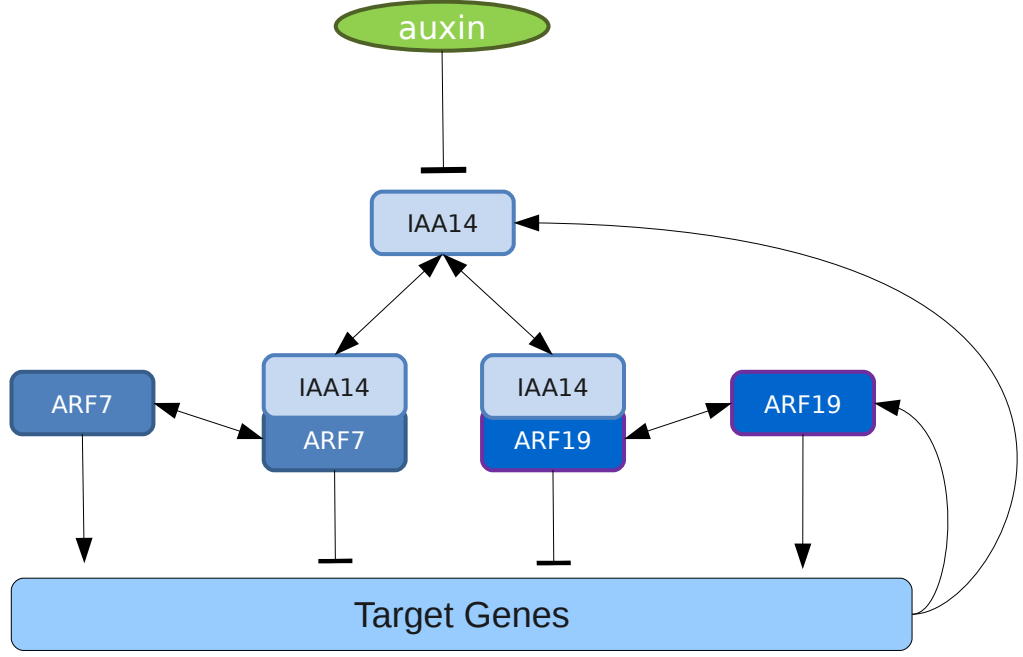


Figure 4.2: Network for ARF19 and ARF7 model. Auxin degrades IAA14 which binds to ARF7 and ARF19 repressing transcription of IAA14 and ARF19. When free from IAA14, both ARF7 and ARF19 activate transcription.

the dimensional model:

$$\frac{dTIR}{dt} = -p_a TIR \text{ auxin} + p_d TIR_a, \quad (4.1a)$$

$$\begin{aligned} \frac{dTIR_a}{dt} &= p_a TIR \text{ auxin} - p_d TIR_a \\ &\quad + (q_d + q_m) TIR_{ai} - q_a TIR_a \text{ IAA}, \end{aligned} \quad (4.1b)$$

$$\frac{dTIR_{ai}}{dt} = -(q_d + q_m) TIR_{ai} + q_a TIR_a \text{ IAA}, \quad (4.1c)$$

$$\begin{aligned} \frac{dIAA}{dt} &= q_d TIR_{ai} - q_a TIR_a \text{ IAA} + \delta_i IAA_m \\ &\quad - k_a ARF \text{ IAA} + k_d AI - f_a A19 \text{ IAA} + f_d AI19, \end{aligned} \quad (4.1d)$$

$$\frac{dARF}{dt} = -k_a ARF \text{ IAA} + k_d AI, \quad (4.1e)$$

$$\frac{dAI}{dt} = k_a ARF \text{ IAA} - k_d AI, \quad (4.1f)$$

$$\frac{dIAA_m}{dt} = F_i(ARF, AI, A19, AI19) - \mu_i IAA_m, \quad (4.1g)$$

$$\frac{dA19}{dt} = -\mu_a A19 + \delta_a A19_m - f_a A19 \text{ IAA} + f_d AI19, \quad (4.1h)$$

$$\frac{dA19_m}{dt} = F_a(ARF, AI, A19, AI19) - \mu_{a_m} A19_m, \quad (4.1i)$$

$$\frac{dAI19}{dt} = f_a A19 \text{ IAA} - f_d AI19, \quad (4.1j)$$

$$TIR + TIR_a + TIR_{ai} = tir_T, \quad (4.1k)$$

$$ARF + AI = arf_T, \quad (4.1l)$$

where:

$$F_i(ARF, AI, A19, AI19) = \frac{\lambda_{i1} \left(\frac{ARF}{\theta_{ia}}\right)^{n_i} + \lambda_{i2} \left(\frac{A19}{\phi_{ia}}\right)^{n_i}}{1 + \left(\frac{ARF}{\theta_{ia}}\right)^{n_i} + \left(\frac{AI}{\theta_{ir}}\right)^{n_i} + \left(\frac{A19}{\phi_{ia}}\right)^{n_i} + \left(\frac{AI19}{\phi_{ir}}\right)^{n_i}},$$

$$F_a(ARF, AI, A19, AI19) = \frac{\lambda_{a1} \left(\frac{ARF}{\theta_{aa}}\right)^{n_a} + \lambda_{a2} \left(\frac{A19}{\phi_{aa}}\right)^{n_a}}{1 + \left(\frac{ARF}{\theta_{aa}}\right)^{n_a} + \left(\frac{AI}{\theta_{ar}}\right)^{n_a} + \left(\frac{A19}{\phi_{aa}}\right)^{n_a} + \left(\frac{AI19}{\phi_{ar}}\right)^{n_a}},$$

Equations (4.1a)-(4.1g) are as in the earlier model (2.3b)-(2.3h), with the additional reactions for binding and unbinding with ARF19 included in equation (4.1d), and the alternative function for transcription, F_i , replacing F_{tc} in (4.1g). Equations (4.1h)-(4.1j) are added to model the evolution over time of ARF19 protein ($A19$), ARF19 mRNA ($A19_m$) and ARF19-IAA14 dimers ($AI19$) respectively. As before, the conservation of bound and unbound TIR1 and ARF is defined as in equations (4.1k) and (4.1l) respectively.

The new functions for transcriptional activity are based on the assumption that all model species compete for the same binding sites, with ARF7 and ARF19 activating (at different maximum rates reflected by the two parameters $\lambda x1$ and $\lambda x2$) if bound, and that the ARF7-IAA14 and ARF19-IAA14 dimers repress when bound. Auxin is treated as a parameter, effectively increasing the rate of degradation of Aux/IAA, rather than a model variable, with the basal level defined as aux_0 .

Nondimensionalisation

Scaling TIR , TIR_a , and TIR_{ai} with tir_t , ARF , AI , $A19$ and $AI19$ with arf_t , IAA_m with λ_i/μ_{i_m} , $A19_m$ with λ_a/μ_{a_m} , and time with $1/\mu_{i_m}$ gives the

nondimensional model:

$$\frac{dTIR}{dt} = -p_a TIR \text{ auxin} + p_d TIR_a, \quad (4.2a)$$

$$\begin{aligned} \frac{dTIR_a}{dt} &= p_a TIR \text{ auxin} - p_d TIR_a \\ &\quad + (q_d + q_m) TIR_{ai} - q_a TIR_a \text{ IAA}, \end{aligned} \quad (4.2b)$$

$$\frac{dTIR_{ai}}{dt} = -(q_d + q_m) TIR_{ai} + q_a TIR_a \text{ IAA}, \quad (4.2c)$$

$$\begin{aligned} \frac{dIAA}{dt} &= \eta_{iaa} (q_d TIR_{ai} - q_a TIR_a \text{ IAA}) + \delta_i IAA_m \\ &\quad - k_a ARF \text{ IAA} + k_d AI - f_a A19 \text{ IAA} + f_d AI19, \end{aligned} \quad (4.2d)$$

$$\frac{dARF}{dt} = -k_a ARF \text{ IAA} + k_d AI, \quad (4.2e)$$

$$\frac{dAI}{dt} = k_a ARF \text{ IAA} - k_d AI, \quad (4.2f)$$

$$\frac{dIAA_m}{dt} = F_i(ARF, AI, A19, AI19) - IAA_m, \quad (4.2g)$$

$$\frac{dA19}{dt} = -\mu_a A19 + \delta_a A19_m - f_a A19 \text{ IAA} + f_d AI19, \quad (4.2h)$$

$$\frac{dA19_m}{dt} = \mu_{a_m} (F_a(ARF, AI, A19, AI19) - A19_m), \quad (4.2i)$$

$$\frac{dAI19}{dt} = f_a A19 \text{ IAA} - f_d AI19, \quad (4.2j)$$

$$TIR + TIR_a + TIR_{ai} = 1, \quad (4.2k)$$

$$ARF + AI = 1, \quad (4.2l)$$

where:

$$F_i(ARF, AI, A19, AI19) = \frac{\frac{ARF}{\theta_{ia}} + \lambda_i \frac{A19}{\phi_{ia}}}{1 + \frac{ARF}{\theta_{ia}} + \frac{AI}{\theta_{ir}} + \frac{A19}{\phi_{ia}} + \frac{AI19}{\phi_{ir}}},$$

$$F_a(ARF, AI, A19, AI19) = \frac{\frac{ARF}{\theta_{aa}} + \lambda_{a2} \frac{A19}{\phi_{aa}}}{1 + \frac{ARF}{\theta_{aa}} + \frac{AI}{\theta_{ar}} + \frac{A19}{\phi_{aa}} + \frac{AI19}{\phi_{ar}}}.$$

For ease of notation, each variable and parameter has been replaced by its non-dimensional equivalent as defined in Table 4.1. Scaling ARF , AI , $A19$ and $AI19$ with arf_T enables us to compare binding parameters and peak transcription rates in the function $F_x(ARF, AI, A19, AI19)$ directly, and make further model simplifications below.

Quasi Steady State Approximation

To simplify the model for steady state analysis and time course simulations we can make further assumptions and approximations as detailed below.

Assuming the binding of auxin and Aux/IAA with the TIR1 receptors happens on a rapid timescale means the derivatives of TIR , TIR_a , and

Table 4.1: Nondimensional parameters and variables from the model given by equations (4.2a)-(4.2l), and relationship to dimensional parameters and variables from equations (4.1a)-(4.1j).

Non-dimensional parameter	Dimensional parameter equivalent
η_{iaa}	$\frac{tir_T}{arf_T}$
p_a	$\frac{p_a a u x_0}{\mu_{im}}$
p_d	$\frac{p_d}{\mu_{im}}$
q_a	$\frac{q_a ar f_T}{\mu_{im}}$
q_d	$\frac{q_d}{\mu_{im}}$
q_m	$\frac{q_m}{\mu_{im}}$
k_a	$\frac{k_a ar f_T}{\mu_{im}}$
k_d	$\frac{k_d}{\mu_{im}}$
f_a	$\frac{f_a ar f_T}{\mu_{im}}$
f_d	$\frac{f_d}{\mu_{im}}$
θ_{ia}	$\frac{\theta_{ia}}{arf_T}$
θ_{ir}	$\frac{\theta_{ir}}{arf_T}$
ϕ_{ia}	$\frac{\phi_{ia}}{arf_T}$
ϕ_{ir}	$\frac{\phi_{ir}}{arf_T}$
λ_i	$\frac{\lambda_{i2}}{\lambda_{j1}}$
θ_{aa}	$\frac{\theta_{aa}}{arf_T}$
θ_{ar}	$\frac{\theta_{ar}}{arf_T}$
ϕ_{aa}	$\frac{\phi_{aa}}{arf_T}$
ϕ_{ar}	$\frac{\phi_{ar}}{arf_T}$
λ_a	$\frac{\lambda_{a2}}{\lambda_{a1}}$
δ_i	$\frac{\delta_i \lambda_{i1}}{\mu_{im}^2}$
δ_a	$\frac{\delta_a \lambda_{a1}}{\mu_{am} \mu_{im}}$
μ_{am}	$\frac{\mu_{im}}{\mu_a}$
μ_a	μ_{im}
$auxin$	$\frac{auxin}{aux_0}$
Non-dimensional variable	Dimensional variable equivalent
TIR	$\frac{TIR}{tir_T}$
TIR_a	$\frac{TIR_a}{tir_T}$
TIR_{ai}	$\frac{TIR_{ai}}{tir_T}$
IAA	$\frac{IAA}{arf_T}$
ARF	$\frac{ARF}{arf_T}$
AI	$\frac{AI}{arf_T}$
IAA_m	$\frac{\mu_{im} IAA}{\lambda_i}$
$A19$	$\frac{A19}{arf_T}$
$A19_m$	$\frac{\mu_{am} IAA}{\lambda_a}$
$AI19$	$\frac{AI19}{arf_T}$

TIR_{ai} can be neglected and the model simplified as follows:

$$\frac{dIAA}{dt} = \frac{-\eta auxin IAA}{QP + Qauxin + auxin IAA} + \delta_i IAA_m - k_a ARF IAA + k_d AI - f_a A19 IAA + f_d AI19, \quad (4.3a)$$

$$\frac{dIAA_m}{dt} = F_i(ARF, AI, A19, AI19) - IAA_m, \quad (4.3b)$$

$$\frac{dARF}{dt} = -k_a ARF IAA + k_d AI, \quad (4.3c)$$

$$\frac{dAI}{dt} = k_a ARF IAA - k_d AI, \quad (4.3d)$$

$$\frac{dA19}{dt} = -\mu_a A19 + \delta_a A19_m - f_a A19 IAA + f_d AI19, \quad (4.3e)$$

$$\frac{dA19_m}{dt} = \mu_{a_m}(F_a(ARF, AI, A19, AI19) - A19_m), \quad (4.3f)$$

$$\frac{dAI19}{dt} = f_a A19 IAA - f_d AI19, \quad (4.3g)$$

$$TIR^* = \frac{QP}{QP + Qauxin + auxin IAA}, \quad (4.3h)$$

$$TIR_a^* = \frac{Qauxin}{QP + Qauxin + auxin IAA}, \quad (4.3i)$$

$$TIR_{ai}^* = \frac{auxin IAA}{QP + Qauxin + auxin IAA}, \quad (4.3j)$$

where $Q = (q_d + q_m)/q_a$, $P = p_d/p_m$, $\eta = q_m \eta_{iaa}$ and TIR^* , TIR_a^* and TIR_{ai}^* are the quasi-steady state values of TIR , TIR_a , and TIR_{ai} respectively.

Further assuming that binding and unbinding in the dimerisation reactions happens rapidly, and so neglecting the derivatives of ARF , AI , $A19$,

and $AI19$ and rearranging gives:

$$\frac{dIAA}{dt} = \frac{-\eta auxin IAA}{QP + Qauxin + auxin IAA} + \delta_i IAA_m, \quad (4.4a)$$

$$\frac{dIAA_m}{dt} = F_i \left(\frac{K}{IAA + K}, \frac{IAA}{IAA + K}, A19, \frac{A19 IAA}{\kappa} \right) - IAA_m, \quad (4.4b)$$

$$\frac{dA19}{dt} = -\mu_a A19 + \delta_a A19_m, \quad (4.4c)$$

$$\frac{dA19_m}{dt} = \mu_{a_m} \left(F_a \left(\frac{K}{IAA + K}, \frac{IAA}{IAA + K}, A19, \frac{A19 IAA}{\kappa} \right) - A19_m \right) \quad (4.4d)$$

$$ARF^* = \frac{K}{IAA + K}, \quad (4.4e)$$

$$AI^* = \frac{IAA}{IAA + K}, \quad (4.4f)$$

$$AI19^* = \frac{A19 IAA}{\kappa}, \quad (4.4g)$$

$$TIR^* = \frac{QP}{QP + Qauxin + auxin IAA}, \quad (4.4h)$$

$$TIR_a^* = \frac{Qauxin}{QP + Qauxin + auxin IAA}, \quad (4.4i)$$

$$TIR_{ai}^* = \frac{auxin IAA}{QP + Qauxin + auxin IAA}, \quad (4.4j)$$

where $K = k_d/k_a$, $\kappa = f_d/f_a$, and ARF^* , AI^* and $AI19^*$ are the quasi-steady state values of ARF , AI and $AI19$ respectively.

4.2.2 ARF7 and ARF19 share parameter values

Intuitively, since ARF19 is an activator it is to be expected that adding it to the model will result in a positive feedback. The situation is complicated however, by the fact that it is also able to dimerise with Aux/IAA and form repressors, which may at least in part offset the activatory effect (Figure 4.2). To test the degree to which the balance of repression to activation may be altered by changing parameter values in the model we first look at the special case where ARF7 and ARF19 behave identically in every way other than their regulation.

Steady State Analysis

If we assume that ARF7 and ARF19 are similar in all ways other than their regulation, so that they share binding and unbinding rates with Aux/IAs and gene promoters, and transcription rates are equal, then we assume $\kappa = K$, all binding parameters are equal (θ), all co-operativity coefficients are equal to one, and $\lambda_i = \lambda_a = 1$, so that:

$$F_i = F_a = \frac{ARF + A19}{\theta + ARF + AI + A19 + AI19}$$

Using equations (4.2l), (4.4e) and (4.4g) and substituting for $ARF + AI$, ARF and $AI19$ in the equation above gives:

$$F_i = \frac{\frac{K}{IAA+K} + A19}{\theta_x + 1 + A19 \left(\frac{IAA+K}{K} \right)}. \quad (4.5)$$

At steady state all derivatives equal zero, so from 4.4a-4.4j we have:

$$IAA_m^* = \frac{\eta auxin IAA^*}{\delta_i(QP + Qauxin + auxin IAA^*)}, \quad (4.6a)$$

$$IAA_m^* = \frac{\frac{K}{IAA^*+K} + A19^*}{\theta + 1 + A19^* \left(\frac{IAA^*+K}{K} \right)}, \quad (4.6b)$$

$$A19_m^* = \frac{\mu_a}{\delta_a} A19^*, \quad (4.6c)$$

$$A19_m^* = \frac{\frac{K}{IAA^*+K} + A19^*}{\theta + 1 + A19^* \left(\frac{IAA^*+K}{K} \right)}, \quad (4.6d)$$

where the $*$ superscript represents steady state values. To simulate the *arf19* mutant we set $A19 = 0$ so that:

$$IAA_m^* = \frac{\eta auxin IAA^*}{\delta_i(QP + Qauxin + auxin IAA^*)}, \quad (4.7a)$$

$$IAA_m^* = \frac{\frac{K}{IAA^*+K}}{\theta_i + 1}. \quad (4.7b)$$

For a steady state to exist the two functions (4.7a) and (4.7b) must intersect for some $IAA^* > 0$. By inspection, equation (4.7a) is a monotonically increasing function of IAA^* , with $IAA_m^* = 0$ when $IAA^* = 0$, and $IAA_m^* \rightarrow \frac{\eta}{\delta_i}$ as $IAA^* \rightarrow \infty$. Increasing auxin has the effect of decreasing the value of IAA^* at which half the maximum IAA_m occurs (Figure 4.3). In contrast, the expression on the right hand side of (4.7b) is monotonically decreasing with increasing IAA^* , with $IAA_m^* = \frac{1}{\theta+1}$ when $IAA^* = 0$ and $IAA_m^* \rightarrow 0$ as $IAA^* \rightarrow \infty$. As shown graphically in Figure 4.3, this means that in the absence of ARF19 the system will always have a unique steady state.

When including ARF19 in the model, the steady state is more difficult to find analytically. However, if we assume that for a given value for auxin, a positive steady state for ARF19 exists ($A19 = A19^*$), then from (4.6b), we have $IAA_m^* = \frac{1+A19^*}{\theta+1+A19^*}$ when $IAA^* = 0$ and $IAA_m^* \rightarrow 0$ as $IAA^* \rightarrow \infty$. Again, we show graphically in Figure 4.3 this must result in a unique steady state for IAA_m . However, in this case we must take into account that for increasing values of *auxin*, so too will the steady state of ARF19 increase. Nonetheless, for a given auxin concentration, assuming there is a unique steady state for ARF19, the steady state IAA_m expression will be greater in the model with ARF19 than without if for all $IAA^* > 0$:

$$\frac{\frac{K}{IAA^*+K} + A19^*}{\theta + 1 + A19^* \left(\frac{IAA^*+K}{K} \right)} > \frac{\frac{K}{IAA^*+K}}{\theta + 1},$$

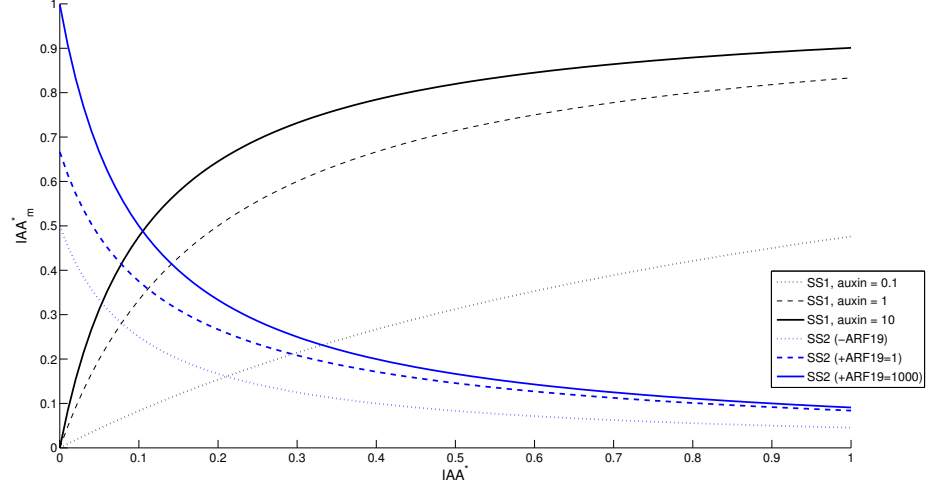


Figure 4.3: Equation 4.6a against IAA for three values of auxin (SS1), and equation 4.6b with and without ARF19 (SS2). The intersections between lines represent steady states for Aux/IAA mRNA and protein. For each value for auxin the mRNA steady state is unique, and higher in the model with ARF19. ARF19 steady state is set to 1 or 1000. $P, \theta, \eta/\delta_i = 1, Q, K = 0.1$.

Table 4.2: Default nondimensional parameters for model defined by 4.4a-4.4j

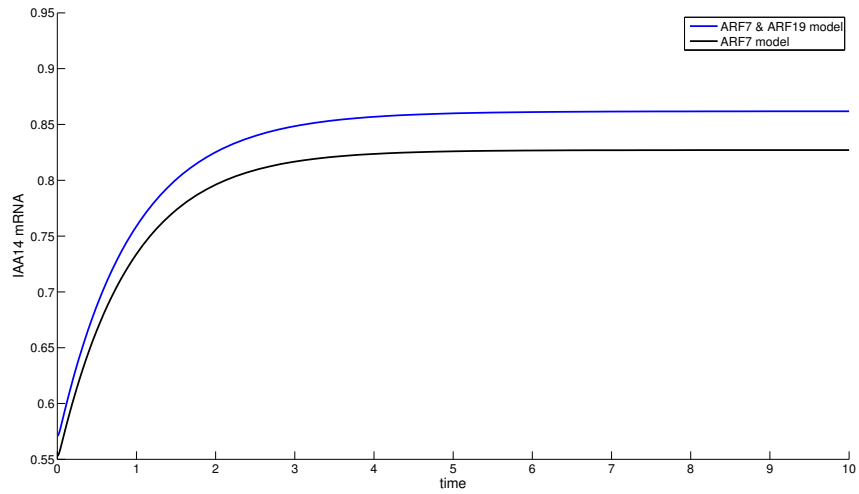
$Q = 0.1$	$P = 0.1$	$K = 0.1$	$\kappa = 0.1$	$\eta = 10$
λ_i	$\theta_{ia} = 0.1$	$\theta_{ir} = 0.1$	$\phi_{ia} = 0.1$	$\phi_{ir} = 0.1$
λ_a	$\theta_{aa} = 0.1$	$\theta_{ar} = 0.1$	$\phi_{aa} = 0.1$	$\phi_{ar} = 0.1$
$\delta_a = 1$	$\mu_a = 1$	$\mu_{a_m} = 1$	$\delta_i = 1$	

which can be shown by cross-multiplying the denominators as follows:

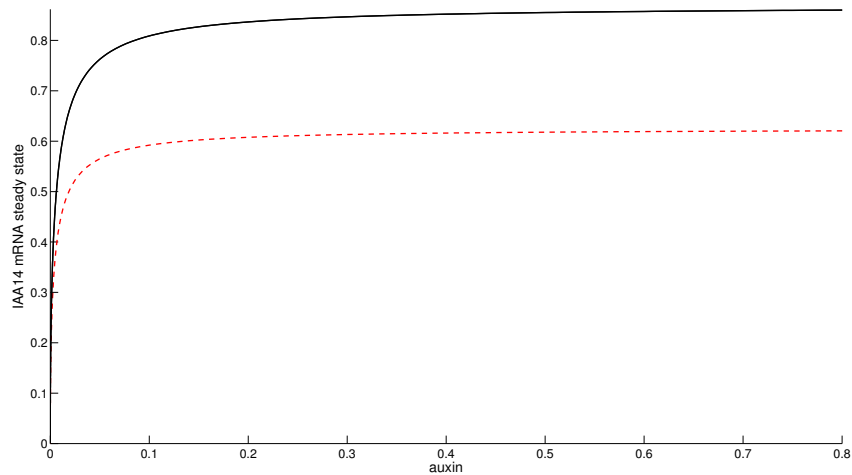
$$\frac{K}{IAA^* + K}(\theta + 1) + A19^*(\theta + 1) > \frac{K}{IAA^* + K}(\theta + 1) + A19^*.$$

In the above analysis we assume that ARF19 steady state exists, and show that if it does, and all other things being equal, that genes activated by ARF19 in addition to ARF7 will show higher expression levels than those activated by ARF7 alone. Figure 4.4(b) shows the model IAA14 mRNA steady state against increasing auxin concentration for the default parameter set given in Table 4.2. To simulate the *arf19* mutant *A19* is fixed equal to zero and only equations (4.4a) and (4.4b) are used. Figure 4.4(a) shows the time course solution using the same parameters for the model with and without ARF19 as before, following a simulated increase in auxin from initial steady state values at the lower value of auxin.

Looking at steady state, both models begin from zero expression at zero auxin, and increase smoothly with increasing auxin up to a saturating maximum steady state. The steady state for the model with ARF19 is always higher than the model without. As expected, for the time course there is a smooth transition between basal and auxin treated steady state, and both low and high steady states decrease when ARF19 is removed



(a) Model IAA14 mRNA against time, with (blue) and without (black) ARF19 as an activator, from steady state following an increase in simulated auxin from 0.01 to 1. The simulated IAA14 mRNA values are always greater in the model with ARF19 as an activator. Parameter values for all interactions involving ARF7 and ARF19 are shared by both.



(b) Model IAA14 mRNA steady state against auxin, with (black) and without (red, dashed) ARF19 as an activator. For all values of auxin greater than zero, the steady state is higher with ARF19 in the model. Parameter values for all interactions involving ARF7 and ARF19 are shared by both.

Figure 4.4: Model time course and steady state using the parameter values in Table 4.2 in equations (4.4a)-(4.4j). In both cases the *arf19 mutant* is simulated by setting $A19 = 0$ and using just equations(4.4a) and (4.4b).

from the model. This difference can be magnified by changing parameter values, but when parameters are equal for both ARF7 and ARF19, removing ARF19 from the model will always reduce expression.

4.2.3 The ARF7 model can approximate the ARF7 and ARF19 model

While the previous sections shows that if ARF7 and ARF19 share parameter values, there will be quantitative reduction in expression in the model without ARF19. Qualitatively however, model behaviour appears very similar. Because of this, by changing parameter values in the ARF7 only model relative to the ARF7 and ARF19 model, it is possible to approximate the latter model with the former. From equation (4.5), and using the fact that the maximum value for $ARF = 1$, the maximum steady state Aux/IAA mRNA in the ARF7 and ARF19 model, for a given value for $\theta = \theta_1$, is given by:

$$IAA_{m1} = \frac{1 + A19^*}{\theta_1 + 1 + A19^*},$$

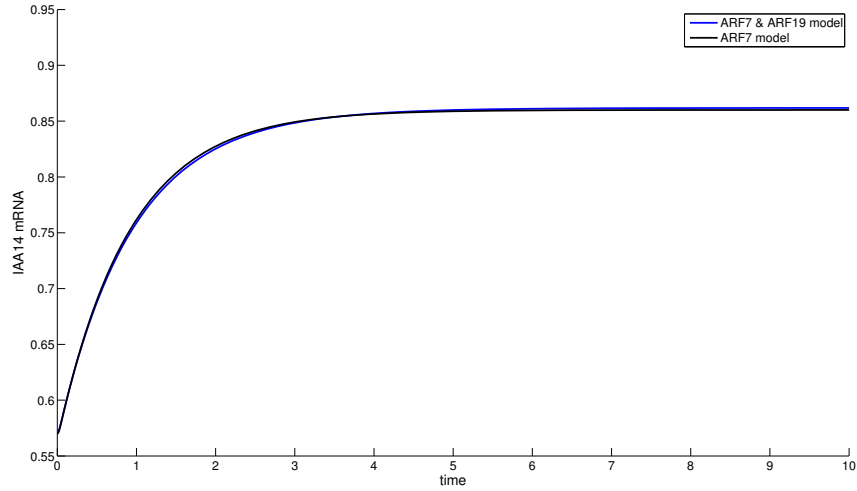
where $A19^*$ is steady state ARF19. Similarly, from equation (4.7b) the maximum steady state Aux/IAA mRNA in the ARF7 only model, for a given value for $\theta = \theta_2$, is given by:

$$IAA_{m2} = \frac{1}{\theta_2 + 1}.$$

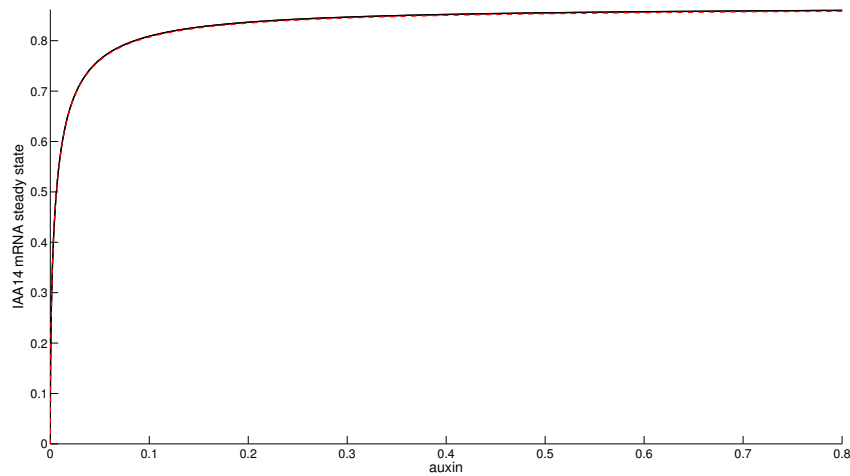
If we then use $\theta_2 = \frac{\theta_1}{1+A19^*}$, with the peak value for steady state ARF19 expression for $A19^*$, the peak steady state expression should be similar for the two models. This is demonstrated to be a reasonable approximation in Figures 4.5(a) and 4.5(b).

4.2.4 ARF19 can act as a transcriptional repressor

The analysis in Section 4.2.2 demonstrates that assuming that the binding and unbinding rates of ARF19 and IAA14 are the same as those for ARF7 and IAA14, that the peak rate of transcription is the same when ARF19 is bound as when ARF7 is bound to a promoter, and that bound or unbound ARF7 or ARF19 have the same affinity to promoters, steady state gene expression will be greater in the model with both ARF7 and ARF19 than in the model with just ARF7. This may be intuitively obvious, but in this section we show that by changing the parameters relating to the assumptions given above, reduced expression can be seen when simulating the ‘wild type’ in comparison to the *arf19* mutant. In other words, differences in parameter values may cause ARF19 to behave as a repressor, as seen experimentally, where there is an increase in LAX3 expression in the *arf19* mutant (equivalent to the ARF7 only model), compared to the wild type (ARF7 and ARF19 model). To obtain solutions to the model given by (4.4a)-(4.4j) that reflect this we must consider the more general case where parameter values relating to ARF7 and ARF19 are different. By changing three parameter values in particular it is possible to see greater expression



(a) Model IAA14 mRNA against time, with (blue) and without (black) ARF19 as an activator, from steady state following an increase in simulated auxin from 0.01 to 1. Parameter values are as in Table 4.2 except for in the ARF7 only model θ_{ai} , θ_{ar} , ϕ_{ia} and ϕ_{ia} are all set equal to $\frac{\theta_1}{1+A19^*}$, where $A19^*$ is the steady state ARF19 for auxin=1 in the full model using the default parameters, so that the ARF7 only model is a good approximation of the ARF7-ARF19 model.



(b) Model IAA14 mRNA steady state against auxin, with (black) and without (red, dashed) ARF19 as an activator. Parameter values are as in Table 4.2 except for in the ARF7 only model θ_{ai} , θ_{ar} , ϕ_{ia} and ϕ_{ia} are all set equal to $\frac{\theta_1}{1+A19^*}$, where $A19^*$ is the steady state ARF19 for auxin=1 in the full model using the default parameters, so that the ARF7 only model is a good approximation of the ARF7-ARF19 model.

Figure 4.5: Model time course and steady state showing how the ARF7 model may approximate the ARF7 and ARF19 model using the parameter values in Table 4.2 (except where stated) in equations (4.4a)-(4.4j). In both cases the *arf19 mutant* is simulated by setting $A19 = 0$ and using just equations(4.4a) and (4.4b).

of auxin responsive genes in the *arf19* mutant model compared to the ‘wild type’ model.

1. κ : **Unbinding of ARF19-IAA14 dimers relative to binding.**

Decreasing κ relative to K (unbinding of ARF7-IAA14 dimers relative to binding) effectively means that ARF19 has a greater affinity with the IAA14 repressors than does ARF7, and since we assume that this binding and unbinding of dimers occurs on a rapid timescale relative to gene expression, then when ARF19 is expressed the proportion of repressors formed relative to activators is higher than when ARF19 is not present. As shown by Figure 4.6a, reducing κ by a factor of two is still insufficient to give significantly higher expression in the *arf19* mutant relative to wild type, while reducing by a factor of ten can give a difference closer to that observed experimentally. It may be possible to estimate a value of κ relative to K from the yeast two-hybrid results given in Fukaki et al. (2005) for the binding of both ARF7 and ARF19 with IAA14. While these results do appear to show in greater affinity of IAA14 for ARF19 than for ARF7 as required, the given experimental value of ARF7-IAA14 dimers is approximately 80% that of ARF19-IAA14 dimers. If we assume this is roughly equivalent to the ratio of κ to K , this difference is not significant enough for the model to account for the observed difference in expression.

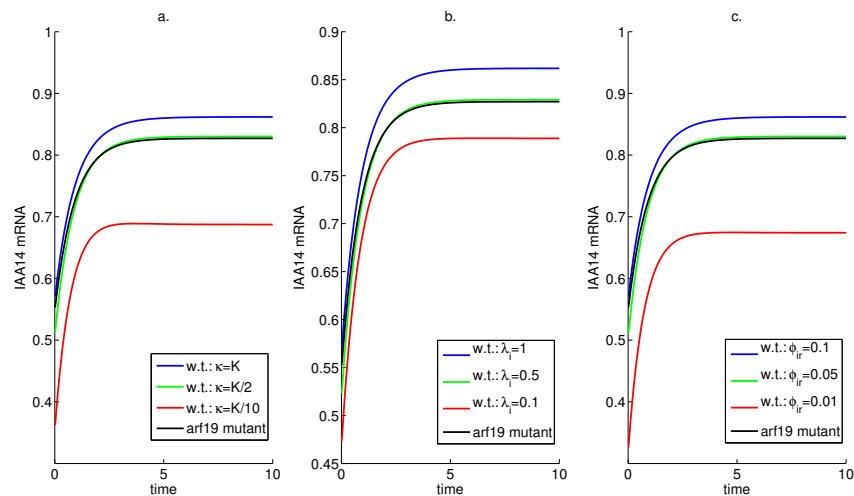


Figure 4.6: Fixing particular parameters relative to others, can result in higher gene expression in the *arf19* mutant relative to the wild type. κ is the affinity of ARF19 to IAA14, ϕ_{ir} is the binding threshold of ARF19-IAA14 dimers with the promoter of *tfX*, and λ_i is the activatory power of ARF19 relative to ARF7.

2. λ_i : **Maximum activation due to ARF19 relative to ARF7.**

The model has the assumption that when either ARF19 or ARF7 is bound to a promoter, it increases the probability of RNA polymerase binding to it, resulting in the gene being transcribed. Previously, it

was assumed that this probability of transcription was equal for both ARF7 and ARF19, by setting the value of the parameter λ for the gene in question to 1. This parameter is effectively a measure of activatory power of ARF19, and so a value of $\lambda > 1$ would simulate ARF19 being a more effective activator than ARF7, while $\lambda < 1$ simulates ARF19 as a less effective activator. If $\lambda = 0$ ARF19 is entirely ineffective as an activator; in other words by competing for the same binding site as ARF7, when bound it will not result in transcription and so ARF19 is effectively a repressor. Because of this, reducing λ_i can result in increased transcription in the *arf19* mutant relative to wild type, as shown in Figure 4.6b. Even for a value of $\lambda_i = 0.1$ the increased expression in the *arf19* mutant is marginal, and a parameter value this low or lower would appear to contradict the assumption that ARF19 is an activator at all.

3. ϕ_{ir} : Binding threshold of ARF19-IAA14 repressors to promoter.

The parameter ϕ_{ir} can be thought of as representing the concentration at which ARF19-IAA14 dimers begin to have a strong probability of binding with the promoter and repressing transcription. If this value is set low, compared to other binding parameter values, then the level of ARF19-IAA14 may have a disproportionately large effect. Figure 4.6c demonstrates this using the model. However, if ARF19-IAA14 dimers are more likely to bind the promoter than ARF7 or ARF7-IAA14 dimers, it might be expected that ARF19 monomers ought also to bind preferentially, and if this is set to be the case by changing the relevant parameter the effective repression by ARF19 is removed.

By changing the key parameters listed above, it is shown that the observed increase in LAX3 expression in the *arf19* mutant may be explained by differences in interaction rates between ARF19, ARF7 and other system components. In general though, these differences strongly reduce the power of ARF19 as an activator in comparison to ARF7, and due to the sequence similarity between ARF7 and ARF19 the differences in parameter values needed may not be biologically realistic. For this reason in the following sections we investigate the possibility that ARF19 is activating another transcription factor that acts as a repressor, and it is this that results in the difference in expression of LAX3 in the wild type and *arf19* mutant backgrounds.

4.3 Models with ARF19 activated repressors

4.3.1 ARF19 activates a single repressor

Using the simple ARF7-ARF19 model in Section 4.2, it was shown in Section 4.2.4 that by changing one or more key parameters, ARF19 may be able to act as a repressor of ARF7 responsive genes. In this way, the model should be able to match qualitatively the increased expression of LAX3

in the *arf19* mutant compared to the wild type. This depends however, on parameter values for ARF19 relative to ARF7 which may not be biologically realistic. An alternative hypothesis to explain the difference between wild type and *arf19* is that ARF19 specifically activates a repressor of LAX3 that ARF7 does not. One set of candidate repressors are the negative ARFs (Guilfoyle and Hagen 2007), which do not generally bind with the Aux/IAs (Vernoux et al. 2011), and may compete with the positive ARFs for AuxRE binding sites. There is an AuxRE binding site on the LAX3 promoter which is a potential site for negative ARFs, and mutating this site does not negatively impact LAX3 induction suggesting the positive ARFs do not bind effectively (Larrieu 2011). The model network shown in Figure 4.7 is therefore formulated in the following section and the resulting predictions compared with the experimental data.

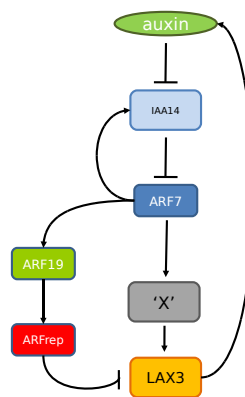


Figure 4.7: Gene network using the single repressor model. ARF7 activates ARF19 which activates an unknown repressor of LAX3.

Model Formulation

The model is formulated similarly to previous models, but with the addition of the proposed negative ARF, *ARFr*, which is able to feed back negatively on the expression of all the other genes. Also, with the exception of IAA14, the protein and mRNA of the induced genes are modelled with a single

equation. This gives the new model:

$$\frac{dIAA}{dt} = \frac{-\eta auxin IAA}{QP + Qauxin + auxin IAA} + IAA_m, \quad (4.8a)$$

$$\frac{dIAA_m}{dt} = F_{tc} \left(\frac{K}{\theta_{ia}(IAA + K)}, \frac{IAA}{\theta_{ir}(IAA + K)}, \frac{ARF_r}{\theta_{in}}, n_i \right) - IAA_m, \quad (4.8b)$$

$$\frac{dX}{dt} = \mu_x \left(F_{tc} \left(\frac{K}{\theta_{xa}(IAA + K)}, \frac{IAA}{\theta_{xr}(IAA + K)}, \frac{ARF_r}{\theta_{xn}}, n_x \right) - X \right), \quad (4.8c)$$

$$\frac{dLAX}{dt} = \mu_l \left(F_{tclax} \left(\frac{X}{\theta_{la}}, \frac{ARF_r}{\theta_{ln}}, n_l, m \right) - LAX \right), \quad (4.8d)$$

$$\frac{dA19}{dt} = \mu_a \left(F_{tc} \left(\frac{K}{\theta_{aa}(IAA + K)}, \frac{IAA}{\theta_{ar}(IAA + K)}, \frac{ARF_r}{\theta_{an}}, n_a \right) - A19 \right), \quad (4.8e)$$

$$\frac{dARF_r}{dt} = \mu_r \left(F_{tc} \left(\frac{A19}{\theta_{ra}}, \frac{A19 IAA}{\theta_{rr} N}, \frac{ARF_r}{\theta_{rn}}, n_r \right) - ARF_r \right), \quad (4.8f)$$

$$\frac{d auxin}{dt} = xaux(\alpha_{aux} + \alpha_{lax} LAX) - \mu_{aux} auxin, \quad (4.8g)$$

where:

$$F_{tc}(ACT, REP1, REP2, n) = \frac{ACT^n}{1 + ACT^n + REP1^n + REP2^n}, \quad (4.8h)$$

$$F_{tclax}(ACT, REP, n, m) = \left(\frac{ACT^n}{1 + ACT^n} \right) \left(\frac{1}{1 + REP^m} \right). \quad (4.8i)$$

Time and auxin are scaled as before, IAA_m , X , LAX , $A19$, ARF_r are scaled with λ/μ (ratio of peak transcription to decay) for each gene, and IAA is scaled with $\frac{\lambda_i \delta_i}{\mu_{im}^2}$.

The key features of the model occur in the form of the functions relating to the transcription of the mRNAs. For simplicity, since as shown in Section 4.2.3 the additional activation by ARF19 can be approximated in the model by adjusting the affinity for ARF7, only ARF_r is activated by ARF19 explicitly, while the other genes are activated by ARF7 only. In both cases ARF_r is able to bind the ARF binding site and repress transcription.

LAX3 is positively activated by the unknown TFX, and repressed by ARF_r , with both able to bind independently to different sites. For transcription to occur we assume that *both* X must be bound to its binding site, and that the ARF binding site is unoccupied. Otherwise transcription is repressed. Because of this the transcription of LAX3 is modelled by the product of the probability that the activatory site is occupied and the probability that the ARF binding site is unoccupied.

Parameter Fitting

Using the parameter fitting algorithm described in Section 2.2, with the above model (4.8a)-(4.8i) it is possible to fit the parameters to match the

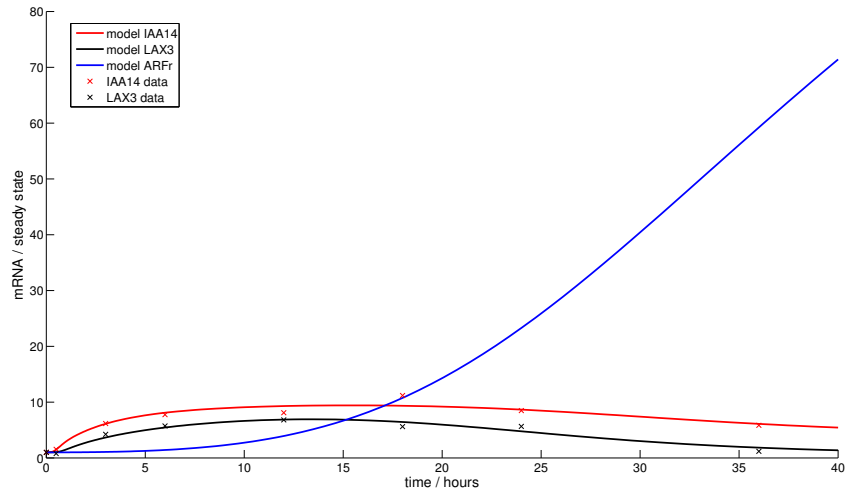
Table 4.3: Fitted parameter values for the model given by equations (4.8a)-(4.8i) to the data in Figure 4.1. Co-operativity coefficients were constrained between 1 and 3, and binding parameters between 0.01 and 100.

$\theta_{ia} = 0.0589$	$\theta_{ir} = 0.0705$	$\theta_{in} = 0.0576$	$n_i = 2.9377$	$P = 0.784$
$\theta_{xa} = 0.5936$	$\theta_{xr} = 0.0497$	$\theta_{xn} = 0.0169$	$n_x = 1.1994$	$\mu_x = 5.8473$
$\theta_{la} = 0.1050$	$n_l = 1.5557$	$\theta_{ln} = 0.0141$	$m = 1$	$\mu_l = 0.6998$
$\theta_{aa} = 0.0989$	$\theta_{ar} = 0.0534$	$\theta_{an} = 0.7072$	$n_a = 3$	$\mu_a = 0.0345$
$\theta_{ra} = 0.1034$	$\theta_{rr} = 100$	$\theta_{rn} = 1.1282$	$n_r = 3$	$\mu_r = 0.0682$
$\alpha_{lax} = 0.3837$	$\mu_{aux} = 9.2349$	$Q = 0.0029$	$K = 0.0202$	$\eta = 13.2518$
$xaux_0 = 0.1004$	$\alpha_x = 0.012$			

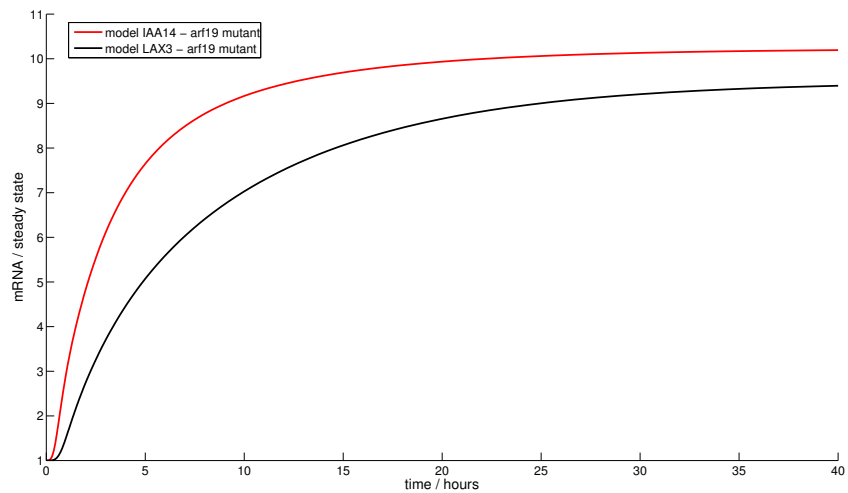
IAA14 and LAX3 qRT-PCR wild type data given in Figure 4.1, with the fitted parameter values shown in Table 4.3). Figure 4.8(a) shows the model fit, along with a prediction for *ARFr* mRNA against time. By peaking late in the time course the additional repressor is able to reduce expression of LAX3 and IAA14 over the second half of the time course. However, as may be expected, when ARF19 is removed, the repressor is no longer induced and the genes remain switched on (Figure 4.8(b)).

An additional result of including the additional repressor in the model is seen in the steady state LAX3 expression with increasing exogenous auxin (Figure 4.9(a)). In previous models, an increase in exogenous auxin will result in an increase in steady state expression. Even in the conjugation model where there may be stable oscillations, these will be about an unstable steady state which increases with increasing auxin signal. In the repressor model however, we see that after increasing from zero auxin signal there may be a fixed value of exogenous auxin signal for which mRNA expression peaks, before returning to at or near the initial zero auxin expression level for high levels of exogenous auxin. This means that both very high and very low auxin treatments may result in low steady state expression of LAX3 mRNA, while an intermediate value for auxin will result in a relatively high steady state expression. The steady state level intracellular auxin concentration with increasing exogenous auxin signal shown in Figure 4.9(b) demonstrates that the expression of the induced repressor does not negatively affect the amount of auxin in the cell. In this case, the key difference in model behaviour between high and low auxin treatment is seen in the time course simulation (Figure 4.9(c)). Here, following an initial increase from basal auxin level, low auxin treatment results in a small and steady increase to a higher steady state expression, while intermediate auxin treatment results in a qualitatively similar increase, but with a much higher fold-change increase in steady state. For the highest auxin treatment, there is temporary increase in expression many fold higher than that seen at either the low or intermediate treatments, before over time the increase in the induced repressor causes the expression level to drop to that below that seen for the low auxin treatment.

The ARF19 activated repressor model describes a possible mechanism by which at high auxin treatment LAX3 mRNA may be expressed tem-

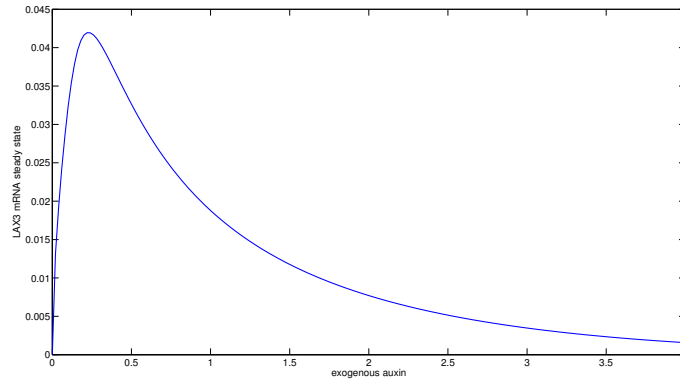


(a) Simulated LAX3 and IAA14 mRNA against time using the model given by equations (4.8a)-(4.8i) with the parameter values in Table 4.3, fitted to the wild type LAX3 and IAA14 qRT-PCR data shown in Figure 4.1.

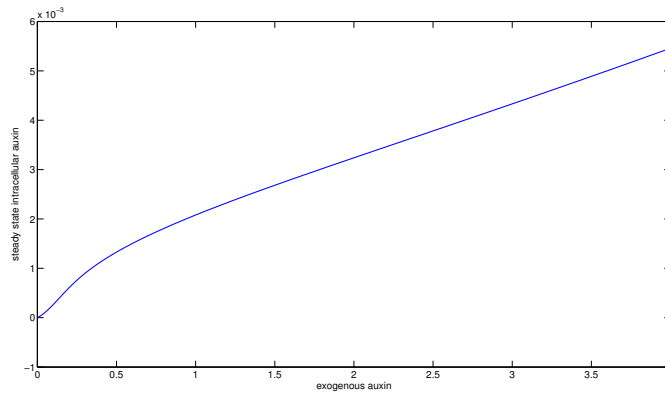


(b) Simulated LAX3 and IAA14 mRNA against time using the model given by equations (4.8a)-(4.8i) with the parameter values in Table 4.3, with ARF19 expression fixed equal to zero. Removing ARF19 from the model, removes all repression, and so both IAA14 and LAX3 remained switched on throughout the time course.

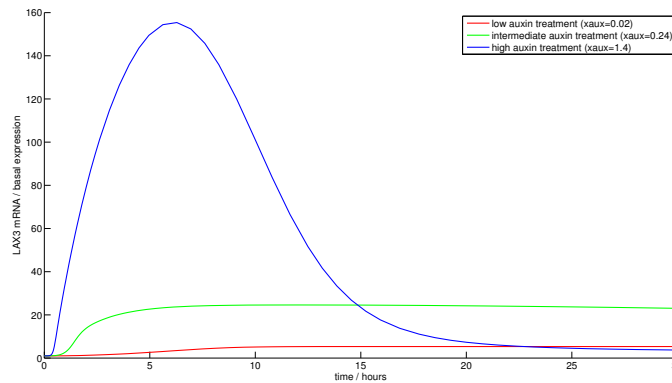
Figure 4.8



(a) LAX3 mRNA steady state with increasing auxin signal (x_{aux}). Steady state expression is low at both low and high x_{aux} , and peaks at intermediate values.



(b) Intracellular auxin steady state increases with increasing auxin signal.



(c) Temporal differences in LAX3 mRNA expression following treatment with low, intermediate or high auxin (see figure legend).

Figure 4.9: LAX3 mRNA (Figure 4.9(a)) and intracellular auxin (Figure 4.9(b)) steady state with increasing exogenous auxin signal, and example time courses at low, intermediate and high auxin treatment (Figure 4.9(c)) using the repressor model (4.8a)-(4.8i) and the parameter values in Table 4.3.

porarily before being down-regulated once more. On its own however, it is insufficient to explain the difference between the wild type and arf19 mutant LAX3 expression, and removing ARF19 from the model removes all downregulation (Figure 4.8(b)). A repression mechanism that may explain this difference is investigated in Section 4.3.2.

4.3.2 Two Repressor Pathway Model

In Section 4.3.1 it is shown that a repressor, possibly a negative ARF, can simulate the experimentally observed LAX3 expression profile of a peak between 10 and 15 hours followed by down-regulation for the remainder of the time course. If this induced repressor is responsible for the shape of the temporal expression profile, then a repressor must also be induced by a pathway independent of ARF19, since this same profile (but with a larger magnitude) is observed in the arf19 mutant plants. If this is the case the effect observed in the arf19 mutant could be a result of a quantitative reduction in total repressor by knocking out the ARF19 specific pathway. This leads to the formulation of an extended ARF7-ARF19 model as summarised in Figure 4.10.

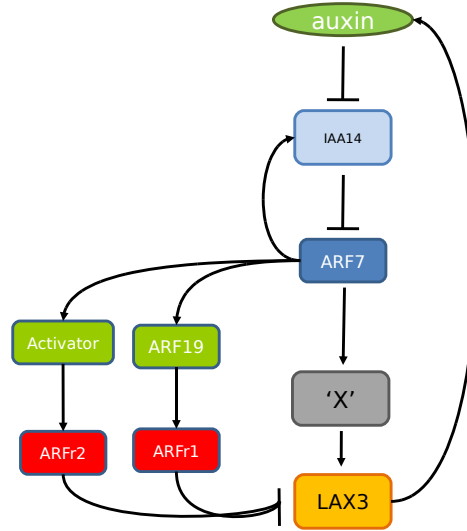


Figure 4.10: Gene network for the two repressor model. As well as a repressor activated by ARF19 which is activated by ARF7, there is also an ARF19 independent repressor which represses LAX3.

Two more unknown genes are expressed in the model which we refer to as $A2$ (activator 2) and $R2$ (repressor 2), which require the addition of two new differential equations to the model given by (4.8a)-(4.8i):

$$\frac{dA2}{dt} = \mu_{a2} \left(F_{tc} \left(\frac{K}{\theta_{a2a}(IAA + K)}, \frac{IAA}{\theta_{a2r}(IAA + K)}, \frac{ARF_r + r2}{\theta_{a2n}}, n_{a2} \right) - X \right), \quad (4.9a)$$

$$\frac{dR2}{dt} = \mu_{r2} \left(F_{tc} \left(\frac{K}{\theta_{r2a}(IAA + K)}, \frac{IAA}{\theta_{r2r}(IAA + K)}, \frac{ARF_r + R2}{\theta_{r2n}}, n_{r2} \right) - X \right). \quad (4.9b)$$

$A2$, and $R2$ are scaled with λ/μ for their respective genes. Also, the genes are now repressed by the total pool of repressors ARF_r and $R2$, and so ARF_r is replaced in the functions for transcription in equations (4.8b)-(4.8f) by $ARF_r + R2$. For example:

$$\frac{dLAX}{dt} = \mu_l \left(F_{tclax} \left(\frac{X}{\theta_{la}}, \frac{ARF_r + R2}{\theta_{ln}}, n_l, m \right) - LAX \right). \quad (4.9c)$$

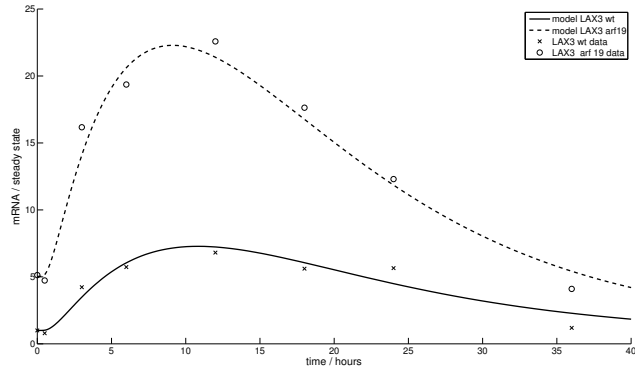
To simulate the *arf19* mutant $A19$ is fixed equal to zero as before. Using this model, and running the parameter fitting algorithm results in a parameter set which gives a good agreement between the model and both the wild type and *arf19* mutant LAX3 expression data (Figure 4.11(a)), and a reasonable agreement with the wild type IAA14 and ARF19 data (Figure 4.11(b)). For parameter values see Table 4.4. This parameter set then gives a prediction for the extra activator and both repressors as shown in Figure 4.11(c). Both repressors peak late in the time course to provide the characteristic expression profile for LAX3.

Table 4.4: Fitted parameter values for the two repressor model given by equations (4.8a)-(4.8i) and (4.9a)-(4.9b) to the wild type LAX3, IAA14 and ARF19, and *arf19* mutant qRT-PCR expression data shown in Figure 4.1. Co-operativity coefficients were constrained between 1 and 2, and binding parameters between 0.01 and 100.

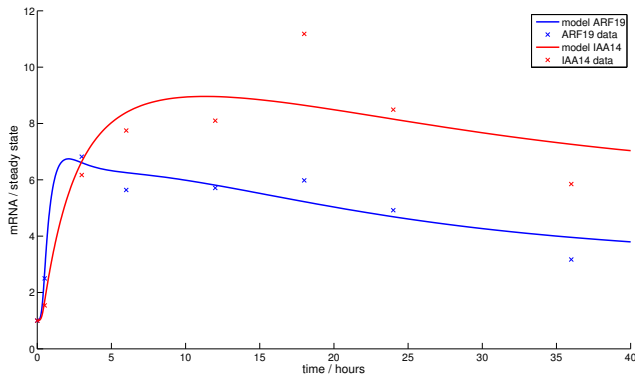
$\theta_{ia} = 0.0587$	$\theta_{ir} = 0.0687$	$\theta_{in} = 0.0621$	$n_i = 1.8962$	$P = 0.226$
$\theta_{xa} = 1.1539$	$\theta_{xr} = 0.1039$	$\theta_{xn} = 0.017$	$n_x = 1.9262$	$\mu_x = 0.8652$
$\theta_{la} = 0.173$	$n_l = 1.1849$	$\theta_{ln} = 0.0142$	$m = 1$	$\mu_l = 0.2818$
$\theta_{aa} = 0.6738$	$\theta_{ar} = 0.5919$	$\theta_{an} = 0.1799$	$n_a = 1.5735$	$\mu_a = 5.3638$
$\theta_{a2a} = 0.1489$	$\theta_{a2r} = 0.0542$	$\theta_{a2n} = 100$	$n_{a2} = 2$	$\mu_{a2} = 2.9999$
$\theta_{ra} = 0.5225$	$\theta_{rr} = 1.9578$	$\theta_{rn} = 2.9371$	$n_r = 1.1454$	$\mu_r = 0.0307$
$\theta_{r2a} = 0.1212$	$\theta_{r2r} = 21.8627$	$\theta_{r2n} = 2.7262$	$n_{r2} = 2$	$\mu_{r2} = 0.0431$
$Q = 0.0012$	$K = 0.0147$	$\eta = 9.3926$	$aux_0 = 0.0248$	$\alpha_{lax} = 0.2833$
$\alpha_x = 0.0042$	$\mu_{aux} = 3.076$			

Figure 4.12 shows time course predictions for intracellular auxin and Aux/IAA in the simulated wild type, and simulated *lax3* and *arf19* mutants. In the *lax3* mutant intracellular auxin increases smoothly to a higher concentration following an increase in the auxin signal. In the wild type, where LAX3 is present, auxin concentration is temporarily amplified due to added auxin influx transport, before LAX3 is repressed again and auxin begins to return toward the value seen in the *lax3* mutant. In the *arf19* mutant this temporary amplification is increased in magnitude due to a reduction in ARF19 dependent repressor causing an increase in LAX3 induction. These changes in intracellular auxin are reflected in the predictions for Aux/IAA, none of which show any significant recovery later on in the time course, since in all three simulations auxin remains high and so despite the positive feedback from increased Aux/IAA mRNA expression the Aux/IAA protein is still rapidly degraded.

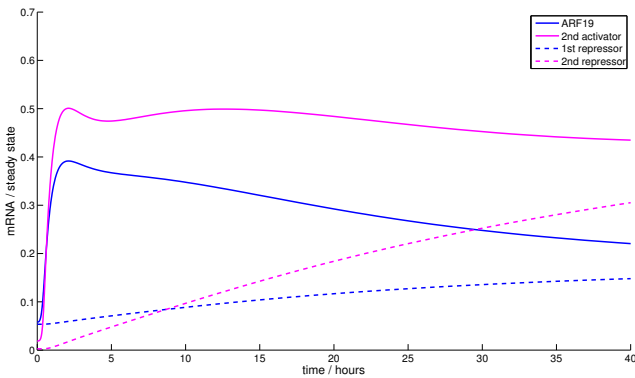
The lack of recovery of Aux/IAA over the latter half of the time course in the two repressor model is contrary to the experimental evidence given



(a) Model and qRT-PCR data for LAX3 in both wild type and *arf19* mutant. The parameters are fitted so that ARF19 and IAA14 w.t. expression data also matches the model.

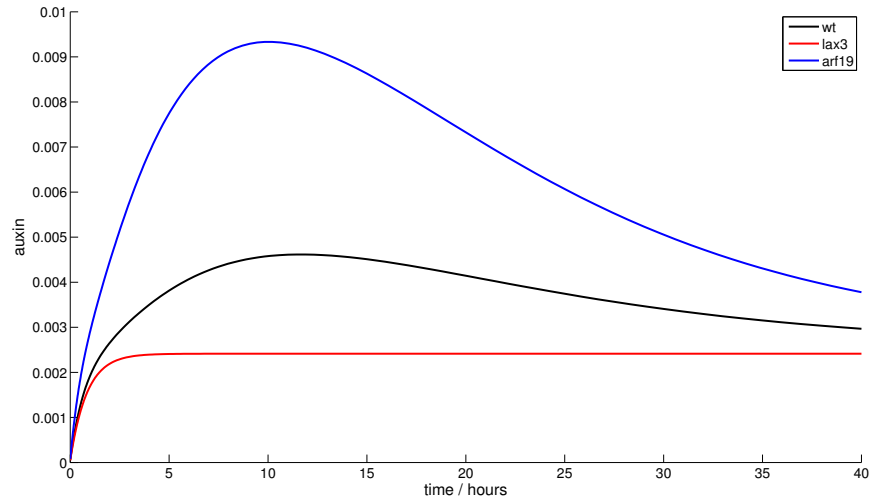


(b) Model and qRT-PCR data for ARF19 and IAA14 against time. The parameters are fitted so that LAX3 w.t. and *arf19* expression data also matches the model.

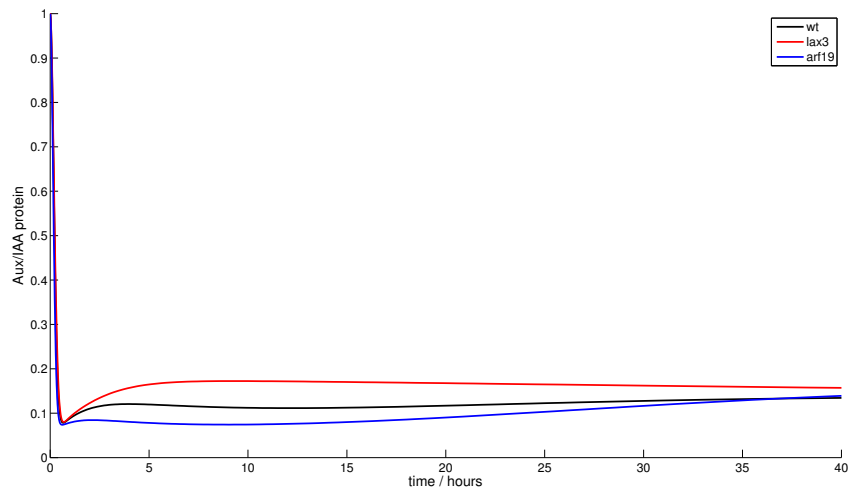


(c) Fitted ARF19, and predictions for the second activator and the two proposed repressors. The parameters are fitted so that LAX3 w.t. and *arf19*, and ARF19 and IAA14 w.t. expression data matches the model.

Figure 4.11: Fitted model wild type LAX3, ARF19, and IAA14 mRNA, and *arf19* mutant LAX3 fitted to the qRT-PCR expression data shown in Figure 4.1, plus predictions for the unknown activator and repressors using the two repressor model given by equations (4.8a)-(4.8i) and (4.9a)-(4.9b).



(a) Intracellular auxin against time, for simulated wild type, and *lax3* and *arf19* mutants.



(b) Aux/IAA protein against time, for simulated wild type, and *lax3* and *arf19* mutants.

Figure 4.12: Prediction of the two repressor model given by equations (4.8a)-(4.8i) and (4.9a)-(4.9b) for intracellular auxin (Figure 4.12(a)), and Aux/IAA protein (Figure 4.12(b)) against time for the ‘wild type’ (black lines), and *arf19* (blue lines) and *lax3* (red lines) mutant simulations, using the parameter values in Table 4.4).

by the 30 hour DII-VENUS data (Section 2.3), in which a recovery of DII-VENUS levels is seen between 10 and 20 hours post-auxin treatment. Because of this, while the two repressor model may be a reasonable model to simulate all the qRT-PCR data, the model prediction for intracellular auxin is not compatible with the DII-VENUS data, and suggests some form of auxin homeostasis is still needed.

4.4 ARF7-ARF19-LAX3 model with auxin homeostasis

In the model given by equations (2.21a)-(2.21g) auxin homeostasis is accounted for empirically by using decay of the exogenous auxin signal following initial treatment as defined by equation (2.19c). For clarity, the model is reproduced below:

$$\frac{d\text{auxin}}{dt} = \alpha_0 + \alpha_{tr}x\text{aux}(t) - \mu_{\text{aux}}\text{auxin}, \quad (4.10a)$$

$$\frac{d\text{IAA}}{dt} = \frac{-\eta\text{auxinIAA}}{QP + Q\text{auxin} + \text{auxinIAA}} + \text{IAA}_m, \quad (4.10b)$$

$$\frac{d\text{IAA}_m}{dt} = \mu_{i_m} \left(F_{tc} \left(\frac{K}{\theta_{ia}(\text{IAA} + K)}, \frac{\text{IAA}}{\theta_{ir}(\text{IAA} + K)}, n_i \right) - \text{IAA}_m \right), \quad (4.10c)$$

$$\frac{dX_m}{dt} = \mu_{x_m} \left(F_{tc} \left(\frac{K}{\theta_{xa}(\text{IAA} + K)}, \frac{\text{IAA}}{\theta_{xr}(\text{IAA} + K)}, n_x \right) - X_m \right), \quad (4.10d)$$

$$\frac{dX}{dt} = \mu_x(X_m - X), \quad (4.10e)$$

$$\frac{d\text{LAX}_m}{dt} = \mu_{l_m} \left(F_{tc} \left(\frac{X}{\theta_{la}}, 0, n_l \right) - \text{LAX}_m \right), \quad (4.10f)$$

$$\frac{d\text{LAX}}{dt} = \mu_l(\text{LAX}_m - \text{LAX}), \quad (4.10g)$$

$$x\text{aux}(t) = (\text{auxin}_{tr} - \text{auxin}_0)e^{-\mu_{tr}t}, \quad (4.10h)$$

where:

$$F_{tc}(\text{ACT}, \text{REP}, n) = \frac{(\text{ACT})^n}{1 + (\text{ACT})^n + (\text{REP})^n}. \quad (4.10i)$$

In this section, the above model is used with the parameters in Table 4.5, which are fitted to the IAA14 mRNA expression data in Figure 4.1 and the DII-VENUS data discussed in Section 2.3, as a basis for investigating ARF19 regulation and activity further.

In this model the only activator is ARF7 (substituted for by its quasi-steady state value), and so if we consider that ARF19 is also regulating LAX3 in some way, it may also be thought of as a model for the *arf19* knockout mutant plant. For this reason, we first fit the existing model to the *arf19* mutant LAX3 data, and then evaluate several models for both the expression of ARF19, and the regulation of LAX3 by ARF19, resulting in a final network model which best describes all the available data.

Table 4.5: Fitted model parameter values from Sections 2.3 and 2.4.1 used in the model variants investigated in Section 4.4.

K	μ_{im}	n_i	θ_{ai}	θ_{ri}	μ_{tr}	α_0
0.1011	0.0915	1.7432	0.1179	0.0021	0.264	2.250
P	Q	η	$auxin_0$	α_{tr}	μ_{aux}	λ_v
5.0006	0.6773	17.5942	0.2717	1.7252	8.2817	0.4229

4.4.1 Expression of LAX3 mRNA : *arf19* mutant

In using the model given by equations (4.10) to simulate the *arf19* mutant we must make some further assumptions. First, that basal auxin in the root is the same in both the wild type and *arf19*. Second, that the auxin response machinery (i.e. the degradation of Aux/IAA in response to auxin) works at the same rate and responsiveness in the two genotypes. Finally, based on the PCR expression data we assume that expression of the main repressor, IAA14, is similar in wild type and *arf19* (Figure 4.1).

With the fitted parameters determined previously, this leaves 8 parameters to be fitted to the LAX3 *arf19* expression data (Figure 4.13). Repeated application of the parameter fitting algorithm shows a consistent agreement with the data, and fitting the model with the *arf19* mutant data rather than the wild type results in a much better fit. The model also gives a range of predictions for tFX in the *arf19* mutant background. There is clear variation in the magnitude of the auxin response of these predicted expression profiles, but there seems to be some consistency in the relative timing in expression. The best fits for the parameter values μ_x , μ_{x_m} , θ_{ax} , θ_{rx} , n_x , μ_{l_m} , θ_{al} , n_l are given in Table 4.7 and used in subsequent models.

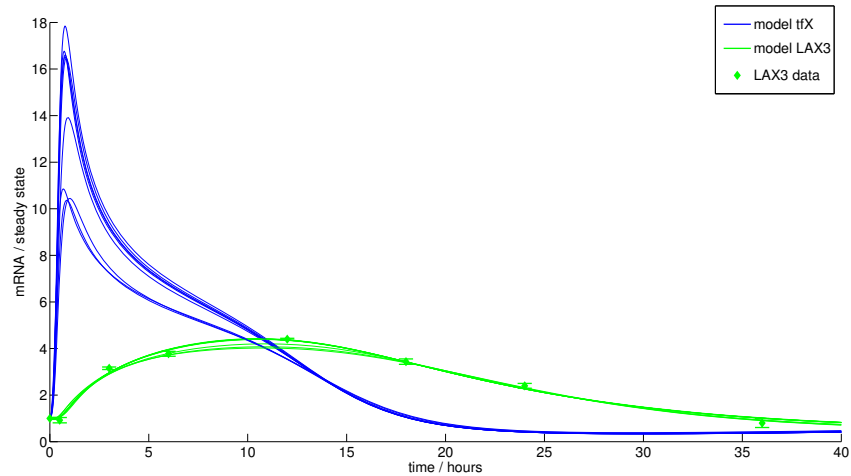


Figure 4.13: Set of model fits of the LAX3 mRNA expression to the LAX3 *arf19* mutant data shown in Figure 4.1, using the model given by equations (4.10a)-(4.10i). Since ARF19 is not included in the model but appears to affect LAX3 expression in the experimental data, the model can be thought of as being of the *arf19* mutant genotype. The set of predictions for tFX differ in magnitude but are consistent in timing.

4.4.2 ARF19 Regulation Models

The PCR data gives evidence that ARF19 is auxin responsive, and at least in part dependent on ARF7 (Figure 4.1). The precise regulation of ARF19 however is unknown. In this section we define four different models for ARF19 regulation (Figure 4.14) and compare the best fits of each to the data. In each case we assume that the downstream targets of ARF19 do not themselves feedback and regulate ARF19 directly or indirectly.

Model 1: ARF19 is a primary response of ARF7 (Figure 4.14, top left).

The simplest model for ARF19 regulation is direct activation by ARF7 only, and repression by ARF7-IAA14 dimers. This requires just one equation in addition to (4.10a)-(4.10i):

$$\frac{dARF19_m}{dt} = \mu_{a_m} \left(F_{tc} \left(\frac{K}{\theta_{aa}(IAA + K)}, \frac{IAA}{\theta_{ar}(IAA + K)}, n_a \right) - ARF19_m \right), \quad (4.11)$$

with four extra model parameters, μ_{a_m} , θ_{aa} , θ_{ra} , n_a .

Model 2: ARF19 is a primary response of ARF7, and also auto-activated (Figure 4.14, top right).

If ARF19 is activated by ARF19 as well as ARF7, we need an additional equation for ARF19 protein:

$$\frac{dARF19}{dt} = \mu_a(ARF19_m - ARF19). \quad (4.12a)$$

Due to the similarity of ARF7 and ARF19 we assume that the activatory power of both ARF7 and ARF19 is equal, and that any co-operativity effect acts on the combined pools of activators and repressors. We also assume that ARF19 can bind with IAA14 to form repressors in a similar way as ARF7 so that formation of ARF19-IAA14 dimers (AI_{19}) is governed by:

$$\frac{dAI_{19}}{dt} = k_a ARF19 IAA - k_d AI_{19}. \quad (4.12b)$$

If we use the same parameter values for k_a and k_d as for binding/unbinding of ARF7-IAA14 dimers we can also assume these processes are relatively rapid on our timescale of interest and make the steady-state approximation:

$$AI_{19}^* = \frac{ARF19 IAA}{K}$$

This means that, with the addition of two new binding parameters θ_{aa_2} and θ_{ar_2} , $ARF19$ and the approximation for AI_{19} are added into equation (4.11) as follows:

$$\frac{dARF19_m}{dt} = \mu_{a_m} \left(F_{tc} \left(\frac{K}{\theta_{aa}(IAA + K)} + \frac{ARF19}{\theta_{aa_2}}, \frac{IAA}{\theta_{ar}(IAA + K)} + \frac{ARF19 IAA}{\theta_{ar_2} K}, n_a \right) - ARF19_m \right). \quad (4.12c)$$

The complete model in nine variables is then defined by equations (4.10a)-(4.10i), (4.12a) and (4.12c).

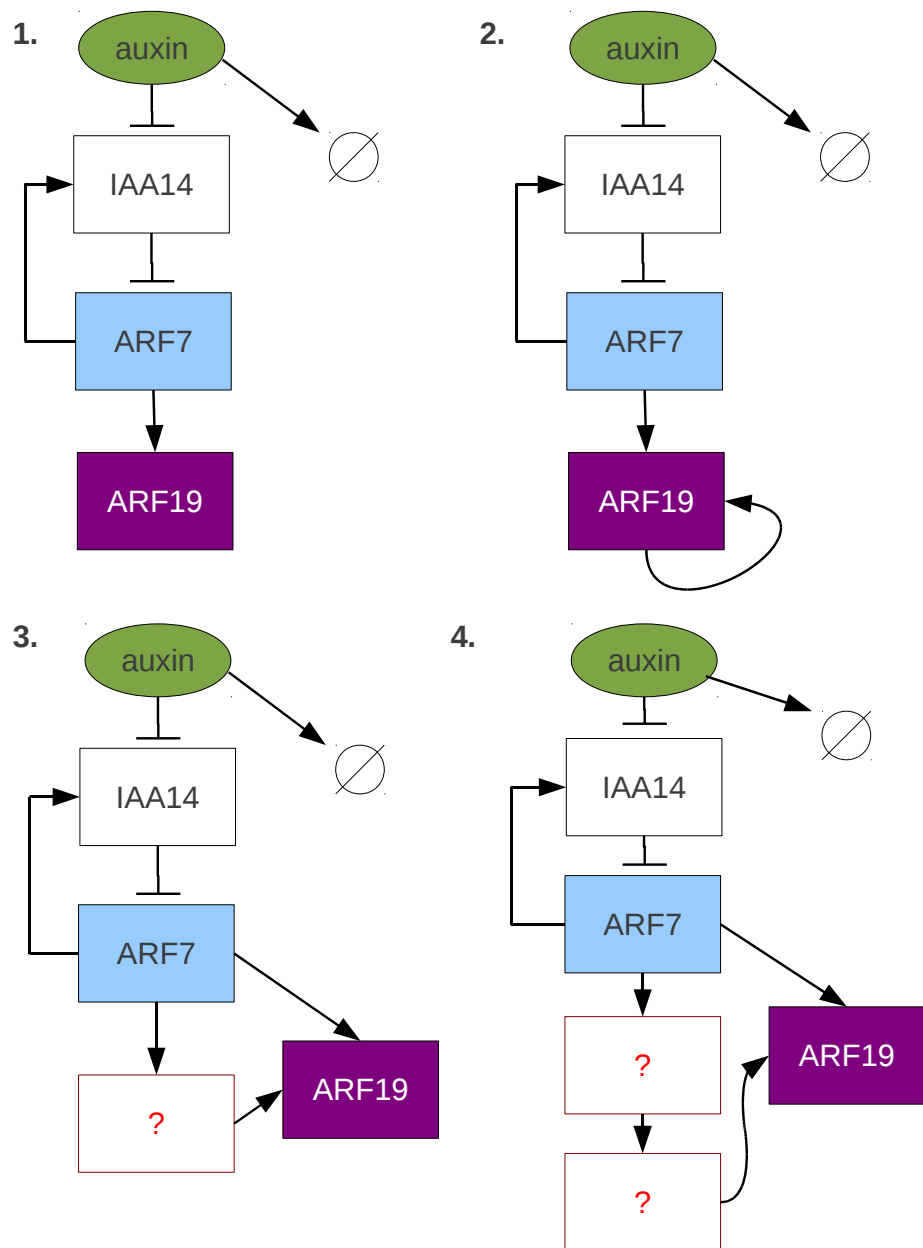


Figure 4.14: Hypothetical regulatory models for ARF19. 1). ARF19 is a primary response of ARF7 (Section 4.4.2, Model 1). 2). ARF is a primary response of ARF7 and is also auto-activated (Section 4.4.2, Model 2). 3). ARF19 is activated by both ARF7 and an unknown ARF7 primary response in a feed-forward loop (Section 4.4.2, Model 3). 4). ARF19 is activated by both ARF7 and an unknown ARF7 secondary response in a feed-forward loop (Section 4.4.2, Model 4).

Model 3: ARF19 is activated by a primary auxin response gene in addition to ARF7 (Figure 4.14, bottom left).

If instead of ARF19 there is an another ARF7 activated gene ($A1$) acting as an additional activator of ARF19 equation, we need two additional equations for $A1$ translation and transcription of its mRNA $A1_m$:

$$\frac{dA1_m}{dt} = \mu_{1_m} \left(F_{tc} \left(\frac{K}{\theta_{1a}(IAA + K)}, \frac{IAA}{\theta_{1r}(IAA + K)}, n_1 \right) - A1_m \right), \quad (4.13a)$$

$$\frac{dA1}{dt} = \mu_1(A1_m - A1), \quad (4.13b)$$

with five new parameters μ_{1_m} , θ_{1a} , θ_{1r} , n_1 and μ_1 . We have ARF7 and $A1$ activating, and ARF7-IAA14 dimers repressing ARF19 so that (4.12c) becomes:

$$\frac{dARF19_m}{dt} = \mu_{a_m} \left(F_{tc} \left(\frac{K}{\theta_{aa}(IAA + K)} + \frac{A1}{\theta_{aa2}}, \frac{IAA}{\theta_{ar}(IAA + K)} \right) - ARF19_m, n_a \right), \quad (4.13c)$$

so that the model in eleven variables is defined by equations (4.10a)-(4.10i), (4.12a) and (4.13a)-(4.13c).

Model 4: ARF19 is activated by a secondary auxin response gene in addition to ARF7 (Figure 4.14, bottom right).

Finally, if the additional activator of ARF19 is a secondary auxin response gene we have the extra two equations for $A2$ protein, whose mRNA $A2_m$ is directly activated by $A1$:

$$\frac{dA2_m}{dt} = \mu_{2_m} \left(F_{tc} \left(\frac{A1}{\theta_{2a}}, 0, n_2 \right) - A2_m \right), \quad (4.14a)$$

$$\frac{dA2}{dt} = \mu_2(A2_m - A2), \quad (4.14b)$$

with the four new parameters μ_{2_m} , θ_{2a} , n_2 and μ_2 . Substituting $A2$ for $A1$ in (4.13c) so that:

$$\frac{dARF19_m}{dt} = \mu_{a_m} \left(F_{tc} \left(\frac{K}{\theta_{aa}(IAA + K)} + \frac{A2}{\theta_{aa2}}, \frac{IAA}{\theta_{ar}(IAA + K)} \right) - ARF19_m, n_a \right), \quad (4.14c)$$

and the model in thirteen variables is defined by (4.10a)-(4.10i), (4.12a), (4.13a)-(4.13b) and (4.14a)-(4.14c).

Parameter fitting

The parameter fitting algorithm was used to find the best fit of each of the four ARF19 regulation models with the wild type ARF19 qRT-PCR mRNA expression data shown in Figure 4.1. The resulting model predictions are shown in Figure 4.15.

The simplest model (model 1) with ARF7 alone activating ARF19 does not fit the data well. It can match the late timepoints (as shown here) or

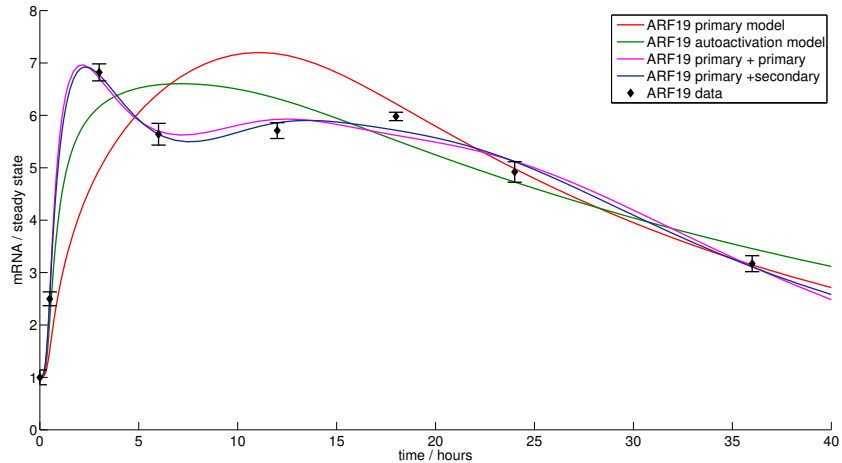


Figure 4.15: Best fit found to the ARF19 mRNA expression data for each of the four hypothetical regulatory models in Figure 4.14. The best fits are found with an additional transcription factor downstream of ARF7 activating with ARF7 in a feed-forward loop.

the early timepoints, but not both with the same parameter set. Having ARF19 feedback and activate itself (model 2) improves the fit slightly, but the constraints of the model still limit the expression profile to a single peak. Adding an ARF19 independent TF to the regulation model (models 3 and 4) allows for an expression profile with two maxima, and a much better fit to the expression data. Model 4, where the activator is a secondary auxin response gives a marginally better fit than model 3. While these models need experimental validation before any biological conclusions can be drawn, especially considering the possibility that adding extra variables and parameters to the overall model may lead to over fitting the data, either model 3 or 4 can be used to simulate the expression profile of ARF19 mRNA and test the effect of ARF19 on potential downstream targets, as in Section 4.4.3.

4.4.3 Regulation of LAX3 by ARF19

The previous models have simulated expression of IAA14 (Section 2.4.1) using fitted parameters from DII-VENUS quantification data (Section 2.3), simulated expression of LAX3 mRNA in the *arf19* mutant background using the data in Figure 4.1 (Section 4.4.1), and simulated expression of ARF19 mRNA using the same data set (Section 4.4.2). To bring these sub-models together we need to combine them and model the apparent negative effect of ARF19 on LAX3 expression. We consider four main possibilities:

1. ARF19 can act as a repressor of LAX3 directly
2. ARF19 activates a repressor of LAX3 (ARF_r)
3. ARF19 acts as a repressor of tfX directly
4. ARF19 activates a repressor of tfX (ARF_r)

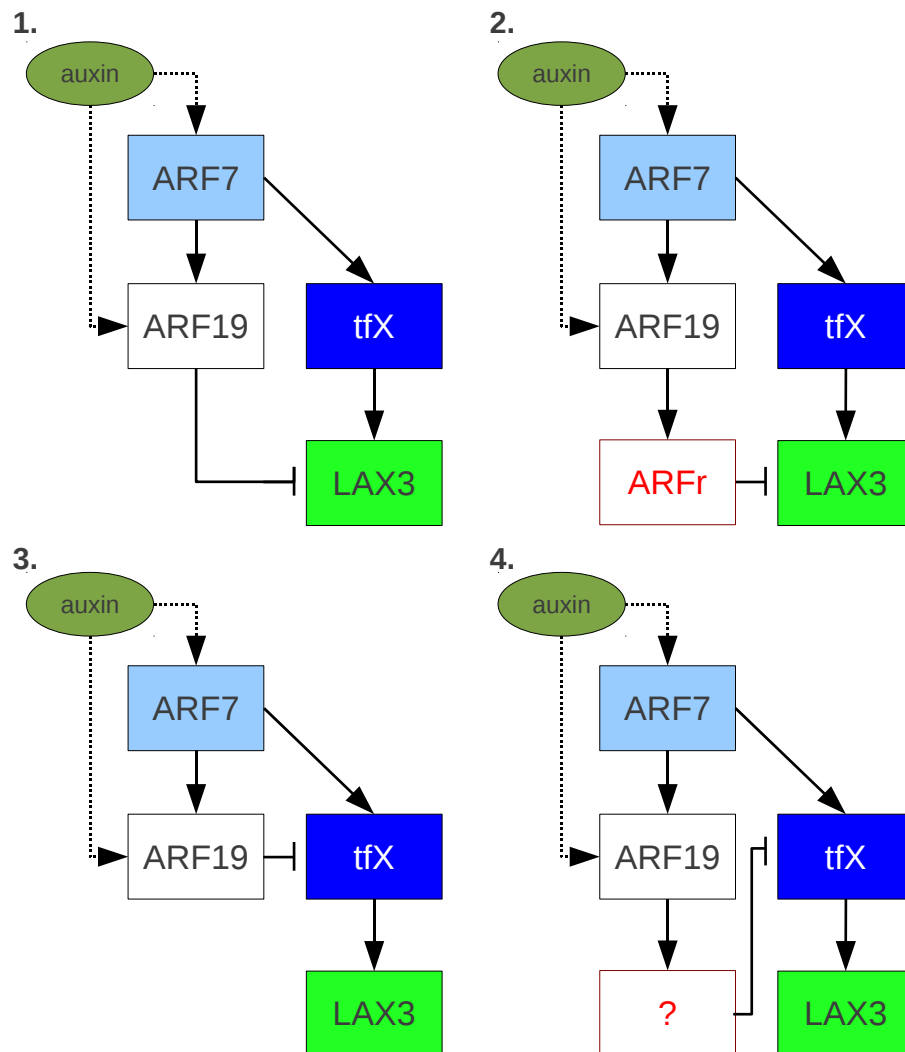


Figure 4.16: Hypothetical gene regulatory networks extending the networks shown in Figure 4.14 by including different possibilities for the transcriptional repression of LAX3 by ARF19, as described in Section 4.4.3. 1) ARF19 acts as a repressor of LAX3 by binding the LAX3 promoter directly. 2) ARF19 activates in intermediate repressor, *ARFr*, which binds and represses the LAX3 promoter. 3) ARF19 acts as a repressor of LAX3 by binding the tfX promoter directly, preventing LAX3 from being activated. 4) 2) ARF19 activates in intermediate repressor, *ARFr*, which binds and represses the tfX promoter, preventing LAX3 from being activated. In each case, ARF7 and ARF19 activates their downstream targets in response to auxin, and among ARF7 targets are ARF19 and tfX.

Gene network diagrams of these four sub-networks are shown in Figure 4.16. In each case, the models will have ARF7 and ARF19 activating their downstream targets in response to auxin, following the degradation of IAA14 which we assume binds to both of the ARFs. While the level of ARF7 remains constant, ARF19 is itself activated by ARF7 as discussed in Section 4.4.2. *tfX* is activated by ARF7 in an auxin responsive manner. Each model is a variant of Model 4 defined in Section 4.4.2 by equations (4.10a)-(4.10i), (4.12a), (4.13a)-(4.13b) and (4.14a)-(4.14c). Each model variant is defined in turn before attempting to fit each model to the LAX3 wild type expression data.

ARF19 can act as a repressor of LAX3 directly

While ARF19 has previously been considered a transcriptional activator (Guilfoyle and Hagen 2007), the simplest model for ARF19 regulation of LAX3 has it repressing LAX3 directly by competing with the same binding site as *tfX*. When ARF19 is bound to the LAX3 promoter in this model, transcription is blocked. To include this repression we amend equation (4.10f) as follows:

$$\frac{dLAX_m}{dt} = \mu_l \left(F_{tc} \left(\frac{X}{\theta_{la}}, \frac{ARF19}{\theta_{lr}}, n_l \right) - LAX_m \right). \quad (4.15)$$

Previously, the following function for transcription (equation (4.10i)) was used:

$$F_{tc}(ACT, REP, n) = \frac{(ACT)^n}{1 + (ACT)^n + (REP)^n}.$$

This is based on activator and repressor competing for the same binding site. If instead, there are two binding sites we use the following function for transcription:

$$F_{tc2}(ACT, REP, n) = \left(\frac{ACT^n}{1 + ACT^n} \right) \left(\frac{1}{1 + REP^n} \right). \quad (4.16)$$

In this case the repressor can bind the LAX3 promoter and repress transcriptional activity even when the activator *tfX* is bound to the other site, and we consider both cases using F_{tc} and F_{tc2} in the parameter fitting for each different variation of the model given below.

Using model 3 or 4 from section for ARF19 mRNA, the profile of ARF19 protein relative to mRNA is free to vary according to a single parameter value μ_a (ARF19 protein turnover rate). With the fitted parameter values for model 4 from Section 4.4.2, Figure 4.17 shows two possible profiles of ARF19 protein in relation to the the fitted mRNA profile for different μ_a . Salmon et al. (2008) gives an experimentally determined half-life of 3.7 hours for ARF1, which corresponds to a value of around $\mu_a = 0.20$. If we use this value as an estimate for ARF19 turnover this results in a relatively slow accumulation of ARF19 protein over the time course, peaking between 15 and 20 hours following auxin treatment. A faster turnover rate results in a profile of ARF19 which more closely matches the mRNA profile. If ARF19 is a direct repressor of LAX3, μ_a is a key model parameter.

ARF19 activates a repressor of LAX3

Here there is an intermediate TF between ARF19, which is modelled by the following two additional equations:

$$\frac{dARFr_m}{dt} = \mu_{r_m} \left(F_{tc} \left(\frac{ARF19}{\theta_{ra}}, \frac{ARF19 IAA}{\theta_{rr}K}, n_r \right) - ARFr_m \right), \quad (4.17a)$$

$$\frac{dARFr}{dt} = \mu_r(ARFr_m - ARFr). \quad (4.17b)$$

Again we use the quasi-steady approximation for ARF19-IAA14 repressor dimers. $ARFr$ is then substituted directly for $ARF19$ in equation (4.15), replacing it with the following equation:

$$\frac{dLAX_m}{dt} = \mu_l \left(F_{tc} \left(\frac{X}{\theta_{la}}, \frac{ARFr}{\theta_{lr}}, n_l \right) - LAX_m \right). \quad (4.17c)$$

The dynamic nature of ARF19 means this gene can be activated in two ways. At low auxin $ARFr$ is repressed by ARF19-IAA14 dimers and so is immediately auxin responsive when auxin is increased and Aux/IAA degraded. In addition though, any increase in ARF19, as seen following auxin treatment, will also tend to increase transcriptional activity. The relative import of these two processes is governed by one parameter value in particular, θ_{rr} , which is the affinity of ARF19-IAA14 dimers to the $ARFr$ promoter (Figure 4.17). For low θ_{rr} the dimers are more likely to bind the promoter, and so the gene is more responsive to the initial auxin treatment. With a higher value for θ_{rr} $ARFr$ expression is less sensitive to the auxin signal, and more responsive to the auxin induced increase in ARF19. Because of this the expression profile of $ARFr$ is sensitive to two key parameters, θ_{rr} and the ARF19 turnover rate, μ_a (Figure 4.17).

ARF19 acts as a repressor of tFX directly

If ARF19 directly targets tFX for repression equation (4.17c) reverts to equation (4.10f), and equation (4.10d) is replaced by:

$$\frac{dX_m}{dt} = \mu_{x_m} \left(F_{tc} \left(\frac{K}{\theta_{xa}(IAA + K)}, \frac{IAA}{\theta_{xr}(IAA + K)} + \frac{ARF19}{\theta_{xr2}}, n_x \right) - X_m \right). \quad (4.18)$$

ARF19 activates a repressor of tFX

In the final model $ARFr$ represses tFX rather than $ARF19$, and so $ARFr$ is substituted for $ARF19$ in equation (4.18):

$$\frac{dX_m}{dt} = \mu_{x_m} \left(F_{tc} \left(\frac{K}{\theta_{xa}(IAA + K)}, \frac{IAA}{\theta_{xr}(IAA + K)} + \frac{ARFr}{\theta_{xr2}}, n_x \right) - X_m \right). \quad (4.19)$$

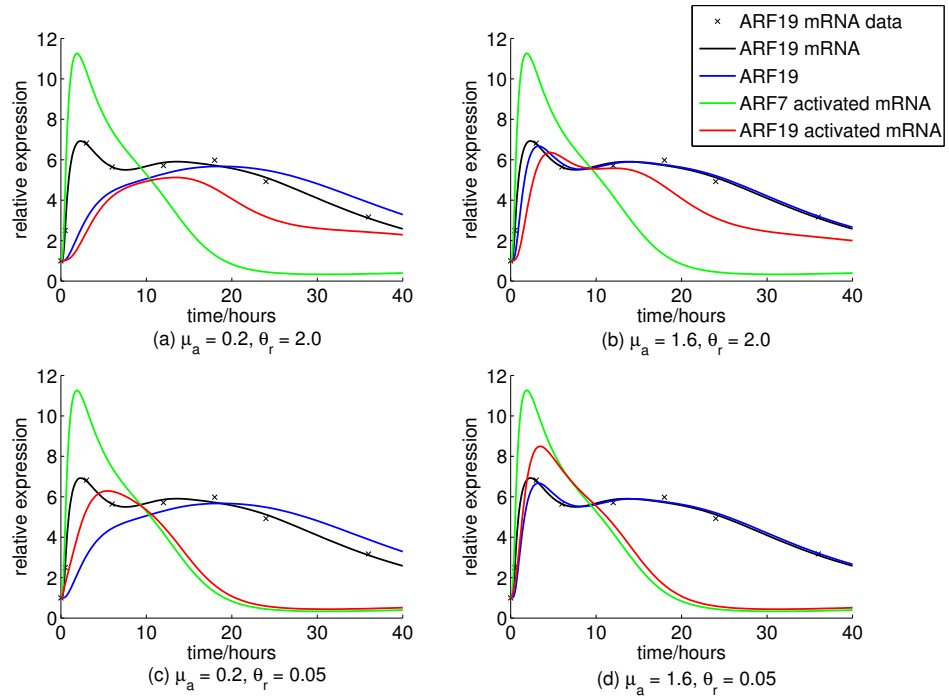


Figure 4.17: Example expression profiles of ARF19 protein, a direct target of ARF19, and a direct target of ARF7 using a range of parameters, using the fitted model of ARF19 mRNA expression (for data, see Figure 4.1). While both the ARF19 and ARF7 genes are auxin responsive due to Aux/IAA degradation, the ARF19 gene has additional feedback from upregulation of ARF19 itself. The parameter θ_r (the affinity of ARF19-IAA14 dimers to the promoter of the target gene) affects the balance between these two activatory components, while the parameter μ_a affect the timing of ARF19 translation, and so the timing of the target gene. In general the ARF19 activated gene shows a broader range of expression profiles than can the ARF7 activated gene. (a) Low μ_a , high θ_r . (b) High μ_a , high θ_r . (c) Low μ_a , low θ_r . (d) High μ_a , low θ_r .

Table 4.6: Best ‘fit value’ found using the hybrid genetic algorithm and directional local minima search for each model variation outlined in Section 4.4.3. The fit value is defined as the sum of squared differences between model and data points, relative to the sum of squared differences between the mean of data points and each data point.

Target	Repressor	Competitive Binding?	Fit value
LAX3	ARF19	yes	0.391
LAX3	ARF19	no	0.441
LAX3	ARFr	yes	0.295
LAX3	ARFr	no	0.083
tfX	ARF19	yes	0.564
tfX	ARF19	no	0.571
tfX	ARFr	yes	0.329
tfX	ARFr	no	0.387

Parameter Fitting

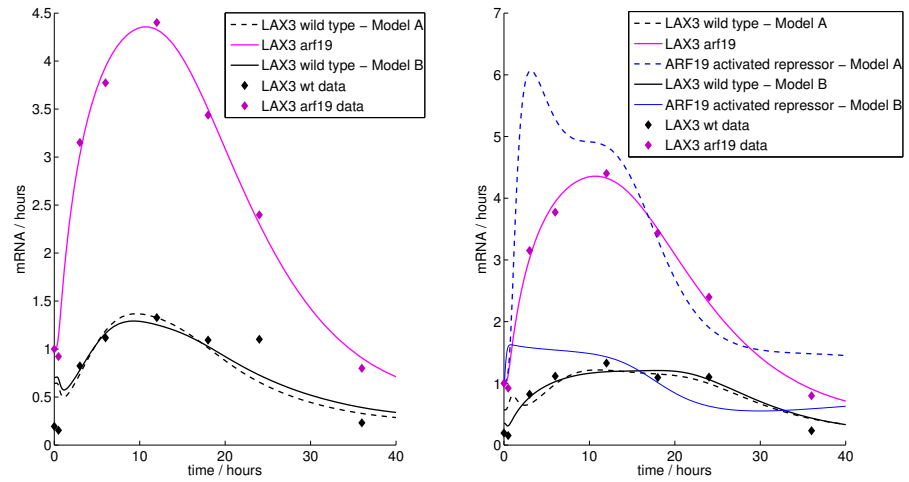
To evaluate the different LAX3 regulatory models each was fitted with the wild type LAX3 expression data shown in Figure 4.1, re-normalised relative to the basal expression in the *arf19* mutant. The parameter values fitted in Section 4.4.1 and shown in Table 4.7 were used so that the *arf19* mutant data would always fit the model, with the differences being in the wild type simulation relative to this. The best fits found for each of the model permutations are shown in Figure 4.18.

In general there is a greater difference in the profiles of the fits between the four main types (based on target and source of repression), than there is between model subtypes (based on the number of binding sites). The poorest fits appear for the model where ARF19 represses tfX directly, while the best fit is for the model where a direct target of ARF19 (ARF_r) represses LAX3, with non-competitive binding with tfX on the LAX3 promoter. It is difficult to differentiate between the other models. Most fit the data for at least part of the time course, but do not match the basal expression of the wild type relative to *arf19*. The goodness of fit is compared quantitatively, by giving the value of the optimisation function for each case in Table 4.6. The final set of fitted parameters is given in Table 4.7.

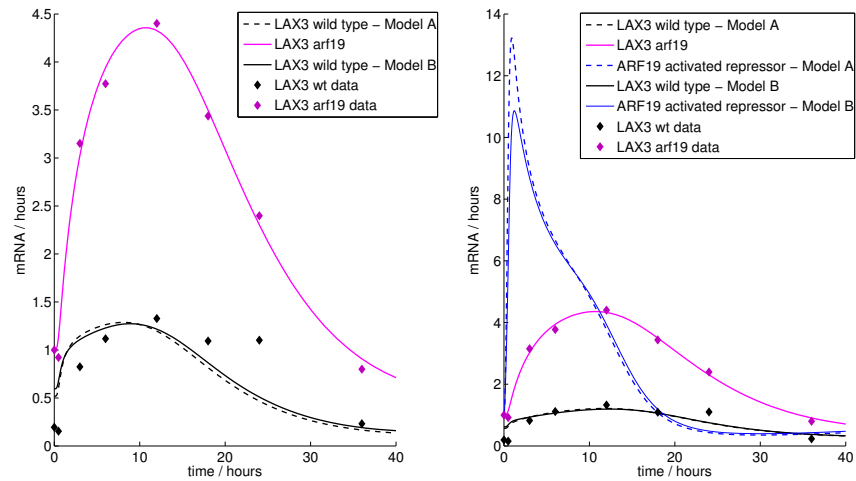
4.5 Discussion and Conclusions

Simple ARF7-ARF19 model

The experimental evidence points to ARF19 being partly induced by ARF7, and so being auxin responsive. If ARF19 targets the same genes as ARF7, it is expected intuitively that adding it to the model system will result in greater expression of genes following an auxin signal. The mathematical modelling of the ARF7-ARF19 system demonstrates that this is the case, provided the parameter values relating to binding of gene promoters, mRNA polymerase, and Aux/IAA repressors are shared between ARF7 and ARF19.



(a) Fits with the data of the model where ARF19 represses LAX3 by binding the promoter directly (left), and the model where ARF19 activates a repressor which then binds LAX3 (right).



(b) Fits with the data of the model where ARF19 represses LAX3 by binding the tfX promoter directly (left), and the model where ARF19 activates a repressor which binds the tfX promoter, effectively repressing LAX3 (right).

Figure 4.18: Best fits of the LAX3 mRNA expression data for each of the hypothetical LAX3 regulatory models. The wild type LAX3 mRNA expression data from Figure 4.1 is renormalised and plotted relative to the *arf19* mutant. Model A: a repressor competes with the activator for the same binding site. Model B: the repressor is able to bind regardless of the presence of an activator (separate binding site). The previously determined parameters for IAA14 and ARF19 expression were used. The closest fit is found using the model where ARF19 activates a repressor of LAX3 which binds to a separate binding site from tfX.

If this is the case it can be shown that the steady state expression of the auxin responsive genes will always be greater with both an inducible ARF19 and a stable ARF7 in the model than in the model with just ARF7.

As well as being induced by ARF7 and activating genes, ARF19 is able to bind with Aux/IAs and form genetic repressors (Fukaki et al. 2005). Since we assume this binding and unbinding occurs at a much more rapid rate than transcription, translation or mRNA/protein degradation, the model predicts a separation of timescales so that increased expression of ARF19 activators is rapidly offset by the formation of more dimer repressors as a proportion of the new ARFs bind with the remaining pool of Aux/IAs. For a stable auxin signal there is constant turnover of Aux/IAA as it is degraded by auxin and replaced by translation of induced mRNA, giving an equilibrium value for the amount of Aux/IAA present. The additional presence of the ARF19-Aux/IAA dimers formed should not change this equilibrium value. It is important to note that this is based on the assumption that when bound to an ARF, the Aux/IAs are unable to be targeted for degradation by TIR1 and auxin. Because of the corresponding increase of repressors along with the induction of ARF19 activators we are able to show that in the absence of any co-operativity effects the ARF7-ARF19 model can be reasonably approximated by the ARF7 only model. Again, this is assuming ARF19 and ARF7 share the same targets and parameter values for all their interactions.

The mRNA expression data shows increased LAX3 expression in the *arf19* mutant, relative to the wild type expression (Figure 4.1). By changing key parameters in the model it is shown that the presence of ARF19 may act as a repressor, by interfering with the activity of ARF7. In particular, parameter values relating to three sets of biological reactions were identified as being important. First, a relatively low rate of unbinding between ARF19 and IAA14 may result in an increased proportion of ARF-Aux/IAA repressors in the wild type compared to *arf19*, limiting transcription rates. Second, a lower rate of transcription ARF19 occurring when it is bound to the promoter, compared to that when ARF7 is bound would reduce transcription due to the competition for binding sites. Finally, an increased affinity of ARF19-IAA14 dimers to gene promoters would again reduce transcription via competition for binding sites with the activators, free ARF7 and ARF19. Figure 4.6 shows that any of these mechanisms may be enough to explain the difference in LAX3 between *arf19* and wild type. However, the relative fold changes in parameter values are so large in each case that the necessary differences are likely to be biologically unrealistic. However, it remains possible that in certain biological contexts ARF19 may lose its activatory power and act as a repressor simply by competing for binding sites with ARF7 or other ARFs.

ARF19-repressor model

A second hypothesis that may explain the observed increase in LAX3 expression in the *arf19* mutant is the repression of LAX3 by an repressor specifically activated by ARF19 and not ARF7. A good candidate for this is a negative or repressing ARF, which may bind the binding site on the

LAX3 promoter, as well as repressing the primary auxin response genes. If this is the case, we see that it is possible for the repressor to cause the observed temporal peak then repression seen in the qRT-PCR expression profile, which was previously modelled by the inclusion of an auxin conjugation mechanism, or by exponentially degrading the initial auxin signal. Without the conjugation mechanism, when ARF19 is removed from the model to simulate the *arf19* mutant, the downregulation is removed and the auxin responsive genes remain switched on. Because of this, a single repressor is insufficient to explain the observed data.

There are many negative ARFs, and if we suppose one or more is also induced by an ARF19 independent, but ARF7 dependent pathway, then this results in a two repressor model (Figure 4.10). Here, when ARF19 is knocked out of the model, rather than a complete removal of repressor, there is instead a quantitative decrease. This means that repressor is still induced by auxin causing the characteristic expression profile, but the repression is reduced so that there is consistently greater mRNA abundance, as observed in the data. Relative timing of the genes is important, as we have LAX3 regulated positively by a primary auxin responsive gene (unknown *tfX*), and negatively by a secondary gene, resulting in the required expression profile.

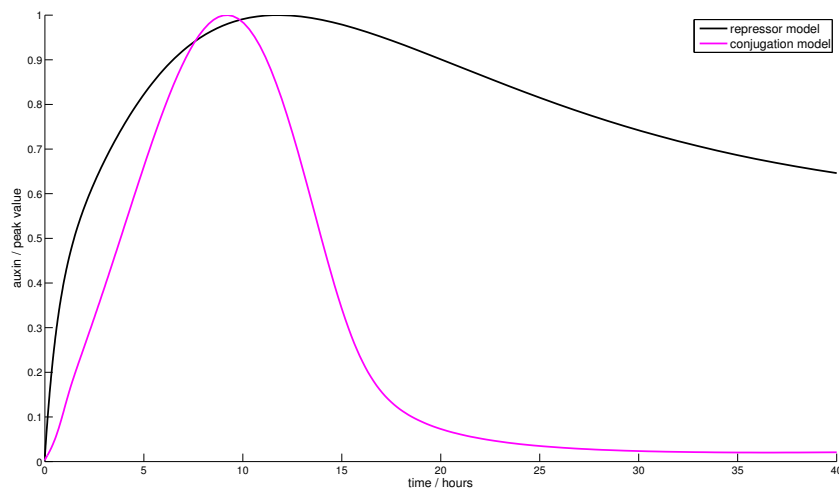


Figure 4.19: Comparison of auxin against time for the repressor model and the auxin conjugation model. In both cases the parameters are fitted so that the model matches the wild type LAX3 expression data.

A key prediction is given by the amount of auxin within the cell over time (Figure 4.19). In the repressor model an increase in auxin signal outside the cell eventually results in a higher steady state auxin within the cell, with a temporary amplification due to LAX3 expression. In other words, while the expression of auxin responsive genes is transient due to the induction of repressor(s), auxin remains high within the cell. By way of contrast, the auxin conjugation model described previously predicts that auxin within the cell will peak due to LAX3 expression, but the expression of the conjugating enzyme GH3 will have a homeostatic effect, and the extra auxin will

eventually be removed from the cell. A similar, but opposite effect is seen

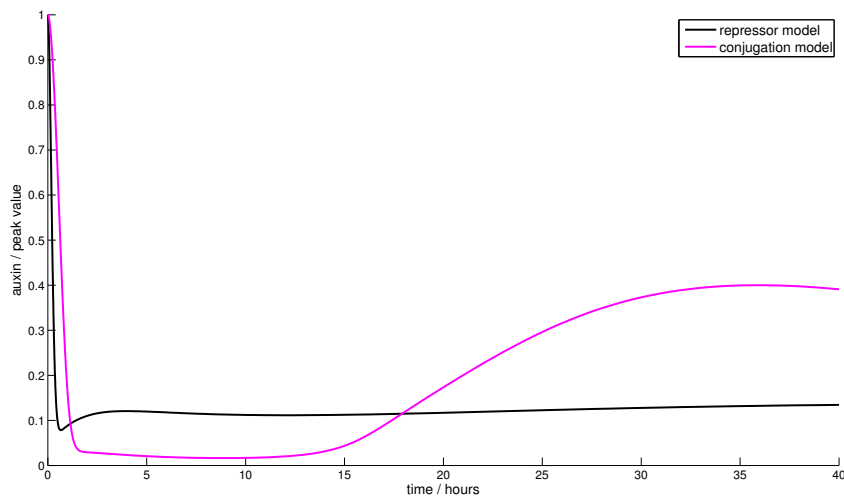


Figure 4.20: Comparison of Aux/IAA against time for the repressor model and the auxin conjugation model. In both cases the parameters are fitted so that the model matches the wild type LAX3 expression data.

when comparing Aux/IAA against time for the two models (Figure 4.20). In both models, Aux/IAA is rapidly degraded following the auxin signal, but while in the repressor model Aux/IAA remains low, in the conjugation model Aux/IAA begins to accumulate once more towards the end of the time course.

In summary, for a stable extracellular auxin signal, the repressor model predicts auxin inside the cell will increase and remain high while gene expression (other than that of the repressors themselves) is eventually switched off, while the conjugation model predicts that late expression of an auxin conjugating gene will eventually remove auxin from the signalling pool causing down-regulation of auxin responsive genes. As shown by the 30 hour DII-VENUS time course data (section 2.3), the observed recovery in DII-VENUS between 10 and 20 hours post-auxin treatment indicates that a recovery in Aux/IAA levels would also be expected, as auxin is gradually removed from the system. Because of this, while the two repressor model can simulate the mRNA expression data, it is not consistent with the observations from the DII-VENUS experiments, which show that some form of auxin homeostasis is still needed.

ARF7-ARF19-LAX3 model with auxin homeostasis

A key qualitative observation from the initial LAX3 model (section 2.2.3) is that given the initial assumption that the exogenous auxin signal from the experimental medium remains constant, and that auxin remains high within the cell, any auxin responsive genes that are upregulated will remain upregulated for as long as the auxin signal persists (Figure 2.5). However, if we instead assume that the auxin signal decays exponentially, the model

can qualitatively match the experimentally observed qRT-PCR expression profiles of upregulation followed by downregulation as shown in Figure 4.1. By combining this signal decay mechanism with an ARF19 dependent LAX3 repression mechanism it is possible to fit the mRNA expression data in both the wild type, and *arf19* mutant plants.

In section 2.3 DII-VENUS was fitted to a model over a 30 hour time course using an exponential decay in the initial auxin signal, giving us a model for auxin within root cells over time following auxin treatment. While feedback from LAX3 may play a role in the overall level of auxin, and will affect auxin distribution spatially, if we have a good model for the auxin input to the system we can omit the LAX3 feedback when trying to fit the model quantitatively with data. This allows us to fit sub-models step by step starting with IAA14 (section 2.4), then fitting LAX3 in the *arf19* mutant (section 4.4.1), then ARF19 itself (section 4.4.2), then finally LAX3 in the wild type (section 4.4.3). This parameter fitting enabled us to select a regulatory model for LAX3, with the best model fit found with an ARF19 activated repressor acting on the LAX3 promoter at a separate site to tfX. The final model network is summarised in Figure 4.21. In addition to the ARF19 activated repressor (ARF_r), there are two further unknown model components, the additional activators of ARF19 ($A1$ and $A2$). The addition of $A2$ may not be necessary, but is included here for completeness. The final model equations are as follows:

$$\frac{d\text{auxin}}{dt} = \alpha_0 + \alpha_{tr}x\text{aux}(t) - \mu_{aux}\text{auxin}, \quad (4.20a)$$

$$\frac{dIAA}{dt} = \frac{-\eta\text{auxin}IAA}{QP + Q\text{auxin} + \text{auxin}IAA} + IAA_m, \quad (4.20b)$$

$$\frac{dIAA_m}{dt} = \mu_{i_m}(F_{tc} \left(\frac{K}{\theta_{ia}(IAA + K)}, \frac{IAA}{\theta_{ir}(IAA + K)}, n_i \right) - IAA_m), \quad (4.20c)$$

$$\frac{dX_m}{dt} = \mu_{x_m} \left(F_{tc} \left(\frac{K}{\theta_{xa}(IAA + K)}, \frac{IAA}{\theta_{xr}(IAA + K)}, n_x \right) - X_m \right), \quad (4.20d)$$

$$\frac{dX}{dt} = \mu_x(X_m - X), \quad (4.20e)$$

$$\frac{dLAX_m}{dt} = \mu_l \left(F_{tc} \left(\frac{X}{\theta_{la}}, \frac{ARFr}{\theta_{lr}}, n_l \right) - LAX_m \right), \quad (4.20f)$$

$$\frac{dLAX}{dt} = \mu_l(LAX_m - LAX), \quad (4.20g)$$

$$\frac{dARF19}{dt} = \mu_a(ARF19_m - ARF19), \quad (4.20h)$$

$$\frac{dARF19_m}{dt} = \mu_{a_m} \left(F_{tc} \left(\frac{K}{\theta_{aa}(IAA + K)} + \frac{A2}{\theta_{aa2}}, \frac{IAA}{\theta_{ar}(IAA + K)} \right) - ARF19_m, n_a \right), \quad (4.20i)$$

$$\frac{dA1_m}{dt} = \mu_{1_m} \left(F_{tc} \left(\frac{K}{\theta_{1a}(IAA + K)}, \frac{IAA}{\theta_{1r}(IAA + K)}, n_1 \right) - A1_m \right), \quad (4.20j)$$

$$\frac{dA1}{dt} = \mu_1(A1_m - A1), \quad (4.20k)$$

$$\frac{dA2_m}{dt} = \mu_{2_m} \left(F_{tc} \left(\frac{A1}{\theta_{2a}}, 0, n_2 \right) - A2_m \right), \quad (4.20l)$$

$$\frac{dA2}{dt} = \mu_2(A2_m - A2), \quad (4.20m)$$

$$\frac{dARFr_m}{dt} = \mu_{r_m} \left(F_{tc} \left(\frac{ARF19}{\theta_{ra}}, \frac{ARF19 IAA}{\theta_{rr}K}, n_r \right) - ARFr_m \right), \quad (4.20n)$$

$$\frac{dARFr}{dt} = \mu_r(ARFr_m - ARFr), \quad (4.20o)$$

$$x\text{aux}(t) = (\text{auxin}_{tr} - \text{auxin}_0)e^{-\mu_{tr}t}, \quad (4.20p)$$

where:

$$F_{tc}(ACT, REP, n) = \frac{(ACT)^n}{1 + (ACT)^n + (REP)^n}. \quad (4.20q)$$

Since the fitting was done relative to the *arf19* basal expression, if we plot the model relative to the wild type using the same parameter values there will be poor agreement between model and data. This is because the model fits the fold-change response relative to a fixed point (either wild type or *arf19* expression at time zero). Changing the fixed point will change

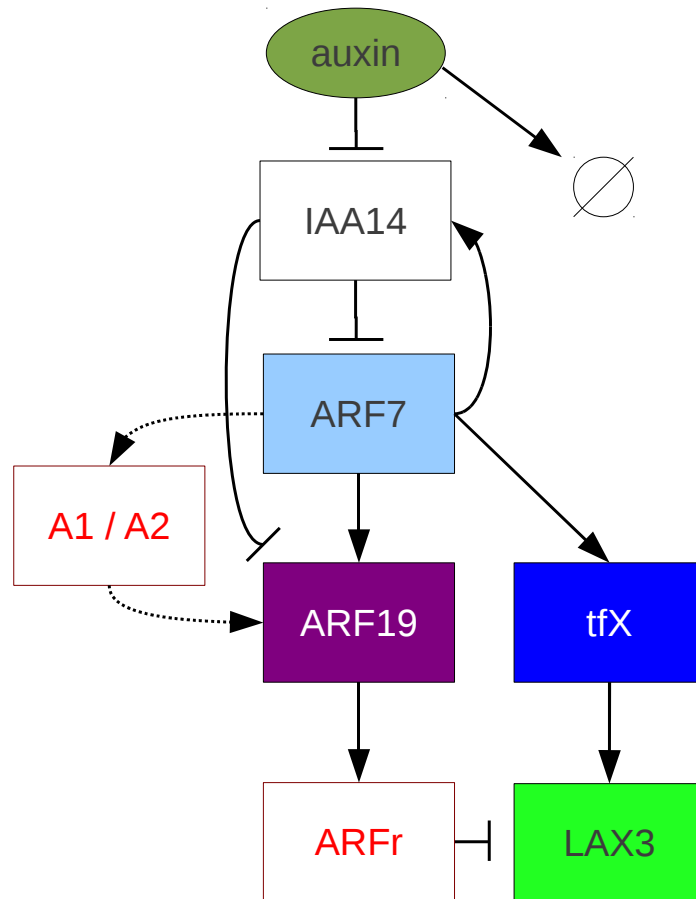


Figure 4.21: Final model network based on the best fitting model variant with the IAA14 wild type expression data, LAX3 wild type and *arf19* expression data (Figure 4.1), and DII-VENUS time course fluorescence data (section 2.3). Auxin accelerates the degradation of IAA14, which frees the repression of ARF7 and ARF19. ARF7 then activates ARF19, IAA14, tfX and A1, which may activate an additional activator of ARF19, A2, or itself activate ARF19 directly. tfX activates LAX3, while ARF19 activates a repressor of LAX3, ARFr. Auxin homeostasis is provided by an exponential degradation of the exogenous auxin signal. The model is defined by equations (4.20a)-(4.20q).

the magnitude of the response. If we refit all parameters directly affecting LAX3 expression using the chosen model with the data renormalised to wild type basal expression, we have a final set of model predictions (Figure 4.22) and parameter values. Table 4.7 shows the fitted values for case when the LAX3 data is normalised to the basal expression in the *arf19* mutant and the case when the LAX3 data is normalised to the basal expression in the wild type. Most of the fitted values remain similar, only θ_{xr} , the affinity of ARF7-IAA14 dimers to the tfX promoter, and θ_{la} the affinity of tfX to the LAX3 promoter are changed. This may be expected since these are the key parameters in determining the magnitude of the response of LAX3 mRNA.

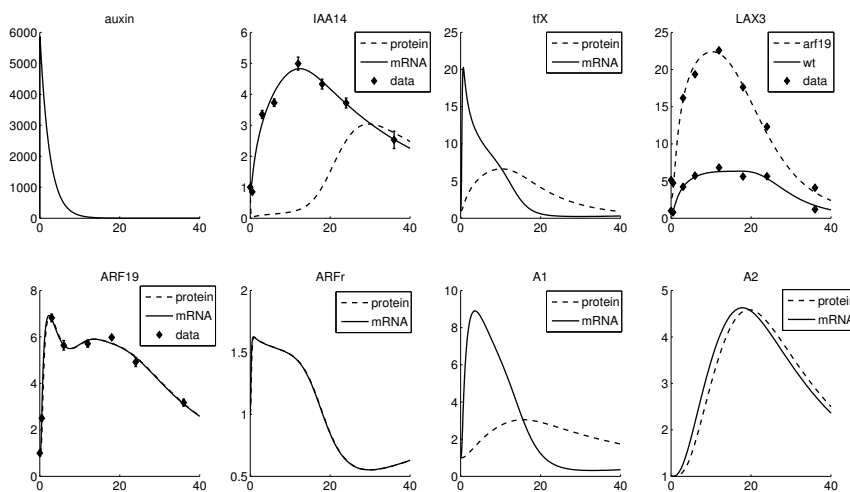


Figure 4.22: Best fit of model *arf19* and wild type model LAX3 mRNA relative to the wild type using the data shown in Figure 4.1. Also shown are the fits to the IAA14 and ARF19 mRNA data using the same set of parameter values (Table 4.7), and predictions for the other model components.

The final model includes a secondary auxin response gene (*A2* activated by *A1*) feeding back on ARF19 expression, as this provided the best fit to data. However, although constraints were placed on the parameter values, as with any model increasing the number of parameters and the complexity of the model will in general increase the likelihood of fitting the data more exactly. With limited data, what appears to be a trend may just be biological noise and in actual fact a simpler model may better describe the biological reality. The inclusion of extra model components and parameters can lead to over fitting. Nonetheless, the fitted model for ARF19 expression was useful to investigate the effect of ARF19 activity.

Similarly, including a extra repressor between ARF19 and LAX3 also adds more parameters to the model. Figure 4.17 shows how in general an extra gene activated by ARF19 may show a wider variety of expression profiles than ARF7 depending on parameter values, giving more freedom to fit the data. In this case however, there is more biological justification to including the additional step due to ARF19's predicted function as a tran-

Table 4.7: Fitted parameter values for final network model given by equations (4.20a)-(4.20q) to the wild type IAA14, ARF19 and LAX3 mRNA and *arf19* mutant LAX3 mRNA data shown in Figure 4.1. In the column headed *arf19*, both wild type and *arf19* LAX3 expression data are normalised to the basal expression in the *arf19* mutant before fitting and, in the column headed wild type, both wild type and *arf19* LAX3 expression data are normalised to the basal expression in the wild type in before fitting.

Parameter	<i>arf19</i>	wild type	Parameter	<i>arf19</i>	wild type
Q	47.6939	47.6939	μ_1	0.0319	0.0319
P	1.5723	1.5723	μ_{1m}	0.4474	0.4474
K	0.0015	0.0015	n_1	1.0906	1.0906
μ_{aux}	100	100	θ_{1a}	0.2871	0.2871
μ_{tr}	0.42	0.42	θ_{1r}	7.2674	7.2674
$xaux_0$	1	1	μ_2	0.6476	0.6476
$xaux_{tr}$	6000	6000	μ_{2m}	0.4784	0.4784
η	16.667	16.667	n_2	0.6956	0.6956
β	8.3623	8.3623	θ_{2a}	0.3978	0.3978
μ_{i_m}	0.034	0.034	μ_a	5.7685	5.9802
n_i	1.2949	1.2949	μ_{a_m}	0.5823	0.5823
θ_{ia}	0.4058	0.4058	n_a	1.3803	1.3803
θ_{ir}	9.0334	9.0334	θ_{aa}	1.62	1.62
μ_x	0.0928	0.0914	θ_{ar}	0.5355	0.5355
μ_{x_m}	11.3317	12.0142	θ_{aa_2}	0.6265	0.6265
n_x	1.0591	1.3444	μ_r	10.0	10.3263
θ_{xa}	0.1327	0.1152	μ_{r_m}	9.319	9.3338
θ_{xr}	4.8924	22.8311	n_r	1.0	1.0
μ_l	0.6805	0.4631	θ_{ra}	0.000013	0.000013
μ_{l_m}	10.7725	11.2889	θ_{rr}	0.0022	0.0022
n_l	1.2797	1.5265			
θ_{la}	0.3013	0.1639			
θ_{lr}	0.3225	0.3361			
θ_{n_r}	1.0	1.0			

scriptional activator (Guilfoyle and Hagen 2007), though it always possible this may change following new experimental discoveries.

Fitting the 30 hour experimental DII-VENUS time course profile allows us to make a prediction for cellular auxin, and so Aux/IAA. This in turn allows us to predict the behaviour of other ARF7 / IAA14 responsive genes. Using the parameter fitting algorithm with the simple ARF7 only model gives a fit value with the LAX3 wild type data of $f = 0.0724$, and gives a prediction for the expression profile of the unknown activator of LAX3 (tfX). With the more complex model including ARF19 mediated repression the fit improves to $f = 0.0287$. In addition, the more complex model demonstrates how ARF19 activated genes may show more complex expression profiles than genes activated by ARF7 only, and also gives a prediction for tfX, along with the ARF19 activated repressor. Embedding these gene network models into a multi-cellular context will give predictions for the spatial distribution for key auxin regulated genes during lateral root emergence.

Chapter 5

Tissue Scale Models of Lateral Root Emergence

5.1 Introduction

5.1.1 Introduction and Biological Background

In the conceptual model published by Swarup et al. (2008) the all or nothing expression pattern of LAX3-YFP is thought to be amplified by positive feedback via increased auxin influx due to LAX3 expression in the specific cells over lateral root primordia. In Chapter 2 it is shown using an ODE model that this all-or-nothing expression pattern may be a result of bistability caused by the LAX3 positive feedback, where small changes in local auxin may result in large changes in gene expression in neighbouring cells. To test this possibility directly in a spatial context, a multiscale model is required, which will combine a tissue scale model of auxin transport and diffusion with a gene network scale model of mRNA transcription and protein translation in each individual cell (Chapter 6). Before this though, in this chapter we formulate a model of auxin transport and diffusion in a realistic cellular structure relevant to the spatial positioning of LAX3 expression during lateral root emergence.

For simplicity, we initially consider a two-dimensional (2-D) cross-section of the mature root in the plane perpendicular to the direction of primary root growth, i.e. the plane in which the cell layers pericycle, endodermis, cortex and epidermis are arranged as concentric rings of cells around the central vascular tissue (Figure 5.1). The reasons for using this particular 2-D cross-section are as follows. Firstly, if a 2-D representation must be used, the radial cross-section is best able to show both the relative position of cells in both the direction of growth of the LRP and the relative position of cells within cell layers. Since the spatial structure of the mature root is mostly conserved in the direction of primary root growth, each cell in the radial cross-section can be considered a file of cells relative to the position of the xylem pole pericycle (XPP) cells where new LRP are initiated. Secondly, the cells are longer in the direction of primary root growth than in the other two dimensions, and so the difference in physical distance between the centre of adjacent cell files is generally much smaller than the distance between

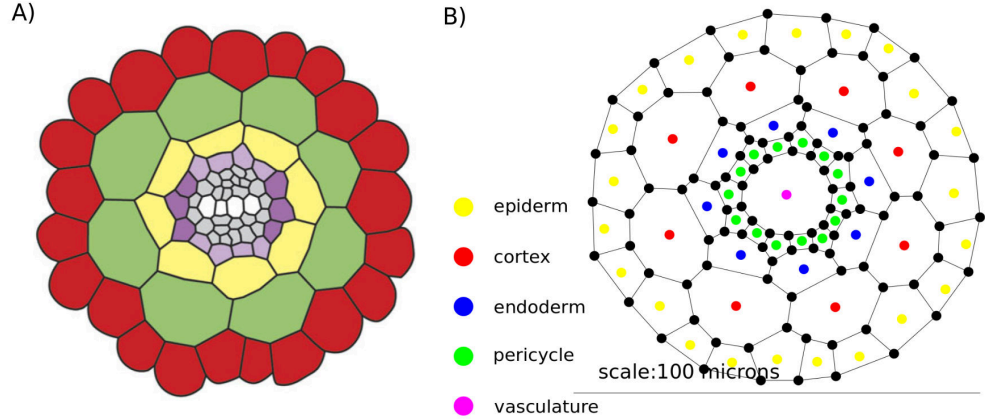


Figure 5.1: A) Original diagram of root cross section from Peret et al. (2009b), and B) version captured manually in the .svg format for use in Open Alea. The key allows cell types to be assigned automatically, and the scale bar converts lengths of walls and areas of cells from *pixels* and *pixels*² to μm and μm^2 .

individual cells, and also the surface area in contact (via the apoplast) between cells in adjacent cell files will be greater than that between cells within a single file. If we keep the assumption that auxin concentration within each cell is spatially uniform, the flux between cells ought to be greatest where the shared surface area is greatest, and so if we simulate the developing primordia as a fixed auxin source in the XPP the spread of auxin ought to be more significant in the radial direction, in comparison to that in the longitudinal direction.

After formulating the most general case of the auxin transport and diffusion model (Section 5.1.2) based on the existing model published by Perrine-Walker et al. (2010) and Band and King (2011) and detailing the software implementation (Section 5.1.3), we look first at the case where auxin is distributed within the root via diffusion only, to compare steady state auxin between neighbouring cells, and in particular how these differences are affected by the rate of intracellular auxin turnover (Section 5.2). Also investigated with the diffusion only model are the affect of adding movement of auxin within the apoplast, in addition to movement between cell and apoplast (and vice versa), and the affect of simulating the Casparian strip, which we assume to prevent all movement of auxin in specific cell walls in the endodermis (Section 5.2.2). To compare the different models we use simulations of two different scenarios, firstly treatment with exogenous auxin, and then simulation of an LRP as producing a strong auxin source from a single XPP cell.

Following the diffusion only model, we look at the affect of adding the expression of auxin influx and efflux carriers to the tissue (Section 5.3). Initially we use a fixed distribution of carriers (Section 5.3.1), before simulating dynamic expression of auxin transporters using a threshold model (Section 5.3.2). In this model, once auxin within a cell passes a prescribed value, influx or efflux carriers are ‘switched on’ in the model and feed back on auxin fluxes. In both cases we may assign the localisation of the carri-

ers to specific cell walls of the cell, but in the case of influx carriers (e.g. LAX3) we assume the carriers are localised to all cell walls of an expressing cell equally.

If a threshold model is also used to simulate the expression of a cell wall remodelling enzyme (CWR) such as polygalacturonase (PG), provided the threshold for the switching on of PG relative to that for LAX3 is high enough, then the LAX3 threshold model shows that without the amplification of cellular auxin due to increased influx via LAX3, that PG will not be expressed. If the expression of CWRs is dependent on the amplification of auxin by LAX3 expression, this provides a link between LAX3 expression and lateral root emergence. Again, the model shows that a relatively high intracellular auxin turnover rate is a key parameter, this time in the power of LAX3 to raise auxin levels relative to neighbouring cells that do not express LAX3.

5.1.2 Model Formulation

The auxin transport model used in the following sections is based on that developed by Band and King (2011) and Perrine-Walker et al. (2010). In this model auxin is present in either a cellular space or in the apoplastic space between two adjoining cells sharing the same cell wall. As described above we use a 2-dimensional cross section to represent the tissue, with each cell consisting of a polygon, each side of which represents a cell membrane. Where two cell membranes meet, as is the case for all but the outer cell membranes, there is an apoplastic space between the two adjacent cells (Figure 5.2). Initially we assume auxin only moves from apoplast to cell or from cell to apoplast, via either diffusion or active transport, with no movement between adjacent apoplastic compartments (this latter possibility is considered in Section 5.2.2). With a single class of influx carriers denoted by *LAX*, and a single class of efflux carriers denoted by *PIN*, the initial model is defined as follows:

$$\frac{d\text{auxin}_i}{dt} = V_i^{-1} \left(\sum_{n \in W_i} S_{i,n} (J_{n,i}^+ \text{apo}_{i,n} - J_{i,n}^- \text{auxin}_i) \right) - \mu_{\text{aux}} \text{auxin}_i + \alpha_i, \quad (5.1a)$$

$$\frac{d\text{apo}_{j,k}}{dt} = \lambda^{-1} (J_{j,k}^- \text{auxin}_j + J_{k,j}^- \text{auxin}_k - (J_{j,k}^+ + J_{k,j}^+) \text{apo}_{j,k}), \quad (5.1b)$$

where:

$$J_{p,q}^+ = A_1 P_{iaah} + A_2 P_{lax} LAX_{q,p} + A_3 P_{pin} PIN_{q,p}, \quad (5.1c)$$

$$J_{p,q}^- = B_1 P_{iaah} + B_2 P_{lax} LAX_{p,q} + B_3 P_{pin} PIN_{p,q}. \quad (5.1d)$$

Each cell in the model tissue is numbered, and so auxin_i denotes the concentration of auxin in cell i , and $\text{apo}_{i,j}$ denotes the concentration of auxin in the apoplast adjoining cells i and j . In each case $\text{apo}_{i,j} = \text{apo}_{j,i}$, $\text{apo}_{i,i} = 0$, and, for non-adjoining cells k and l , $\text{apo}_{k,l} = 0$. The cell walls on the exterior surface of the root are denoted $\text{apo}_{i,0}$, where i is the index of the cell with the external wall. The volume (represented in 2-D by an area) of cell i is denoted V_i , and the surface area (represented in 2-D by a length)

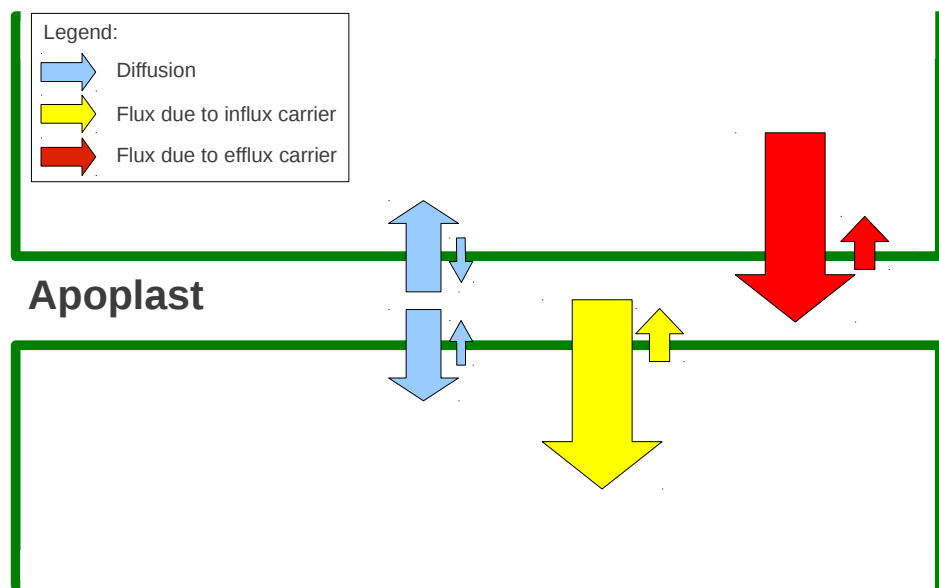


Figure 5.2: Schematic representation of the spatial arrangement of the boundary between two cells in the tissue structure, showing an example of the fluxes present (not to scale). To move from one cell to another, auxin must pass through the apoplastic space. This can occur via diffusion or active transport, with the rate of diffusion from the apoplast into the cell much greater than vice versa. The main direction of flux due to active transport depends on whether the cell has influx or efflux carriers present at the membrane. In this instance the upper cell is expressing an efflux carrier, and the lower an influx carrier, but any other configuration is possible within the model framework.

between adjoining cells i and j is denoted by $S_{i,j}$. As with the apoplastic concentrations, $S_{i,j} = S_{j,i}$, $S_{i,i} = 0$, and for all non-adjoining cells k and l $S_{k,l} = 0$. The surface area of the externally facing wall of an outer cell i is denoted $S_{i,0}$. λ denotes a uniform estimated width for the apoplast.

For each cell, i , there is an associated set of neighbouring cells denoted W_i , and so the overall auxin flux for each cell is calculated by summing the flux between the cell and each neighbouring apoplast. $J_{i,j}^+$ represents the flux from the apoplast between cell i and j into cell j , and $J_{i,j}^-$ represents the flux from cell i into the apoplast between cell i and j . Note that, since there may be different transporter configurations on the membranes either side of the apoplast dividing cell i and cell j , $J_{i,j}^+$ and $J_{j,i}^+$ are defined differently, as are $J_{i,j}^-$ and $J_{j,i}^-$. In addition, $J_{i,i}^+ = 0$, $J_{i,i}^- = 0$, and for non-adjoining cells k and l $J_{k,l}^+ = J_{l,k}^+ = J_{k,l}^- = J_{l,k}^- = 0$.

Each individual flux is calculated by summing the diffusive, influx and efflux components. The diffusive component is proportional to the passive permeability P_{iaah} , the influx component is proportional to the influx permeability P_{iax} and the amount of influx carrier present in cell i at the membrane facing cell j (denoted $LAX_{i,j}$), and the efflux component is proportional to the efflux permeability P_{pin} and the amount of efflux carrier present in cell i at the membrane facing cell j (denoted $PIN_{i,j}$). It is important to note that, in general, $PIN_{i,j}$ is not equal to $PIN_{j,i}$, and $LAX_{i,j}$ is not equal to $LAX_{j,i}$. The differences in flux depending on the direction of auxin movement, either from apoplast to cell or vice versa, is reflected by the proportionality constants A_1 , A_2 , A_3 , B_1 , B_2 and B_3 . Estimated values for these constants are derived in Perrine-Walker et al. (2010). In the case of diffusion the rate of movement across cell membranes from apoplast into cells is significantly greater than movement from cell to apoplast, and so $A_1 > B_1$. For active transport, for both efflux and influx there is movement in both directions across the cell membrane, but for efflux carriers movement from cell to apoplast is favoured so that $B_3 > A_3$, while for influx carriers movement from apoplast to cell is favoured so that $A_2 > B_2$.

The final processes within each cell are the intracellular degradation of auxin at rate μ_{aux} , and possible production within any cell i at rate α_i . Estimates of these two parameters were not found in the literature, and so investigating their effect on model behaviour is a key component of the work. In addition to cellular production and degradation, the presence of an exogenous auxin source is represented by a fixed concentration of auxin, $auxin_0 = \omega$ which can enter the apoplastic compartments on the outer surface of the root, so that:

$$\frac{dapo_{i,0}}{dt} = \lambda^{-1}(J_{i,0}^- auxin_i + J_{0,i}^- \omega - (J_{i,0}^+ + J_{0,j}^+) apo_{i,0}). \quad (5.2)$$

A summary of the default parameter values used is given in Table 5.1, along with a brief description, and source from where the estimate was taken, where appropriate.

Table 5.1: Estimated default parameter values for the auxin transport model given by 5.1a-5.1d, with a brief description and source for the estimate where appropriate. Source references: [1] Perrine-Walker et al. (2010), [2] Band and King (2011), [3] Kramer et al. (2007)

Parameter	Estimate	Description	Source
P_{iaah}	$2016 \mu m \text{ hour}^{-1}$	Passive membrane permeability	[1], [2]
P_{iax}	$2016 \mu m \text{ hour}^{-1}$	Membrane permeability due to LAX3 or AUX1 influx carriers	[1], [2]
P_{pin}	$1008 \mu m \text{ hour}^{-1}$	Membrane permeability due to PIN efflux carriers	[1], [2]
A_1	0.24	Apoplastic proportion of protonated auxin	[1], [2]
A_2	3.57	Relative influx from LAX3 or AUX1 carriers	[1], [2]
A_3	0.034	Relative influx from PIN carriers	[1], [2]
B_1	0.004	Cytoplasmic proportion of protonated auxin	[1], [2]
B_2	0.045	Relative efflux from LAX3 or AUX1 carriers	[1], [2]
B_3	4.68	Relative efflux from PIN carriers	[1], [2]
D_{cw}	$115200^2 \mu m \text{ hour}^{-1}$	Diffusion coefficient in the apoplast	[3]
λ	$0.2 \mu m$	Apoplast thickness	[3]
μ_{aux}	100 hour^{-1}	Intracellular auxin turnover rate	
α_i	$0 \mu M \text{ hour}^{-1}$	Intracellular auxin production rate	
α_p	$100 \mu M \text{ hour}^{-1}$	Intracellular auxin production rate in primordium	

5.1.3 Implementation

To represent mathematically the geometry and topology of the root cell structure, the open source software package OpenAlea was used (<http://openalea.gforge.inria.fr>). This includes a set of Python modules which can take a vector graphic image file produced in a specific .svg format and convert it to a ‘topomesh’ structure (Figure 5.3), within which ODE models can be run. In this case, the image file was traced manually from a diagram of a radial cross section of an *Arabidopsis* root (Peret et al. 2009b), using the open source software package Inkscape (www.inkscape.org) (Figure 5.1). A radial cross section was selected initially, as this would allow for movement of auxin between cells within the same layer, as well between different layers. However, the OpenAlea framework allows for any 2D cell structure to be represented in this way, and so once a model is formulated and implemented in one tissue, it is straightforward to apply it to another. The scale of the visual representation of the tissue is included in the .svg file and used to calculate realistic cell wall lengths and 2-D areas.

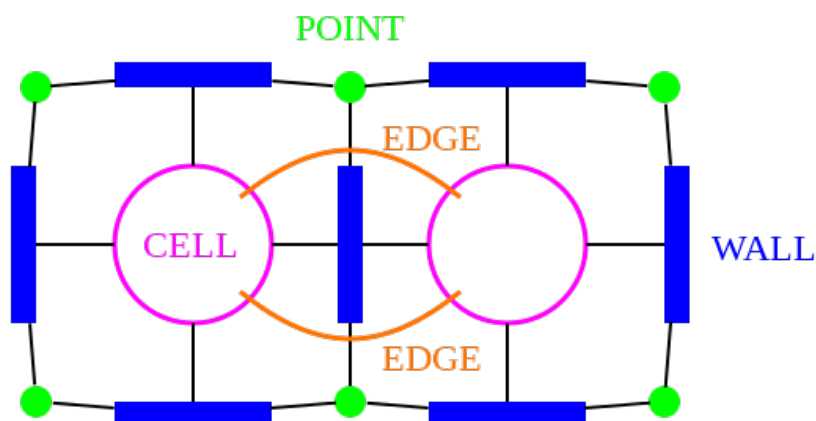


Figure 5.3: Visual description of the topomesh data structure. Walls are described by pairs of points, which in turn represent the cell geometry. Each wall separates two cells, which each have an associated set of points and walls. The relationship between cells is also recorded as a directed graph, with cells as nodes, and walls as edges.

The topomesh data construct consists of points, walls, and cells. The points constitute the geometric description of the vertices in the tissue, and each point is associated with a number of walls leading from it. The walls represent the separation between the cells, and each has two points describing its physical location and length, and the two cells which it separates. The cells have a set of associated points and walls, which describe both its topological relationship to other cells, and its physical area. In addition to this, the software creates a directed graph of the relationship between cells

in the tissue, with the nodes representing the cell centres, and the edges representing cell membranes. Using a combination of the graph and the topomesh data structure allows for physical properties, such as auxin or LAX3, to be assigned to each cell, or in the case of auxin to walls, and the evolution of each over time can be governed by the ODE models developed here. The ODEs are solved using the ‘odeint’ function in the Python package Scipy (<http://www.scipy.org/>). The resulting simulations are visualised using the viewer within OpenAlea or the python package Matplotlib (<http://matplotlib.sourceforge.net/>), and numerical solutions can be output to a text file. The whole simulation exists as a python object referred to as a Tissue Database, which contains the spatial and topological structure, as well as all the user-defined properties assigned to the tissue.

5.2 Auxin distribution: diffusion only

In this section we investigate the effect of diffusion alone on the distribution of auxin within the tissue, with either treatment with exogenous auxin (Section 5.2.1), or an auxin source from a developing lateral root primordium (Section 5.2.3). In Section 5.2.2 we investigate adding the further movement of auxin between apoplastic compartments via diffusion, and also the blocking of apoplastic diffusion that will take place in the Casparian strip.

5.2.1 Simulation of auxin treatment

To simulate treatment of roots with exogenous auxin, we set ω , the concentration of auxin in the space surrounding the outer cells of the root to be non-zero. If auxin is subject to diffusion only, we set $PIN_{i,j} \equiv 0$ and $LAX_{i,j} \equiv 0$ for all i, j so that:

$$J_{p,q}^+ = J_{q,p}^+ = A_1 P_{iaah}, \quad (5.3a)$$

$$J_{p,q}^- = J_{q,p}^- = B_1 P_{iaah} \quad (5.3b)$$

for all adjoining cells p and q .

Figure 5.4 A,C,E shows, using log-log axes, the mean steady state auxin concentration in each cell layer with increasing ω , at three values for the key parameter μ_{aux} , the rate of intracellular auxin turnover (0.1, 1.0, 10.0 $hour^{-1}$). In each case there is a linear relationship between exogenous auxin and the concentration in each cell layer, with the rate of increase with increasing ω decreasing with each layer closer to the central stele. In addition, as the rate of intracellular auxin turnover increases so does the relative steady state difference in auxin between cell layers. This is also demonstrated in Figure 5.4 B,D,F which shows a colour map of the auxin in each cell in the tissue relative to the mean auxin concentration in the epidermis, at each of the three values for μ_{aux} . Clearly, the lower the value for μ_{aux} , the more evenly the auxin from the exogenous treatment is distributed between all the cell layers.

This relationship between μ_{aux} and the relative auxin concentrations in each cell layer is shown more explicitly in Figure 5.5. As the intracellular

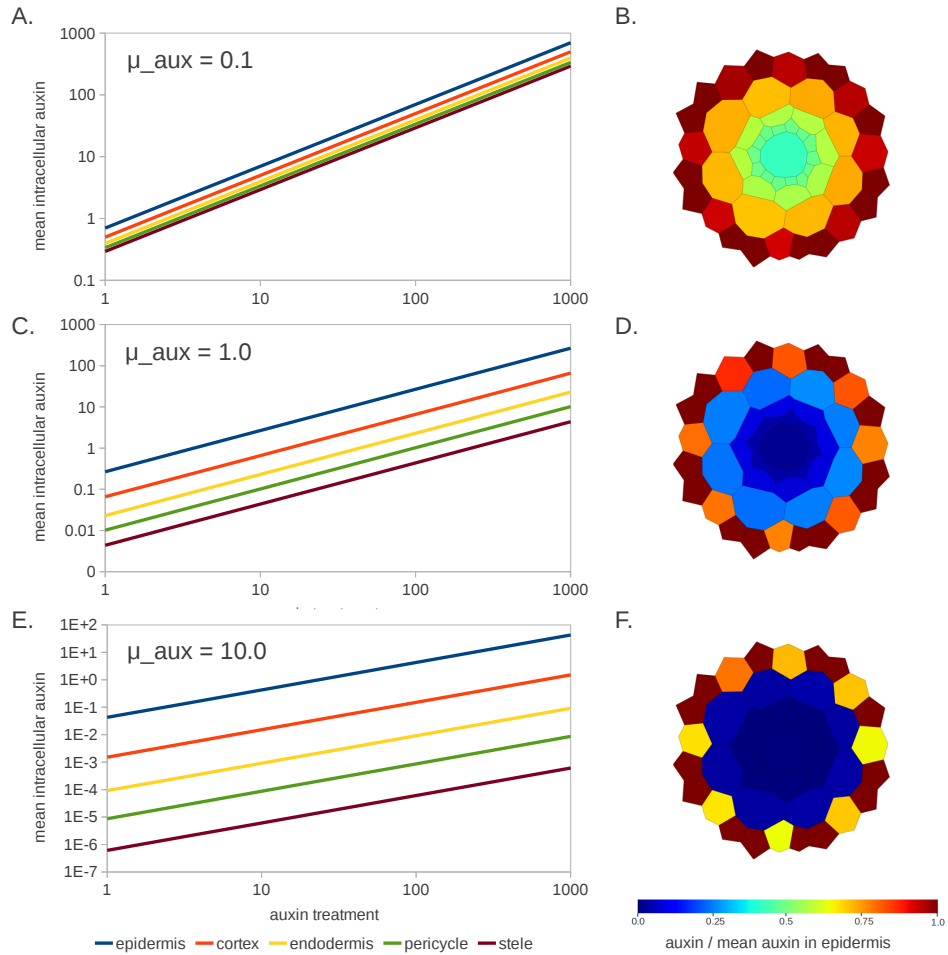


Figure 5.4: Log-log plots of mean steady state auxin by cell layer with increasing exogenous treatment to all outward facing cell walls in the epidermis, at three increasing intracellular auxin turnover rates, μ_{aux} (A,C,E), using the model defined in Section 5.1.2 with the concentration of all auxin carriers fixed to zero. Colour map showing the auxin in each cell, relative the the mean value in the epidermis, for three values of μ_{aux} (B,D,F). The higher the value of μ_{aux} , the greater the relative difference between cell layers, and the shallower the increase of intracellular auxin with increasing signal.

auxin turnover rate increases so the ability of auxin at the root surface to penetrate to the centre of the root decreases. Also affected by the auxin turnover rate is the time taken following treatment for auxin within each cell to reach steady state. Figure 5.7 shows model time courses of mean cortical auxin following simulated 1000 nM exogenous auxin treatment with three values for μ_{aux} . For the lowest value $\mu_{aux} = 0.1 \text{ hour}^{-1}$ it takes between 3 and 6 hours to reach half the final steady state value, while for $\mu_{aux} = 10 \text{ hour}^{-1}$ and $\mu_{aux} = 1000 \text{ hour}^{-1}$ it takes less than 10 minutes and less than 10 seconds respectively. These response times are similar for a given μ_{aux} for every cell layer (Figure 5.8). Given that in Band et al. (2012) a response in DII-VENUS degradation is seen within 2 minutes, possibly accelerating up to about 10 minutes, this would appear to put a lower bound on the value of $\mu_{aux} = 10 \text{ hour}^{-1}$. However as we see in Figure 5.4, at this value of μ_{aux} with the assumptions made in the simulation auxin does not significantly penetrate the innermost layers of the root. This is in contrast to the experimental observation that DII-VENUS appears to be degraded at a similar rate in all cell layers in the mature part of the root following 1000 nM auxin treatment (Band et al. 2012). This may be due in part to the presence of auxin carriers, which are not simulated here yet, and will be investigated further in Section 5.3. In addition, the assumption that auxin only enters the inner layers of the root from the epidermis may not be valid, as auxin may enter the stele from either the root tip, or from upper parts of the seedling which are also exposed to auxin during treatment. This can be easily simulated by adding an auxin source in the stele during the simulation. A final explanation is that diffusion of auxin within the apoplast will add to the penetration of auxin into the interior of the root. This apoplastic diffusion, along with the presence of the Casparian strip which blocks the apoplastic pathway in the endodermis, is added to the model in Section 5.2.2.

5.2.2 Apoplastic diffusion and Casparian strip

Apoplastic Diffusion

In the previous sections the auxin transport model only considers auxin diffusion between apoplast and cell, and at a much slower rate between cell and apoplast. However, the lack of penetration into the inner cell layers of the root seen when simulating exogenous auxin treatment suggests that adding movement of auxin between adjacent apoplastic compartments may provide a more realistic model, by simulating an apoplastic pathway for diffusion within the root (Figure 5.6). In the new model, auxin can diffuse freely between any adjacent apoplastic compartments or, in the OpenAlea terminology, between any adjacent wall compartments, which meet at the vertices or points of the tissue structure. After Band and King (2011), in addition to the existing apoplastic compartments, the auxin concentration in a small compartment representing each vertex is calculated at each step and used to calculate the flux between adjacent wall compartments. The diffusion takes place in the direction of higher to lower gradient in auxin concentration, proportional to a fixed diffusion coefficient, D_{cw} . The value

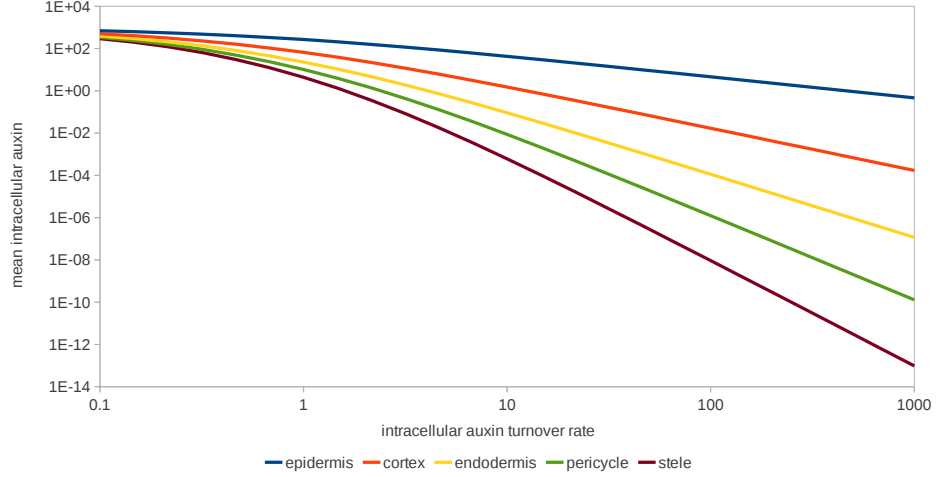


Figure 5.5: Log-log plot of mean steady state auxin by cell layer with increasing intracellular auxin turnover rate (μ_{aux}). The exogenous source of auxin, ω , is set = 1000. As μ_{aux} increases, the penetration of auxin into the inner cell layers decreases more rapidly than in the outer cell layers.

of D_{cw} used is taken from Kramer et al. (2007), which estimates $D_{cw} = 3.2 \times 10^{-11} m^2 s^{-1}$ or $D_{cw} = 115200 \mu m^2 hour^{-1}$. Equation (5.1b) is then replaced by:

$$\frac{dapo_{i,j}}{dt} = \frac{S_{i,j}}{V_{i,j}} (J_{i,j}^- auxin_i + J_{j,i}^- auxin_j - (J_{i,j}^+ + J_{j,i}^+) apo_{i,j}) + \frac{\lambda}{V_{i,j}} (J_{ij1}^a + J_{ij2}^a), \quad (5.4a)$$

where $V_{i,j}$ is the volume of the apoplastic compartment between cell i and cell j , and the diffusive flux either end of the apoplastic compartment is given by:

$$J_{ijk}^a = \frac{2D_{cw}}{S_{i,j} + \lambda} (av_{i,j,k} - apo_{i,j}). \quad (5.4b)$$

The term $av_{i,j,k}$ is defined as the auxin concentration in the small compartment representing the vertices, $k = 1, 2$, either end of the apoplastic compartment dividing cells i and j . The volume of each of these point compartments is the square of the apoplast width (λ^2), and an equal proportion of this volume is subtracted from each of the apoplastic compartments that meet at that point. In most cases, there are three apoplastic compartments meeting at each vertex, and so simplifying the notation by way of illustration, if a_v is the auxin concentration at a vertex, and a_1 , a_2 and a_3 , and S_1 , S_2 , and S_3 are the auxin concentrations and lengths respectively of the three adjoining compartments we have the following differential equation for a_v :

$$\frac{da_v}{dt} = \frac{2D_{cw}}{\lambda} \left(\frac{a_1 - a_v}{\lambda + S_1} + \frac{a_2 - a_v}{\lambda + S_2} + \frac{a_3 - a_v}{\lambda + S_3} \right). \quad (5.4c)$$

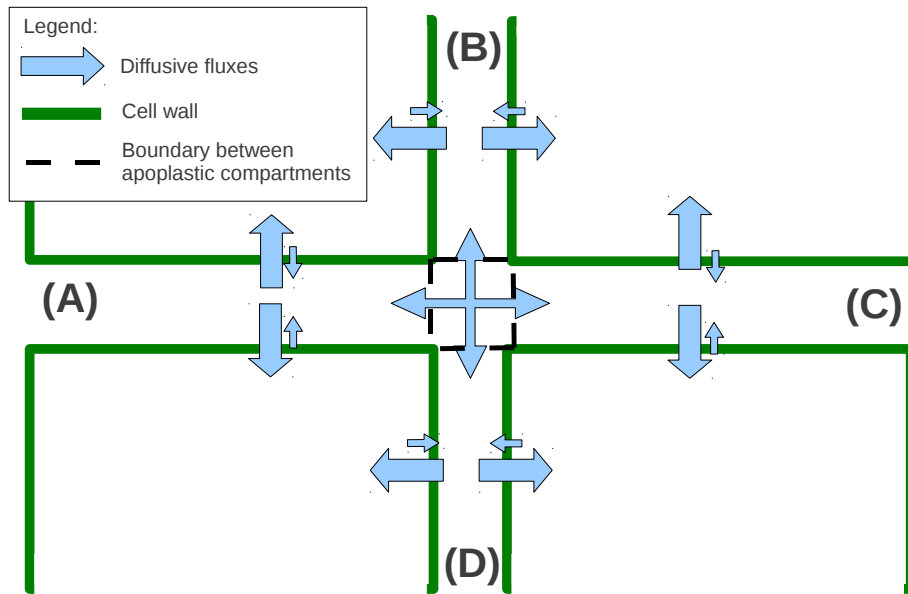


Figure 5.6: Schematic representation of the diffusive fluxes present when apoplastic diffusion is added to the model. The apoplast is divided into compartments, one compartment per wall in the data structure, plus small compartments at each vertex or point. The auxin in these small compartments is assumed to be at quasi-steady state and is approximated at each time step to calculate the flux between each apoplastic space meeting at that point. When n walls meet at a point in the mesh, there are n compartments in addition to the point compartment, and an equal proportion of the small volume of the point compartment is removed from each of the n walls. As before, from each apoplastic compartment, there is diffusion into the two cells it divides (or single cell in the case of an external wall), and a much slower rate of diffusion from the two cells in the apoplast. In addition, auxin can diffuse freely between each of the apoplastic compartments that meet at each point.

For small values of λ we can neglect the derivative in equation (5.4c) and rearrange, giving the following expression for a_v :

$$a_v = \frac{\frac{a_1}{\lambda+S_1} + \frac{a_2}{\lambda+S_2} + \frac{a_3}{\lambda+S_3}}{\frac{1}{\lambda+S_1} + \frac{1}{\lambda+S_2} + \frac{1}{\lambda+S_3}}. \quad (5.4d)$$

Similarly, for vertices with just two compartments, the expression for a_v is the same as equation (5.4d), with just the first two terms in both the numerator and denominator. More generally, using the earlier notation we can write:

$$av_{i,j,k} = \frac{\sum_{(p,q) \in W_{ijk}} \left(\frac{ap_{p,q}}{S_{p,q} + \lambda} \right)}{\sum_{(p,q) \in W_{ijk}} (S_{p,q} + \lambda)^{-1}}, \quad (5.4e)$$

where W_{ijk} is a list of apoplastic compartments in the form of (p, q) pairs denoting the cells they divide.

Casparian strip

A realistic model of the apoplastic pathway in plants is further complicated by the presence of the Casparian strip, an impermeable barrier in the endodermis, which will act to block the diffusion and carrier mediated transport of auxin in the cell walls where it is present. In the model this is simulated by fixing auxin in the walls between pairs of endodermal cells to zero, and preventing any auxin flux in or out of these walls. These zero flux walls are indicated on the diagram in Figure 5.9.

Figure 5.7 compares time courses of mean auxin in the cortical cell layers following a simulated exogenous auxin treatment of 1000 nM, with and without both apoplastic auxin diffusion and the Casparian strip, at three values of μ_{aux} . As we have already seen, increasing μ_{aux} has the effect of reducing steady state auxin in the cortex, and also reducing the time taken to reach steady state. In addition, as may be expected, adding the apoplastic diffusion pathway to the model increases steady state auxin in the cortex, compared to the model without. Furthermore, the comparative effect of the apoplastic pathway is magnified as μ_{aux} increases, so that the relative difference in steady state auxin with and without apoplastic diffusion is much greater for $\mu_{aux} = 1000$ than for $\mu_{aux} = 0.1$. The presence of the Casparian strip only has a very slight effect on cortical cell auxin concentration when the apoplastic pathway is present, with a very slight increase when the Casparian Strip is present due to a small amount of auxin being prevented from moving into the interior of the root via the apoplastic pathway. Clearly, removing the apoplastic pathway altogether will remove this effect and so there is no apparent difference with or without the Casparian strip when the apoplastic pathway is not included.

The effect of the Casparian strip following simulated auxin treatment can be seen more clearly in the inner cell layers (Figure 5.8). The pericycle in particular shows a clear reduction in steady state auxin when the Casparian Strip is included in the model, as would be expected as the only pathway by which auxin can enter the pericycle cells is via diffusion out

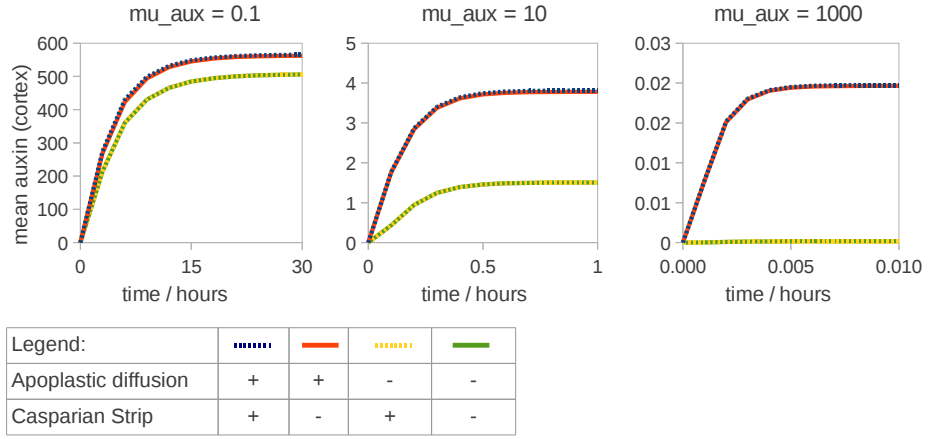


Figure 5.7: Time course of mean cortical auxin, with a simulated exogenous treatment $\omega = 1000$, at three values of auxin turnover, μ_{aux} . For each plot the model is solved both with and without apoplastic diffusion, and with and without a simulated Casparian strip. Increasing μ_{aux} reduces the time taken to reach steady state from zero auxin, and increases the relative importance of the apoplastic diffusion pathway. The presence of not of the Casparian strip has a limited effect on cortical auxin with the exogenous auxin source simulated at the outer epidermal cell walls.

of the endodermis. A slight reduction is seen in the endodermis when the Casparian strip is present as it has the effect of reducing the surface area of the cells around which auxin is able to flow freely.

Also shown in Figure 5.8 is the effect of increasing the diffusion coefficient D_{cw} , which has the effect of further increasing the penetration of auxin into the centre of the root. When the Casparian Strip is present however, even with a four-fold increase in D_{cw} , auxin is unable to enter the pericycle cells to any significant degree.

Clearly, the addition of apoplastic diffusion of auxin to the model increases the spread of auxin throughout the tissue, and increasing the diffusion coefficient within the apoplast increases the degree of penetration from the outer cell layers to the inner of the root when simulating an auxin source at the roots surface. As would be expected, simulating a barrier for auxin in the endodermal cell walls, to represent the Casparian Strip, is able to block most of the auxin reaching the inner cells in the pericycle and stele.

5.2.3 Simulation of primordium auxin source

To simulate an auxin source in the developing primordium, we set $\alpha_i > 0$ in one of the central xylem pole pericycle (XPP) cells either side of the stele, or by way of comparison all three XPP cells on one side are set to produce auxin. The model is then run to steady state, under the effect of diffusion only, and the steady state auxin in each of the eight cortical cells compared relative to each other, and to the primordia source cell. Figure 5.9 shows the numerical key used to identify each of the cortical cells, and the

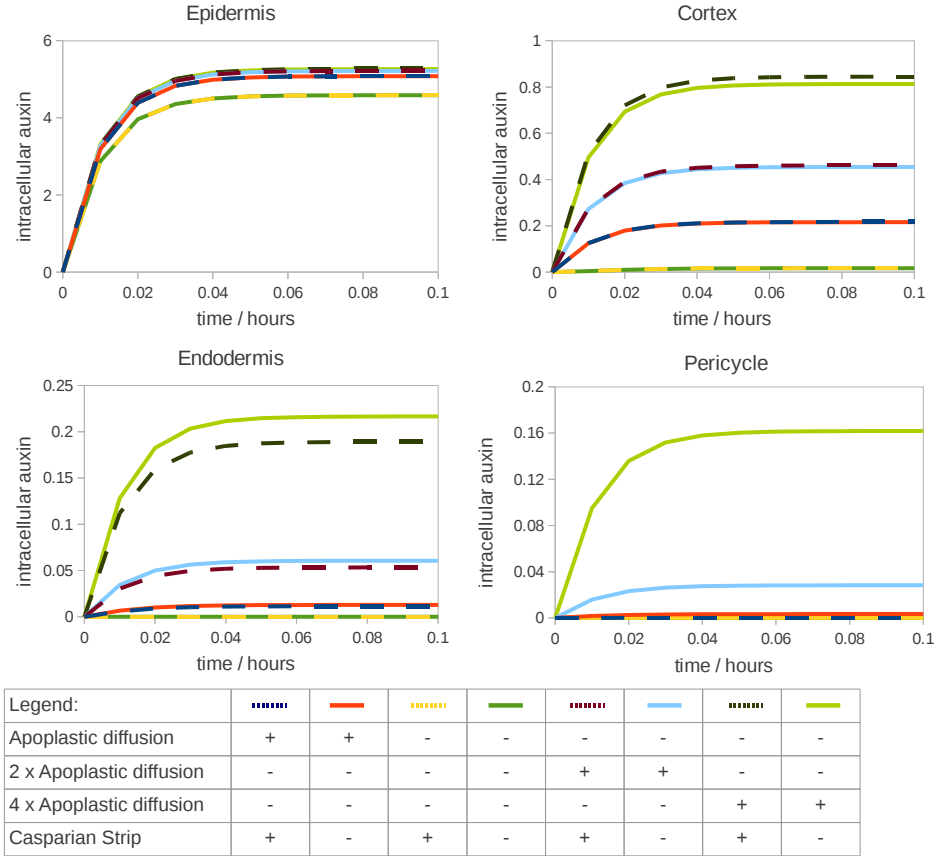


Figure 5.8: Time course of mean auxin in each of the four outer cell layers, with a simulated exogenous treatment $\omega = 1000$, for $\mu_{aux} = 100$. For each plot the model is solved both with and without apoplastic diffusion, with and without a simulated Casparian strip. The model solution is also shown with double and four times the apoplastic diffusion coefficient, D_{cw} , again with and without the Casparian strip. For the three outer cell layers, epidermis, cortex, and endodermis, the key determinant in the steady state auxin value is the value of D_{cw} . With no apoplastic diffusion $D_{cw} = 0$, and this results in the lowest values of intracellular auxin, and as D_{cw} increases so too does the steady state auxin in each of the three outer cell layers. In addition, the relative effect of the apoplastic pathway increases towards the centre of the root. The Casparian strip has the greatest effect towards the centre of the root as it blocks auxin in the endodermal cell layer.

position of the XPP set to be the auxin source for most of the simulations. Initially the model has apoplastic diffusion of auxin and the Casparian strip (Section 5.2.2), but later the effect of removing one or both of these model components is investigated.

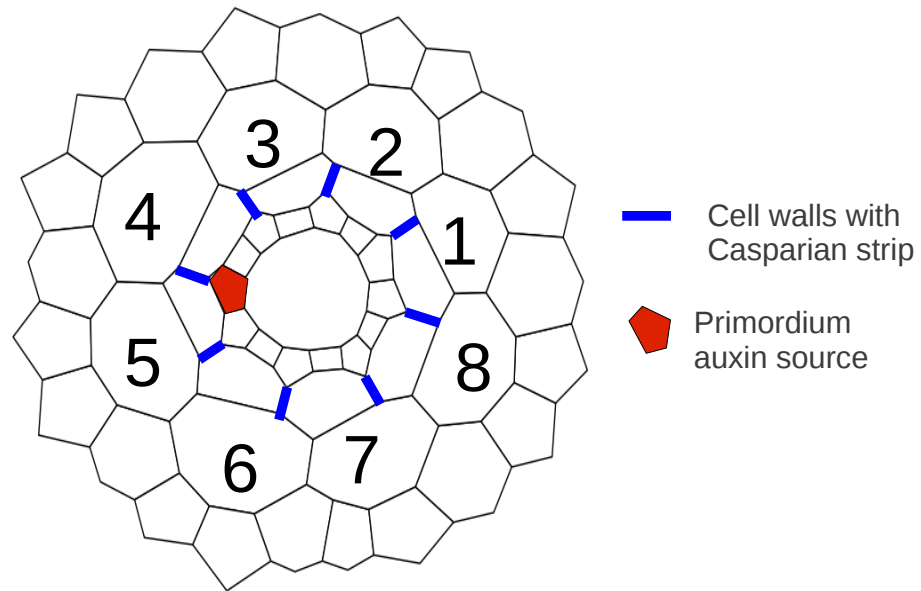


Figure 5.9: Schematic view of the root cross section, showing the location of the XPP cell primed as the auxin source representing a LRP used in most of the simulations, the cell walls set to have zero auxin flux to represent the Casparian strip, and the labelling of the cortical cells used in Figures 5.10 and 5.11.

The initial purpose of the simulation is to investigate the auxin levels in cortical cells relative to their spatial position in the tissue to a primordium auxin source. The conceptual model for LAX3 mediated lateral root emergence (Swarup et al. 2008) has positive feedback from LAX3 auxin influx acting to focus auxin in specific cortical cells close to the LRP. However, the positive feedback on those cells must act on some initial asymmetry in auxin distribution in order to be effective. Clearly, the asymmetry will be due to the spatial positioning of the cortical cells nearest to the primordium source, which are likely to receive more auxin than those cells further away. In the cross section used in Figure 5.9, it is to be intuitively expected that cells 4 and 5 will receive the most auxin from the primordium source cell, while cells 1 and 8 would get the least. The initial aim of the primordium simulation then, is to quantify the relative differences in auxin between cells in the cortex that may occur due to diffusion alone (either trans-cellular or apoplastic).

Looking at the diffusion only model in isolation from a model in which LAX3 is expressed in response to auxin and feeds back on the system is

further justified by considering the timescales on which auxin diffusion and LAX3 expression are taking place. While it takes at least 5 to 10 hours for LAX3 mRNA to be expressed following an increase in auxin signal (Figure 4.1), for all but unrealistically low rates of intracellular auxin turnover (μ_{aux}), auxin is redistributed to steady state within the tissue within minutes or even seconds of the introduction of an auxin source. Because of this, for realistic values of μ_{aux} , it is expected that the diffusion only simulation of a primordium auxin source represents the establishment of an initial spatial auxin distribution on which future expression of influx or efflux carriers may act.

Effect of intracellular auxin turnover (μ_{aux})

Figure 5.10 shows the relative steady state level of auxin in each of the eight cortical cells against μ_{aux} , using a value of $\alpha_i = 100$ in the central XPP cell to the left of the stele (as in Figure 5.9). The values for each of the cells is given relative to the ‘dominant’ auxin receiving cell, cell 5, and the model includes both trans-cellular and apoplastic diffusion, and the simulated Casparian Strip.

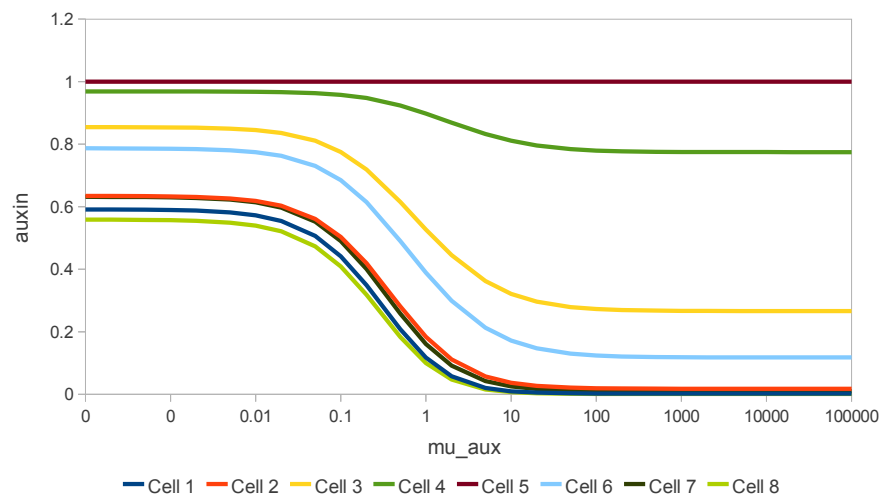


Figure 5.10: Steady state intracellular auxin in each of the eight cortical cells 1-8 (see Figure 5.9 for cell labels) with increasing auxin turnover rate, μ_{aux} (log x-axis), relative to the steady state value in cell 5, following the introduction of an auxin signal in a single cell in the pericycle representing a primordium. The primordium cell is as indicated in Figure 5.9, with the strength of the auxin source, $\alpha_i = 100$. Both apoplastic diffusion and the Casparian strip are included in the model. The distribution of steady state auxin by cortical has a narrow distribution in auxin for $\mu_{aux} < 0.01$, where each cell has more than 50% of the value of the greatest cell (cell 5), and a much broader distribution of auxin for $\mu_{aux} < 10$, with all but the cell adjacent to cell 5 (i.e. cell 4), having less than 40% of the auxin in cell 5.

The rate of intracellular auxin turnover (μ_{aux}) has a clear effect on the relative auxin distribution in the cortex, with a smaller range between the highest and lowest auxin containing cells seen at low μ_{aux} than at higher values. Below around $\mu_{aux} = 0.01$ the distribution between cells is similar for all values of μ_{aux} , with the cell with the least auxin containing more than 50% that of the cell with the most. Above around $\mu_{aux} = 100$, there is also a consistent distribution between the cells, but with a much greater range of auxin concentrations. Here, the cell with the least auxin has less than 0.2% that of the cell with the greatest. For $0.01 < \mu_{aux} < 100$ there is a transition between the two modes of auxin distribution.

Of particular interest is the comparison between the two cells receiving the most auxin (cells 4 and 5, Figure 5.9), and their nearest neighbours (cells 3 and 6, respectively). This is because of the observed expression pattern of LAX3 (Swarup et al. 2008), following which it would be predicted that cells 4 and 5 would express LAX3, while cells 3 and 6 do not. Since LAX3 is expressed in response to auxin, it follows then that there is sufficient auxin in cells 4 and 5 to trigger LAX3 expression, while in cells 3 and 6 there is either insufficient auxin to ever trigger LAX3 expression, or that LAX3 accumulates more rapidly in cells 4 and 5 and the positive feedback on their auxin levels depletes auxin in the neighbouring cells so that LAX3 is not expressed. Either way, a greater difference between the two cells with the most auxin and their neighbours will result in greater robustness to biological variation, and help restrict LAX3 expression to the specific observed expression pattern. In the simulation, the auxin in the neighbour cells (cells 3 and 6) relative to the main cortical cells (cells 4 and 5) ranges from 0.87 and 0.77 respectively at $\mu_{aux} = 0.01$ to 0.35 and 0.12 respectively at $\mu_{aux} = 100$. This means that for μ_{aux} in the upper range there may be between 3 and 8 times as much auxin in the two main cortical cells compared to their nearest neighbours, giving a fairly broad spatial distribution of auxin on which the positive feedback due to LAX3 expression may operate. This range of μ_{aux} is also consistent with the minimum estimate for the true value of μ_{aux} based on the time taken for auxin to reach steady state following exogenous treatment discussed in Section 5.2.1.

A key point to make is that, as well as increasing the difference in auxin between neighbouring cells in the cortex, increasing μ_{aux} also greatly increases the difference between auxin in the cortical cells with greatest auxin and the auxin producing primordium cell. Using $\alpha_i = 100$, for the low range of μ_{aux} auxin in the main auxin receiving cell (i.e. cell 5) is around 0.14 times the value in the primordium, while for $\mu_{aux} = 100$ auxin in cell 5 is less than 5.0×10^{-6} times the primordium value (Figure 5.11). Increasing α_i to 1000 or decreasing it to 10 has little or no effect on these relative values. Similarly, there is little or no difference when comparing the values of auxin in the different cortical cells relative to cell 5 at $\alpha_i = 100$, to those for either $\alpha_i = 1000$ and $\alpha_i = 10$, for all values of μ_{aux} used.

Model variations

Figure 5.11 shows the relative auxin in each of the eight cortical cells against μ_{aux} , for the model with both apoplastic diffusion and the Casparian strip as

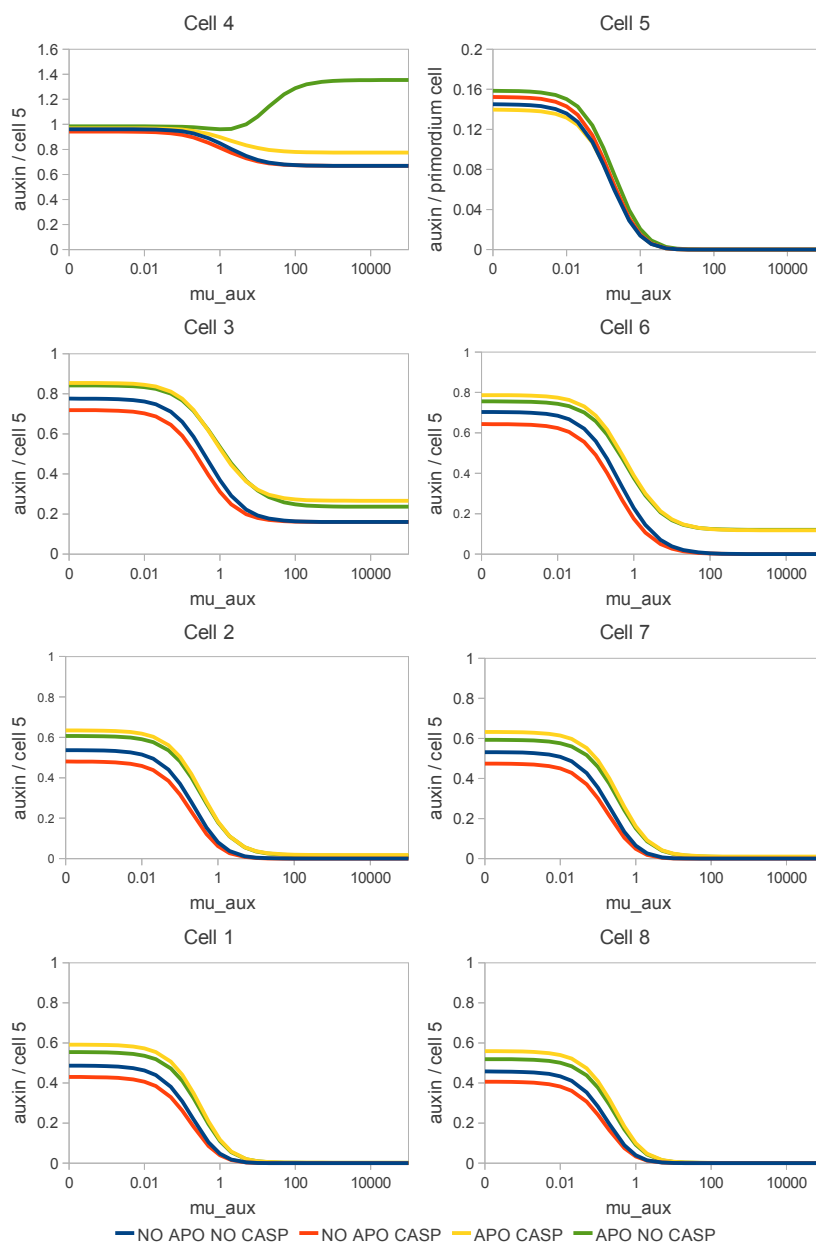


Figure 5.11: Steady state auxin in each of the cells 1-8 (see Figure 5.9 for cell labels) against turnover rate μ_{aux} (log x-axis), following the introduction of an auxin signal in a single cell in the pericycle representing a primordium. The primordium cell is as indicated in Figure 5.9, with the strength of the auxin source, $\alpha_i = 100$. The values in cell 5 are shown relative to the value in the primordium, and the other cells are shown relative to the value in cell 5. Each plot shows the model with and without apoplastic diffusion (APO/NO APO), and with and without the Casparian strip (CASP / NO CASP). The plot for cell 5 demonstrates that as well as the distribution of auxin within the cortex widening with increasing μ_{aux} , as μ_{aux} increases the value of auxin in the cell 5 drops rapidly relative to the value in the primordium.

in Figure 5.10, but also showing the effect of removing one or both of those model components. The values of auxin shown for each cell are relative to the value in cell 5, which generally receives the most auxin, with the exception of the values for cell 5 itself which are shown relative to the value in the primordium. The results are qualitatively very similar, regardless of the model used, though there are some subtle differences, in particular in the relative values of cell 4 and cell 5. Looking at the values for cell 5 gives a measure of how much auxin is reaching the cortex in each case, with the most auxin seen in the model with apoplastic diffusion, but no Casparian strip, and the least when both apoplastic diffusion and the Casparian strip are present. In the latter case the block on the apoplastic pathway in the endodermis prevents as much auxin reaching the cortical cells. In any case, the choice of model appears to have less effect on distribution in the cortex than the value of μ_{aux} , and so in future we use the model which best reflects the biological reality and keep the apoplastic diffusion and Casparian strip in all further simulations.

To test the importance of the physical size of the auxin maximum, the simulations were repeated with all three of the left-hand XPP cells set as the primordium source, rather than just the central cell (Figure 5.12). Looking qualitatively, differences between the simulated one cell auxin source and three cell auxin source are not visible at low and intermediate values of μ_{aux} . At high μ_{aux} , there does appear to be an increased spread of auxin in the cortex with the three cell auxin source, and a slight increase in some epidermal cells. However, these changes in the relative values are much less significant than the changes seen by varying μ_{aux} itself. In addition, to test whether the results were unique to the choice of XPP cell, the simulations were also repeated with the opposite central XPP cell set as the primordium source (Figure 5.12(C)). The results were qualitatively very similar as for the other XPP (Figure 5.12(A)), though further repetition on a range of cross sections would provide further corroboration.

The implication of the above results is that for the current parameter values used in the auxin transport model, in the range of primordia signal strengths tested, the relative spatial auxin distribution depends mainly on the rate of intracellular degradation, and not on the rate of auxin production within the primordium. In addition, for $\mu_{aux} > 10$, which was estimated previously as a lower bound for the true value of μ_{aux} , there is a relatively large spread of values of auxin within the cortex (several fold-change in auxin between each cortical cell and its nearest neighbour). However, as μ_{aux} increases the relative amount of auxin that reaches any of the cortical cells is greatly reduced.

If we use an estimated value of $\mu_{aux} = 100 \text{ hour}^{-1}$, so that steady state is reached quickly and there is close to a maximum range of relative auxin distribution in the cortex, when $\alpha_i = 100 \mu M \text{ hour}^{-1}$, the steady state concentration of auxin in the primordium is just under $1 \mu M$. This is just below the lower end of the range estimated by Petersson et al. (2009) of 1 to $50 \mu M$ auxin concentration within the cells near the root tip, and so these estimates appear to be reasonable estimates to use as a basis for further investigation. With these estimates however, the value of auxin in the two

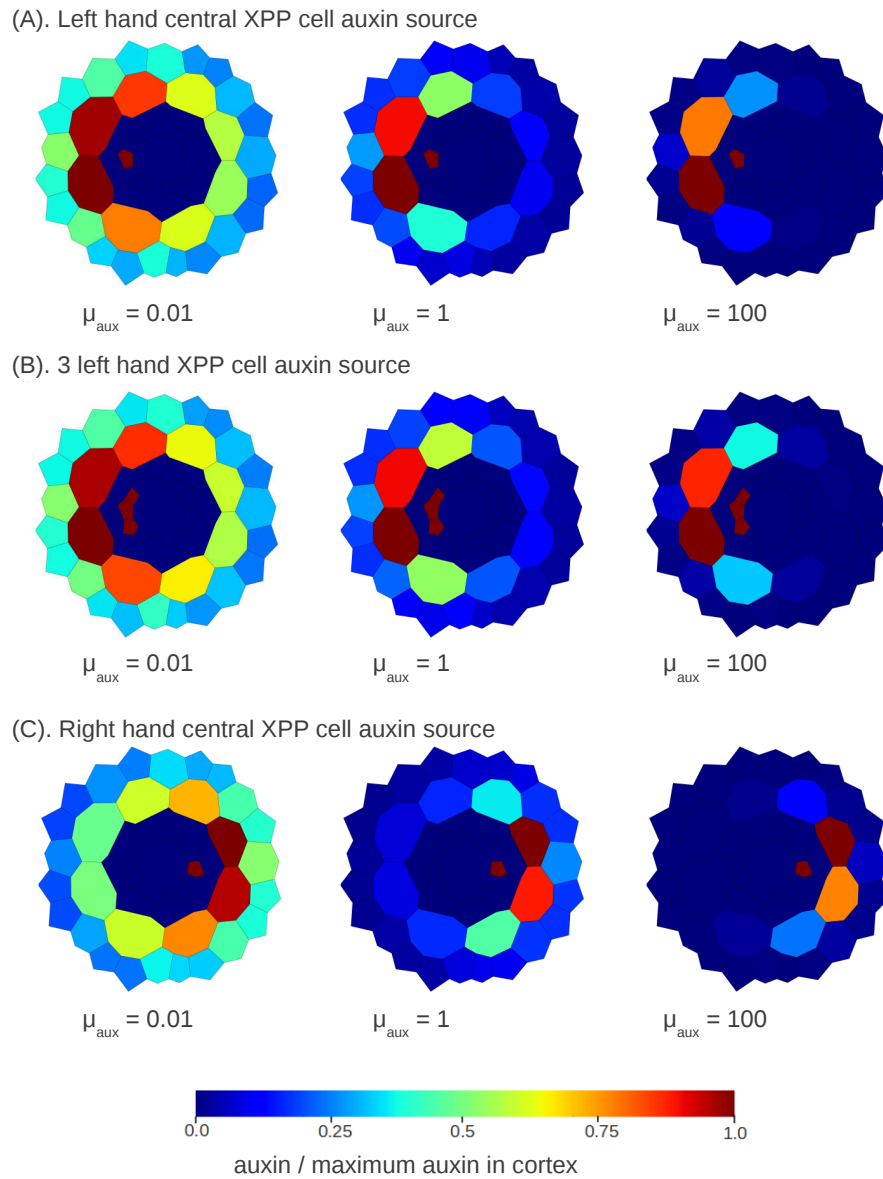


Figure 5.12: Colour maps of the steady state distribution of auxin in the cortex and epidermis following the introduction of an auxin signal in one or more cells in the pericycle. Each colour map is shown for low, intermediate and high values of the auxin turnover rate μ_{aux} , relative to the value in the cortical cell with most auxin. For clarity, auxin is not shown in the endodermis, pericycle or stele, except for those cells set to be auxin sources. (A) auxin source in central left-hand XPP cell, (B) auxin source in all three left-hand XPP cells, (C) auxin source in central right-hand XPP cell.

cortical cells that would be expected to ultimately express LAX3 (i.e. cells 4 and 5) is $3.34 \times 10^{-6} \mu M$ and $4.28 \times 10^{-6} \mu M$, which may be too low to produce an auxin response. As discussed above, one way of increasing cortical auxin is to simulate a fold-change increase in primordium signal strength, which will produce an equivalent fold-change increase in cortical auxin. However, increasing auxin in the primordium much beyond $1 \mu M$ may take it outside of a realistic physiological range. An alternative solution may be to investigate the effect of adding auxin influx and efflux carriers to the model, as in the following Section (5.3.1).

5.3 Modelling of influx and efflux carriers

5.3.1 Fixed distribution of influx and efflux carriers

To test the effects of the presence of fixed auxin carriers in the tissue, various configurations were added to the tissue (Figure 5.13), by setting the terms $LAX_{q,p}$ and/or $PIN_{q,p}$ equal to one for specific values of p, q corresponding to the required cells and cell membranes. For each configuration, with parameter values $\mu_{aux} = 100$ and $\alpha_i = 0$ except in the primordium cell as indicated in Figure 5.9, where $\alpha_i = 100$, the model was run to steady state, and the final auxin concentrations compared to the results with no carriers present as shown in Figure 5.14. The various carrier configurations are discussed in more detail below.

Influx carriers in stele

The first configuration has influx carriers on every face of the stele (Figure 5.13a) since, for simplicity, the stele is modelled throughout as a single cell, rather than modelling each individual cell. The presence of influx carriers in the stele is based on the experimental observation that the auxin influx carrier LAX3 has been observed to be expressed in the stele (Swarup et al. 2008). While the precise localisation of the carriers within the individual cells in vascular tissue is unclear, we approximate their presence by setting influx carriers around the circumference of the stele.

With this configuration, the stele retains more auxin than without carriers, with a direct effect that less auxin remains in the pericycle cells, marginally restricting the spread of auxin in the pericycle layer (Figure 5.14). This has a knock on effect in the endodermis and cortex, where the spread of auxin relative to the cells that receive most is also slightly reduced.

AUX1 in primordia / pericycle

There is also experimental evidence that the auxin influx carrier AUX1 is expressed in the developing primordia (Marchant et al. 2002). This is simulated in the model in two ways. Firstly, AUX1 is localised to all membranes of the central, auxin producing XPP cell (Figure 5.13b), and secondly AUX1 is localised to all membranes of all three XPP cells on the side where the auxin source is located (Figure 5.13c). The former arrangement results in

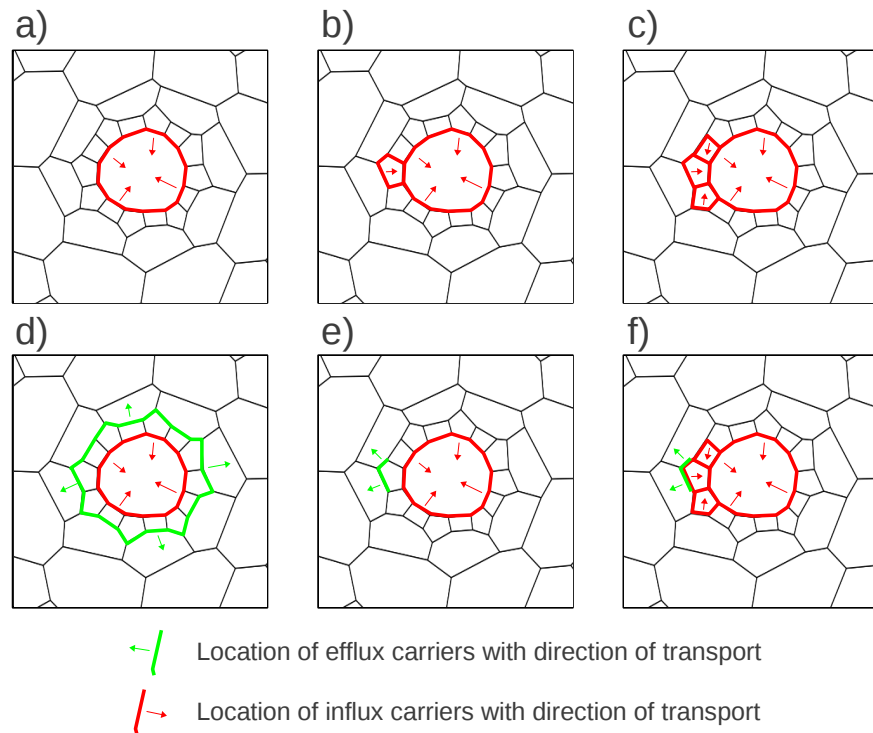


Figure 5.13: Schematic diagrams of the various configurations of fixed auxin carriers tested with the model. a) Influx carriers are expressed in the stele and localised to each cell wall facing the pericycle. b) Influx carriers in stele, plus in each of the walls of the primordium cell. c) Influx carriers in stele, plus in each of the walls of the three XPP cells. d) Influx carriers in stele, plus efflux carriers in pericycle localised to each cell wall facing the endodermis. e) Influx carriers in stele, plus efflux carriers in primordium localised to each cell wall facing the endodermis. f) as e), plus influx carriers in each of the walls of the three XPP cells.

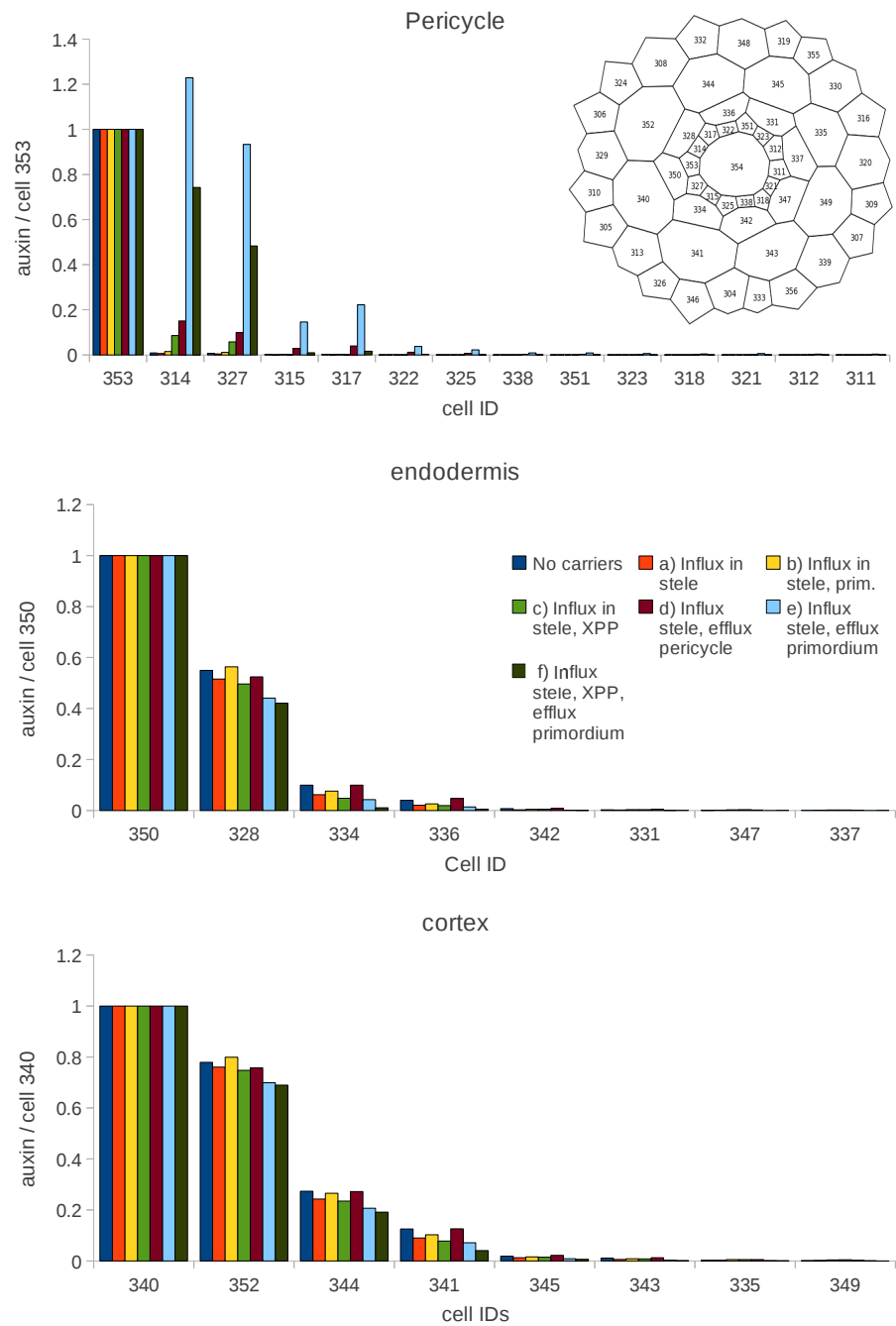


Figure 5.14: Relative steady state distribution of auxin in the pericycle, endodermis, and cortex, with simulated auxin source in a single pericycle cell (cell 353) and $\mu_{aux} = 100$, for each of the fixed carrier configurations shown in Figure 5.13, plus the values with no carriers. For cell id's see diagram in top right of figure.

only a marginal reduction in the spread of auxin in the endodermis and cortex, relative to the case with no carriers (Figure 5.14), with the latter arrangement showing slightly more restriction in the spread of auxin in the cortex, relative to the cell receiving most auxin (i.e. cell 340).

PIN in pericycle / primordia

In the cases above, and the case without any carriers at all, the absolute value of auxin that reaches the cortex relative to the concentration in the primordium is very low. To assist the spread of auxin from inner to outer cell layers, the effect of adding PIN efflux transporters in the pericycle cell layer was investigated. This was done in two ways. Firstly, by localising PINs to the outward facing (relative to the centre of the root) cell membranes of all cells in the pericycle (Figure 5.13d), and secondly by localising PINs to the outward facing membranes in just the primordium auxin source cell (Figure 5.13e). In both cases we retain the influx transporters in the stele.

In both cases when PINs are added to the pericycle, there is around a fifty-fold increase in the absolute quantity of auxin reaching the cortex, when compared to the values without the PINs. When PIN is expressed throughout the pericycle, there is a marginal increase in the spread of auxin within cortex, relative to the case when the only carrier is AUX1 in the stele (Figure 5.14). This is most likely due to the PINs in the pericycle aiding the spread of auxin radially around the root, as well as from inner to outer cell layers. For the case where PIN is only expressed in the primordium, however, there is reduction in the spread of auxin in the cortex, as more auxin is focused into the cortical cells closest to the primordium (Figure 5.14).

AUX1 and PIN in primordia cells

In the final case, PIN is localised to the outward facing membranes of the central primordium cell, and AUX1 is localised to all membranes of all three XPP cells on the side with the primordium, and to the stele. With this arrangement, there is not only significantly more auxin reaching the cortical cells than when the PINs are not present, but the relative spread of auxin within the cortex is the most restricted of all the carrier arrangements tested, with the value in the cell with the third most auxin out of the eight cortical cells (i.e. cell 344) receiving less than 20% of the auxin that the cell with the most (i.e. cell 340) receives (Figure 5.14).

Though in relative terms the differences in auxin in the cortical cells are marginal between the different carrier configurations, in general adding fixed auxin carriers to the tissue in the experimentally observed locations generally increases the difference between the auxin in the two cortical cells which are expected to express LAX3, with that in their neighbours. If LAX3 is expressed in a switch like manner, increasing the differences in auxin between adjacent cells ought to widen the range of concentrations in which LAX3 may be expressed, so leading to greater robustness to biological variability. In addition, the presence of PINs in the tissue has a significant effect on increasing the absolute quantity of auxin reaching those cells, which

means they will not need to be as sensitive to the presence of very low levels of auxin.

5.3.2 Threshold model for expression of LAX3

In the previous section, it was shown that adding fixed auxin carriers to the model, based on experimental evidence, can subtly change the relative distribution of auxin between cells in the cortex. In this section, a threshold model for LAX3 expression is used so that when auxin in either cortical or epidermal cells exceeds a prescribed value, LAX3 is localised to all membranes of the cell, resulting in an increased auxin influx rate to that cell. The model given in 5.1.2 is amended so that for all cell ids, i , in the cortex or epidermis, if:

$$auxin_i > \theta_{lax}, LAX_{i,j} = 1, \forall j \in W_i,$$

where θ_{lax} is the threshold for activation of LAX3 expression.

Given that it takes several hours following the auxin signal for LAX3 to be expressed, and that with a sufficiently high value for μ_{aux} , the model predicts that auxin within the tissue will re-equilibrate following a perturbation in auxin signal within minutes or seconds, we assume that auxin within the tissue is at steady state before any expression of LAX3 occurs. For this reason the model is run to steady state for a given parameter set first, with all LAX3 switched off, with a fixed auxin signal in the pericycle to represent a primordium. The model is then run from steady state, with LAX3 expressed in the cells above a given auxin threshold, as described above. The LAX3 is localised instantly at the beginning of each time step if auxin is above the required threshold. Clearly in reality the transcription, translation and localisation of mature LAX3 will all take time, and this will be considered further in Chapter 6. For the time being however, the model will give a prediction on the effect LAX3 has on intracellular auxin pre- and post-expression.

Using the default parameter values $\mu_{aux} = 100$ and $\alpha_i = 100$ in the primordium the model was run for three increasing values of θ_{lax} , selected so that 3, 2 and 1 cortical cells are triggered to produce LAX3 immediately after an initial timestep. As shown in Figure 5.15, in all three cases, after LAX3 is switched on, auxin in the cortex quickly finds a new steady state within less than 6 minutes. The values of auxin shown in the figure are relative to the auxin at time zero in the cell receiving most auxin before LAX3 is triggered (cell A). Clearly, if θ_{lax} is greater than this value, LAX3 will not be triggered for expression in any of the cells.

When θ_{lax} is set such that three cells are triggered, cells A, B, and C produce LAX3, and their auxin concentration is increased due to the extra influx rate. Cell A eventually has almost double its original value, while cell B's auxin is increased to greater than that of cell A before the LAX3 is added.

This is critical when considering the effect LAX3 may have on the production of CWREs such as PG. In the conceptual model published in

Swarup et al. (2008), the expression of CWREs is dependent on the focusing of additional auxin in specific cells via the positive feedback on auxin caused by the expression of LAX3. This hypothesis is supported by qRT-PCR data, which in the wild type shows late induction of PG, following the expression of LAX3. In the *lax3* mutant this induction is impaired (Figure 4.1). A robust biological system would seek to limit the expression of CWREs only to very specific cells in order to maintain the integrity of the root's cellular structure. One way to ensure this is the presence of a genetic switch, in which only cells with very high auxin will ever express PG. In the context of the threshold model described here, the threshold for PG expression ought to be higher than that for LAX3 expression, so that only the additional auxin influx caused by LAX3 expression is sufficient to trigger PG, and the remodelling of cell walls. In the *lax3* mutant, the lack of additional influx means that PG is not expressed.

In Figure 5.15 we see that if θ_{lax} is in the range such that both cells A and B express LAX3, the result is that both of these cells end up with more auxin than either had previously, possibly within the threshold for PG expression. However, even if the threshold for LAX3 expression is sufficiently low so that cell C also expresses LAX3, the resulting increase of auxin in that cell is not enough to reach the level of cell A or B pre-LAX3 expression. Since we assume that the auxin needs to exceed this level in order for PG expression to occur, this helps ensure that PG is not expressed outside of a narrow spatial domain.

For a given value of μ_{aux} there is a range of values for θ_{lax} for which LAX3 is expressed in the two cortical cells nearest the primordium as per the observed spatial expression pattern. Figure 5.16 shows how the relative breadth of this range changes as μ_{aux} varies, and also how the final steady state auxin in each of the four nearest cells to the primordium varies with μ_{aux} , for θ_{lax} in each of the three ranges.

The range of auxin concentrations for which one or two cortical cells express LAX3 broadens as μ_{aux} increases. In addition, as μ_{aux} increases the range of values for which three or more cells express LAX3 decreases, relative to the maximum auxin at $t = 0$. In general, the broader the range of auxin that produces the desired expression pattern, the more robust the system ought to be to biological variation. Again, a relatively high value for μ_{aux} would appear to be desirable. This is also the case when looking at the steady state values as μ_{aux} varies. The lower the value of μ_{aux} , the lower the proportional increase in intracellular auxin after LAX3 is triggered. For high values of μ_{aux} , when θ_{lax} is set so that LAX3 is triggered in cells A and B, there is almost a doubling in auxin concentration post-LAX3 induction in the affected cells, while as μ_{aux} is lowered this proportion is reduced, to the extent that for the lowest value of μ_{aux} there is only a 3% increase in auxin in cell A, and cell B only attains 99% of the value of cell A pre-LAX3 induction. If a significant increase in auxin post-LAX3 expression is required to further trigger the expression of CWRs such as PG, a relatively high value for μ_{aux} will be most effective. A final point is that should θ_{lax} be low enough so that a third cell is triggered to express LAX3 (i.e. cell C), as μ_{aux} increases the steady state value of auxin this cell attains post-LAX3

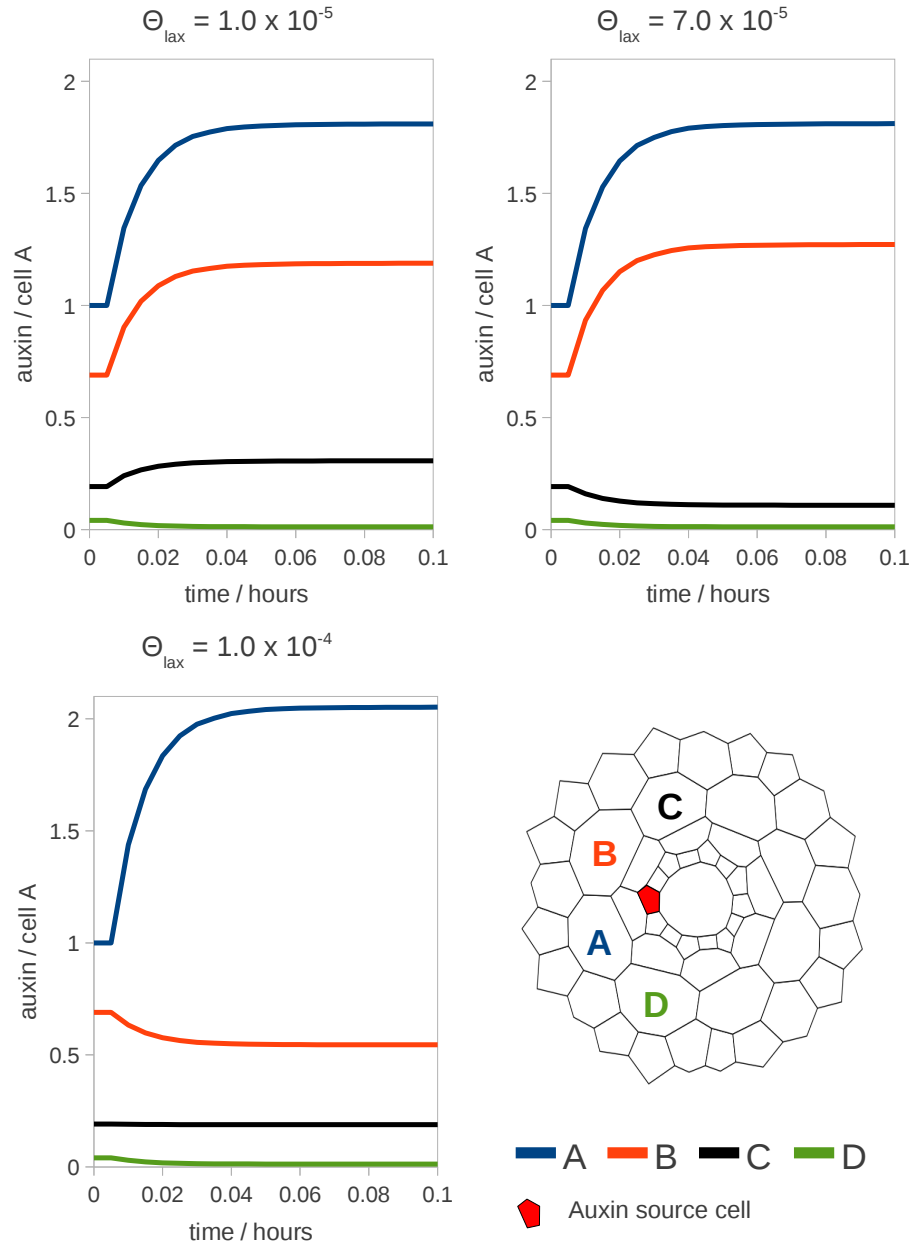


Figure 5.15: Model time courses for the cortical cells labelled A,B,C,D (bottom left) from steady state with a single cell primordium auxin source following the expression of LAX3 after an initial time step. Depending on the value of θ_{lax} , 1 (bottom left), 2 (top right), or 3 (top left) cortical cells begin to express LAX3. Intracellular auxin turnover, $\mu_{aux} = 100$. In each case there is a clear increase in auxin in cell A to almost or more than double the initial value within around 5 minutes. If cell B is triggered to express LAX3 (two top plots), its auxin level increases over a similar time-frame, and eventually exceeds the initial value in cell A pre-LAX3 expression. Even if the threshold for LAX3 is such that LAX3 is triggered in cell C, the increase of auxin in that cell is not sufficient to exceed the initial values in either cells A or B. This lack of overlap in the range of auxin concentrations in cells A and B, and the other cells, may help restrict the expression of CWRs to the two cells nearest the LRP only.

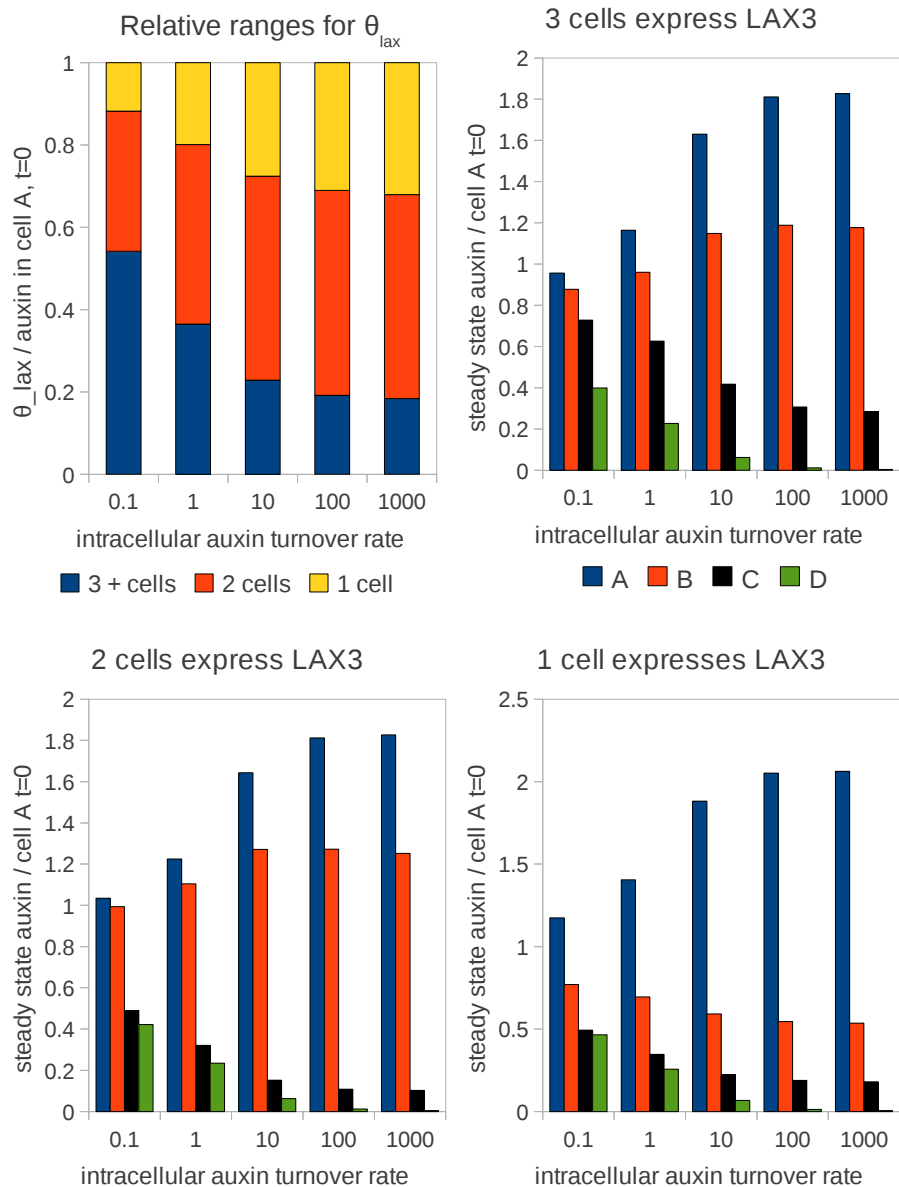


Figure 5.16: Top left: Ranges of the the values θ_{lax} may take, relative to the value in cell A at steady state pre-LAX3 expression, so that 1, 2 or 3 or more cells are triggered to express LAX3 in the threshold model with a simulated single cell primordium auxin source (see Figure 5.9 for location), for increasing values of μ_{aux} , the auxin turnover rate. Top right, bottom left, bottom right: Respective steady state auxin values after θ_{lax} is set so that 3, 2, and 1 cells are triggered to express LAX3 in each of the cells A,B,C,D, for increasing values of μ_{aux} . As μ_{aux} increases the range of auxin values for which two cells are triggered to express LAX3 increases, and so too does the fold-change increase in auxin increase following LAX3 expression. See Figure 5.15 for the position of cells A-D in the tissue.

expression drops relative to the other two LAX3 expressing cells (A and B). Again, a high value for μ_{aux} increases robustness, by reducing the chances that a high concentration of auxin will occur in any cortical cell other than the two closest to the primordium.

5.4 Discussion and conclusions

Analysis of the LAX3 model at the network scale shows that it is possible to have switch-like behaviour of LAX3 mRNA expression with an increasing auxin signal (Chapter 2). Depending on key parameters relating to promoter co-operativity and the strength of positive feedback on auxin due to LAX3, the switch from low to high expression can occur gradually over a relatively broad range of auxin concentrations, rapidly over a very narrow range of auxin (ultra-sensitivity), or the switch can be bistable (i.e. there is a range of auxin at which both high and low steady states can occur). Moving from the network scale into the tissue scale, it is observed that only the specific cortical cells over lateral root primordia express LAX3 during emergence. For this expression pattern of LAX3 to occur, there needs to be either a large difference in auxin concentration between adjacent cells in the cortex, or a sharp switch in LAX3 expression with the threshold value for change from low to high tuned precisely between the auxin values in the adjacent cells. While it is unlikely that this latter mechanism alone will be robust to biological variation, a combination of the two mechanisms ought to provide a much more reliable system to ensure that only specific cells express LAX3 and so go on to express the CWRs needed for lateral root emergence. A key purpose of the tissue scale model then is to investigate how auxin is spatially distributed radially within the root, in particular in the cortex in response to a source in the pericycle simulating a LRP, and what factors or parameter values affect that distribution.

Initially the model was used to simulate an exogenous source of auxin around the circumference of the root, with just diffusion between cell and apoplast. The intracellular turnover of auxin (μ_{aux}) was identified to be a key parameter in the steady state distribution of auxin between cell layers, with the difference in concentration between adjacent layers increasing as the turnover rate increases. Adding diffusion of auxin between adjoining apoplastic spaces was shown to significantly increase the penetration of auxin into the root. In the interests of adding biological realism to the model, the apoplastic diffusion is therefore retained in future simulations, along with a simulated barrier in the endodermis to represent the Casparian strip. Though the lack of penetration of auxin to the centre of the root shows that attempting to simulate auxin treatment by restricting the auxin source to the outer surface of the root may be unrealistic, the model clearly shows the importance of the intracellular auxin turnover rate and the apoplastic diffusion pathway on the auxin distribution in the radial root cross-section. An alternative method to better simulate exogenous auxin treatment is given in Chapter 6.

The lateral root primordia is simulated in the model by a fixed source of auxin in one of the central XPP cells. As with the exogenous auxin treat-

ment simulation, the key parameter in determining the relative auxin distribution is the intracellular auxin turnover. At high turnover rates there is more than double the auxin in the two cortical cells nearest the primordium than in their nearest neighbours, while at low turnover values the auxin is distributed much more evenly around the ring of cortical cells, with the auxin in the neighbouring cells receiving around 80% of the auxin of the two main cells. These relative values are subtly changed by removing either or both of apoplastic diffusion and the Casparian strip, but neither have as significant an effect on the relative values as μ_{aux} . If there is a switch in LAX3 activation with increasing auxin signal, the greater difference in auxin at high μ_{aux} in adjacent cells allows for a less sharp switch, and greater robustness to biological variability. At low μ_{aux} however, the switch will need to be much sharper and more precisely tuned, in order to see the observed all or nothing LAX3 spatial expression pattern. It is important to note that increasing μ_{aux} reduces the amount of auxin reaching the cortex, relative to primordium concentration, though the difference between primordium and cortex can be reduced by adding PIN transporters to the primordium, or pericycle layer. Adding a fixed distribution of auxin carriers in the stele and XPP has the effect of slightly increasing the difference in steady state auxin between the two main cortical cells and their two nearest neighbours.

If LAX3 expression is set to be triggered when auxin in any cortical or epidermal cell exceeds a pre-defined threshold, it is possible to see the effect the feedback LAX3 has on the final steady state auxin post-LAX3 expression by changing the value of the threshold so that specific cells in the cortex are triggered. By looking at the steady state auxin distribution pre-LAX3 expression, it is shown that the threshold values resulting in 1, 2 or 3 cortical cells to be triggered are much closer together at low μ_{aux} than at high μ_{aux} . In addition, at high μ_{aux} , when the threshold is set so that just the main two cortical cells are triggered, there is nearly a doubling of auxin in those two cells post-LAX3 expression, with both cells ultimately receiving more auxin than either pre-LAX3 expression. This latter point is important when considering the proposed conceptual model for CWRE expression in the cortex, where LAX3 is required to amplify auxin in specific cells in order for them to be able to express the CWREs. If the CWREs also have switch-like activation with increasing auxin, it would be expected that the threshold for CWR expression is greater than that for LAX3, preventing the unwanted expression of CWREs. The higher this threshold for CWRE expression, the more robust the system to small changes in auxin concentration. At low μ_{aux} , the triggering of LAX3 results in a relatively small fold-change in steady state auxin, with the cell with the second most auxin pre-LAX3 expression failing to exceed the value of the cell with the most pre-LAX3 expression. In other words, in order for both these cells to express CWREs, the auxin threshold for CWRE expression would need to be similar to that for LAX3, meaning that the amplification of auxin by LAX3 is not required. In this case, it would be expected that removing LAX3, as in the case of the *lax3* mutant, would have little or no effect on CWRE expression, which is not the case for the expression of the CWRE PG (Figure 4.1).

In general, the tissue scale model shows that with a high rate of intra-

cellular auxin turnover, the spatial arrangement of cells in the cortical cell layer relative to a primordium auxin source provides a wide distribution of auxin between adjacent cells in the cortex. Following the introduction of the auxin source, the action of diffusion, via both apoplastic and transcellular pathways, results in a steady state redistribution of auxin within minutes. The experimental evidence indicates that it takes several hours before LAX3 is expressed and so this steady state distribution represents the initial conditions for the production of the LAX3 expression pattern. A broad distribution of auxin in the cortex then provides an effective basis on which a switch-like expression of LAX3 can operate. In addition, a high auxin turnover rate increases the power of LAX3 expression to raise the auxin level of cells in which it is expressed, consistent with the conceptual model that the magnification of auxin by LAX3 is required for the expression of CWRs. The current model does not, however, take into account the timing of gene expression events, or demonstrate that a range of auxin signals may produce the same LAX3 expression pattern. To do this the tissue scale auxin transport model needs to be coupled with the network scale models for LAX3 expression (Chapters 2-4), as described in the following chapter (Chapter 6).

Chapter 6

Multi-scale Models of Lateral Root Emergence

In the previous chapter (Chapter 5), a tissue scale model of auxin transport within a mature *Arabidopsis* root cross section was used to show the auxin distribution following both simulated auxin treatment and the introduction of an auxin source in a single pericycle cell to represent a LRP. The first step in linking the tissue scale model to a gene network scale model is made by modelling the relationship between cellular auxin and the degradation of Aux/IAA within each cell. Initially this is done using a simpler model of the DII-VENUS sensor, which is expressed constitutively and does not feedback on its own expression rate (Section 6.2), and then by explicitly modelling the expression of Aux/IAA mRNA in response to the level of Aux/IAA protein (Section 6.3). Next, the secondary auxin response gene LAX3 is modelled in Section 6.4. LAX3 is able to feedback on cellular auxin levels by increasing the rate of transport into the cell. Finally, the expression of a tertiary response gene, hypothesised to be the CWRE PG, is modelled in Section 6.5. A schematic digram of the gene network is shown in Figure 1.10. In the model PG is only expressed in the cortical cells which have elevated auxin concentration due to the expression of LAX3, matching experimental observation. Before developing the multiscale model, however, we return to the problem of simulating exogenous auxin treatment in the multicellular context (Section 6.1).

6.1 Initial conditions for auxin transport simulations

6.1.1 Exogenous auxin treatment

In Section 5.2 exogenous auxin treatment of *Arabidopsis* roots was simulated by setting a fixed concentration of auxin at the boundary of the tissue. Using this method it is seen that the intracellular auxin turnover rate is a key parameter in determining the degree of penetration of auxin from outer to inner cell layers, with a higher turnover rate resulting in a greater decrease in auxin concentration between adjacent cell layers as the auxin passes from the epidermis to the central stele. Further analysis of the

model shows that significant auxin turnover within cells is necessary both to provide a sufficient gradient of auxin between cells in the cortex so that the domain of expression of LAX3 may be restricted (Section 5.2.3), and to provide a significant fold-increase in auxin in cells when LAX3 is expressed, compared to the level without LAX3 expression (Section 5.3). However, the predicted gradient of auxin from outer to inner cell layers seen in the exogenous auxin simulation when using a high turnover of cellular auxin is not consistent with experimental observations using the auxin sensor DII-VENUS. When treating roots with exogenous auxin the degradation of the DII-VENUS sensor in the mature part of the root appears to occur equally and simultaneously in all cell layers, with the possible exception of the epidermis, which may actually show less DII-VENUS degradation (Band et al. 2012).

This indicates that rather than a sharp negative gradient in auxin from outer to inner cell layers following exogenous treatment, as predicted by the earlier simulation, in reality the increase in cellular auxin following treatment is fairly uniform, save in the epidermis where less auxin is detected. A possible explanation for this uniform increase is that rather than being restricted to entering the cross-section used in the simulation via the surface of the root, the auxin from the experimental medium enters via every possible pathway, including the vascular tissue. Simulating exogenous treatment in this way, should result in a uniform increase of auxin throughout the cross-section. The reduced response of DII-VENUS in the epidermis may be due to an increased auxin turnover rate in those cells compared to other cell layers, possibly as a protective mechanism for the outer cell layer, but this question is left to future study.

To approximate the uniform increase in auxin due to exogenous treatment, rather than using a fixed auxin concentration at the tissue boundary as previously, the production rate in each cell, α_i , as defined in the model given by equations (5.1a), (5.1c), (5.1d), (5.4a), (5.4b) and (5.4e), is increased such that the resulting steady state concentration in each cell for a given auxin turnover rate is approximately equal to the treatment concentration. The values for α_i for each treatment are given in Table 6.1. It is important to note that though using these parameter values results in dimensional auxin concentrations in the cells roughly equal to the treatment concentrations, this is not necessarily the case biologically. However, as shown in Chapter 5, the absolute values of cellular auxin are less important in the model than the relative values between cells and cell layers, and choosing the parameters in this way is convenient to give some reference to known treatment concentrations.

Figure 6.1 shows the time course of mean intracellular auxin in the tissue cross section for the first six minutes post-auxin treatment, for the range of treatments and corresponding estimates for α_i given in Table 6.1. As discussed in Section 5.3.1, there is a fixed distribution of influx carriers surrounding the outer faces of the stele to simulate the stele acting as a sink for auxin, but the influx carriers in the stele still only produce a very slight differential in auxin between inner and outer cell layers of less than one percent (not shown). The model is run from the steady state values

Table 6.1: Values for α_i in every cell in the auxin transport model given by (5.1a), (5.1c), (5.1d), (5.4a), (5.4b) and (5.4e), with the default parameters in Table 5.1, used to approximate the given range of auxin treatments, or no auxin treatment (n.t.). The no treatment or basal value for α_i was determined by parameter fitting (Section 6.2)

Treatment concentration (nM)	α_i
n.t.	0.06256
1	0.1
5	0.5
10	1.0
100	10.0
1000	100.0

using the estimated basal rate for α_i determined in the following Section (6.2). In each case the new steady state is reached within 6 minutes (0.1 hours), with half the new steady state reached within around 30 seconds. This is consistent with the rapid response of DII-VENUS within two minutes following auxin treatment seen by Band et al. (2012). This simulation of exogenous auxin treatment is used to model the response of DII-VENUS in the multicellular model in Section 6.2.

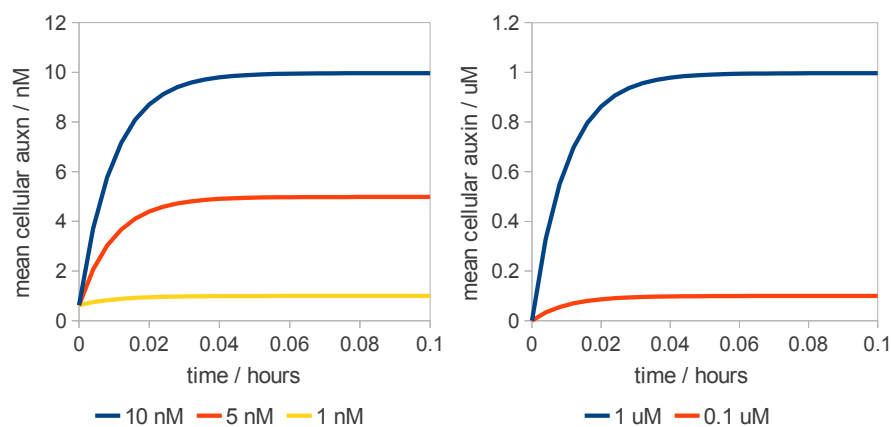


Figure 6.1: Mean intracellular auxin in the model tissue versus time for the range of exogenous auxin treatment simulations and parameter values given in Table 6.1. In each case the model given by (5.1a), (5.1c), (5.1d), (5.4a), (5.4b) and (5.4e) is run from the basal steady state or no treatment value as given in Table 6.1 and determined in Section 6.2.

6.1.2 Simulation of LRP auxin source

An estimate for cellular auxin concentration near the maxima found at the root tip of between 1 and 50 μM is given in Petersson et al. (2009). Using a

value of $\alpha_i = 5000$ in the cell representing the primordium, and a turnover rate of $\mu_{aux} = 100$, results in the concentration in the primordia within this estimated range, with a steady state concentration of around $17 \mu M$. Figure 6.2 shows the cellular distribution of auxin in the tissue relative to that in the primordia using this value for the primordium auxin production, with the value of α_i in the others cells remaining at the basal level given in Table 6.1. In addition, as in Section 5.3.1, influx carriers are fixed to all membranes of the three XPP cells near the primordium, and efflux carriers are fixed to the membranes of the primordium facing the endodermis.

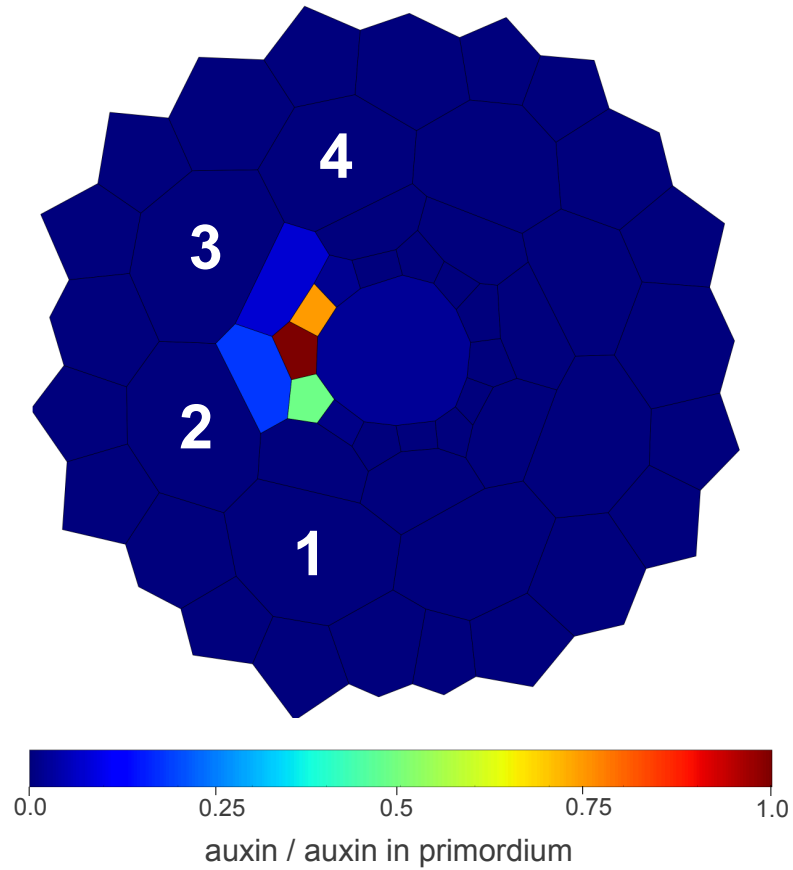


Figure 6.2: Steady state cellular auxin distribution using a value for $\alpha_i = 5000$ in the simulated primordium, $\alpha_i = 0.06256$ elsewhere, and $\mu_{aux} = 100$, using the model given by (5.1a), (5.1c), (5.1d), (5.4a), (5.4b) and (5.4e) with the value of all auxin carriers fixed to zero. Auxin in the primordium cell is around $17 \mu M$, and the auxin turnover rate, and acid trapping mechanism prevents widespread distribution of auxin in this high concentration range. Instead, auxin in the cortical cells labelled 1 to 4 is in the nanomolar range with cell 1 = 0.84 nM , cell 2 = 5.8 nM , cell 3 = 4.2 nM and cell 4 = 1.6 nM , in comparison to the basal level of around 0.63 nM .

Clearly the intracellular auxin turnover and preferential diffusion of

auxin from apoplast to cell rather than vice versa prevents a wide spread of auxin throughout the tissue, with only the cells immediately adjacent to the primordium showing a visible elevation of auxin with the colourbar scale used. However, looking at the numerical values of steady state auxin in the cortex shows that the cells labelled 2 and 3 in the figure have increased in auxin from around 0.6 nM to around 5.7 nM and 4.1 nM respectively. Auxin in the neighbouring cortical cells, 1 and 4 only increased to 0.83 nM and 1.6 nM respectively, so that there is more than double the auxin in the two cortical cells nearest the LRP compared to their nearest neighbours. In addition, based on the data from the DII-VENUS sensor these values are in the physiological range in which an auxin response may be expected (Band et al. 2012). To see an all-or-nothing response however, a non-linear response of the target gene to cellular auxin concentration would be needed. In the following Sections 6.2-6.4 an ODE model is used to show that the auxin distribution shown in Figure 6.2 can be used as the basis for the experimentally observed LAX3 expression pattern, and reinforced by the positive feedback from LAX3 influx transporter activity.

6.2 Multiscale model of the DII-VENUS auxin sensor

Before adding LAX3 expression and feedback to the model in Section 6.4, the link between auxin and the auxin response must be first added. This is provided by the expression of Aux/IAA mRNA and translation of Aux/IAA protein as described in Section 6.3. First however, in this section the auxin transport model is linked with the model for DII-VENUS and parameter values found for which the model is able to approximate to the DII-VENUS data from Chapter 2 and Band et al. (2012) in the multi-cell context. These parameters can then be used as an estimate to model the auxin dose response of Aux/IAA protein.

The equation used to model the level of DII-VENUS is of a similar form to that given in Section 2.3, but with $\beta = 1$ so that:

$$\frac{dDII_i}{dt} = 1 + \frac{-\eta auxin_i DII_i}{QP + Qauxin_i + auxin_i DII_i} - \lambda_v DII_i, \quad (6.1)$$

where the subscript i denotes the concentration in cell i . This equation is then coupled with equations (5.1a), (5.1c), (5.1d), (5.4a), (5.4b) and (5.4e) to give a multicell model for the level of DII-VENUS dependent on the level of cellular auxin.

Using a fixed value for $auxin_i$ effectively reduces the model to a single cell model, behaving as one would expect each cell in the multicell model to behave for that value of auxin. Doing this enables model parameters in the single cell model to be fitted using the fitting algorithm described in Section 2.2, so that the multicell model then approximates the DII-VENUS data without fixing the level of auxin, but instead using the values for α_i for each concentration as given in Table 6.1. Setting the α_i and μ_{aux} so that the cellular concentration is approximately the same as the treatment

concentration means that $auxin_i$ can be set equal to 0.001, 0.005, 0.01, 0.1, and 1.0, to represent 1, 5, 10, 100 and 1000 nM treatments respectively, and fitted with the experimental data. α_i for the non-treated data is set as an additional parameter to be fitted using the algorithm.

The response of the multicell model using the parameter set given in Table 6.2 is shown in Figure 6.3. Figure 6.3(a) shows mean intracellular model DII-VENUS versus time for the first two hours following a range of auxin treatments, and Figure 6.3(b) a colourmap of the steady state distribution of model DII-VENUS for the same range of treatment concentrations. Comparison of the time course plots with the data shown in Figure 2.13(a) shows that both the timing and the dose response of the multicell model are a good approximation to the data, and the the colourmap plots show that, as would be expected, the distribution of DII-VENUS for a given simulated auxin treatment is uniform throughout the tissue.

The precise strength of the auxin signal from the developing LRP remains unknown. However, using the model it should be possible to predict the expected distribution of DII-VENUS for a given signal strength, which can then be tested experimentally (Figure 6.4). At the lowest value for the auxin production in the primordium (α_p) there is little or no degradation of DII-VENUS save in the cells immediately adjacent to the LRP cell, while at the highest value for α_p there is clear degradation in all of cells in the stele, pericycle, and endodermis, and most of the cells in the cortex and epidermis to the left hand side of the cross-section. At the intermediate values of α_p , the greatest degradation in the two outer cell layers is seen in the two cortical cells nearest the LRP. In particular, for $\alpha_p = 5000$, there is strong degradation of DII-VENUS in these two cells, but low to intermediate degradation in the neighbouring cells. Using the assumption that the degradation of DII-VENUS is an approximation for the degradation of Aux/IAA, this suggests that with this primordium signal strength there would be a strong auxin response in the two nearest cortical cells, and a lower auxin response in the adjacent cells. This, in conjunction with a switch-like or non-linear transcriptional response to auxin, could provide a basis for the spatial expression pattern of LAX3.

6.3 Primary auxin response: expression of Aux/IAA

Though DII-VENUS is a mutated domain II of IAA28, and so both the timing and auxin dose response of the degradation of IAA14 may be different to that of DII-VENUS, in the absence of other data the parameters found in Section 6.2 remain the best estimate of how IAA14 may respond to auxin. The key difference when modelling an Aux/IAA such as IAA14 to modelling DII-VENUS is the induction of IAA14 mRNA in response to auxin, rather than constitutive expression as with DII-VENUS. Following the single cell model described in Section 2.2.3, the expression of IAA14

Table 6.2: Default gene network parameter values used in equations (6.2a)-(6.2j), in conjunction with equations (5.1a), (5.1c), (5.1d), (5.4a), (5.4b) and (5.4e), and the default parameter values for auxin transport given in Table 5.1 describing the complete multiscale model.

parameter	default estimate	description
Q	34.9898	balance between binding and unbinding of Aux/IAA and TIR1
P	0.0254	balance between binding and unbinding of auxin and TIR1
η	177.6257	maximum rate of IAA14 protein decay
$auxin_0$	0.0006256	basal intracellular auxin concentration (nM)
K	0.0914	balance of binding and unbinding of IAA14 and ARF
μ_{im}	0.1153	turnover rate of IAA14 mRNA
θ_{ia}	1.98	binding of ARF to IAA14 promoter
θ_{ir}	0.9646	binding of ARF-IAA14 dimers to IAA14 promoter
n_i	3.3849	co-operativity coefficient of binding on IAA14 promoter
μ_x	1.0	turnover rate of tfX protein
μ_{xm}	2.0	turnover rate of tfX mRNA
θ_{xa}	0.05046	binding of ARF to tfX promoter
θ_{xr}	10.367	binding of ARF-IAA14 dimers to tfX promoter
n_x	4.0	co-operativity coefficient of binding on IAA14 promoter
μ_l	1.0	turnover rate of LAX3 protein
μ_{lm}	0.2	turnover rate of LAX3 mRNA
θ_l	1.0×10^{-8}	binding of tfX to LAX3 promoter
n_l	4.0	co-operativity coefficient of binding on IAA14 promoter
μ_{pa}	4.0	turnover rate of PGa
n_a	4.0	co-operativity coefficient of binding on PGa promoter
θ_{aa}	0.05046	binding of ARF to PGa promoter
θ_{ar}	10.367	binding of ARF-IAA14 dimers to PGa promoter
μ_{pb}	0.1	turnover rate of PGb
θ_b	3.0×10^{-8}	binding of PGa to PGb promoter
n_b	4.0	co-operativity coefficient of binding on PGb promoter
μ_{pg}	0.2	turnover rate of PG
θ_p	0.65	binding of PGb to PG promoter
n_p	4.0	co-operativity coefficient of binding on PG promoter

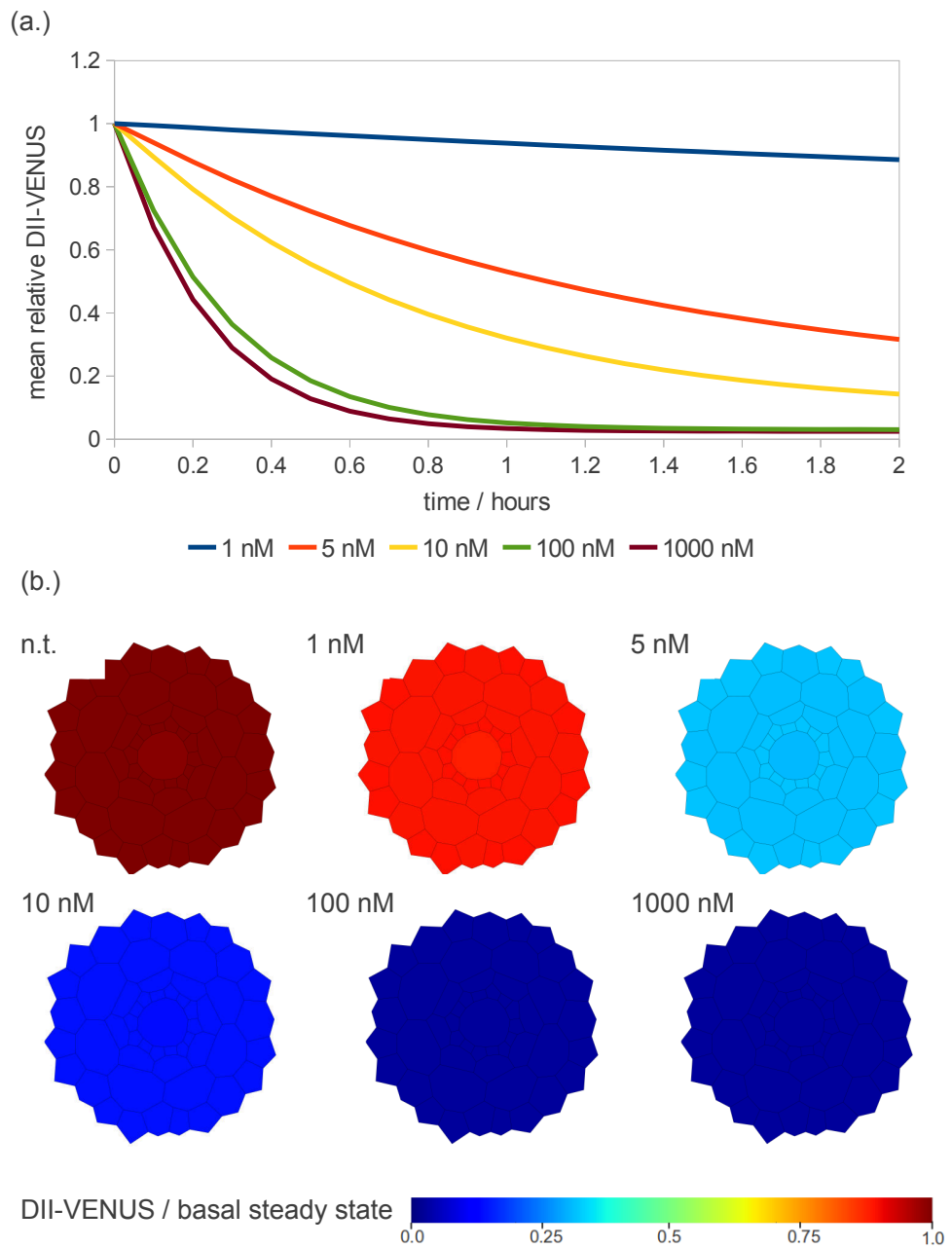


Figure 6.3: (a.) Mean multicell model DII-VENUS against time using the parameters in Tables 5.1, 6.1 and 6.2, for simulated treatment with 1, 5, 10, 100, and 1000 nM exogenous auxin, using the model given by equations (5.1a), (5.1c), (5.1d), (5.4a), (5.4b), (5.4e) and (6.1). (b.) Colour maps showing DII-VENUS in each cell for basal or non-treated (n.t.) tissue, and the simulated treatment concentrations.

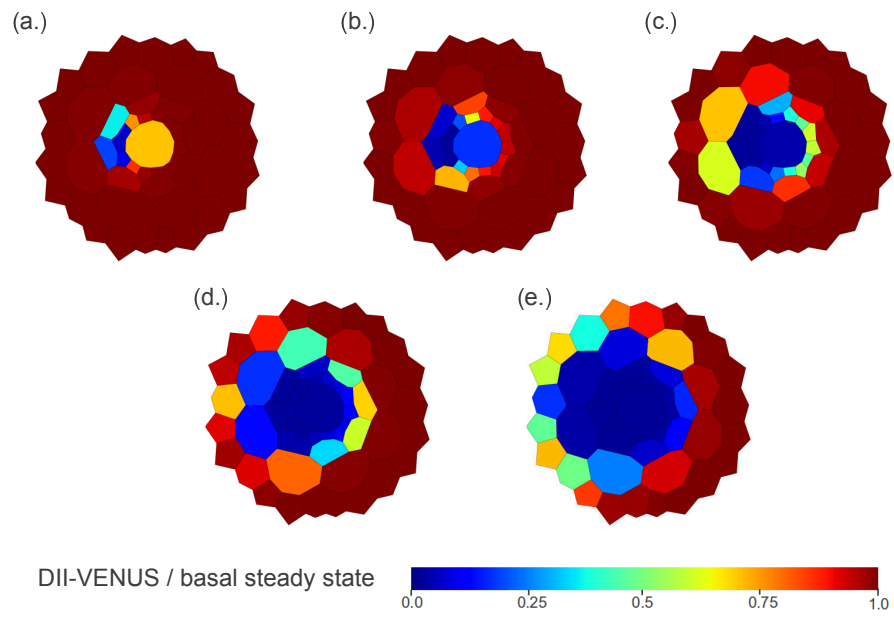


Figure 6.4: Predictions for DII-VENUS distribution in the model given by equations (5.1a), (5.1c), (5.1d), (5.4a), (5.4b), (5.4e) and (6.1) relative to basal steady state with a fixed auxin source representing a LRP in the left-hand central XPP cell, and increasing values for the signal strength in that cell, α_p . (a.) $\alpha_p = 5$, (b.) $\alpha_p = 50$, (c.) $\alpha_p = 500$, (d.) $\alpha_p = 5000$, (e.) $\alpha_p = 50000$. The other parameter values are as shown in Tables 5.1, 6.1 and 6.2.

protein and mRNA is therefore governed by the following two equations:

$$\frac{dIAA_i}{dt} = \frac{-\eta auxin_i IAA_i}{QP + Qauxin_i + auxin_i IAA_i} + IAAm_i, \quad (6.2a)$$

$$\frac{dIAAm_i}{dt} = \mu_{i_m} \left(F_{tc} \left(\frac{K}{\theta_{ia}(IAA_i + K)}, \frac{IAA_i}{\theta_{ir}(IAA_i + K)}, n_i \right) - IAAm_i \right), \quad (6.2b)$$

where the subscript i refers to the concentration in cell i, and:

$$F_{tc}(ACT, REP, n) \equiv \frac{(ACT)^n}{1 + (ACT)^n + (REP)^n}. \quad (6.2c)$$

The default parameters shown in Table 6.2 were selected to replicate the timing and magnitude of the early part of the IAA14 mRNA time course expression profile as shown in Figure 1.9. Figure 6.5a shows the model time course response from basal steady state of IAA14 protein and mRNA for the first 20 hours post 1000 nM simulated auxin treatment. The IAA14 protein is rapidly degraded to its minimum value within two hours, before recovering very slightly in response to increased mRNA expression, while the mRNA begins to be up-regulated almost immediately, gradually increasing over the early part of the time-course before plateauing near its maximum value after around ten to fifteen hours post-treatment. The apparent homeostasis of the auxin response seen experimentally is discussed in Chapters 2 and 3, but without a homeostasis mechanism as is the case here, IAA14 mRNA will remain upregulated as long as the increase in auxin signal persists. This is not initially investigated further as the first objective is to obtain parameter estimates for the early response of IAA14 which may be applied to the simulation of the auxin signal from a LRP. The steady state response of IAA14 mRNA and protein in the model using the parameter estimates in Table 6.2, with a simulated LRP of auxin signal strength $\alpha_p = 5000$ is shown in Figure 6.5b. The distribution of IAA14 is similar to that of DII-VENUS at the same primordia signal strength, but with a smaller relative magnitude of degradation due to the feedback on protein levels from increased mRNA expression. There is a clear induction of IAA14 mRNA throughout the pericycle, greater in magnitude on the side of the root near the primordium, while there is strong induction in half of the endodermal cells, and the two cortical cells nearest the LRP, and weaker induction in the adjacent cells. This expression pattern ought to be indicative of what may be expected for primary auxin response genes. For secondary response genes, such as LAX3, the relative expression between cells may be sharper depending on the relationship between the auxin activated transcription factor and the downstream target gene.

6.4 Secondary auxin response: expression of LAX3

Following the single cell model described in Chapter 2, the expression of LAX3 is activated by the unknown activator tfX, which is itself a primary

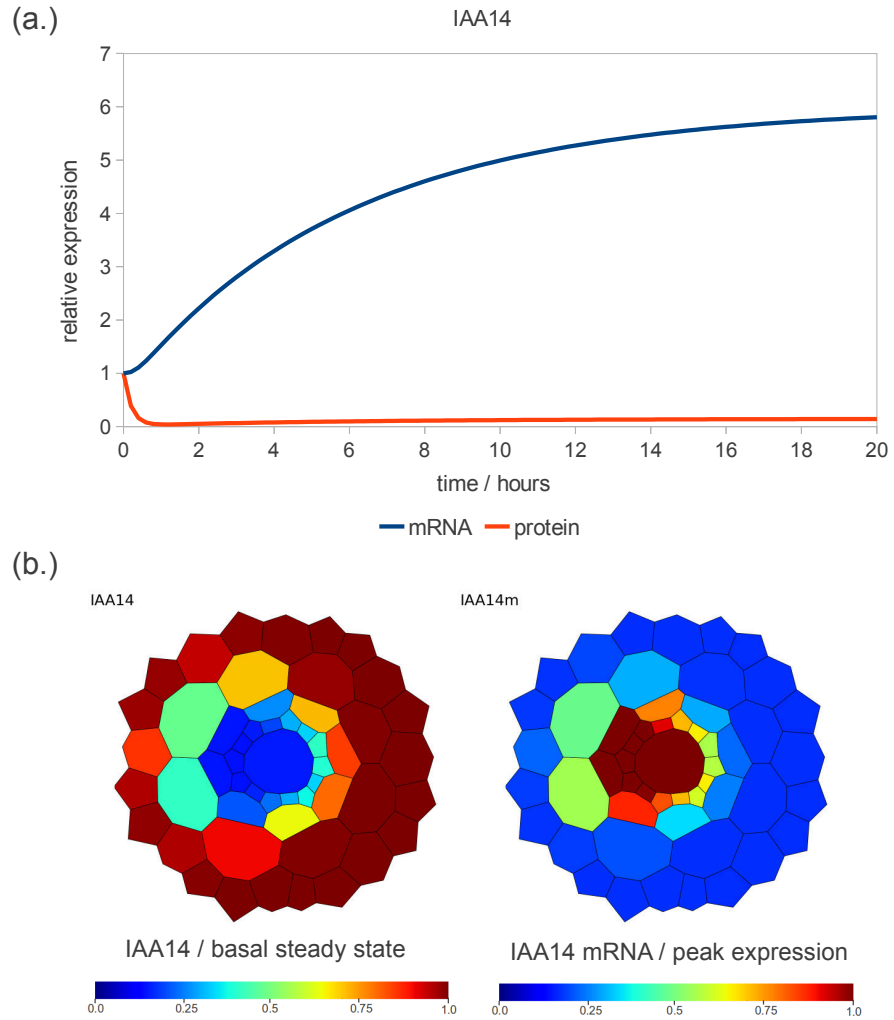


Figure 6.5: (a.) Mean cellular IAA14 mRNA and protein following simulated 1000 nM auxin treatment using the parameters given in Tables 6.1 and 6.2 in the model given by equations (6.2a)-(6.2c), (5.1a), (5.1c), (5.1d), (5.4a), (5.4b) and (5.4e). (b.) Steady state distribution of IAA14 mRNA and protein using the same model and parameters, but with a simulated LRP auxin source ($\alpha_i = 5000$) in the left-hand central XPP cell.

auxin response gene. Using the same notation as in previous models the evolution over time of LAX3 and tfX mRNA and protein is governed by the following equations:

$$\frac{dX_{m_i}}{dt} = \mu_{x_m} \left(F_{tc} \left(\frac{K}{\theta_{xa}(IAA_i + K)}, \frac{IAA_i}{\theta_{xr}(IAA_i + K)}, n_x \right) - X_{m_i} \right), \quad (6.2d)$$

$$\frac{dX_i}{dt} = \mu_x (X_{m_i} - X_i), \quad (6.2e)$$

$$\frac{dLAX_{m_i}}{dt} = \mu_{l_m} \left(\frac{X_i^{n_l}}{\theta_l^{n_l} + X_i^{n_l}} - LAX_{m_i} \right), \quad (6.2f)$$

$$\frac{dLAX_i}{dt} = \mu_l (LAX_{m_i} - LAX_i), \quad (6.2g)$$

where as before the subscript i refers to the concentration in cell i , and F_{tc} and the parameters are defined as previously. In contrast to $auxin_i$, DII_i , IAA_i and $IAAm_i$ which are defined for all cells in the tissue, X_{m_i} , X_i , LAX_{m_i} and LAX_i are only defined for cells within the cortex and epidermis. When this model for LAX3 expression is used in conjunction with the auxin transport model given by equations (5.1a), (5.1c), (5.1d), (5.4a), (5.4b) and (5.4e), and the model for IAA14 expression given by (6.2a)-(6.2c), the feedback of the level of LAX3 on cellular auxin is included by setting $LAX_{i,j} = LAX_i$ for all i in equation (5.1d), so that LAX3 is localised to every cell membrane of the cell where it is expressed. In biological reality, there may be a delay to this localisation process and the relationship between expressed mRNA and membrane bound protein may even be non-linear, but this is left to future study.

The parameters governing the magnitude and auxin sensitivity of tfX mRNA expression, θ_{xa} , θ_{xr} , and n_x , are selected so that steady state tfX mRNA increases with increasing auxin within the range of auxin expected in the cortical cells near the developing LRP (Figure 6.6, for parameter values see Table 6.2). The timing of the tfX mRNA and protein response depends on the parameters μ_{x_m} and μ_x , and to ensure a relatively rapid response of tfX we set $\mu_{x_m} = 2.0$ and $\mu_x = 1.0$. The equation for LAX3 mRNA expression includes a Hill function setting the rate of transcription for a given value of tfX protein. By setting the co-operativity coefficient (n_l) sufficiently high, and the value of half maximum expression (θ_l) between the value for tfX when auxin is in the range expected in the two cortical cells nearest the LRP and the value for tfX when auxin is in the range expected in the two neighbouring cells, the steady state expression of LAX3 mRNA has a sigmoidal shape with increasing auxin, as shown in Figure 6.6. The default parameters used are given in Table 6.2.

The temporal response of a single cell in the model in response to simulated auxin treatment can be tested by fixing $auxin_i$ to the basal value of $0.000625 \mu M$, running to steady state, and then changing $auxin_i$ to the fixed treatment value of $1.0 \mu M$. The time course solution of the model for the first 40 hours post-treatment is shown in Figure 6.7. The mRNA of tfX is the first model species to peak after around two hours, before settling

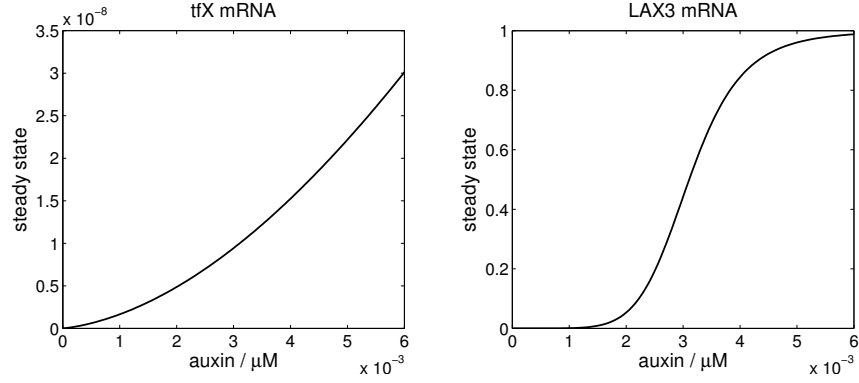


Figure 6.6: Steady state tfX and LAX3 mRNA using the parameter values in Table 6.2 in the model given by equations (6.2) for increasing fixed values of $auxin_i$ in every cell.

at a lower, though still many-fold greater than basal, steady state level between 10 and 20 hours post-treatment, with tfX protein following the mRNA with a 2 to 3 hour delay. The drop in tfX expression following the initial peak may be due to increased IAA14 protein levels. LAX3 mRNA begins to be expressed as the tfX protein is produced, but in the absence of a homeostasis mechanism continues to climb up to between 10 and 20 hours post-treatment. The timing of this accumulation of LAX3 may be altered by changing the value of the parameter μ_{l_m} , but using the default value of $\mu_{l_m} = 0.2$ produces a result roughly comparable with the early timing of LAX3 mRNA accumulation seen experimentally (Figure 4.1). As with tfX there is a delay in the time course profiles between mRNA and protein, but in the case of LAX3 a value for $\mu_l = 0.2$ results in a delay of several hours between the mRNA and protein. This is again consistent with experimental observations of the time taken post-auxin treatment for LAX3-YFP to be visible (Silvana Porco, personal communication), compared with the up-regulation of the mRNA, though it may be that part of that delay is taken up by the localisation and maturation of the LAX3-YFP protein.

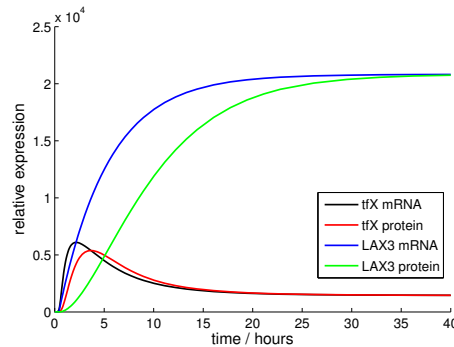


Figure 6.7: Time course of tfX and LAX3 mRNA and protein using the the model given by equations (6.2), using the parameter values in Table 6.2, following a change in the fixed value value of $auxin_i$ in every cell from the basal value of 0.000625 to $auxin_i = 1.0$, to simulate treatment with $1 \mu M$ exogenous auxin.

Transferring the model to the multi-cellular context by using the pri-

mordium simulation as described previously results in the time-courses and spatial distributions of model species as shown in Figures 6.8 and 6.9. The addition of the auxin signal results in the rapid increase in cellular auxin in each of the four labelled cortical cells, with a much greater fold-change seen in the two central cells (labelled 2 and 3). This increase in auxin is manifested by a decrease in IAA14, and up-regulation of the primary response genes. Again, this up-regulation is much greater in cells 2 and 3, and furthermore the recovery of IAA14 protein resulting from the up-regulation of the mRNA is proportionally greater in the two outer cells (labelled 1 and 4) further limiting the steady state expression of auxin responsive genes in those cells. The non-linear auxin dose response of *tfX* widens the difference in expression between the two outer and two inner cells, and this is further magnified in the expression of *LAX3*, where there is clearly strong expression in cells 2 and 3 and little to no expression in cells 1 and 4. Once *LAX3* is expressed, the positive feedback on auxin further widens the difference in expression between the two central cortical cells and two neighbouring cells. The increase of auxin in cells 2 and 3 is such that the final level of auxin in both those cells is greater than that following the initial increase caused by the introduction of the auxin signal in the LRP. This elevation of cellular auxin by *LAX3* will become important when modelling the expression of the cell wall remodelling enzyme (CWRE) PG, as described in the following section.

6.5 Tertiary auxin response: expression of PG

Though little is yet known about the regulation of polygalacturonase, in Swarup et al. (2008) it is shown to be expressed in the cortical cells near developing LRP, depend on *LAX3* for this induction, and to be induced by auxin. Its role as a CWRE (Kim et al. 2006) provides a link between the expression of *LAX3* and the the expression of PG and normal lateral root emergence. The qRT-PCR data shown in Figure 4.1 shows a long temporal delay of between 3 to 5 hours post-auxin treatment before PG begins to be expressed. This time delay leads to the hypothesis that PG may be at least a tertiary auxin response gene, i.e. a primary auxin gene is regulated directly by the interactions of ARFs and Aux/IAAs, which activates a secondary response gene, which then activates PG. If we denote the primary auxin response (PGa) in cell *i* by PGa_i , the secondary response (PGb) in cell *i* as PGb_i , along with PG in cell *i* (PG_i) they can be modelled by the following equations:

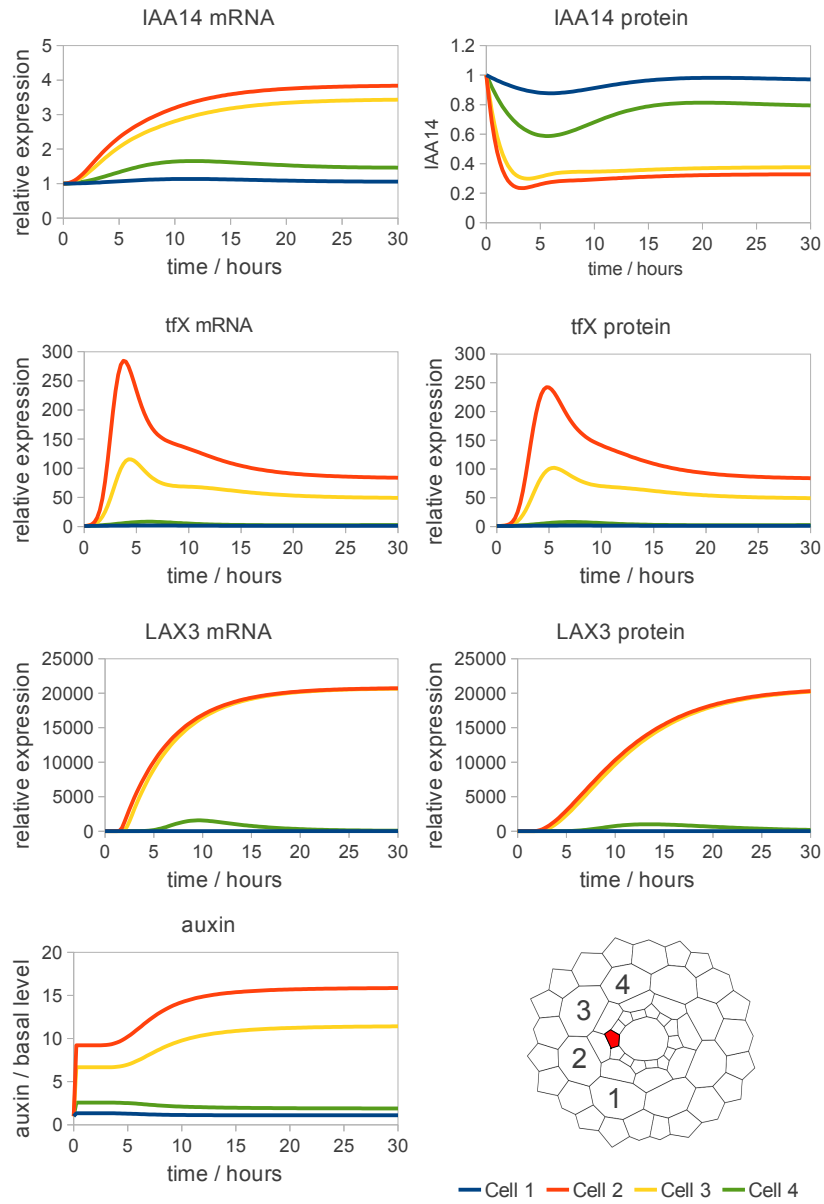


Figure 6.8: Timecourses of each model species in the model given by equations (5.1a), (5.1c), (5.1d), (5.4a), (5.4b), (5.4e) and (6.2a)-(6.2g) for each of the four cortical cells nearest the simulated LRP (labelled 1-4 at bottom right of figure, the red cell is the cell with the auxin source) for the first 30 hours following the switching on of the auxin signal ($\alpha_i = 5000$) in the source cell. In each case the plots are shown relative to the basal steady state at $t = 0$. LAX3 protein is only strongly expressed in the two central cells (2 and 3), and results in elevation of auxin levels in both these cells greater than that caused by the initial signal from the LRP alone. For parameter values see Tables 5.1 and 6.2.

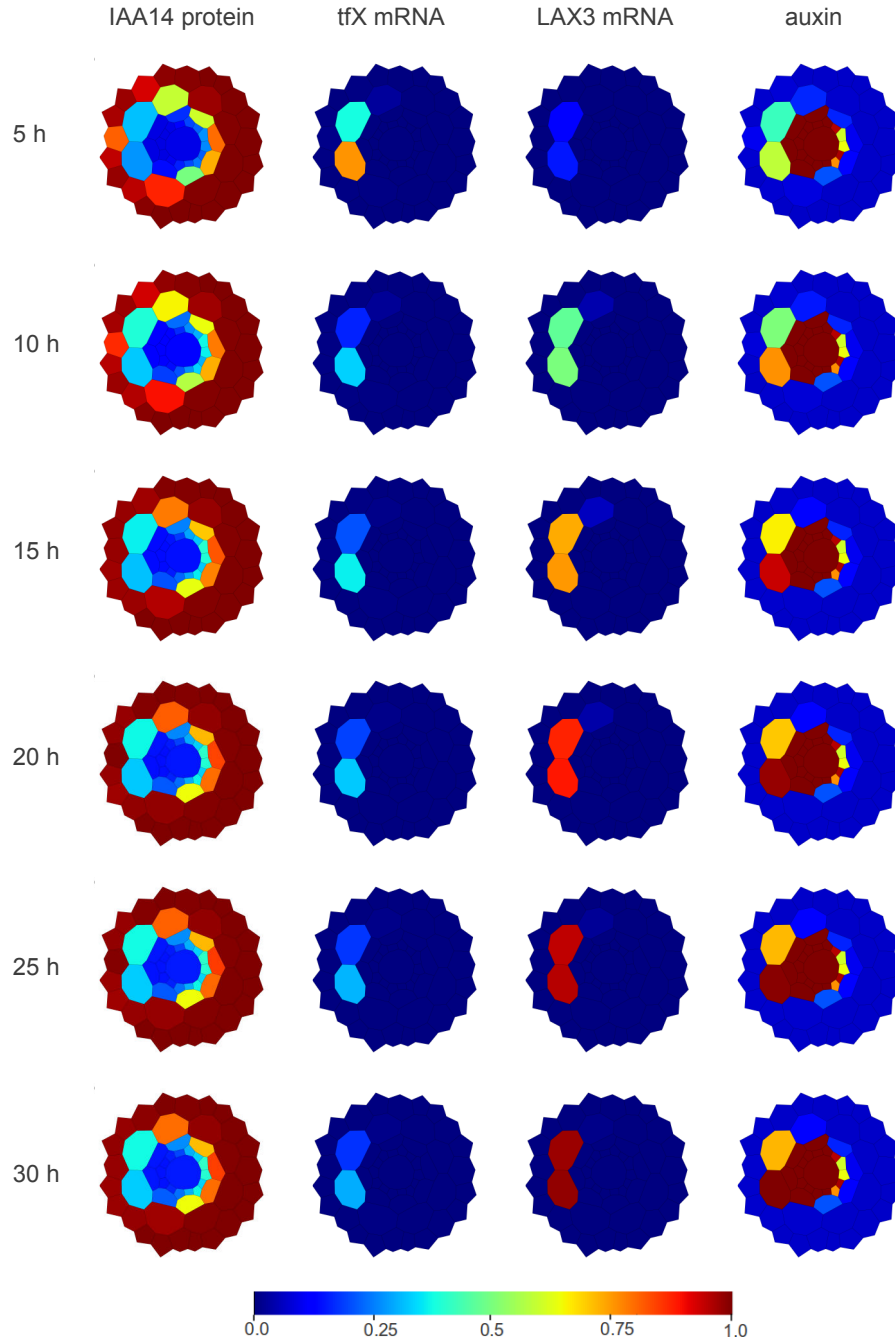


Figure 6.9: Spatial distribution of IAA14 protein, tfX mRNA, LAX3 mRNA, and auxin at 5 hour intervals after the introduction of an auxin source simulating a LRP at time = 0.0 using the model given by equations (5.1a), (5.1c), (5.1d), (5.4a), (5.4b), (5.4e) and (6.2a)-(6.2g) run from basal steady state. The primordium is simulated by increasing α_i to 5000 in the central XPP cell on the left-hand side of the cross-section. Each colour map is scaled relative to the maximum value seen for each model species within the cortex. For parameter values see Table 6.2.

$$\frac{dPGa_i}{dt} = \mu_{pa} \left(F_{tc} \left(\frac{K}{\theta_{aa}(IAA_i + K)}, \frac{IAA_i}{\theta_{ar}(IAA_i + K)}, n_a \right) - PGa_i \right), \quad (6.2h)$$

$$\frac{dPGb_i}{dt} = \mu_{pb} \left(\frac{PGa_i^{n_b}}{\theta_b^{n_b} + PGa_i^{n_b}} - PGb_i \right), \quad (6.2i)$$

$$\frac{dPG_i}{dt} = \mu_{pg} \left(\frac{PGb_i^{n_p}}{\theta_p^{n_p} + PGb_i^{n_p}} - PG_i \right), \quad (6.2j)$$

where we keep the convention that the μ parameters refer to turnover rates, the θ parameters binding thresholds, and n parameters co-operativity coefficients, and the subscripts a , b and p refer to the genes PGa, PGb and PG respectively. For simplicity, the mRNA and proteins of PGa, PGb and PG are combined into single equations for each gene, with the assumption that any delay between the expression of mRNA and protein can be accounted for by the values of the parameters μ_{pa} , μ_{pb} and μ_{pg} .

The parameter values for the PG model are selected so that there is a switch in expression with increasing auxin steady state, with expression kept as low as possible for values of cortical auxin seen before the feedback from LAX3 is present, and high expression for the values of fixed auxin seen in the cells following LAX3 expression. The default parameter values chosen are given in Table 6.2, and the steady state expression of PG and activators with increasing auxin is shown in Figure 6.10.

There is very low steady state PG expression when auxin is fixed below the maximum level seen in the cortex pre-LAX3 expression ($0.0057 \mu M$), and a rapid switch to higher PG expression for auxin above that level. Because of this, strong PG expression would only be expected to be seen in cells which also express LAX3 strongly, as the positive feedback on auxin from LAX3 is required to elevate auxin sufficiently for PG expression to occur. If the *lax3* mutant is simulated by switching off the expression of LAX3 in the model, PG expression would be expected to be greatly limited.

Also shown in Figure 6.10 is the predicted time course of PG mRNA for simulated $1 \mu M$ auxin treatment. The parameter values are chosen so that the timing of expression is roughly comparable with that seen experimentally (Figure 4.1), with little or no PG expression seen before 5 hours post-treatment, and then gradual accumulation of PG mRNA up to around 20 hours. As with the other genes, in the absence of a homeostasis mechanism the level of expression remains high throughout the time course, in contrast to the experimental data where PG expression appears to be returning to the basal level at the final 36 hour time point.

To test whether the model can simulate the lack of PG expression in the *lax3* mutant in comparison to the wild type, where PG expression is strong but restricted to the specific cortical cells over LRP, the primordium simulation was run with LAX3 set equal to zero in every cell, and compared with the ‘wild type’ simulation with LAX3 expressed normally as described previously. The model time courses for PG mRNA for the two cortical cells nearest the LRP, in both wild type and the simulated *lax3* mutant, are shown in Figure 6.11, which also shows colour maps at regular time

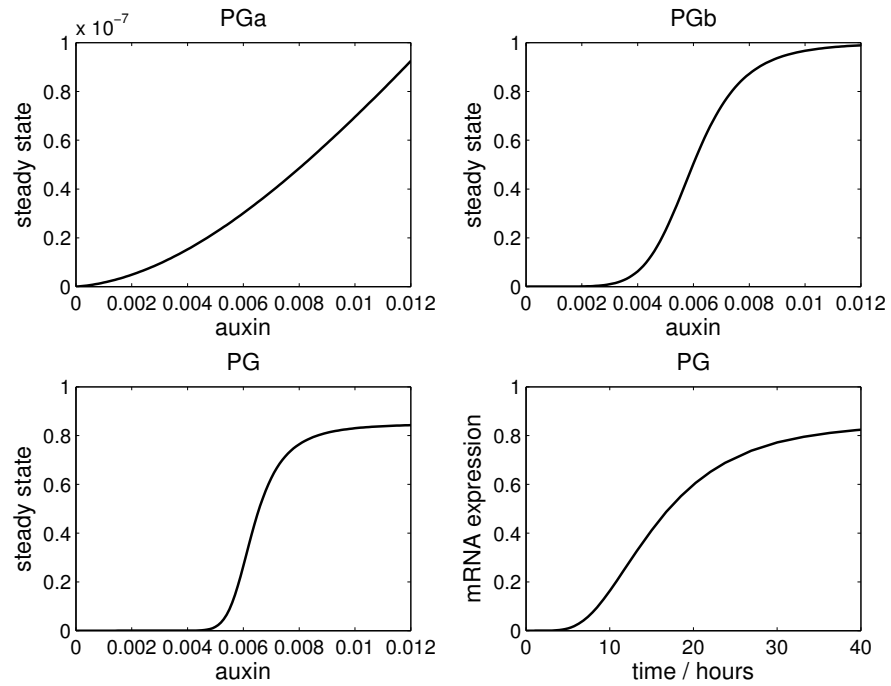


Figure 6.10: Top left, top right, bottom left: Steady state PGa , PGb and PG with increasing auxin in the range seen in the four cortical cells nearest the LRP in the primordium simulation, using the parameter values given in Table 6.2 in the model given by equations (6.2a)-(6.2j) for increasing fixed values for $auxin_i$. Bottom right: Model PG mRNA expression against time using the same parameter values following an increase in the fixed value of $auxin_i$ to simulate treatment with $1 \mu M$ exogenous auxin.

points showing the level and spatial distribution of PG in both the simulated genotypes.

Expression of PG is very close to zero in all but the two cells for which the time courses are shown (cells 2 and 3). For the first 5 hours following the introduction of the LRP signal there is little to no PG induction in either simulated wild type or *lax3* mutant. Between 5 and 10 hours there is a similar induction of PG in both genotypes, with slightly higher PG expression in cell 2 than in cell 3. After 10 hours the difference between the wild type and *lax3* mutant becomes clearer. While in the wild type PG expression continues to rise in both cells up to the end of the 40 hour time course, in the *lax3* mutant, the final level of PG expression is much lower in both cells compared to the wild type. Though the auxin signal from the primordium is sufficient to trigger transient expression of PG, the lack of positive feedback on cellular auxin provided by LAX3 expression means that that expression is not sustained as is the case in the wild type, where the sustained induction results in strong PG expression in both the cortical cells nearest the LRP.

For the time-course simulations above, the auxin signal in the LRP is fixed at an estimate of $\alpha_p = 5000$. In Figure 6.12 the effect of changing this parameter on steady state expression of LAX3 and PG is tested. With increasing α_p there is a clear switch from low to high LAX3 expression in the two cortical cells nearest the LRP between around $\alpha_p = 1000$ and $\alpha_p = 3000$, with expression in cell 2 switched on at a slightly lower signal strength than that in cell 3. Above $\alpha_p = 10000$ LAX3 expression in cell 4 is switched on, but expression in cell 1 remains low even at the maximum value for α_p simulated. As expected, a higher auxin signal is required to switch on PG, with the switch from minimum to maximum expression in cells 2 and 3 between around $\alpha_p = 2000$ and $\alpha_p = 6000$, with expression in cell 4 not switched on below $\alpha_p = 15000$. Because of this, even when the primordium signal strength is sufficiently high to switch on expression in three cortical cells, this is not enough to switch on expression of PG outside of the region required for lateral root emergence.

In the absence of LAX3, as in the *lax3* mutant simulation, the expression of PG is clearly not switched on in both cells 2 and 3 until a higher primordium signal strength is reached than in the wild type simulation. With the estimate for $\alpha_p = 5000$, as used for the time course simulations, expression in cell 3 remains very low, while in cell 2 expression of PG is only around a quarter of the value seen in the wild type. If high expression of PG is needed in both of the two cortical cells nearest the primordium for normal emergence to occur, this will clearly be impaired in the *lax3* mutant.

6.6 Discussion

By embedding a version of the single cell LAX3 expression model from Chapter 2 into a multicellular framework it is possible to show that provided there is a sufficiently sharp switch in LAX3 expression with increasing auxin signal, it is possible to simulate the experimentally observed expression pattern of LAX3 in the specific cortical cells over the developing LRP.

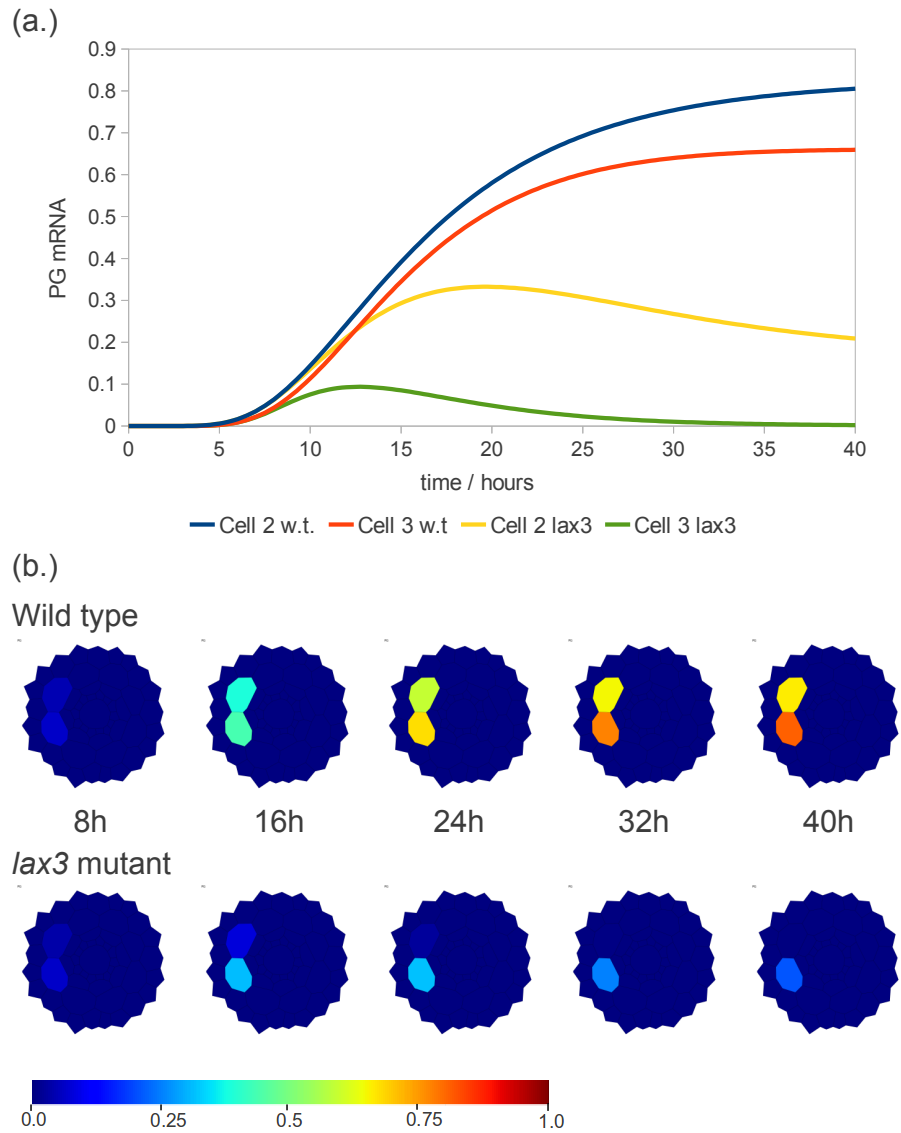


Figure 6.11: (a.) Time course of model PG mRNA in the two cortical cells nearest the LRP, following the introduction of an auxin signal in the primordium cell, for both the simulated wild type and *lax3* mutant. In the *lax3* mutant, LAX3 is set equal to zero in every cell. The locations of the cells annotated cell 2 and 3, and the primordium cell are as shown in Figure 6.8. (b.) Spatial distribution of PG expression in both the wild type and *lax3* mutant simulations at eight hour intervals following the introduction of the LRP auxin signal. The model is given by equations (5.1a), (5.1c), (5.1d), (5.4a), (5.4b), (5.4e) and (6.2a)-(6.2j) and the parameter values are as shown in Tables 5.1 and 6.2.

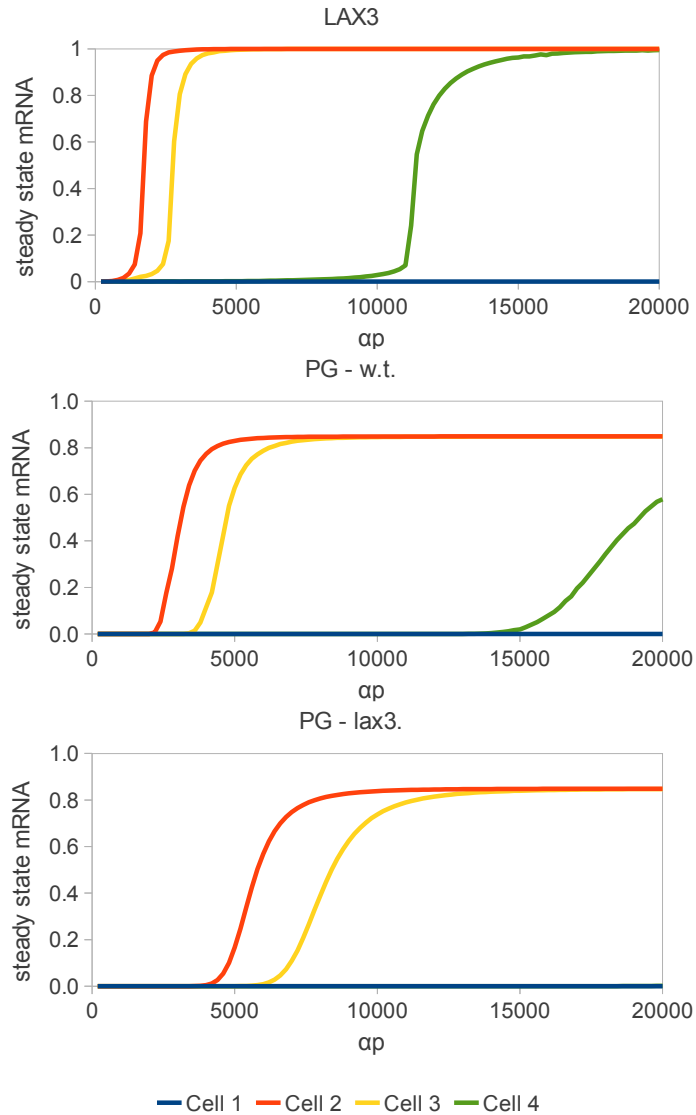


Figure 6.12: Steady state LAX3 mRNA (top), PG mRNA in the wild type simulation (middle), and PG mRNA in the *lax3* mutant simulation (bottom) in each of the four cortical cells labelled 1-4 in Figure 6.8, with increasing primordium signal strength α_p . The absence of LAX3 as in the *lax3* mutant clearly impairs the expression of PG at lower auxin signal strength. The model is given by equations (5.1a), (5.1c), (5.1d), (5.4a), (5.4b), (5.4e) and (6.2a)-(6.2j), the parameter values are as shown in Tables 5.1 and 6.2 and the locations of the cells annotated 1 to 4, and the primordium cell are as shown in Figure 6.8.

Furthermore, by changing the signal strength of the auxin source in the cell simulating the LRP it is seen that a broad range of auxin concentrations in the primordium will replicate this expression pattern. The model is also able to show the same spatial pattern for PG, with expression limited to the two cortical cells nearest the LRP. In addition, with the parameter values used, there is a range of primordium signal strengths for which expression of PG is dependent on the positive feedback from LAX3 on intracellular auxin, so that in the *lax3* mutant simulation the expression of PG is clearly impaired. If PG is required for emergence, the simulation demonstrates that without LAX3 then emergence may be impaired.

While there is likely to be biological variability in the strength of auxin signal from the primordium, the model system ensures that even at an extremely high auxin signal such that LAX3 is expressed outside of the expected two cells in the cortex, the spatial expression pattern of PG can remain restricted to the two cells between which the growing primordium is expected to pass. This robustness of the PG spatial expression pattern to high primordium signal strength may help protect the root from the unwanted softening of cell walls outside of the region necessary for emergence. By a similar argument, in the *lax3* mutant an unusually high signal strength may still result in high PG expression in the cells necessary for emergence, despite the lack of positive feedback from LAX3. However, as observed in Swarup et al. (2008), emergence is impaired rather than blocked entirely in the *lax3* mutant, and so there is a possibility that PG may still be intermittently expressed correctly in the *lax3* mutant, as is the case in the model simulation for a high primordium signal strength.

In addition to replicating the steady state spatial expression pattern for LAX3 and PG expression over a realistic range of auxin concentrations, by comparison with experimental data the model is also able to replicate the timing of the key events leading to the expression of LAX3 and PG, which ultimately leads to lateral root emergence. The most rapid event is the redistribution of auxin following a change in source signal or carrier distribution which over a time scale of seconds to a few minutes, consistent with the rapid early response of DII-VENUS seen in response to auxin treatment (Band et al. 2012). The DII-VENUS is also used to approximate the temporal and dose response of Aux/IAA protein to different auxin distributions in the multicellular context, which as the key regulator of auxin responsive genes partly determines the rapidity of response of mRNA expression of the hypothetical primary response genes *tfX* and *PGa*, and of the known primary response gene *IAA14* mRNA. While the level of Aux/IAA is set to change from one steady state to another following a redistribution of auxin within around 2 hours, depending on the turnover rates the response mRNAs may change to a new level quickly within a few hours, or as in the case of *IAA14* accumulate more slowly before reaching a peak in expression after ten hours. The secondary response genes are delayed further with LAX3 continuing to accumulate for 15-20 hours, and the tertiary response genes may be delayed further still.

By working with the hypothesis that PG is a tertiary response gene, its expression is delayed by the time taken to transcribe and translate the two

precursors needed for its expression. With the parameter values used, there is little or no expression of PG for five hours following the introduction of the auxin signal, and following this it takes 10 or more hours before it is strongly expressed. In addition, the nonlinear regulation of the intermediate genes may be a mechanism to sharpen the switch-like response of PG expression, to produce the all-or-nothing spatial expression pattern, and limit its expression in order to maintain the integrity of the root structure. Regulating PG in this ways ensures that a strong persistent auxin signal is required in order for the CWRE PG to be expressed, and prevents small transient fluctuations in auxin resulting in the major changes in cell wall structure seen during emergence.

Chapter 7

Concluding Remarks

7.1 Bistability in LAX3 mRNA expression

The single cell model of LAX3 mRNA expression described in Chapter 2 is able to show hysteresis when changing the value of auxin signal, so that at low auxin signal there is a stable steady state of low expression of LAX3, at high auxin signal there is a stable steady state of high expression, and for an intermediate range of auxin signal there is bistability, where both high and low stable steady state expression may occur. Though in the bistable region there is an additional steady state at which LAX3 is expressed at intermediate values, this steady state is unstable and so persistent expression at intermediate values is very unlikely. In the plant, LAX3 protein appears to be strongly expressed only in a small number of cells directly over lateral root primordia, with no expression visible in the adjacent cells. The model shows that this observed all or nothing LAX3 expression pattern may be formed and maintained by the jump from low to high expression as auxin in the cortical cells increases closer to a lateral root primordium.

Based on the biological evidence that LAX3 is a secondary auxin response a transcriptional activator of LAX3 (tfX), itself a primary auxin response, is included in the model. Study of a model in which LAX3 is instead a primary auxin response may help establish a biological function for tfX if it is shown that the additional downstream transcription factor is required for bistability in the model, or at least broadens the range of key parameters needed for bistability. If this is the case the extra step between primary auxin response and LAX3 expression may have a role in sharpening the response of LAX3 to a range of auxin signals. Furthermore, if tfX can be identified, this could possibly be tested experimentally by expressing LAX3-YFP under the activation of the tfX promoter in a *lax3* mutant background. If the additional step sharpens the expression pattern of LAX3, expressing it as a primary auxin response ought to broaden its domain of expression. More directly, a marker for tfX expression, once identified, can be compared with the LAX3 expression pattern. Identification of tfX will also allow study of the number of ARF binding sites (AuxREs) on its promoter, and the possible binding sites for tfX on the LAX3 promoter. A large number of binding sites would support the bistable model since a high co-operativity of transcription factor binding on both the tfX

and LAX3 promoters are shown to be important parameters in introducing bistability to the model. Again, this could be tested further experimentally by mutating binding sites and observing any resulting differences in LAX3 expression. At the time of writing a strong candidate for *tfX* has been identified and the results of experiments currently underway will hopefully form the basis of ongoing collaboration.

7.2 Sources of auxin homeostasis

An initial qualitative observation drawn from the qRT-PCR data is that the induction of LAX3 and other mRNAs following exogenous auxin treatment is transient, i.e. there is an initial up-regulation of mRNA before the expression level peaks and returns in time to around the basal level of expression. However, if we assume that the exogenous auxin signal is persistent over time the initial model is unable to capture this behaviour. In contrast, introducing a decay to the auxin signal, distinct from the intracellular turnover rate, allows the model to fit the qRT-PCR data quantitatively and results in the prediction that as the level of cellular auxin and mRNA drops there is a matching recovery in the level of Aux/IAA as its rate of degradation returns to the basal level. Experimental evidence for this recovery is given by quantification of DII-VENUS over a 30 hour time period in which a similar recovery is seen. Two possible explanations for the apparent reduction in cellular auxin over time following an initial increase post-treatment are the degradation in light of the auxin in the experimental medium and some endogenous mechanism by which the plant is able to maintain auxin homeostasis. The former was tested by measuring the rate of decay of auxin in the medium due to exposure to light alone. While significant degradation of auxin does occur, adding this rate of decay to the auxin signal in the model is insufficient to match the recovery in the DII-VENUS data over the 30 hour time course. The prediction of the model that the measured rate of decay is too slow to explain may be tested further by repeating the DII-VENUS quantification at a range of auxin treatments.

The second hypothesis explaining the transient response of DII-VENUS and ARF target mRNAs to auxin treatment is the presence of an endogenous auxin homeostasis mechanism. One possible mechanism was modelled in Chapter 3, in which a member of the primary auxin responsive gene family GH3 increases the rate of intracellular auxin turnover by binding with it and conjugating it with amino acids. A combination of positive feedback to auxin from LAX3 expression and negative feedback to auxin from GH3 can result in damped or persistent oscillations in gene expression depending on model parameter values, and parameter sets exist in which the model can match the LAX3 and IAA14 mRNA expression data via one such damped oscillation. However, the oscillations in expression depend on a slower accumulation of GH3 protein in response to auxin relative to that of LAX3, which, since GH3 is a primary auxin response gene and LAX3 is at least a secondary response gene may be biologically unrealistic. Experimental data relating to the GH3 conjugation model is currently limited. Useful data to test the model further would include qRT-PCR following auxin treatment

of the GH3s which are involved in auxin conjugation, and LAX3 mRNA expression data in plants missing one or more functional GH3s. If GH3 has a role in reducing cellular auxin post-treatment it is expected that auxin induced expression will remain higher for longer in mutant plants when compared to wild type. It may be necessary to create mutants missing multiple GH3s to observe any effect due to genetic redundancy. Another line of investigation is to look at the long term behaviour of DII-VENUS in *gh3* mutant plants. Here it would be expected that the recovery of DII-VENUS over time following its initial degradation post-auxin treatment would occur more slowly in the mutants.

Though the GH3 based auxin homeostasis model requires experimental validation it seems likely that the degradation of auxin in the experimental medium is unable to account fully for the apparent removal of excess auxin from the cell, and that a combination of decay in the medium and some as yet unconfirmed endogenous homeostasis mechanism acts to produce a transient genetic auxin response post- exogenous treatment.

7.3 The role of ARF19 in LAX3 expression

The question of how ARF19 may act as a repressor of LAX3 was addressed in Chapter 4. Firstly, several parameters determining the behaviour of ARF19 were identified that, when the values used were sufficiently different relative to the equivalent values for ARF7, allowed it to repress transcription of target genes. These included the strong binding of ARF19 to IAA14, so that though the total level of ARF19 is increased following auxin treatment, its strong affinity with IAA14 means a large proportion of this is bound with the Aux/IAA and so acts as a transcriptional repressor. Some work has been done to establish that IAA14 binds with both ARF7 and ARF19 in a yeast two hybrid system (Fukaki et al. 2005), but further experiments are needed to establish the relative importance of these interactions in the plant. For example, how does mutating domains III and IV of ARF19 affect gene expression? These domains are thought to facilitate dimerisation of ARF19 with Aux/IAs and so blocking this interaction ought to prevent formation of repressors, and an increase in LAX3 expression relative to wild type may give evidence of the importance of the interaction between IAA14 and ARF19 in repressing LAX3. Another important parameter determining the relative expression of target genes in the wild type and *arf19* mutant simulations is the relative power of ARF19 to activate transcription relative to that of ARF7. A low value for this parameter means that regardless of whether or not an Aux/IAA is bound to it, if ARF19 is bound to a gene promoter transcription is very unlikely to be activated. In this way an increased pool of ARF19 will act to repress transcription by occupying binding sites which may otherwise be occupied by ARF19. An experiment to test this would be to observe the affect of replacing domain II in ARF19 with that of ARF7, or otherwise mutating it to remove its function. If this domain determines the activatory (or repressive) power of ARF19, and is more effective in ARF7, replacing it with the ARF7 domain II should increase expression of target genes.

The remainder of Chapter 4 presents a number of hypothetical gene regulatory networks for the ARF19 mediated repression of LAX3, and the ability of each to fit the available data is tested using the parameter fitting algorithm. In general terms, the best models appear to need an unidentified transcription factor, activated by ARF19, binding to the LAX3 promoter and repressing its transcription, in addition to a decay over time in the auxin signal. Some models with additional regulatory components may improve the fit of model to data, but it is unclear whether this is due to a closer reflection of the biological reality or simply a result of adding more components and parameters. The use of some method to stastically compare the goodness of fit of the different models (e.g. Akaike information criterion) would help in model selection. Despite differences between regulatory models, a common prediction is the relatively flat time course profile of the protein repressing LAX3 (whether this is an ARF19 activated gene or ARF19 itself), possibly due to slow turnover of the protein, low responsiveness to auxin, or a combination of the two. This observation then leads to the possibility that the auxin responsiveness of the LAX3 repressor may not be required at all to obtain the observed wild type expression profile of LAX3. The hypothesis can be tested using the model by fixing a constant level of ARF19, rather than having it induced by auxin, and experimentally by having ARF19 expressed constitutively in an *arf19* mutant background, though there may be confounding effects from ARF19 being expressed in this way. A follow on question then is, if ARF19 does not necessarily need to be auxin inducible to mimic wild type expression of LAX3, is the up-regulation of ARF19 by auxin important in the normal expression of other genes? Additionally, what is the biological role of ARF19 mediated repression of LAX3? One possibility is that it helps spatially restrict LAX3 expression only to cells where it is required, a hypothesis that may be tested in future using the multicellular modelling framework developed in Chapters 5 and 6.

7.4 Multiscale Model and Ongoing Challenges

Simulating the diffusion of auxin from a primordium source cell in the pericycle throughout a root cross-section using the multicellular framework described in Chapter 5 gives predictions for the cellular auxin distribution that may be present in a living root. A key parameter affecting this distribution is the rate of intracellular auxin turnover, with a low rate resulting in smaller relative differences between cells, and a high rate producing much larger relative differences in auxin concentrations between cells. In the latter case the greater difference in auxin signal between adjacent cells in the cortical cell layer means that any switch-like response of LAX3 to auxin would need to be much less finely tuned than for a low intracellular auxin turnover rate. The intracellular auxin turnover rate also affects the power of LAX3 to amplify the relative level of auxin within cells, with a high turnover rate resulting in a much greater fold-change increase in intracellular auxin concentration post-LAX3 expression than that seen in the model with a low auxin turnover rate. This is important since if the extra auxin

in cells due to LAX3 is required to switch on the expression of CWREs, a larger difference in cellular auxin pre and post-LAX3 expression will help to further focus the auxin in the local region only into those specific cells expressing LAX3.

A key problem with the model with a high auxin turnover rate is that the difference in auxin concentration between the primordium source cell and in the cortical cells nearest to it varies by around two orders of magnitude, so that if auxin in the source cell is around $1 \mu M$, the maximum auxin in the cortex is around $1 pM$, which may not be enough to trigger an auxin response. This relative difference is partly reduced by including apoplastic movement of auxin in the model, but this transport route may in reality be blocked by the presence of the Casparian strip in the endodermis. Further investigation of lateral root emergence in mutants defective in Casparian strip formation may help determine the relative importance of this pathway. Adding PIN transporters directing auxin from pericycle to endodermis also reduces the relative auxin difference between pericycle and cortex, and so better determining the usual configuration of PINs in the radial cross-section using either existing or new images will help produce a more realistic model. In particular, this should include modelling the individual cells and PIN and auxin distribution within the stele, for which data is available suggesting that auxin is directed by PINs towards opposing xylem poles (Bishopp et al. 2011), which may help reinforce the maxima in primordia in the pericycle. Finally, it is always possible that another mechanism, such as diffusion through plasmodesmata, which would enable movement of auxin between cells without traversing cell walls, may allow greater movement of auxin from the primordium source to the overlying cortical cells, and this should be considered in future models.

In Chapter 6, the asymmetry in cortical auxin distribution relative to a pericycle auxin source is used in conjunction with switch-like expression of *tfX* and LAX3 to produce very strong expression of LAX3 in only the two cells nearest the primordium, matching the experimentally observed expression pattern. The positive feedback on auxin in these two cells from LAX3 active transport reinforces the spatial expression further, and increases auxin in these two cells sufficiently so that the CWRE polygalacturonase (PG), which is modelled as a tertiary auxin response gene, is eventually expressed. The high auxin threshold required for the switching on of PG ensures that if LAX3 is removed from the model, as when simulating the *lax3* mutant, PG expression is all but removed, matching experimental observation. Furthermore, in the wild type simulation, even if the auxin signal in the primordium is greatly increased so that LAX3 is switched on in more than two cells, the expression of PG is still restricted only to the two cells nearest the primordium.

In addition to matching the observed spatial expression patterns of PG and LAX3, the model also gives predictions for the spatial distribution of IAA14 and DII-VENUS protein in response to a simulated auxin source in the primordium. A key experiment then is to obtain and quantify DII-VENUS data for root cross-sections at various stages during primordia development and emergence and compare with model predictions. One diffi-

culty that will arise from this highlights a limitation of the model, specifically that over the full time scale of emergence (30 to 40 hours) the model tissue structure remains static, while over the same time period the lateral root primordium undergoes major cell division and growth, with correspondingly large changes to the overlying tissue structure as the new root emerges. However, the data and modelling suggests that the spatial distribution of both auxin and DII-VENUS should respond relatively quickly to the introduction of the primordium auxin signal, so the static tissue is still a useful comparison with data for the early stages of emergence.

Adding cell division and growth to the tissue structure of the model presents a significant technical challenge. Currently both processes can be modelled using the OpenAlea framework, but must be uncoupled from the ODEs governing gene expression and auxin transport, so that the ODE model is run for a time step, the results of which can be used as a decision to divide cells according to some defined rule, and then the cells of the tissue are able to grow according to another set of rules, after which the state of the tissue at that time is used as the initial conditions to run the ODE model for another time step, and so on. Though there are numerous cell divisions occurring within the primordium during development and emergence, these divisions are possibly less important to the question of emergence than the overall growth of the primordium itself, and so the growth of the primordium could initially be modelled as a single cell. However, the more cell divisions occur, and the larger the primordia gets, the more there will in reality be spatial distributions of model components such as auxin within it, so this approach would only be effective up to a point. Defining exactly how the primordia will grow will also be a challenge, and will need to incorporate rules to define both the direction of growth and the change in shape driven by cell divisions. An initial approach may be to evolve the spatial cellular structure over a series of pre-determined ‘snapshots’ of developmental steps with the concentrations in each cell of model components at the end of each time step passed to the corresponding cell at the beginning of the following time step. Confocal images of a single emerging primordium over the full time scale of emergence could be used to determine the change in cellular structure over time. Though such a model could predict the expected auxin distribution and spatial expression pattern of key genes over time for a changing cellular structure, the growth and emergence of the primordium would be pre-determined, with no feedback on growth from auxin regulated gene expression.

The obvious source of feedback from the existing model to the ability of the primordium to emerge is the LAX3 dependent expression of PG in the cortex. Polygalacturonases promote the degradation of pectin, reducing adhesion between adjacent cell walls and allowing cell separation (Swain et al. 2011). The expression of PG in the specific cortical cells over the growing primordium, in addition to the forces generated from primordium growth may be what allows smooth emergence of new lateral roots. Including this feedback in the model, however, is not straightforward and would require the introduction of cell wall mechanics in addition to the programming challenges presented by the inclusion of growth and cell division mentioned

above. In addition to regulation of cell separation from PG, such a model would also need to take into account differential expansion and relaxation of cell walls due to the forces generated by a growing primordium, possibly regulated by the expression of other cell wall remodelling enzymes. Furthermore, the model framework would also need to address the problem of a change in topology of the tissue structure over time as the growing primordium moves between cells in overlying cell layers. This will require rules as to how and when separation occurs. For example, is cell separation modelled by the addition of a new spatial compartment representing a space between cells, or does the number of compartments remain the same, with the cell separation and emergence modelled solely by movement or addition of vertices to the tissue structure?

The current model makes the assumption that since the cellular structure is largely maintained in the direction of root growth, the 2-D cross section used is a reasonable approximation for the radial spread of auxin in the root. Obviously to test this assumption and other questions a true 3-D root simulation is desirable. Additional work will be needed for the software framework to be able to perform the necessary calculations to solve the model in 3-D, and in addition there will be challenges to overcome in order to produce the initial cellular structure used by the model. Finally, different tools will be needed to view the model output in 3-D than are currently used. A more direct way to simulate the spread of auxin and LAX3 in the direction of lateral root growth is to use the existing model with a 2-D cross section of the root in this plane.

Though several challenges remain to be overcome, the multicellular model developed here represents an important first step in creating a more complete model of lateral root emergence that includes the regulation by auxin of genes that feed back on the mechanical processes governing growth and development. The current model and software framework developed may also be used to address additional questions relating to gene regulation and auxin transport during lateral root emergence. In particular the model can be used to simulate the spread of auxin and gene expression in other plant species, such as cereals, with a more complex cellular root structure, and in which the cortex presents a more significant barrier to emergence than in *Arabidopsis*.

Bibliography

- S. Abel and A. Theologis. Early genes and auxin action. *Plant Physiol*, 111 (1):9–17, 1996.
- S. Abel, P. W. Oeller, and A. Theologis. Early auxin-induced genes encode short-lived nuclear proteins. *Proc Natl Acad Sci U S A*, 91(1):326–330, 1994.
- S. Abel, M. D. Nguyen, and A. Theologis. The PS-IAA4/5-like family of early auxin-inducible mRNAs in *Arabidopsis thaliana*. *J Mol Biol*, 251 (4):533–549, 1995.
- G. K. Ackers, A. D. Johnson, and M. A. Shea. Quantitative model for gene regulation by lambda phage repressor. *Proc Natl Acad Sci U S A*, 79(4): 1129–1133, 1982.
- U. Alon. *An Introduction To Systems Biology: Design Principles Of Biological Circuits*. Chapman and Hall/CRC, 2007.
- E. R. Alvarez-Buylla, A. Chaos, M. Aldana, M. Benitez, Y. Cortes-Poza, C. Espinosa-Soto, D. A. Hartasanchez, R. B. Lotto, D. Malkin, G. J. Escalera Santos, and P. Padilla-Longoria. Floral morphogenesis: stochastic explorations of a gene network epigenetic landscape. *PLoS One*, 3(11): e3626, 2008.
- K. Bainbridge, S. Guyomarc’h, E. Bayer, R. Swarup, M. Bennett, T. Mandel, and C. Kuhlemeier. Auxin influx carriers stabilize phyllotactic patterning. *Genes Dev*, 22(6):810–823, 2008.
- L. R. Band and J. R. King. Multiscale modelling of auxin transport in the plant-root elongation zone. *J Math Biol*, 65(4):743–785, 2011.
- L. R. Band, D. M. Wells, A. Larrieu, J. Sun, A. M. Middleton, A. P. French, G. Brunoud, E. Mendocilla Sato, M. H. Wilson, B. Peret, M. Oliva, R. Swarup, I. Sairanen, G. Parry, K. Ljung, T. Beeckman, J. M. Garibaldi, M. Estelle, M. R. Owen, K. Vissenberg, T. C. Hodgman, T. P. Pridmore, J. R. King, T. Vernoux, and M. J. Bennett. Root gravitropism is regulated by a transient lateral auxin gradient controlled by a tipping-point mechanism. *Proc Natl Acad Sci U S A*, 109(12):4668–4673, 2012.
- BBSRC. Overview to food security - BBSRC, 2012. URL <http://www.bbsrc.ac.uk/research/topical/food/food-security-an-overview.aspx>.

- A. Becskei, B. Sraphin, and L. Serrano. Positive feedback in eukaryotic gene networks: cell differentiation by graded to binary response conversion. *EMBO J*, 20(10):2528–2535, 2001.
- R. Benjamins and B. Scheres. Auxin: the looping star in plant development. *Annu Rev Plant Biol*, 59:443–465, 2008.
- E. Benkova and J. Hejtko. Hormone interactions at the root apical meristem. *Plant Mol Biol*, 69(4):383–396, 2009.
- E. Benkova, M. Michniewicz, M. Sauer, T. Teichmann, D. Seifertov, G. Jrgens, and J. Friml. Local, efflux-dependent auxin gradients as a common module for plant organ formation. *Cell*, 115(5):591–602, 2003.
- M. J. Bennett, A. Marchant, H. G. Green, S. T. May, S. P. Ward, P. A. Millner, A. R. Walker, B. Schulz, and K. A. Feldmann. Arabidopsis AUX1 gene: a permease-like regulator of root gravitropism. *Science*, 273(5277):948–950, 1996.
- R. P. Bhalerao, J. Eklof, K. Ljung, A. Marchant, M. J. Bennett, and G. Sandberg. Shoot-derived auxin is essential for early lateral root emergence in *Arabidopsis* seedlings. *Plant J*, 29(3):325–332, 2002.
- A. Bishopp, H. Help, S. El-Showk, D. Weijers, B. Scheres, J. Friml, E. Benkova, A. P. Mahonen, and Y. Helariutta. A mutually inhibitory interaction between auxin and cytokinin specifies vascular pattern in roots. *Curr Biol*, 21(11):917–926, 2011.
- I. Blilou, J. Xu, M. Wildwater, V. Willemsen, I. Paponov, J. Friml, R. Heidstra, M. Aida, K. Palme, and B. Scheres. The PIN auxin efflux facilitator network controls growth and patterning in *Arabidopsis* roots. *Nature*, 433(7021):39–44, 2005.
- W. Boerjan, M. T. Cervera, M. Delarue, T. Beeckman, W. Dewitte, C. Bellini, M. Caboche, H. Van Onckelen, M. Van Montagu, and D. Inze. Superroot, a recessive mutation in *Arabidopsis*, confers auxin overproduction. *Plant Cell*, 7(9):1405–1419, 1995.
- I. Bohn-Courseau. Auxin: a major regulator of organogenesis. *C R Biol*, 333(4):290–296, 2010.
- L. J. Bridge, G. R. Mirams, M. L. Kieffer, J. R. King, and S. Kepinski. Distinguishing possible mechanisms for auxin-mediated developmental control in *Arabidopsis*: models with two Aux/IAA and ARF proteins, and two target gene-sets. *Math Biosci*, 235(1):32–44, 2012.
- G. Brunoud, D. M. Wells, M. Oliva, A. Larrieu, V. Mirabet, A. H. Burrow, T. Beeckman, S. Kepinski, J. Traas, M. J. Bennett, and T. Vernoux. A novel sensor to map auxin response and distribution at high spatio-temporal resolution. *Nature*, 482(7383):103–106, 2012.

- I. Casimiro, A. Marchant, R. P. Bhalerao, T. Beeckman, S. Dhooge, R. Swarup, N. Graham, D. Inze, G. Sandberg, P. J. Casero, and M. Bennett. Auxin transport promotes *Arabidopsis* lateral root initiation. *Plant Cell*, 13(4):843–852, 2001.
- N. Cholodny. Beitrge zur analyse der geotropischen reaktion. *Jahrbuch Wiss. Bot.*, 65:447–459, 1926. (in German).
- F. Darwin and C. Darwin. *the Power of Movement in Plants*. John Murray, 1880.
- P. B. de Reuille, I. Bohn-Courseau, K. Ljung, H. Morin, N. Carraro, C. Godin, and J. Traas. Computer simulations reveal properties of the cell-cell signaling network at the shoot apex in *Arabidopsis*. *Proc Natl Acad Sci U S A*, 103(5):1627–1632, 2006.
- B. De Rybel, V. Vassileva, B. Parizot, M. Demeulenaere, W. Grunewald, D. Audenaert, J. Van Campenhout, P. Overvoorde, L. Jansen, S. Vanneste, B. Muller, M. Wilson, T. Holman, G. Van Isterdael, G. Brunoud, M. Vuylsteke, T. Vernoux, L. De Veylder, D. Inze, D. Weijers, M. J. Bennett, and T. Beeckman. A novel Aux/IAA28 signaling cascade activates GATA23-dependent specification of lateral root founder cell identity. *Curr Biol*, 20(19):1697–1706, 2010.
- I. De Smet, T. Tetsumura, B. De Rybel, N. F. Frey, L. Laplace, I. Casimiro, R. Swarup, M. Naudts, S. Vanneste, D. Audenaert, D. Inze, M. J. Bennett, and T. Beeckman. Auxin-dependent regulation of lateral root positioning in the basal meristem of *Arabidopsis*. *Development*, 134(4):681–690, 2007.
- I. De Smet, V. Vassileva, B. De Rybel, M. P. Levesque, W. Grunewald, D. Van Damme, G. Van Noorden, M. Naudts, G. Van Isterdael, R. De Clercq, J. Y. Wang, N. Meuli, S. Vanneste, J. Friml, P. Hilson, G. Jurgens, G. C. Ingram, D. Inze, P. N. Benfey, and T. Beeckman. Receptor-like kinase ACRA restricts formative cell divisions in the *Arabidopsis* root. *Science*, 322(5901):594–597, 2008.
- S. Depuydt and C. S. Hardtke. Hormone signalling crosstalk in plant growth regulation. *Curr Biol*, 21(9):R365–R373, 2011.
- N. Dharmasiri, S. Dharmasiri, A. M. Jones, and M. Estelle. Auxin action in a cell-free system. *Curr Biol*, 13(16):1418–1422, 2003.
- N. Dharmasiri, S. Dharmasiri, and M. Estelle. The F-box protein TIR1 is an auxin receptor. *Nature*, 435(7041):441–445, 2005.
- Z. Ding, B. Wang, I. Moreno, N. Duplkov, S. Simon, N. Carraro, J. Reemer, A. Penck, X. Chen, R. Tejos, P. Skupa, S. Pollmann, J. Mravec, J. Petresek, E. Zazimalova, D. Honys, J. Rolck, A. Murphy, A. Orellana, M. Geisler, and J. Friml. ER-localized auxin transporter PIN8 regulates auxin homeostasis and male gametophyte development in *Arabidopsis*. *Nat Commun*, 3:941, 2012.

- L. Dolan, K. Janmaat, V. Willemsen, P. Linstead, S. Poethig, K. Roberts, and B. Scheres. Cellular organisation of the *Arabidopsis thaliana* root. *Development*, 119(1):71–84, 1993.
- K. A. Dreher, J. Brown, R. E. Saw, and J. Callis. The *Arabidopsis* Aux/IAA protein family has diversified in degradation and auxin responsiveness. *Plant Cell*, 18(3):699–714, 2006.
- J. G. Dubrovsky, M. Sauer, S. Napsucially-Mendivil, M. G. Ivanchenko, J. Friml, S. Shishkova, J. Celenza, and E. Benkova. Auxin acts as a local morphogenetic trigger to specify lateral root founder cells. *Proc Natl Acad Sci U S A*, 105(25):8790–8794, 2008.
- J. R. Dunlap and K. M. Robacker. Nutrient salts promote light-induced degradation of indole-3-acetic acid in tissue culture media. *Plant Physiol*, 88(2):379–382, 1988.
- A. Durbak, H. Yao, and P. McSteen. Hormone signaling in plant development. *Curr Opin Plant Biol*, 15(1):92–96, 2012.
- Bard Ermentrout. *Simulating, Analyzing, and Animating Dynamical Systems: A Guide to XPPAUT for Researchers and Students*. SIAM, Philadelphia, 2002.
- C. Espinosa-Soto, P. Padilla-Longoria, and E. R. Alvarez-Buylla. A gene regulatory network model for cell-fate determination during *Arabidopsis thaliana* flower development that is robust and recovers experimental gene expression profiles. *Plant Cell*, 16(11):2923–2939, 2004.
- J. E. Ferrell and W. Xiong. Bistability in cell signaling: How to make continuous processes discontinuous, and reversible processes irreversible. *Chaos*, 11(1):227–236, 2001.
- Food and Agriculture Organization of the United Nations. World food situation : Fao cereal supply and demand brief, 2012. URL <http://www.fao.org/worldfoodsituation/wfs-home/csdb/en/>.
- J. Friml, E. Benkov, I. Blilou, J. Wisniewska, T. Hamann, K. Ljung, S. Woody, G. Sandberg, B. Scheres, G. Jurgens, and K. Palme. AtPIN4 mediates sink-driven auxin gradients and root patterning in *Arabidopsis*. *Cell*, 108(5):661–673, 2002a.
- J. Friml, J. Wisniewska, E. Benkova, K. Mendgen, and K. Palme. Lateral relocation of auxin efflux regulator PIN3 mediates tropism in *Arabidopsis*. *Nature*, 415(6873):806–809, 2002b.
- J. Friml, A. Vieten, M. Sauer, D. Weijers, H. Schwarz, T. Hamann, R. Offringa, and G. Jurgens. Efflux-dependent auxin gradients establish the apical-basal axis of *Arabidopsis*. *Nature*, 426(6963):147–153, 2003.
- H. Fukaki, S. Tameda, H. Masuda, and M. Tasaka. Lateral root formation is blocked by a gain-of-function mutation in the SOLITARY-ROOT/IAA14 gene of *Arabidopsis*. *Plant J*, 29(2):153–168, 2002.

- H. Fukaki, Y. Nakao, Y. Okushima, A. Theologis, and M. Tasaka. Tissue-specific expression of stabilized SOLITARY-ROOT/IAA14 alters lateral root development in *Arabidopsis*. *Plant J*, 44(3):382–395, 2005.
- L. Glweiler, C. Guan, A. Muller, E. Wisman, K. Mendgen, A. Yephremov, and K. Palme. Regulation of polar auxin transport by AtPIN1 in *Arabidopsis* vascular tissue. *Science*, 282(5397):2226–2230, 1998.
- Z. H. Gonzalez-Carranza, K. A. Elliott, and J. A. Roberts. Expression of polygalacturonases and evidence to support their role during cell separation processes in *Arabidopsis thaliana*. *J Exp Bot*, 58(13):3719–3730, 2007.
- W. M. Gray, S. Kepinski, D. Rouse, O. Leyser, and M. Estelle. Auxin regulates SCF(TIR1)-dependent degradation of Aux/IAA proteins. *Nature*, 414(6861):271–276, 2001.
- V. A. Grieneisen, J. Xu, A. F. Mearns, P. Hogeweg, and B. Scheres. Auxin transport is sufficient to generate a maximum and gradient guiding root growth. *Nature*, 449(7165):1008–1013, 2007.
- G. E. Gudesblat and E. Russinova. Plants grow on brassinosteroids. *Curr Opin Plant Biol*, 14(5):530–537, 2011.
- T. J. Guilfoyle and G. Hagen. Auxin response factors. *Curr Opin Plant Biol*, 10(5):453–460, 2007.
- T. Hamann, E. Benkova, I. Burle, M. Kientz, and G. Jurgens. The *Arabidopsis* BODENLOS gene encodes an auxin response protein inhibiting MONOPTEROS-mediated embryo patterning. *Genes Dev*, 16(13):1610–1615, 2002.
- C. S. Hardtke and T. Berleth. The *Arabidopsis* gene MONOPTEROS encodes a transcription factor mediating embryo axis formation and vascular development. *EMBO J*, 17(5):1405–1411, 1998.
- P. Hinsinger, G. R. Gobran, P. J. Gregory, and W. W. Wenzel. Rhizosphere geometry and heterogeneity arising from root-mediated physical and chemical processes. *New Phytol*, 168(2):293–303, 2005.
- F. Hochholdinger and R. Zimmermann. Conserved and diverse mechanisms in root development. *Curr Opin Plant Biol*, 11(1):70–74, 2008.
- F. Hochholdinger, W. J. Park, M. Sauer, and K. Woll. From weeds to crops: genetic analysis of root development in cereals. *Trends Plant Sci*, 9(1):42–48, 2004.
- A. Hodge. Plastic plants and patchy soils. *J Exp Bot*, 57(2):401–411, 2006.
- P. D. Jenik, C. S. Gillmor, and W. Lukowitz. Embryonic patterning in *Arabidopsis thaliana*. *Annu Rev Cell Dev Biol*, 23:207–236, 2007.

- A. R. Jones, E. M. Kramer, K. Knox, R. Swarup, M. J. Bennett, C. M. Lazarus, H. M. Leyser, and C. S. Grierson. Auxin transport through non-hair cells sustains root-hair development. *Nat Cell Biol*, 11(1):78–84, 2009.
- H. Jonsson and P. Krupinski. Modeling plant growth and pattern formation. *Curr Opin Plant Biol*, 13(1):5–11, 2010.
- H. Jonsson, M. Heisler, G. Venugopala Reddy, V. Agrawal, V. Gor, B. E. Shapiro, E. Mjolsness, and E. M. Meyerowitz. Modeling the organization of the WUSCHEL expression domain in the shoot apical meristem. *Bioinformatics*, 21 Suppl 1:i232–i240, 2005.
- H. Jonsson, M. G. Heisler, B. E. Shapiro, E. M. Meyerowitz, and E. Mjolsness. An auxin-driven polarized transport model for phyllotaxis. *Proc Natl Acad Sci U S A*, 103(5):1633–1638, 2006.
- S. Kepinski and O. Leyser. The *Arabidopsis* F-box protein TIR1 is an auxin receptor. *Nature*, 435(7041):446–451, 2005.
- J. Kim, K. Harter, and A. Theologis. Protein-protein interactions among the Aux/IAA proteins. *Proc Natl Acad Sci U S A*, 94(22):11786–11791, 1997.
- J. Kim, S. Shiu, S. Thoma, W. Li, and S. E. Patterson. Patterns of expansion and expression divergence in the plant polygalacturonase gene family. *Genome Biol*, 7(9):R87, 2006.
- E. M. Kramer. A mathematical model of pattern formation in the vascular cambium of trees. *J Theor Biol*, 216(2):147–158, 2002.
- E. M. Kramer. Computer models of auxin transport: a review and commentary. *J Exp Bot*, 59(1):45–53, 2008.
- E. M. Kramer and M. J. Bennett. Auxin transport: a field in flux. *Trends Plant Sci*, 11(8):382–386, 2006.
- E. M. Kramer, N. L. Frazer, and T. I. Baskin. Measurement of diffusion within the cell wall in living roots of *Arabidopsis thaliana*. *J Exp Bot*, 58(11):3005–3015, 2007.
- P. Krupinski and H. Jonsson. Modeling auxin-regulated development. *Cold Spring Harb Perspect Biol*, 2(2):a001560, 2010.
- L. Laplace, E. Benkova, I. Casimiro, L. Maes, S. Vanneste, R. Swarup, D. Weijers, V. Calvo, B. Parizot, M. B. Herrera-Rodriguez, R. Offringa, N. Graham, P. Doumas, J. Friml, D. Bogusz, T. Beeckman, and M. J. Bennett. Cytokinins act directly on lateral root founder cells to inhibit root initiation. *Plant Cell*, 19(12):3889–3900, 2007.
- A. Larrieu. *Dissection of the auxin response pathway using functional and chemical genetic approaches*. PhD thesis, The University of Nottingham, 2011.

- M. Laskowski, S. Biller, K. Stanley, T. Kajstura, and R. Prusty. Expression profiling of auxin-treated *Arabidopsis* roots: toward a molecular analysis of lateral root emergence. *Plant Cell Physiol*, 47(6):788–792, 2006.
- M. Laskowski, V. A. Grieneisen, H. Hofhuis, C. A. Ten Hove, P. Hogeweg, A. F. Maree, and B. Scheres. Root system architecture from coupling cell shape to auxin transport. *PLoS Biol*, 6(12):e307, 2008.
- M. Laurent and N. Kellershohn. Multistability: a major means of differentiation and evolution in biological systems. *Trends Biochem Sci*, 24(11):418–422, 1999.
- T. Lenser, G. Theissen, and P. Dittrich. Developmental robustness by obligate interaction of class B floral homeotic genes and proteins. *PLoS Comput Biol*, 5(1):e1000264, 2009.
- B. I. Linkohr, L. C. Williamson, A. H. Fitter, and H. M. Leyser. Nitrate and phosphate availability and distribution have different effects on root system architecture of *Arabidopsis*. *Plant J*, 29(6):751–760, 2002.
- K. Ljung, R. P. Bhalerao, and G. Sandberg. Sites and homeostatic control of auxin biosynthesis in *Arabidopsis* during vegetative growth. *Plant J*, 28(4):465–474, 2001.
- K. Ljung, A. K. Hull, M. Kowalczyk, A. Marchant, J. Celenza, J. D. Cohen, and G. Sandberg. Biosynthesis, conjugation, catabolism and homeostasis of indole-3-acetic acid in *Arabidopsis thaliana*. *Plant Mol Biol*, 49(3-4):249–272, 2002.
- J. C. Locke, A. J. Millar, and M. S. Turner. Modelling genetic networks with noisy and varied experimental data: the circadian clock in *Arabidopsis thaliana*. *J Theor Biol*, 234(3):383–393, 2005.
- S. A. Lokerse and D. Weijers. Auxin enters the matrix—assembly of response machineries for specific outputs. *Curr Opin Plant Biol*, 12(5):520–526, 2009.
- J. Lopez-Bucio, A. Cruz-Ramirez, and L. Herrera-Estrella. The role of nutrient availability in regulating root architecture. *Curr Opin Plant Biol*, 6(3):280–287, 2003.
- J. Lynch. Root architecture and plant productivity. *Plant Physiol*, 109(1):7–13, 1995.
- J. E. Malamy and P. N. Benfey. Organization and cell differentiation in lateral roots of *Arabidopsis thaliana*. *Development*, 124(1):33–44, 1997.
- Y. Mano and K. Nemoto. The pathway of auxin biosynthesis in plants. *J Exp Bot*, 63(8):2853–2872, 2012.
- A. Marchant, R. Bhalerao, I. Casimiro, J. Eklof, P. J. Casero, M. J. Bennett, and G. Sandberg. AUX1 promotes lateral root formation by facilitating indole-3-acetic acid distribution between sink and source tissues in the *Arabidopsis* seedling. *Plant Cell*, 14(3):589–597, 2002.

- A. M. Middleton, J. R. King, M. J. Bennett, and M. R. Owen. Mathematical modelling of the Aux/IAA negative feedback loop. *Bull Math Biol*, 72(6):1383–1407, 2010.
- A. M. Middleton, S. Ubeda-Tomas, J. Griffiths, T. Holman, P. Hedden, S. G. Thomas, A. L. Phillips, M. J. Holdsworth, M. J. Bennett, J. R. King, and M. R. Owen. Mathematical modeling elucidates the role of transcriptional feedback in gibberellin signaling. *Proc Natl Acad Sci U S A*, 109(19):7571–7576, 2012.
- K. Mockaitis and M. Estelle. Auxin receptors and plant development: a new signaling paradigm. *Annu Rev Cell Dev Biol*, 24:55–80, 2008.
- J. Mravec, M. Kubes, A. Bielach, V. Gaykova, J. Petresek, P. Skupa, S. Chand, E. Benkova, E. Zazimalova, and J. Friml. Interaction of PIN and PGP transport mechanisms in auxin distribution-dependent development. *Development*, 135(20):3345–3354, 2008.
- J. Mravec, P. Skopa, A. Bailly, K. Hoyerova, P. Krecek, A. Bielach, J. Petresek, J. Zhang, V. Gaykova, Y. D. Stierhof, P. I. Dobrev, K. Schwarzerova, J. Rolcik, D. Seifertova, C. Luschnig, E. Benkova, E. Zazimalova, M. Geisler, and J. Friml. Subcellular homeostasis of phytohormone auxin is mediated by the ER-localized PIN5 transporter. *Nature*, 459(7250):1136–1140, 2009.
- A. Muller, C. Guan, L. Galweiler, P. Tanzler, P. Huijser, A. Marchant, G. Parry, M. Bennett, E. Wisman, and K. Palme. AtPIN2 defines a locus of *Arabidopsis* for root gravitropism control. *EMBO J*, 17(23):6903–6911, 1998.
- D. Muraro, H. Byrne, J. King, U. Voss, J. Kieber, and M. Bennett. The influence of cytokinin-auxin cross-regulation on cell-fate determination in *Arabidopsis thaliana* root development. *J Theor Biol*, 283(1):152–167, 2011.
- C. Mussig, G. Shin, and T. Altmann. Brassinosteroids promote root growth in *Arabidopsis*. *Plant Physiol*, 133(3):1261–1271, 2003.
- R. Narsai, K. A. Howell, A. H. Millar, N. O’Toole, I. Small, and J. Whelan. Genome-wide analysis of mRNA decay rates and their determinants in *Arabidopsis thaliana*. *Plant Cell*, 19(11):3418–3436, 2007.
- J. L. Nemhauser, L. J. Feldman, and P. C. Zambryski. Auxin and ETTIN in *Arabidopsis* gynoecium morphogenesis. *Development*, 127(18):3877–3888, 2000.
- A. Nordstrom, P. Tarkowski, D. Tarkowska, R. Norbaek, C. Astot, K. Dolezal, and G. Sandberg. Auxin regulation of cytokinin biosynthesis in *Arabidopsis thaliana*: a factor of potential importance for auxin-cytokinin-regulated development. *Proc Natl Acad Sci U S A*, 101(21):8039–8044, 2004.

- J. Normanly. Approaching cellular and molecular resolution of auxin biosynthesis and metabolism. *Cold Spring Harb Perspect Biol*, 2(1):a001594, 2010.
- M. Ogawa, P. Kay, S. Wilson, and S. M. Swain. ARABIDOPSIS DEHISCENCE ZONE POLYGALACTURONASE1 (ADPG1), ADPG2, and QUARTET2 are polygalacturonases required for cell separation during reproductive development in *Arabidopsis*. *Plant Cell*, 21(1):216–233, 2009.
- Y. Okushima, P. J. Overvoorde, K. Arima, J. M. Alonso, A. Chan, C. Chang, J. R. Ecker, B. Hughes, A. Lui, D. Nguyen, C. Onodera, H. Quach, A. Smith, G. Yu, and A. Theologis. Functional genomic analysis of the AUXIN RESPONSE FACTOR gene family members in *Arabidopsis thaliana*: unique and overlapping functions of ARF7 and ARF19. *Plant Cell*, 17(2):444–463, 2005.
- Y. Okushima, H. Fukaki, M. Onoda, A. Theologis, and M. Tasaka. ARF7 and ARF19 regulate lateral root formation via direct activation of LBD/ASL genes in *Arabidopsis*. *Plant Cell*, 19(1):118–130, 2007.
- K. S. Osmont, R. Sibout, and C. S. Hardtke. Hidden branches: developments in root system architecture. *Annu Rev Plant Biol*, 58:93–113, 2007.
- F. Ouellet, P. J. Overvoorde, and A. Theologis. IAA17/AXR3: biochemical insight into an auxin mutant phenotype. *Plant Cell*, 13(4):829–841, 2001.
- P. J. Overvoorde, Y. Okushima, J. M. Alonso, A. Chan, C. Chang, J. R. Ecker, B. Hughes, A. Liu, C. Onodera, H. Quach, A. Smith, G. Yu, and A. Theologis. Functional genomic analysis of the AUXIN/INDOLE-3-ACETIC ACID gene family members in *Arabidopsis thaliana*. *Plant Cell*, 17(12):3282–3300, 2005.
- I. A. Paponov, W. D. Teale, M. Trebar, I. Blilou, and K. Palme. The PIN auxin efflux facilitators: evolutionary and functional perspectives. *Trends Plant Sci*, 10(4):170–177, 2005.
- B. Parizot, L. Laplaze, L. Ricaud, E. Boucheron-Dubuisson, V. Bayle, M. Bonke, I. De Smet, S. R. Poethig, Y. Helariutta, J. Haseloff, D. Chriqui, T. Beeckman, and L. Nussaume. Diarch symmetry of the vascular bundle in *Arabidopsis* root encompasses the pericycle and is reflected in distich lateral root initiation. *Plant Physiol*, 146(1):140–148, 2008.
- W. A. Peer, J. J. Blakeslee, H. Yang, and A. S. Murphy. Seven things we think we know about auxin transport. *Mol Plant*, 4(3):487–504, 2011.
- B. Peret, B. De Rybel, I. Casimiro, E. Benkova, R. Swarup, L. Laplaze, T. Beeckman, and M. J. Bennett. *Arabidopsis* lateral root development: an emerging story. *Trends Plant Sci*, 14(7):399–408, 2009a.

- B. Peret, A. Larrieu, and M. J. Bennett. Lateral root emergence: a difficult birth. *J Exp Bot*, 60(13):3637–3643, 2009b.
- B. Peret, K. Swarup, A. Ferguson, M. Seth, Y. Yang, S. Dhondt, N. James, I. Casimiro, P. Perry, A. Syed, H. Yang, J. Reemmer, E. Venison, C. Howells, M. A. Perez-Amador, J. Yun, J. Alonso, G. T. Beemster, L. Laplaze, A. Murphy, M. J. Bennett, E. Nielsen, and R. Swarup. AUX/LAX genes encode a family of auxin influx transporters that perform distinct functions during *Arabidopsis* development. *Plant Cell*, 24(7):2874–2885, 2012.
- F. Perrine-Walker, P. Doumas, M. Lucas, V. Vaissayre, N. J. Beauchemin, L. R. Band, J. Chopard, A. Crabos, G. Conejero, B. Peret, J. R. King, J. Verdeil, V. Hocher, C. Franche, M. J. Bennett, L. S. Tisa, and L. Laplaze. Auxin carriers localization drives auxin accumulation in plant cells infected by *Frankia* in *Casuarina glauca* actinorhizal nodules. *Plant Physiol*, 154(3):1372–1380, 2010.
- S. V. Petersson, A. I. Johansson, M. Kowalczyk, A. Makoveychuk, J. Y. Wang, T. Moritz, M. Grebe, P. N. Benfey, G. Sandberg, and K. Ljung. An auxin gradient and maximum in the *Arabidopsis* root apex shown by high-resolution cell-specific analysis of IAA distribution and synthesis. *Plant Cell*, 21(6):1659–1668, 2009.
- J. Petresek and J. Friml. Auxin transport routes in plant development. *Development*, 136(16):2675–2688, 2009.
- E. H. Rademacher, B. Muller, A. S. Lokerse, C. I. Llavata-Peris, W. van den Berg, and D. Weijers. A cellular expression map of the *Arabidopsis* AUXIN RESPONSE FACTOR gene family. *Plant J*, 68(4):597–606, 2011.
- J. W. Reed. Roles and activities of Aux/IAA proteins in *Arabidopsis*. *Trends Plant Sci*, 6(9):420–425, 2001.
- D. Reinhardt, E. Pesce, P. Stieger, T. Mandel, K. Baltensperger, M. Bennett, J. Traas, J. Friml, and C. Kuhlemeier. Regulation of phyllotaxis by polar auxin transport. *Nature*, 426(6964):255–260, 2003.
- A. Rolland-Lagan and P. Prusinkiewicz. Reviewing models of auxin canalization in the context of leaf vein pattern formation in *Arabidopsis*. *Plant J*, 44(5):854–865, 2005.
- S. Sabatini, D. Beis, H. Wolkenfelt, J. Murfett, T. Guilfoyle, J. Malamy, P. Benfey, O. Leyser, N. Bechtold, P. Weisbeek, and B. Scheres. An auxin-dependent distal organizer of pattern and polarity in the *Arabidopsis* root. *Cell*, 99:463–472, 1999.
- J. Salmon, J. Ramos, and J. Callis. Degradation of the auxin response factor ARF1. *Plant J*, 54(1):118–128, 2008.
- A. Santner and M. Estelle. Recent advances and emerging trends in plant hormone signalling. *Nature*, 459(7250):1071–1078, 2009.

- A. Sato and K. T. Yamamoto. What's the physiological role of domain II-less Aux/IAA proteins? *Plant Signal Behav*, 3(7):496–497, 2008.
- M. Sauer and J. Kleine-Vehn. AUXIN BINDING PROTEIN1: the outsider. *Plant Cell*, 23(6):2033–2043, 2011.
- E. Scarpella, D. Marcos, J. Friml, and T. Berleth. Control of leaf vascular patterning by polar auxin transport. *Genes Dev*, 20(8):1015–1027, 2006.
- X. Shan, J. Yan, and D. Xie. Comparison of phytohormone signaling mechanisms. *Curr Opin Plant Biol*, 15(1):84–91, 2012.
- L. E. Sieburth. Auxin is required for leaf vein pattern in *Arabidopsis*. *Plant Physiol*, 121(4):1179–1190, 1999.
- S. Simon and J. Petresek. Why plants need more than one type of auxin. *Plant Sci*, 180(3):454–460, 2011.
- R. S. Smith and E. M. Bayer. Auxin transport-feedback models of patterning in plants. *Plant Cell Environ*, 32(9):1258–1271, 2009.
- R. S. Smith, S. Guyomarc'h, T. Mandel, D. Reinhardt, C. Kuhlemeier, and P. Prusinkiewicz. A plausible model of phyllotaxis. *Proc Natl Acad Sci U S A*, 103(5):1301–1306, 2006.
- S. Smith and I. De Smet. Root system architecture: insights from *Arabidopsis* and cereal crops. *Philos Trans R Soc Lond B Biol Sci*, 367(1595):1441–1452, 2012.
- K. Sorefan, T. Girin, S.J. Liljegren, K. Ljung, P. Robles, C.S. Galvan-Ampudia, R. Offringa, J. Friml, M.F. Yanofsky, and L. Ostergaard. A regulated auxin minimum is required for seed dispersal in *Arabidopsis*. *Nature*, 459(7246):583–586, 2009.
- P. E. Staswick, B. Serban, M. Rowe, I. Tiryaki, M. T. Maldonado, M. C. Maldonado, and W. Suza. Characterization of an *Arabidopsis* enzyme family that conjugates amino acids to indole-3-acetic acid. *Plant Cell*, 17(2):616–627, 2005.
- S. Swain, P. Kay, and M. Ogawa. Preventing unwanted breakups: using polygalacturonases to regulate cell separation. *Plant Signal Behav*, 6(1):93–97, 2011.
- K. Swarup, E. Benkov, R. Swarup, I. Casimiro, B. Peret, Y. Yang, G. Parry, E. Nielsen, I. De Smet, S. Vanneste, M. P. Levesque, D. Carrier, N. James, V. Calvo, K. Ljung, E. Kramer, R. Roberts, N. Graham, S. Marillonnet, K. Patel, J. D. Jones, C. G. Taylor, D. P. Schachtman, S. May, G. Sandberg, P. Benfey, J. Friml, I. Kerr, T. Beeckman, L. Laplaze, and M. J. Bennett. The auxin influx carrier LAX3 promotes lateral root emergence. *Nat Cell Biol*, 10(8):946–954, 2008.

- R. Swarup, E. M. Kramer, P. Perry, K. Knox, H. M. Leyser, J. Haseloff, G. T. Beemster, R. Bhalerao, and M. J. Bennett. Root gravitropism requires lateral root cap and epidermal cells for transport and response to a mobile auxin signal. *Nat Cell Biol*, 7(11):1057–1065, 2005.
- H. Szemenyei, M. Hannon, and J. A. Long. TOPLESS mediates auxin-dependent transcriptional repression during arabidopsis embryogenesis. *Science*, 319(5868):1384–1386, 2008.
- X. Tan, L. I. Calderon-Villalobos, M. Sharon, C. Zheng, C. V. Robinson, M. Estelle, and N. Zheng. Mechanism of auxin perception by the TIR1 ubiquitin ligase. *Nature*, 446(7136):640–645, 2007.
- W. D. Teale, I. A. Paponov, and K. Palme. Auxin in action: signalling, transport and the control of plant growth and development. *Nat Rev Mol Cell Biol*, 7(11):847–859, 2006.
- Q. Tian and J. W. Reed. Control of auxin-regulated root development by the *Arabidopsis thaliana* SHY2/IAA3 gene. *Development*, 126(4):711–721, 1999.
- S. B. Tiwari, G. Hagen, and T. Guilfoyle. The roles of auxin response factor domains in auxin-responsive transcription. *Plant Cell*, 15(2):533–543, 2003.
- S. B. Tiwari, G. Hagen, and T. J. Guilfoyle. Aux/IAA proteins contain a potent transcriptional repression domain. *Plant Cell*, 16(2):533–543, 2004.
- S. Ubeda-Tomas, R. Swarup, J. Coates, K. Swarup, L. Laplaze, G. T. Beemster, P. Hedden, R. Bhalerao, and M. J. Bennett. Root growth in arabidopsis requires gibberellin/DELLA signalling in the endodermis. *Nat Cell Biol*, 10(5):625–628, 2008.
- T. Ulmasov, G. Hagen, and T. J. Guilfoyle. ARF1, a transcription factor that binds to auxin response elements. *Science*, 276(5320):1865–1868, 1997a.
- T. Ulmasov, J. Murfett, G. Hagen, and T. J. Guilfoyle. Aux/IAA proteins repress expression of reporter genes containing natural and highly active synthetic auxin response elements. *Plant Cell*, 9(11):1963–1971, 1997b.
- T. Ulmasov, G. Hagen, and T. J. Guilfoyle. Dimerization and DNA binding of auxin response factors. *Plant J*, 19(3):309–319, 1999a.
- T. Ulmasov, G. Hagen, and T. J. Guilfoyle. Activation and repression of transcription by auxin-response factors. *Proc Natl Acad Sci U S A*, 96(10):5844–5849, 1999b.
- S. Vanneste, B. De Rybel, G. T. Beemster, K. Ljung, I. De Smet, G. Van Isterdael, M. Naudts, R. Iida, W. Gruissem, M. Tasaka, D. Inze, H. Fukaki,

- and Tom Beeckman. Cell cycle progression in the pericycle is not sufficient for SOLITARY ROOT/IAA14-mediated lateral root initiation in *Arabidopsis thaliana*. *Plant Cell*, 17(11):3035–3050, 2005.
- T. Vernoux, G. Brunoud, E. Farcot, V. Morin, H. Van den Daele, J. Legrand, M. Oliva, P. Das, A. Larrieu, D. Wells, Y. Guedon, L. Armitage, F. Picard, S. Guyomarc'h, C. Cellier, G. Parry, R. Koumproglou, J. H. Doonan, M. Estelle, C. Godin, S. Kepinski, M. Bennett, L. De Veylder, and J. Traas. The auxin signalling network translates dynamic input into robust patterning at the shoot apex. *Mol Syst Biol*, 7:508, 2011.
- D. Weijers, M. Sauer, O. Meurette, J. Friml, K. Ljung, G. Sandberg, P. Hooykaas, and R. Offringa. Maintenance of embryonic auxin distribution for apical-basal patterning by PIN-FORMED-dependent auxin transport in *Arabidopsis*. *Plant Cell*, 17(9):2517–2526, 2005.
- F. Went. On growth accelerating substances in the coleoptile of *Avena sativa*. *Proc. K. Akad. Wetensch. Amsterdam*, 30:10–19, 1926.
- J. C. Wilmoth, S. Wang, S. B. Tiwari, A. D. Joshi, G. Hagen, T. J. Guilfoyle, J. M. Alonso, J. R. Ecker, and J. W. Reed. NPH4/ARF7 and ARF19 promote leaf expansion and auxin-induced lateral root formation. *Plant J*, 43(1):118–130, 2005.
- A. W. Woodward and B. Bartel. Auxin: regulation, action, and interaction. *Ann Bot*, 95(5):707–735, 2005.
- World Health Organisation. WHO: Food Security, 2012a. URL <http://www.who.int/trade/glossary/story028/en/>, <http://www.emro.who.int/nutrition/food-security/>.
- World Health Organisation. WHO: Food Security - Nutrition, 2012b. URL <http://www.emro.who.int/nutrition/food-security/>.
- C. K. Worley, N. Zenser, J. Ramos, D. Rouse, O. Leyser, A. Theologis, and J. Callis. Degradation of Aux/IAA proteins is essential for normal auxin signalling. *Plant J*, 21(6):553–562, 2000.
- E. Zazimalova, A. S. Murphy, H. Yang, K. Hoyerov, and P. Hosek. Auxin transporters—why so many? *Cold Spring Harb Perspect Biol*, 2(3):a001552, 2010.
- N. Zenser, A. Ellsmore, C. Leasure, and J. Callis. Auxin modulates the degradation rate of Aux/IAA proteins. *Proc Natl Acad Sci U S A*, 98(20):11795–11800, 2001.
- H. Zhang and B. G. Forde. An arabidopsis MADS box gene that controls nutrient-induced changes in root architecture. *Science*, 279(5349):407–409, 1998.